3D Structural Characterization of Mesoporous Materials by Electron Tomography

TECHNISCHE
UNIVERSITÄT
DARMSTADT

Dissertation approved by

the Department of Materials- and Geosciences,

Technical University of Darmstadt

in fulfilment of the requirements for the degree of

Doctor rerum naturalium

(Dr. rer. nat.)

by

Xiaohui Huang

M.Sc. in Physical Chemistry

Born on December 13, 1993 at Yulin, Guangxi, China

Referee: Prof. Dr. Christian Kübel

Co-referee: Prof. Dr. Ulrich Tallarek

Date of submission: 03.11.2022

Date of oral exam: 20.12.2022

Darmstadt 2022

Erklärung zur Abschlussarbeit
gemäß § 22 Abs. 7 und § 23 Abs. 7 APB der TU Darmstadt

Hiermit versichere ich, Xiaohui Huang, die vorliegende Doctoral dissertation ohne Hilfe Dritter und nur mit den angegebenen Quellen und Hilfsmitteln angefertigt zu haben. Alle Stellen, die Quellen entnommen wurden, sind als solche kenntlich gemacht worden. Diese Arbeit hat in gleicher oder ähnlicher Form noch keiner Prüfungsbehörde vorgelegen.

Mir ist bekannt, dass im Fall eines Plagiats (§ 38 Abs. 2 APB) ein Täuschungsversuch vorliegt, der dazu führt, dass die Arbeit mit 5,0 bewertet und damit ein Prüfungsversuch verbraucht wird. Abschlussarbeiten dürfen nur einmal wiederholt werden.

Bei der abgegebenen Thesis stimmen die schriftliche und die zur Archivierung eingereichte elektronische Fassung gemäß § 23 Abs. 7 APB überein.

Bei einer Thesis des Fachbereichs Architektur entspricht die eingereichte elektronische Fassung dem vorgestellten Modell und den vorgelegten Plänen.

Darmstadt, 8. Februar 2023

_____

F. Surname

Abstract

Mesoporous materials, with pore size of 2-50 nm, are gaining increasing attention in applications such as gas separation, purification of wastewater, energy storage, drug deliver and catalytic processes due to their high surface area, tunable pore structure and large pore volume. In all of these applications, the desired performance depends strongly on the pore structure, such as pore size, pore length, tortuosity, volume and connectivity. Understanding the structure-performance relationship and exploiting it to the development of advanced mesoporous materials require an unambiguous understanding of the three dimensional (3D) pore structures. This requires reliable relevant characterization techniques. Electron tomography (ET) is a powerful technique to obtain 3D morphological information at the corresponding length scale for mesoporous materials. A very promising feature of ET is that no prior assumptions on the pore shape are needed, which is normally inevitable when using traditional diffraction or diffusion based bulk characterization techniques, allowing it to be particularly suitable for analyzing complex disordered pore structures.

However, an accurate quantitative interpretation of the solid/void network from ET is still a challenge. The reconstruction of a 3D volume from a tilt series is mathematically an underdetermined problem due to the discrete sampling and limited practical tilt range, which means that there is no analytical solution and an approximation to the original structure is therefore pursued using appropriate algorithms. In addition, constraints and imperfections (e.g. noise, limited tilting parameters and misalignment of projections) in an experimental setup inevitably cause artifacts and errors in the final reconstruction. The overall aim of the thesis is to develop and evaluate approaches to extract an accurate quantitative 3D morphological description of the pore network in mesoporous materials. To achieve this, two aspects are considered: evaluating the reconstruction performance and improving the experimental methodology.

In a fundamental study, the reconstruction accuracy of the three main-stream algorithms simultaneous iterative reconstruction technique (SIRT), total variation minimization (TVM) and discrete algebraic reconstruction technique (DART) were systematically investigated for mesoporous materials using different realistic tilt-series based on a set of phantom simulations. While the reconstruction accuracy has been partially addressed in previous publications focusing on the residual number of misclassified pixels, this analysis has been extended to consider effects on the pore morphology and diffusion properties due to aggregated reconstruction artifacts (inhomogeneously distributed misclassified pixels) thereby developing a more relevant estimate of the reconstruction performance. It was found that DART outperforms the other two methods in reliably revealing small pores and narrow channels, especially when the number of projections and the tilt-range are limited. The accurately segmented reconstruction from DART makes it possible to achieve reliable quantification of pores structure, which in turn leads to a reliable evaluation of effective diffusion coefficients. Moreover, the influence of different acquisition and reconstruction parameters on the reconstructed 3D volume and a quantitative analysis of pore features is discussed. With this, a practical guide for optimizing acquisition and reconstruction parameters and how to evaluate the accuracy when describing the mesoporous structure is provided.

As seen in the fundamental parameter study, one of the strongest limitations in electron tomography is the limited tilt-range. To ultimately solve this missing wedge problem, 360° ET can be used by tilting a needle-shaped specimen over the full tilt range and thus filling the missing information. Obviously, the necessity of specimen processing to a needle shape with a diameter of a few tens of nanometer limits this technique for a wide range of materials, e.g. porous materials and any material in form of loose powders. Driven by this consideration, a new universal, yet facile sample preparation method for 360° ET was developed. A single nanoparticle or a few separate nanoparticles are selected in a TEM or SEM and the selected objects with the supporting film are adhered to an easily prepared sharp tungsten tip, which is mounted to a full-range tomography holder tip. This method shows great flexibility and works for almost all types of powder materials without invasive FIB processing directly on the sample. Test results for 360° tomography are shown using a Pt@TiO$_2$ hollow cage catalyst.

Finally, as an example for a real application, ET is applied to uncover the leaching behavior of Pd nanoparticles supported on mesoporous carbon (CMK3) during formic acid decomposition in batch and fixed bed reactors. Using the knowledge from the first part (fundamental study) as guideline, the DART algorithm with optimized reconstruction parameters was used to quantitatively characterize the spatial and size distribution of the Pd nanoparticles in the three Pd@CMK3 catalysts before and after the reaction. A quantitative analysis of the tomographic data enables precise tracking of the evolution of the supported particles with a statistical analysis of the distribution on the internal and external support surface. Based on this quantitative analysis, the evolution of Pd nanoparticles during the catalytic process is discussed and related to the catalytic performance differences observed for the fixed bed and batch reactor. In the future, this information can be used to design catalysts with improved properties to optimize the reaction conditions.

Contents

List of Figures

List of Tables

List of Acronyms

1D	one dimensional
2D	two dimensional
3D	three dimensional
ADM	alternating direction method
ADMET	acyclic diene metathesis
AET	atomic electron tomography
ALM	augmented Lagrangian method
AMS-n	anionic-surfactant-templated mesoporous silica
ART	algebraic Reconstruction Technique
BET	Brunauer–Emmett–Teller
BF	bright field
BFP	back focus plane
BP	Backprojection
BSE	backscattered electrons
Cc	chromatic aberration
CCF	cross-correlation function
CFET	continuous fast ET
CL	cathodoluminescence
CLD	chord length distribution
CM	center of mass
CMK-n	ordered mesoporous carbon
Cn-TMA	alkyltrimethylammonium cationic surfactants
CNTs	carbon nanotubes
Cs	spherical aberration
DART	discrete algebraic reconstruction technique
DF	dark field
DMSNs	dendritic mesoporous silica nanoparticles
EDS	energy dispersive X-ray spectroscopy
EELS	electron energy loss spectroscopy
EFTEM	energy filtered TEM
EMI	Electric and Musical Industries
ET	Electron tomography
etc.	et cetera
FA	formic acid
FDU-n	Fudan University Material
FIB	focus ion beam
GENFIRE	generalized Fourier iterative reconstruction

GIS	gas injection system
HAADF	high-angle annular dark field
HHT	high-heat treated carbon nanofibers
ICP-AES	inductively coupled plasma atomic emission spectrometer
IFET	incremental fast ET
IUPAC	the international Union of Pure and Applied Chemistry
KIT-n	Korea Advanced Institute of Science and Technology
LOHC	liquid orangic hydrogen carriers
MIP	mercury intrusion porosimetry
MMC	macro(mono)cyclization
MSU-n	Michigan State University material
N-CNFs	N-functionalized carbon nanofibers
NaOH	sodium hydroxide
NMCNs	N-doped mesoporous carbon nanospheres
NPs	nanoparticles
ORR	oxygen reduction reaction
PDM	projection distance minimization
PSD	pore size distribution
RCM	ring-closing metathesis
rNMP	relative number of misclassified pixels
ROI	region of interest
SAXS	small-angle X-ray scattering
SBA-15	Santa Barbara Amorphous no 15
SDD	silicon drift EDS detector
SE	secondary electrons
SIRT	simultaneous iterative reconstruction technique
STEM	scanning transmission electron microscopy
TEM	transmission electron microscopy
TVM	total variation minimization
VRT	texture-based volume rendering
WBP	weighted back projection

1. Introduction

In this chapter, a brief history of mesoporous materials, their types, applications and the correlation between pore structure and some of performance aspects will be introduced. This will be followed by a brief introduction of gas adsorption, mercury intrusion porosimetry (MIP) and small-angle X-ray scattering (SAXS) as three bulk characterization techniques for mesoporous materials. A more detailed overview of the application and the state of the art in electron tomography of mesoporous materials will conclude this chapter.

1.1. Motivation and background

Porous media are present in nature at a variety of length scales: sponges that live under water absorb nutrients through centimeter to millimeter interconnecting pores in their bodies; natural cork with micrometer pores has been widely used as stoppers to provide added value to wine by allowing a very small amount of air to gradually enter the bottle, allowing the wine to slowly grow in the bottle, making the wine more mellow; natural zeolites, formed from volcanic rocks and ash layers reacting with alkaline groundwater, have a porous structure with pore size smaller than 1 nm that can accommodate a wide variety of cations (such as K^+, Na^+, Ca^{2+}, Mg^{2+}) and are able to adsorb certain sized molecules. [1] It can be seen that nature is like a craftsman with rich experience, using his ingenious skills to build thousands of pore structures, and the developments in science and technology have further enriched these pore structures. More and more artificial porous materials with sophisticated and complex structures are being constructed and excavated, e.g. porous plastics, porous carbon, porous silicon, porous metals (oxides), porous glass, et cetera (etc.). With the characteristics of large specific surface area, high porosity, low density and high specific strength, porous materials are widely used in various fields, ranging from environment, health, energy to heterogenous catalysis.

Mesoporous materials with pore sizes between 2 to 50 nm have larger pores and allow faster mass transfer than microporous materials. Compared with macroporous materials, they show greater specific surface area and more prominent nano-confinement effects. These outstanding properties make mesoporous materials of great interest to both academia and industry. In the area of environmental protection, mesoporous materials are used for wastewater treatment by adsorbing organic dyes and pollutants from wastewater. [2] In the medical field, mesoporous materials are used as drug carriers and controlled-release systems, controlling the rate and period of drug delivery (i.e. time-release dosage). [3], [4] In the field of energy, mesoporous materials are commonly used as electrodes for energy storage in batteries and capacitors. With the ultra-high specific surface area and tailored pore structure, they are able to improve the storage capacity and the ion transmission efficiency. [5], [6] In heterogenous catalysis, mesoporous materials are utilized in applications such as cracking and other petrochemical conversions, acid/base reactions for fine chemicals synthesis, redox catalysis, etc., which has been well documented in recent reviews. [7]–[9]

In all applications of mesoporous materials, the performance is strongly affected by the specific pore structure. As an example, a heterogenous catalyst consists of a porous support and the active material (Figure

1.1), the main role of porous support is to increase the interaction between reactants and active sites by increasing the dispersion of active sites, thus increasing the catalytic activity. In addition, the stability and catalytic selectivity can also be optimized by tuning the pore size due to confinement effects inside the pores. [10] The variation in pore size and connectivity may also affect the catalytic performance by controlling the diffusion rate of reactants and products during the reaction. [11] More detailed examples of such structure-performance relationships can be seen in section 1.2.4. The development of characterization techniques to understand this pore structures is therefore crucial to design and optimize new, improved materials for catalysis.

Mesoporous support:
Pore size & volume?
Connectivity?
Tortuosity?
Mass transport?

Supported nanoparticles:
Location?
Size?
Shape?
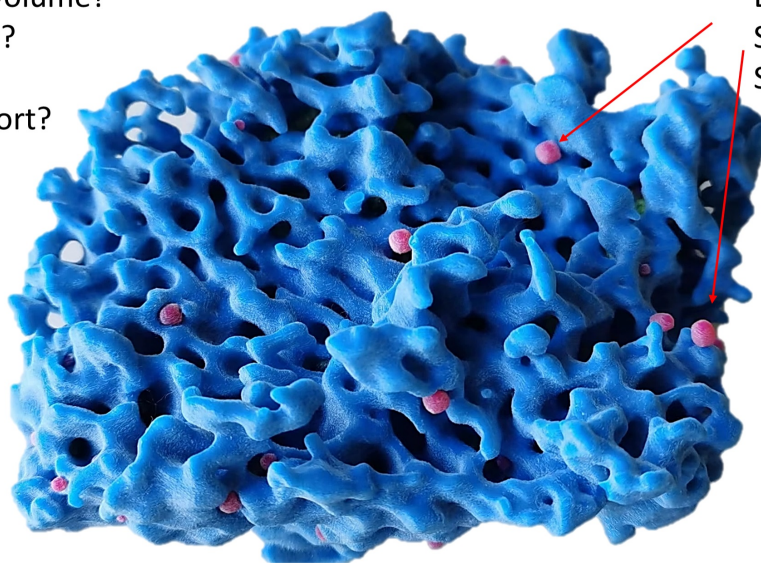
Figure 1.1: Some of the factors that affect the catalytic performance of a heterogenous catalyst consisting of a porous support and the active nanoparticles.

Various characterization techniques have been used to extract pore information from mesoporous materials, such as gas physisorption, MIP and SAXS. However, these bulk measurements rely on an assumption of a specific geometry of the pore shape and are not sufficient to fully describe disordered pore structures. As an alternative, ET has been shown to provide statistically relevant information on pore structures by reconstructing the 3D pore network from a sufficient number of different projections of a porous material. [12]–[14] However, a quantitative interpretation of ET results is still far from straightforward and an accurate quantification of the pore space is challenging because of constraints from the experimental setups during data acquisition such as missing wedge and limited sampling as well as reconstruction artifacts introduced by alignment errors and the reconstruction algorithm. Based on these considerations, the aim of this thesis is to improve the accuracy of tomographic reconstruction of mesoporous structures by using advanced reconstruction algorithms and improved experimental data acquisition.

1.2. Mesoporous materials

According to the definition from the international Union of Pure and Applied Chemistry (IUPAC) in 1985, porous materials are classified into three major categories depending on their pore sizes: microporous materials with pore sizes below 2 nm, mesoporous materials with pore sizes between 2 and 50 nm, and macroporous materials with pore sizes exceeding 50 nm. [15]

1.2.1. Research history

The first report of mesoporous materials came from Yanagisawa et al. [16] in 1990, in which one kind of mesoporous silica with pore size around 2-4 nm was synthesized using ion exchange of the layered polysilicate kanemite with alkyltrimethylammonium cationic surfactants (Cn-TMA). Unfortunately, the limited characterization data in this work led to disregard of their results. In 1992, Kresge et al. [17] from Mobil research and development corporation reported the preparation of a family of ordered mesoporous molecular sieves (M41S) with pore sizes of 1.6-10 nm by a block copolymer template mechanism. Three different mesophases in this family including lamellar (MCM-50) [18], hexagonal (MCM-41) [19] and cubic (MCM-48) [20] phases have been identified by transmission electron microscopy (TEM). These impressive discoveries resulted in a worldwide resurgence and dramatic increase in the number of publications in this area. In 1998, Zhao et al. [21] reported the synthesis of another type of hexagonal array of pores namely Santa Barbara Amorphous no 15 (SBA-15) with tunable pore size (4.6-30 nm). This new mesoporous material has not only shown larger pores and thick pore walls, but also excellent thermal, mechanical and chemical resistance, which makes it a super star and expands its applications in many areas such as catalysis [22], adsorption and separation [23], [24]. Their emerging applications have boosted the development of many other ordered mesoporous silica materials such as Fudan University Material (FDU-n) series [25], [26], Michigan State University material (MSU-n) series [27], Korea Advanced Institute of Science and Technology (KIT-n) series [28] and anionic-surfactant-templated mesoporous silica (AMS-n) series [29]. Meanwhile, ordered mesoporous silica has also been used as a template for the synthesis of other ordered mesoporous materials, such as the families of ordered mesoporous carbon (CMK-n) series: CMK-1 from MCM-48, CMK-2 from SBA-1, CMK-3 from SBA-15, CMK-4 from MCM-48 and CMK-5 from SBA-15. [30]–[32] Figure 1.2 shows the numbers of published papers in the field of mesoporous materials since 1992, according to the web of science, demonstrating the progress in this field.
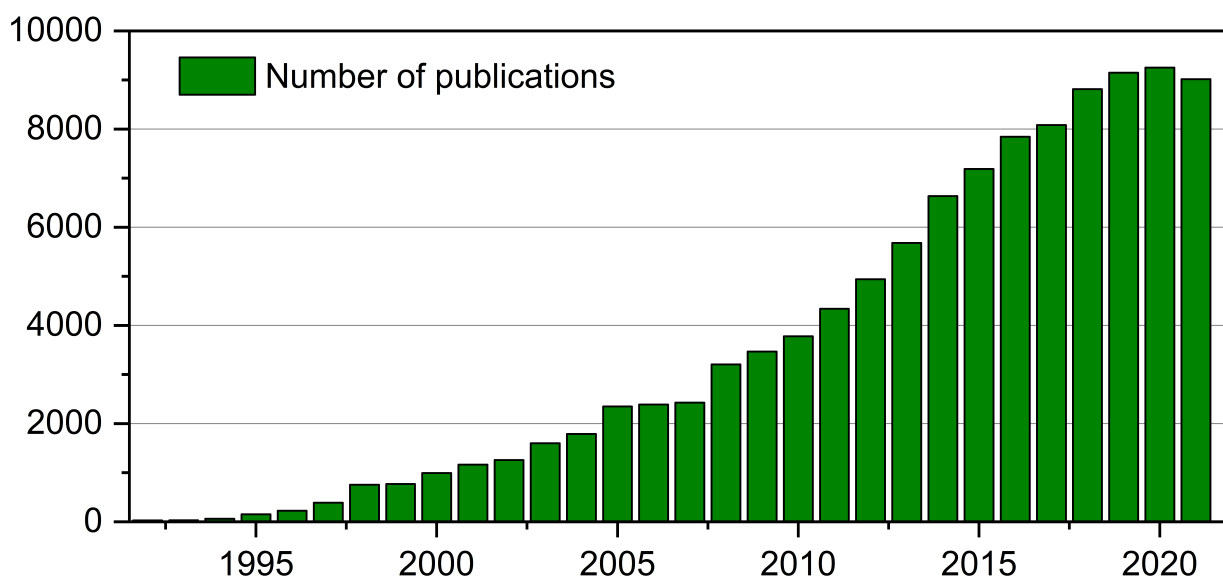
Figure 1.2: Numbers of published papers in the field of mesoporous materials since 1992 (source: web of science).

1.2.2. Types of mesoporous materials

Many types of mesoporous materials have been reported during the past few decades, which include carbon materials [32], carbon nitrides [33], silica materials [34], metal oxides [35], metal sulfides [36], metal nitrides [37] and metal organic frameworks (MOFs) [38]. They can be generally divided into two categories according to the characteristics of the pore arrangement: ordered mesoporous materials and disordered mesoporous materials. It is worth noting that different from traditional crystal structures at the atomic scale, the general designation of "ordered mesoporous materials" is referring to the regular pore space arrangement, whereas the structure of ordered mesoporous material itself is indeed amorphous.

Figure 1.3 shows the representative structure of several ordered mesoporous silica materials. The first one is two-dimensionally ordered hexagonal phase with the $P6mm$ symmetry, which was built by close-packed hexagonal arrays of cylindrical surfactant micelles, such as MCM-41 [19] and SBA-15 [21]. It should be noted that SBA-15 also exhibits large complementary micropores, which are arranged in a disordered fashion interconnecting adjacent mesopores. [39]–[41] The second one represents three-dimensionally ordered cubic phases with different symmetry. For example, the face-centered cubic ($Fm3\bar{m}$) pore structure is regarded as close packing of spherical mesopores, each connected to 12 nearest neighbor mesopores, such as FDU-12 [26] and KIT-5 [42], while for the body-centered cubic ($Im3\bar{m}$) pore structure, each mesopore is connected to 8 neighboring mesopores such as SBA-16 [43] and FDU-1 [25]. Therefore, in a cubic cage structure there can be different spatial arrangements of spherical micelles. The bicontinuous cubic gyroid phase with $Ia3\bar{d}$ symmetry is another even more complex cubic mesophase that can be regarded as 2 interwoven cylindrical channels, which leads to adsorption properties similar to two dimensional (2D) hexagonal materials without pore blocking effects, such as MCM-48 [44] and KIT-6 [28]. Another ordered mesoporous structure with lamellar symmetry such as MCM-50 [18] consists of interlayers.

For disordered mesoporous materials, there is no single structural description such as unit cell, space group and symmetry as for ordered mesoporous materials, since all of them show irregular pore networks. However, these materials can also be described by mesopore characteristics including diameter, length, volume, connectivity and tortuosity. Compared to well-ordered pores, the disordered pore networks allow for a higher
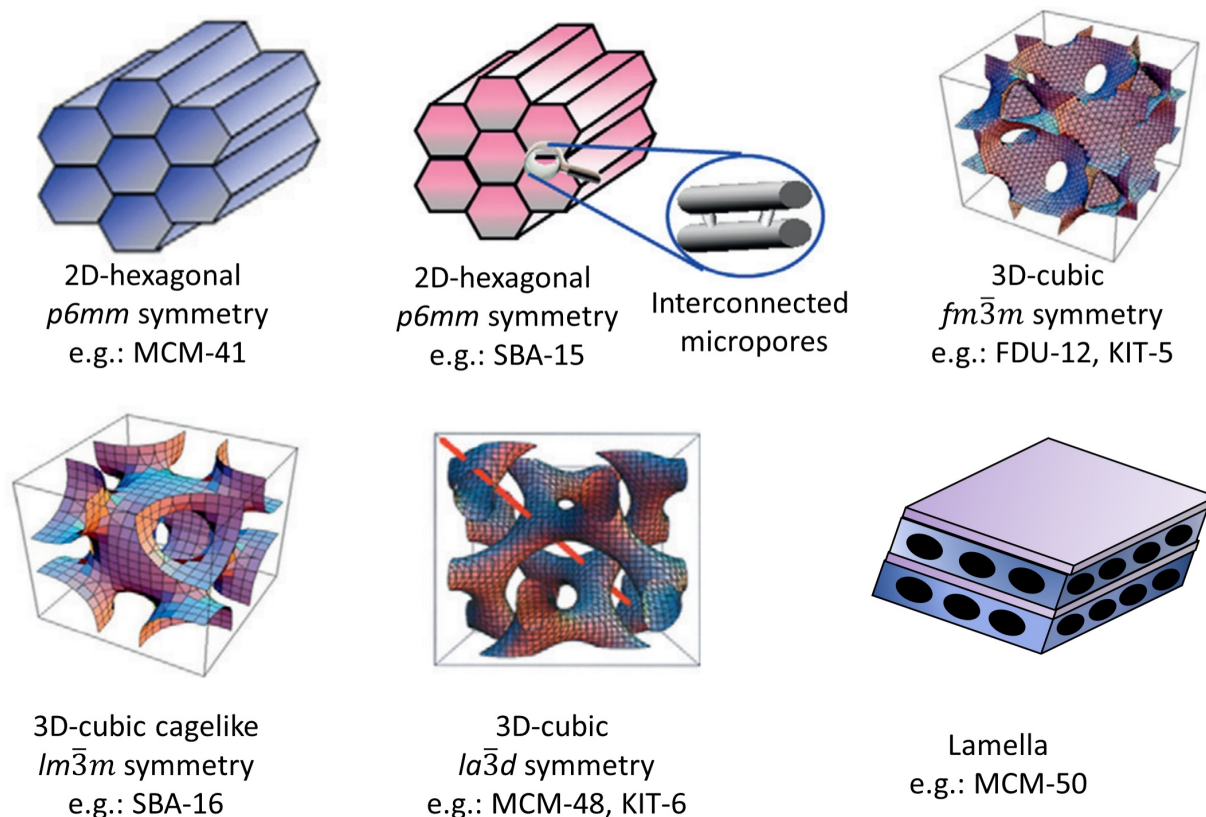
Figure 1.3: Models of different mesoporous structures, including their symmetries and the representative examples (modified from literature [34]).

3D interconnectivity inside the pore domain, providing more variety of the pore structure. Other outstanding properties of such disordered pores can be found in their large surface area, high plasticity, and usually no template is required during the synthesis. Overall, this has resulted in disordered mesoporous materials as an important class of materials with a wide application range in many fields.

To get a better understanding of the pore distribution inside a solid phase, a more generic classification can be used to describe the pores according to their availability to an external fluid. As shown in Figure 1.4a, pores that are completely isolated from their neighbors are described as closed pores (like region a). This type of pore is not contributing to fluid flow and adsorption of gases, but it influences the macroscopic properties of solid materials such as bulk density, mechanical strength and thermal conductivity. In contrast, the pores connected to the external surface of the body are described as open pores. Among them, those open only at one end (like regions b and f) are described as blind or dead-end pores, and others that are open at two ends (like region e) are named as through pores. Pores may also be classified according to their shape, such as cylindrical (cylinder closed at one end or cylinder open at both ends), cone shaped, slit shaped, interstice between closed-packing spheres and inkbottle (Figure 1.4b). These assumptions on the pore shape play an important role for some conventional bulk characterization techniques to extract quantitative pore information, as will be discussed in next section.
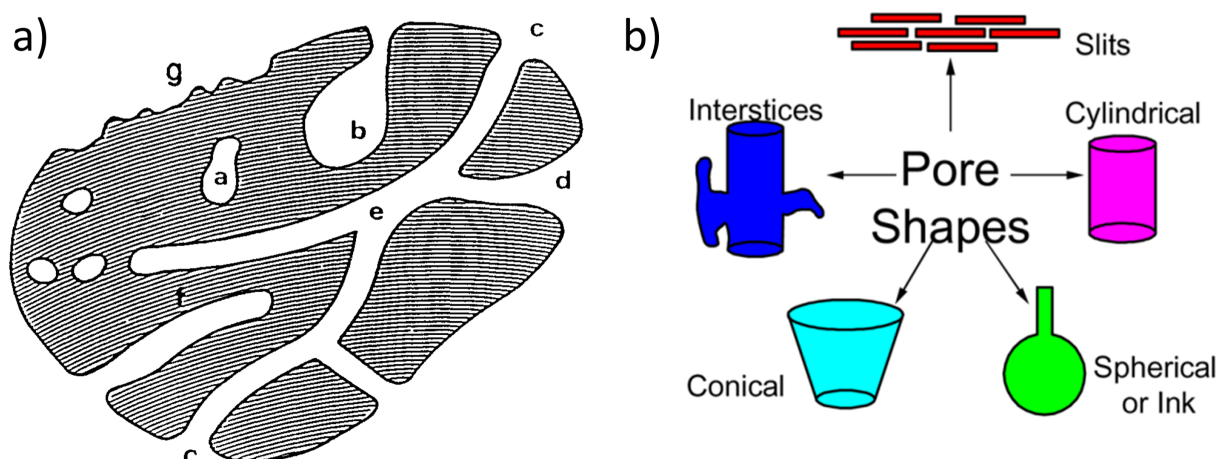
Figure 1.4: (a) Schematic cross-section of a porous solid, adapted from [45] and (b) schematic pore classification, according to their availability to the surrounding, figure adapted from [46].

1.2.3. Application

In addition to application in electrodes, water treatment, drug delivery and heterogenous catalysis mentioned in section 1.1, mesoporous materials have been reported to be used in many other research fields, such as gas storage [47], capturing and binding of carbon dioxide (CO) [48], sensors [49], biomass conversion [50], biodegradation of inorganic materials [51], phase separation in liquid chromatography [52], etc. For medical applications, related works can be seen in magnetic resonance imaging (MRI) studies [53], ultrasound therapy [54], enzyme immobilization [55], antigen targeting [56], etc.

1.2.4. Structure-performance relationship of mesoporous materials

In all the applications mentioned above, the performance of mesoporous materials depends on the pore structure including the mesopore size, pore shape, volume, surface area and connectivity. In the case of heterogeneous catalysis, confinement and mass transfer effects have been identified to lead to optimum conditions for the formation of a specific product during the catalytic reaction. As indicated in Figure 1.1, mesoporous materials play an important role as support for the active metal particles by immobilizing them inside the pores, thus improving their stability during catalyst synthesis and catalytic reactions. In addition, defined pore structures not only allow reaction mixtures (including reactant and product molecules) with a certain size to access and detach from the active sites, but also reduce the diffusion speed of large molecules, thus affecting the catalytic activity and selectivity. [10], [57] In contrast to macropores, which are responsible for advection-dominated transport through the material, diffusion-limited transport prevails in the mesoporous space. [11] The complex mesoporous structure tunes the diffusion rate of reactants and products during the chemical reaction, which also influences the activity and selectivity for specific catalytic products. These effects of the mesoporous support enable optimization of the catalytic performance by modifying the pore size and pore morphology based on an understanding of the structure-performance relationship. [58]

For example, Ziegler and coworkers presented a new approach that utilizes spatial confinement to optimize macrocyclization selectivity in olefin metathesis using a Ru catalyst selectively immobilized inside SBA-15 silica with tunable pore size. [59] As shown in Figure 1.5a, parallel reactions of ring-closing metathesis (RCM) and acyclic diene metathesis (ADMET) oligomerization compete to a substantial extent during olefin

metathesis. For catalysts supported in SBA-15 with the right pore diameter, confinement allows unhindered access to the catalyst only for one single diene molecule at a time, thus blocking simultaneous access of several diene molecules. This results in macrocyclization dominating over oligomerization, leading to an increasing selectivity of the macro(mono)cyclization (MMC) product. However, the conversion shows an opposite trend due to the limited diffusion of reactant molecules inside the SBA-15 particles under experimental conditions (Figure 1.5b). Smaller pore sizes slow down the transport of the reaction mixtures to and from the catalytic centers, which explains the lower activity. In this way, a correlation between the catalytic performance and the pore size of support was established, enabling the determination of a narrow operational window for optimal macrocyclization selectivity.
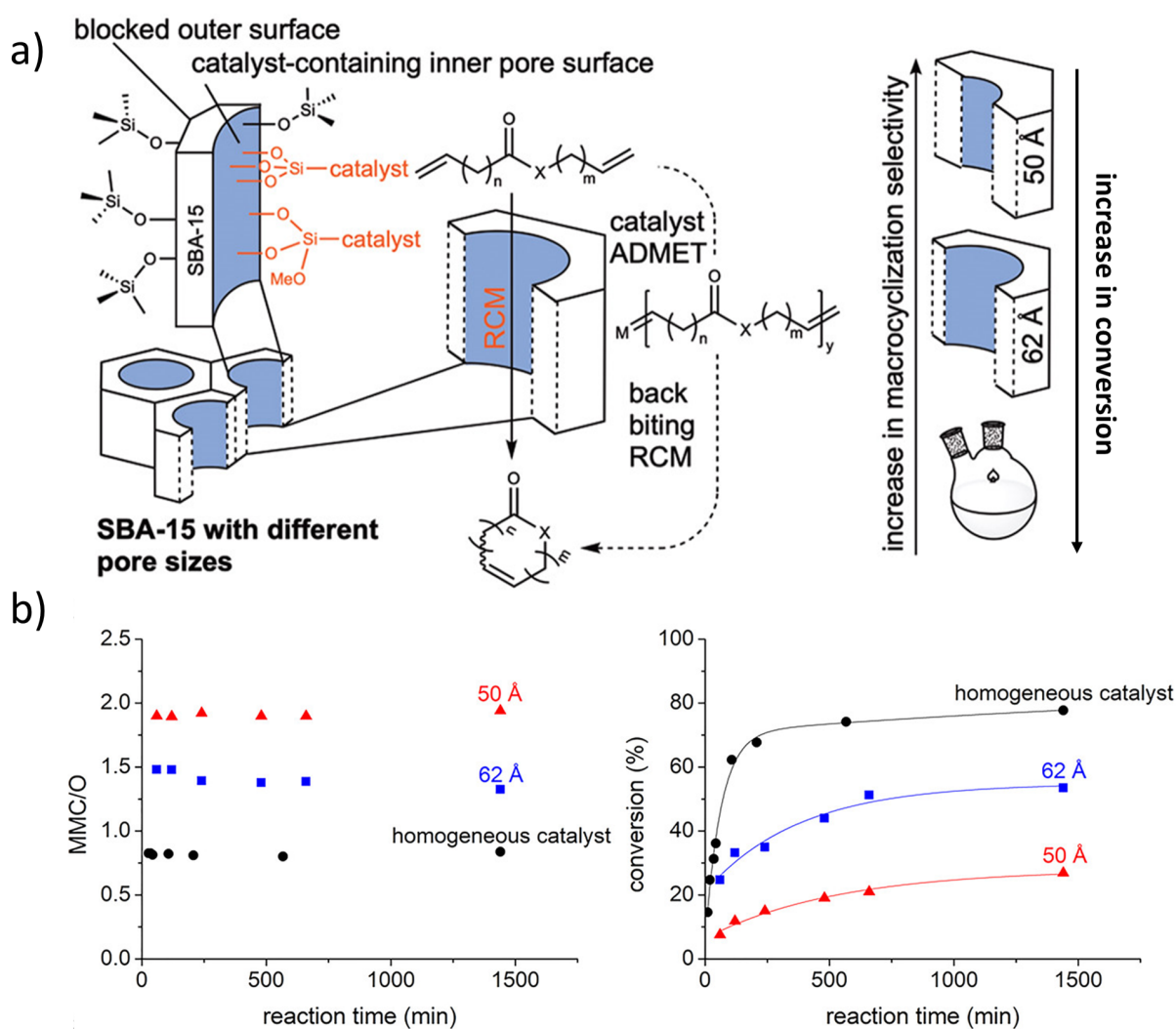
Figure 1.5: (a) Schematic illustration of macrocyclization in confined geometries and (b) the ratio between MMC product and all undesired oligomerization products and conversion as a function of reaction time obtained in the RCM using two SBA-15 supported Ruthenium catalysts with average pore diameters of 5 and 6.2 nm and a homogeneous catalyst, reproduced from [59].

Such tunable catalytic performance affected by pore size can also be seen in the work from Zhao's group, where N-doped mesoporous carbon nanospheres (NMCNs) with large tunable pore sizes showed different

electrocatalytic activity in oxygen reduction reaction (ORR) as shown in Figure 1.6a,b. [60] With increasing pore size, the onset potential is shifted to more positive values and the limiting current density becomes higher, resulting in a better electrocatalytic activity for the ORR. As another example, by constructing a set of Au/TiO$_2$ catalysts (Figure 1.6c,d), where Au nanoparticles are immobilized on hierarchical bouquet-like mesoporous TiO$_2$ supports with different porous frameworks, the same group showed the dependence of the catalytic performance for cis-semihydrogenation of alkynes on the pore morphology. [61] Both the activity and selectivity increase with the increasing architectural complexity of the mesoporous TiO$_2$. This performance improvement is attributed to an efficient mass transfer due to the high interconnectivity of the mesopores inside the super-structured support, providing an increasing interaction between the active sites and surrounding reactants.
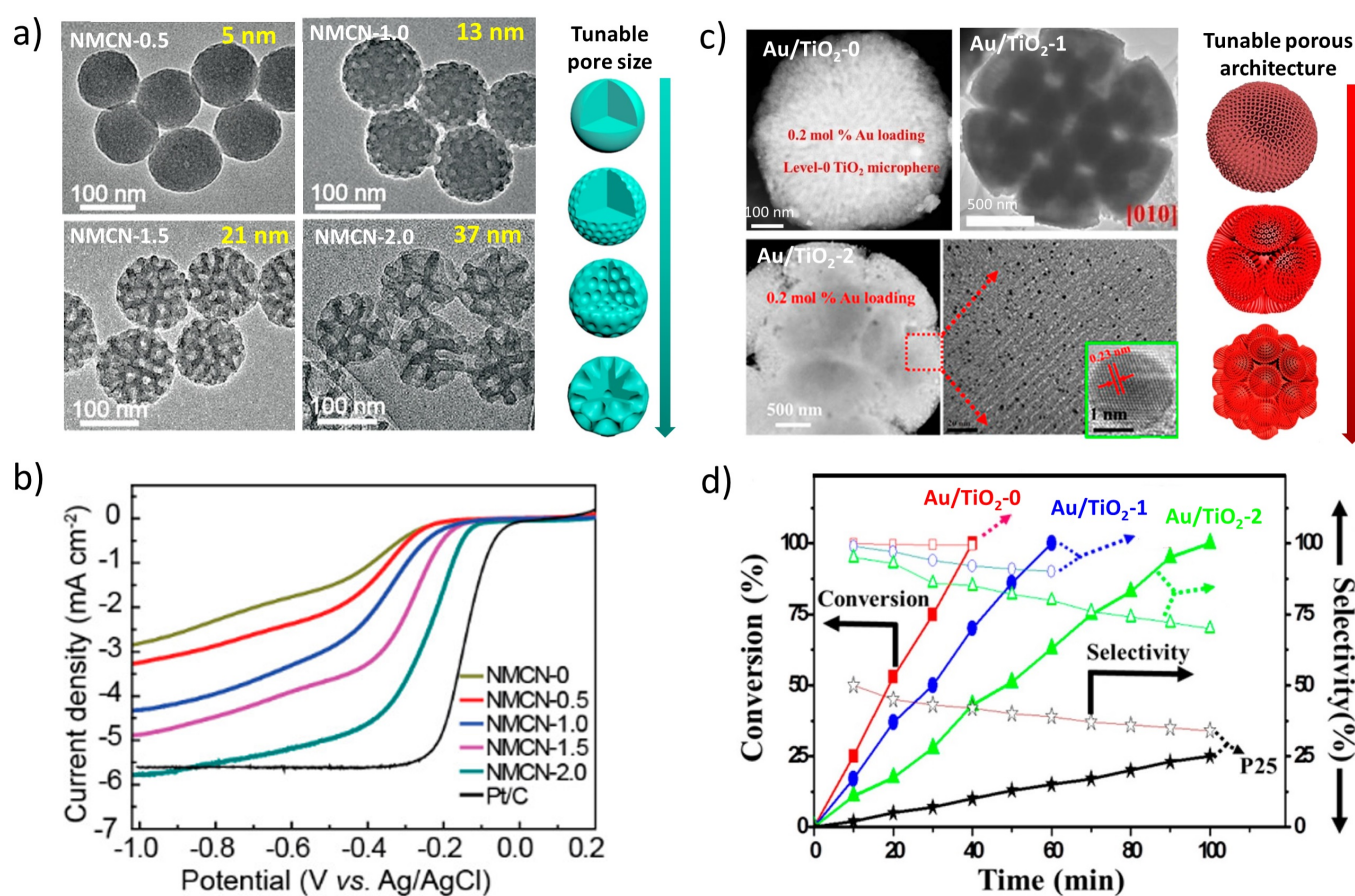
Figure 1.6: (a) Illustration and scanning electron microscopy images of NMCNs with various pore sizes, (b) ORR catalytic activities of the series of NMCNs and Pt/C electrodes, modified from [60]. (c) Illustration and (S)TEM images of Au/TiO$_2$ catalysts with various architectural TiO$_2$ supports, and (d) semi-hydrogenation performance of the 3D mesoporous bouquet-posy-like TiO$_2$ superstructure supported catalysts, modified from [61].

For usage in drug delivery, mesoporous materials are usually soaked in a highly concentrated drug solution before drying to incorporate the medication. The release rate can be experimentally measured by emerging the drug-charged carriers into simulated target fluids (e.g. stomach or proximal intestine fluids) and following the drug concentration evolution. Both incorporation and release are mainly based on the adsorption/desorption properties of mesoporous materials. One key parameter for such deliver is pore size, as shown in the work from Horcajada et al., where they found a decrease in the delivery rate when ibuprofen was incorporated

into MCM-41 mesoporous materials as the pore size decreases from 3.6 to 2.5 nm. [62] In addition, the surface physicochemical properties (roughness, stiffness, etc.) of the porous carrier also play a critical role for intracellular drug deliver by modifying their interaction with cell membranes. For example, Wang et al. have fabricated a novel virus-like mesoporous silica nanoparticle with uniform particle size and a spiky tubular surface via a single-micelle epitaxial growth approach. [63] In comparison to conventional mesoporous silica nanoparticles with smooth surfaces, the virus-like nanoparticles show superior cellular uptake, unique internalization pathways and extended blood circulation duration.

All the examples mentioned above illustrate that establishing the structure-performance relationship requires an unambiguous understanding of the mesopore structure, including the morphology of the solid phase, the pores and the structure of the interior surfaces. Therefore, it is necessary to develop reliable structure characterization techniques.

1.3. General characterization of mesoporous materials

In this section, three commonly used bulk characterization techniques for mesoporous materials including gas adsorption, mercury intrusion porosimetry and small-angle X-ray scattering will be introduced briefly.

1.3.1. Gas adsorption

Gas adsorption is one of the major characterization techniques for porous materials, allowing determination of the specific surface area, pore volume and pore size. Various gas molecules such as N_2, H_2O, Ar, CO_2 and He can be used as probe molecules for the analysis of porous systems. Figure 1.7a shows an illustration of different stages for gas adsorption on a rough solid surface. The gas adsorption starts from the gas molecules adsorbed randomly on the sample surface by van der Waals forces at low pressure. As gas pressure increases, all adsorbed molecules are in contact with the surface layer of the adsorbent, leading to monolayer adsorption. Further increasing the gas pressure will cause the beginning of multi-layer coverage, where not all adsorbed molecules are in direct contact with the adsorbent surface. At this stage, the surface area of porous materials is usually evaluated by the Brunauer–Emmett–Teller (BET) method, an extension of the Langmuir model of monolayer adsorption to multilayer adsorption. [64] In mesopores, multilayer adsorption is followed by pore/capillary condensation, a phenomenon where the gas condenses to a liquid-like phase in the pore at a pressure p less than the saturation pressure p^0 of the bulk liquid. [65] This liquid-like adsorbed phase has a meniscus where the curvature is associated with the Kelvin equation [66], thus the pore size can be evaluated using the BJH (Barret, Joyer and Halenda) method, based on the assumption that all pores are rigid and of regular shape, and that there are no micropores or macropores beyond the scope of the isotherm [67]. At higher gas pressure, a complete coverage of the sample by adsorbed molecules is possible and all the pores are filled, enabling determination of the pore volume.

The primary data obtained during a gas adsorption experiment is the dependence of the amount of adsorbed probe gas on the relative equilibrium pressure, the so-called physisorption isotherm (Figure 1.7b). For mesoporous materials, it is widely accepted that there is a correlation between the shape of the hysteresis loop and the pore structure of the adsorbent. As shown in Figure 1.7c-f, the shape of the hysteresis loop is characteristic for the underlying desorption mechanisms and enables discrimination of various pore connectivity types. [65] However, it should be noted that a detailed interpretation of such a correlation is difficult and ambiguous as the standard analysis depends on an assumption of the pore morphology.
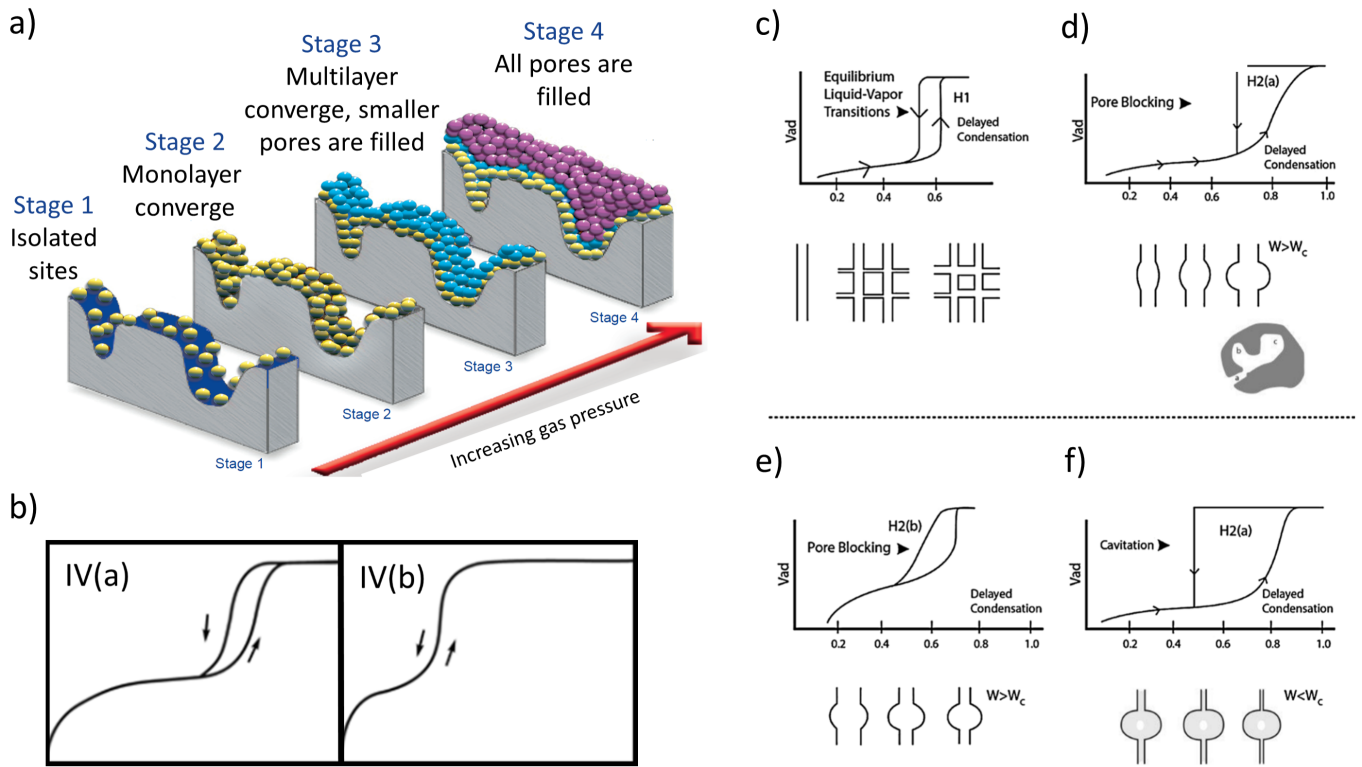
Figure 1.7: (a) Illustration of gas adsorption on a rough solid surface at different gas pressure (adapted from Micromeritics Instrument Corporation), (b) classification of physisorption isotherms and (c-f) hysteresis loops and their correlation with pore structure, adapted from [65], [68].

1.3.2. Mercury intrusion porosimetry

MIP is recommended by the IUPAC as a standard measure of total pore volume and pore size distribution (PSD) in the macro- and mesopore range. [45] The principle of MIP is that mercury intrusion into pores requires application of a high pressure since mercury does not wet the solid spontaneously. In practice, mercury is introduced by progressively increasing the pressure to fill the dried sample, where the air/fluid inside the pores has been removed in advance. The corresponding volume V of the intruded mercury with increased pressure P is monitored, resulting in an accessible pore volume as a function of the applied pressure. According to the Young-Laplace equation [69], [70], the pressure difference ΔP between the pressure P_{Hg} in the mercury and P_g in the gas phase can be described by the surface tension γ_{Hg} of mercury and the radius r_m of the spherical meniscus:

$$\Delta P = P_{Hg} - P_g = -2\gamma_{Hg}/r_m \tag{1.1}$$

For cylindrical pores with radius r_p and $r_p = r_m \cos\theta_c$, the Washburn equation [71] can be obtained by:

$$r_p = -\left(2\gamma_{Hg}\cos\theta_c\right)/\Delta P \tag{1.2}$$

where θ_c is the contact angle between mercury and the solid surface. With this, the PSD can be inferred by plotting the cumulative pore volume or its first derivative as a function of pore diameter/radius.

However, it is worth noting that pores are not perfectly uniform for real porous materials, in which the entrance opening to a pore is usually smaller than the actual cavity. Therefore, one may argue that MIP actually measures the entrance size at the sample surface towards that pore, as it determines the mercury intrusion pressure, rather than the internal or average pore size. It can also not be used to analyze closed pores as the mercury has no access to those pores. Thus, MIP will always show smaller pore sizes than the real physical sizes. [72] The misinterpretation of pore size distribution from MIP can be seen in the work by Sidney Diamond, who states that MIP measurements should be abandoned as measure of the actual pore sizes present in hydrated cementitious materials. [73]

1.3.3. Small-angle X-ray scattering

Early in the 1950s, SAXS has been used to study nanoparticles [74] and became an immensely powerful method to determine object size, size distribution, shape, and surface structure [75]. Depending on the electron density of the material, the scattered X-ray intensity distribution provides structural information in reciprocal space. SAXS represents commonly the region of scattering angle below 5° in X-ray diffraction, within which a decrease in intensity with increasing angle due to the electronic density heterogeneities of the medium can be observed without the disturbance of sharp maxima due to long-range periodicity in solids. [76] As SAXS measures only electron density differences, a nanopore can be regarded as an "inverse" nanoparticle, allowing one to adapt the same principles and theory for colloidal particles to examine nanoporous structures. Generally, SAXS is used to determine the pore size distribution and specific surface area of both closed and open pores, whose sizes are in the range from micropores to macropores ($\sim$0.5-100 nm). SAXS data are often presented as a plot of the logarithm of the scattering intensity I, as a function of the scattering vector/momentum transfer q, defined as:

$$q = 4\pi \sin \theta_x / \lambda \tag{1.3}$$

where λ is the X-ray wavelength and 2θ is the scattering angle. For regions where the scattering vector is approaching zero ($q < 1.3/R_G$), Guinier demonstrated that the scattering curve depends on the diameter of scattering object [74]:

$$I(q) = I(0) \exp\left(-R_G{}^2 q^2/3\right) \tag{1.4}$$

Here, R_G is the electronic radius of gyration of a particle about its electronic center of mass. Therefore, the logarithm of I is proportional to q^2, and the corresponding R_G can be obtained. With an assumption of the pore shape, R can also be calculated. For instance, for a spherical pore of radius R, $R_G = (3/5)^{1/2} R$ and for a thin disk-shaped pore with radius R, R_G is given by $R_G = (1/2)^{1/2} R$. Thereby the mean pore radius can be obtained. In addition, the total surface area per unit mass (S_{SAXS}) of the interface of the particles can be also obtained from the SAXS data using Porod's law at the high q regime: [77], [78]

$$S_{SAXS} = \frac{\pi \phi (1 - \phi) \lim_{q \to \infty} \left\{ q^4 I(q) \right\}}{\int_0^\infty q^2 I(q) dq} \tag{1.5}$$

where ϕ is the porosity of the solid. It is worth noting that ϕ must be determined by independent means before calculation of S_{SAXS}. The pore volume cannot be obtained from SAXS measurements.

1.4. 3D characterization of mesoporous materials by electron tomography

Compared to the bulk techniques mentioned above, which provide an average measure of the pore structure and pore volume based on standard pore models such as slit-shaped or cylindrical pores, numerous reports have demonstrated that ET is able to provide high quality 3D structural information at the nanoscale without any assumption on the pore shape. [13], [79]–[81] This makes it a promising and widely used technique for pore structure analysis, especially for materials with irregular pores. Based on the segmented 3D reconstruction, quantitative information on the pore network such as pore size, pore length, tortuosity and connectivity can be extracted by using skeletonization and chord length distribution (CLD) analysis. More details about the pore analysis by ET can be found in Chapter 2. ET has been extensively applied in heterogeneous catalysis, mainly focusing on the 3D morphology of supports and the 3D distribution/location of supported metal nanoparticles (NPs).

1.4.1. Support morphology

The first application of ET in heterogenous catalyst was published by Koster et al., in which the 3D structure of a metal/zeolite crystal (Ag/NaY) was determined and the viability of 3D imaging of mesopores in zeolites was shown by bright field ET. [84] Since then, ET has been widely used to study how pre- or post- treatments, e.g.
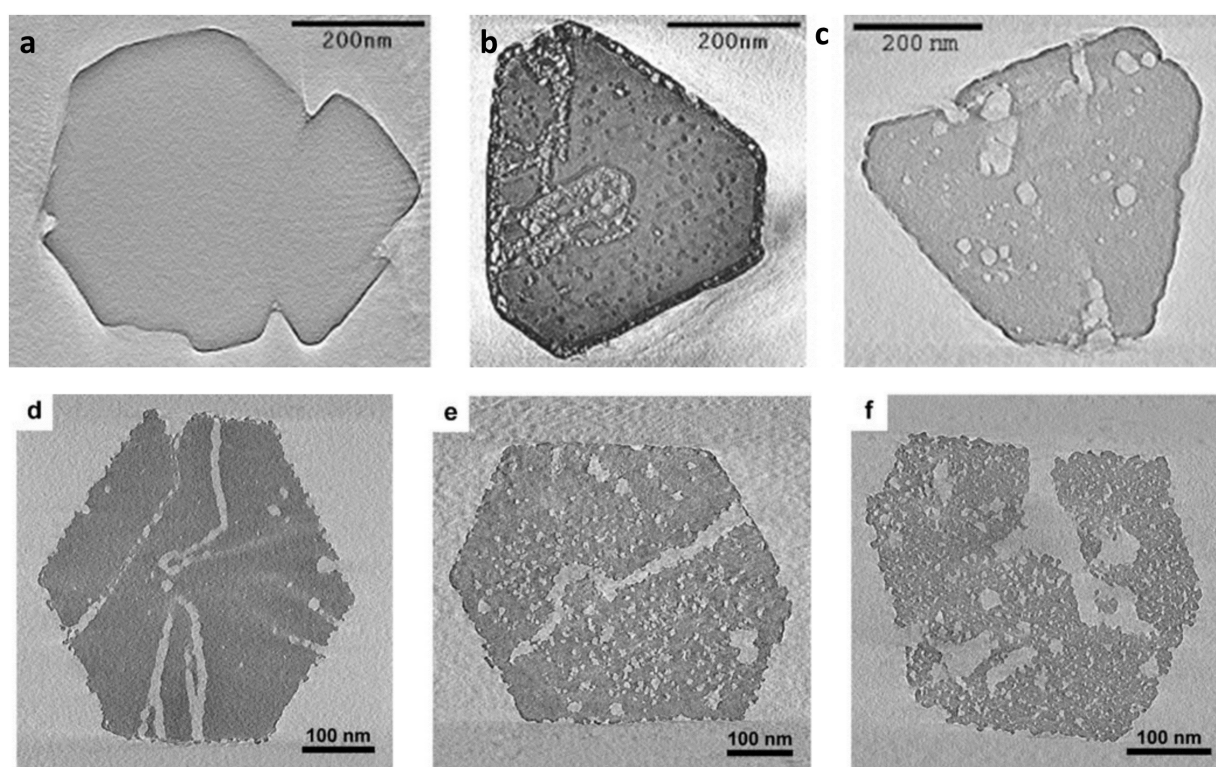
Figure 1.8: Cross-sections through 3D reconstructions from electron tomography reveal the variations of mesoporous structures in zeolite crystals caused by different post-synthesis treatments: (a) zeolite Y, (b) steamed zeolite Y (USY) and (c) steamed and acid leached zeolite Y, adapted from [82]; (d) commercial zeolite Y (HY-30), (e) base-leached HY-30 with 0.05m NaOH (HY-A) and (f) base-leached HY-30 with 0.10m NaOH (HY-B), adapted from [83].

steaming [85], [86], acid leaching [82], base leaching [83] and carbon templating [87] affect the size, shape, 3D distribution and connectivity of the mesopores in zeolites during synthesis. Figure 1.8 shows variations of the mesoporous structure in zeolite crystals caused by different post-synthesis treatments, which indicates that steaming, acid and base leaching treatments are efficient ways to obtain highly mesoporous zeolite Y crystals. As the mesopores control accessibility and transport of reactants and products, they have great influence on catalytic activity, selectivity and stability. Therefore, there is great interest in characterization of the shape and connectivity of mesopores in zeolite crystals, e.g. for application in cracking of heavy oil fractions, cumene production, alkane hydroisomerization and fine chemicals synthesis. [88]

Apart from zeolites, ET has also been widely used for structural elucidation of mesoporous silicas, which is a commonly used support for heterogenous catalysts due to their high specific surface area and versatile pore structures. Ulrich Tallarek's group has studied morphology–transport relationships quantitatively for ordered mesoporous silicas such as SBA-15 and KIT-6 [89], [90] and disordered mesoporous silicas [13],
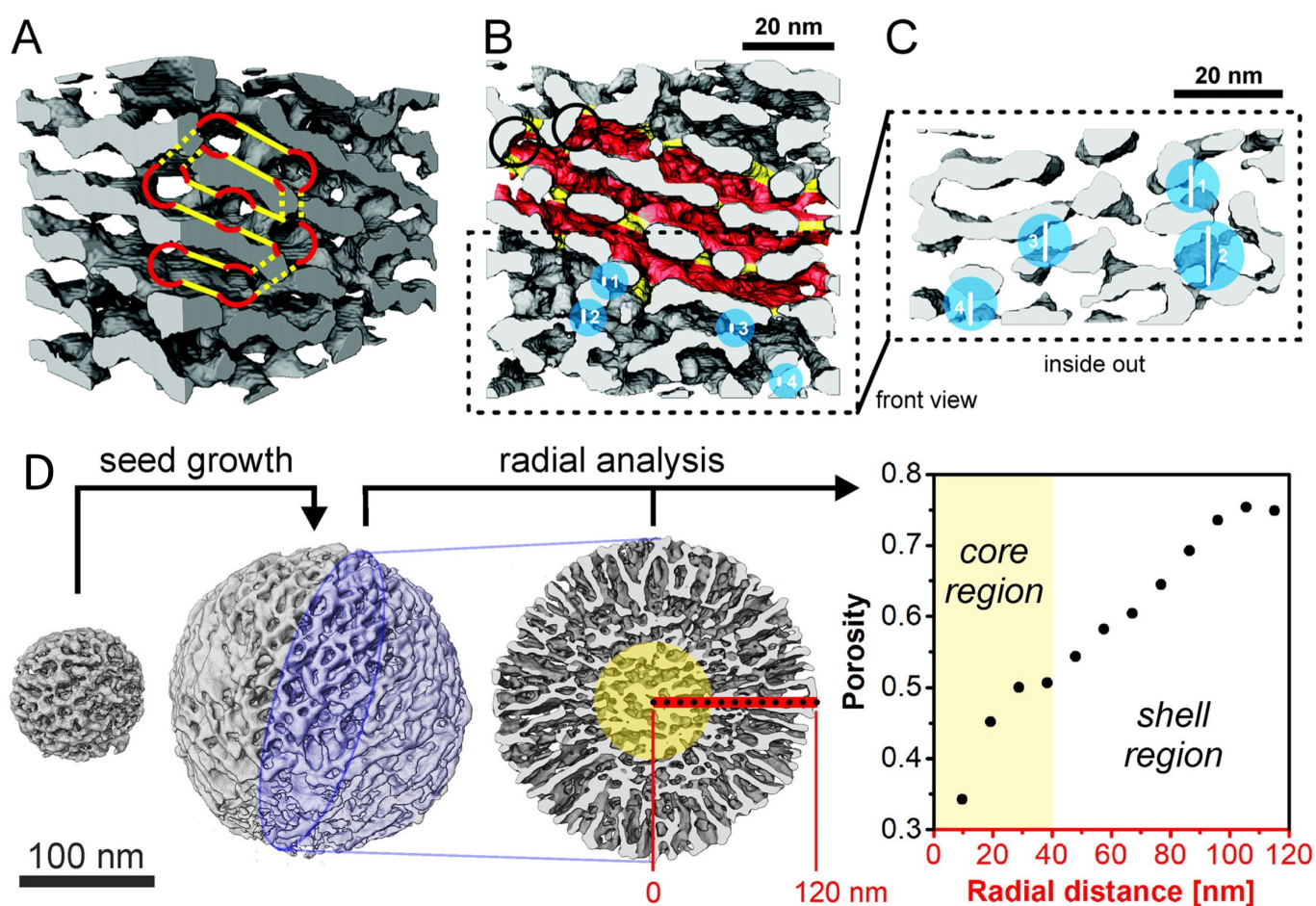
Figure 1.9: (a-c) Sections from two reconstructed SBA-15 silica blocks, highlighting important morphological features of the prepared SBA-15 silica sample, adapted from [89]; (d) particle size tuning of dendritic mesoporous silica nanoparticles (DMSNs) by seed-growth method and radial analysis of porosity in the core and the shell region of the particle based on 3D tomographic reconstruction, adapted from [14]

[14] by means of direct numerical simulation of hindered diffusion in realistic geometrical models of the pore space obtained from the segmented reconstructions by ET. As shown in Figure 1.9a-c, the morphological features of SBA-15 were revealed from a tomographic reconstruction, where the hexagonally arranged primary

mesopores are laterally connected by secondary (intrawall) mesopores. [89] Based on the 3D tomographic reconstructions of dendritic mesoporous silica nanoparticles (DMSNs), the dependency of 3D pore structures on the particle diameter can be obtained using a radial analysis of the porosity in the core and shell regions, as seen in Figure 1.9d. [14] The 3D morphology of other mesoporous silica materials, e.g. MCM-48 [91] and FDU-12 [92] have also been revealed by ET. Using electron tomography, local fine structural details inside the pore space can be detected quantitatively, which could not be identified by bulk analysis methods (e.g., nitrogen physisorption and SAXS).

Another example for the application of ET in mesoporous oxides can be seen in Figure 1.10, where mesoporous CeO_2 synthesized by thermal hydrolysis is used as a case study to elucidate the transformation of a disordered mesopore space upon thermally induced crystallization and sintering. [81] From the segmentation results of the fresh sample and that after aging at 800°C in water atmosphere, it is clear that both samples exhibit highly disordered porous structures, while the CeO_2 networks get thicker and the pores get larger after aging. The pore size distributions obtained from the skeletonization analysis of the 3D reconstructions for both samples are in good agreement with that obtained by N_2 physisorption.
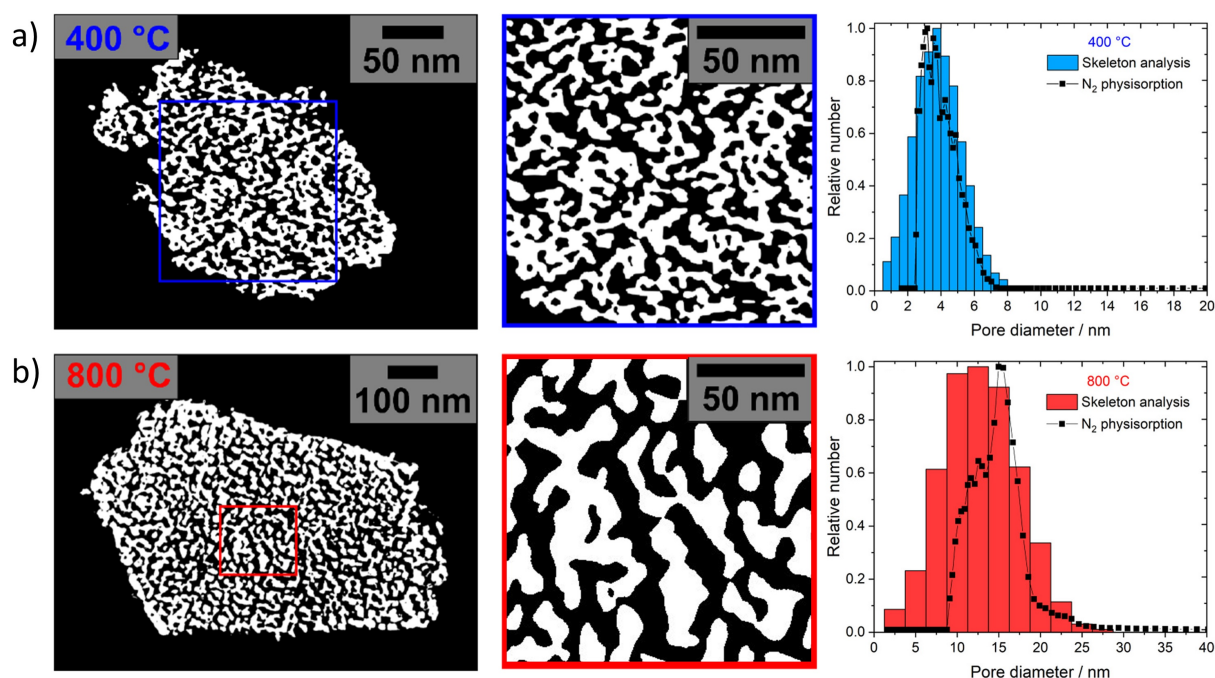
Figure 1.10: Segmented slices and the corresponding pore size distribution of (a) fresh (400°C) and (b) aged (800°C) CeO_2 samples, adapted form [81].

1.4.2. 3D distribution and location of supported NPs

Various studies have shown that the catalytic performance is highly correlated with the local distributions of nanoparticles supported on porous catalysts, mainly due to confinement effects, transport properties and interaction with the support surface. One example is a carbon nanotubes (CNTs) supported catalyst, where it has been demonstrated that PtRu nanoparticles inside the CNTs are more active than those on the external surface of CNTs for cinnamaldehyde hydrogenation. [93] Similar work by Villa et al. showed that impregnated Au nanoparticles trapped within N-functionalized carbon nanofibers (N-CNFs) are more active for polyol

oxidation and promote a selectivity towards di-acid products, whereas Au NPs trapped on the surface by sol immobilization result in C–C cleavage as major byproduct. [94] More details about confinement effects inside carbon nanotubes can be found in a review by X. Bao et. al. [95] For other supported catalysts using more complex porous supports, ET has shown the promising ability to precisely determine the location of nanoparticles. In a series works by the research groups of Krijn P. de Jong [96], [97] and Paul A. Midgley [98]–[100], the 3D morphology and location of small metal (< 10 nm) particles, e.g. Cu, CuZn, NiO, RuPt, Au and ZrO_2, deposited inside SBA-15 and disordered mesoporous silica have been revealed by ET. Figure 1.11 shows recent work by W. Wang et al., [101] where the different 3D distribution of Pd nanoparticles on three Pd/CMK-3 catalysts synthesized by different methods including incipient wetness impregnation (Pd_{IW}/CMK-3), wet impregnation (Pd_{IMP}/CMK-3) and sol immobilization (Pd_{PVA}/CMK-3) was demonstrated using quantitative ET method. The resulting structural differences have been correlated with their diverse catalytic performance in furfural hydrogenation.

Pd_{IW}/CMK-3 **Pd_{IMP}/CMK-3** **Pd_{PVA}/CMK-3**
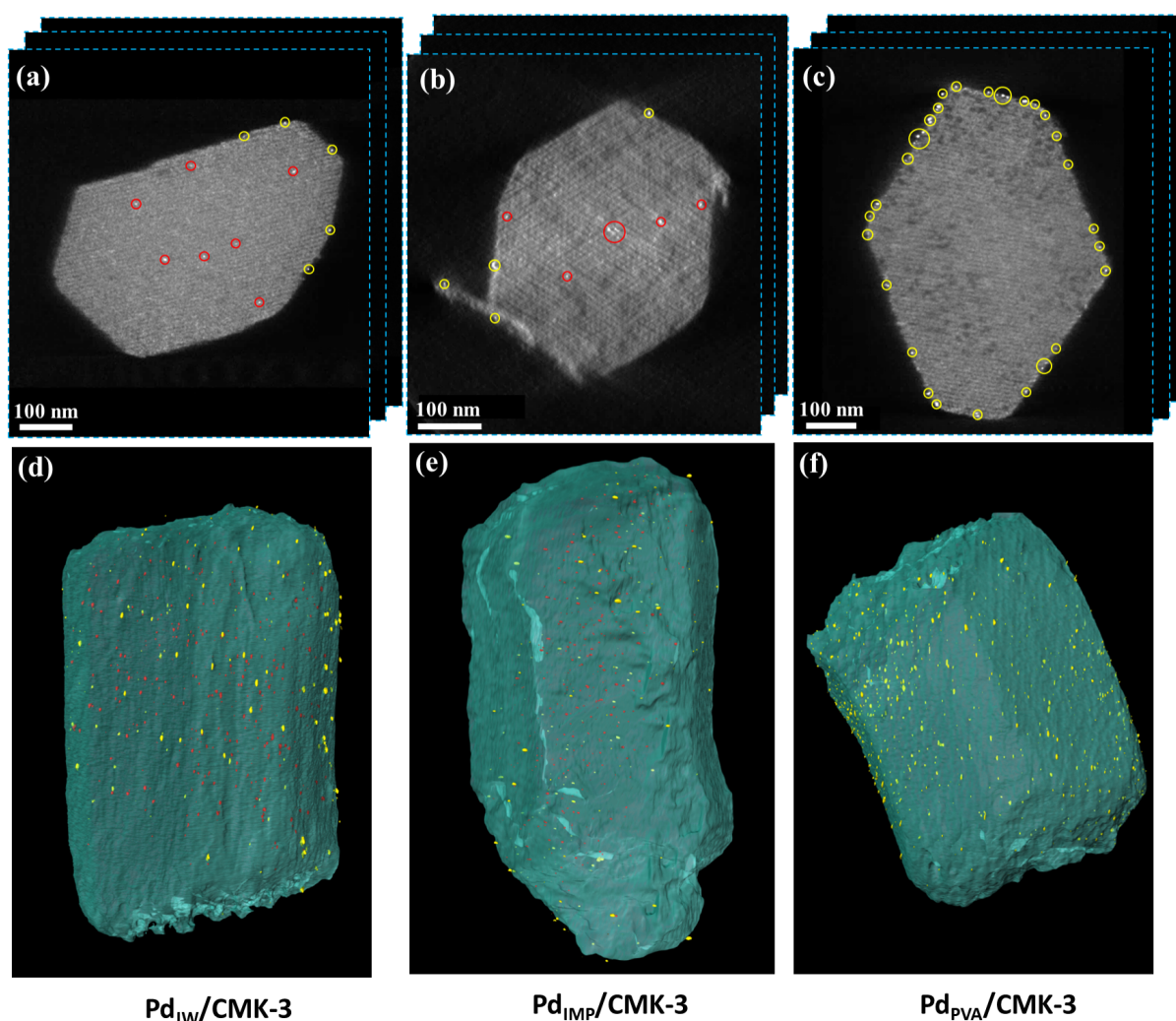
Figure 1.11: 2D slices of (a) Pd_{IW}/CMK-3, (b) Pd_{IMP}/CMK-3 and (c) Pd_{PVA}/CMK-3 reconstruction and the corresponding representative 3D visualization (d–f). The yellow and red circles in a-c highlight Pd nanoparticles on the external surface and inside of the porous support, adapted from [101].

ET is also widely used in other fields in addition to catalysis. As an example for lithium ion batteries, where mesoporous materials are usually applied as Li-metal 'host' to inhibit lithium dendrite growth and

protect the Li anode [102], ET has shown promising ability in monitoring the structural evolution during the charge-discharge process. With this, a deeper understanding of the lifetime, reliability and capacity of the tested battery can be achieved. A study by Lin and coworkers describes the propagation and deformation processes of lithiation fronts in a NiO nanoplate. [103] The authors revealed that the NiO-Ni transition on the electrode surface is an inhomogeneous phase transition process. Using ET, they found that the Ni particles are in contact with each other and form a 3D porous network rather than being distributed discretely. Such an interconnected architecture not only enhances the charge transfer, but also plays an important role in structural integrity. In a very recent study by Jin et al., the 3D interconnected porous structure inside the entire body of a mesoporous single-crystalline lithium titanite microrod was revealed by high-angle annular dark field (HAADF) - scanning transmission electron microscopy (STEM) tomography, which is responsible for the high rate capability. [104] This superior property can be explained by a communicating pore structure, as it provides an efficient percolation channel for electrolyte permeation and enables rapid diffusion of Li^+ during charge-discharge cycling. Another example for the application of ET in mesoporous materials can be found in chromatographic adsorbents. [105] Based on a tomographic reconstruction, the geometry and the interconnectivity of the pore network of three adsorbents was extracted quantitatively. Such structural information can then be used as input parameters for a structural evaluation and construction of engineered pore models, and further for the study of solute intraparticle transport.

1.4.3. Electron tomography containing chemical information

Not limited to the conventional bright field (BF)-TEM or (HA)ADF-STEM projections, spectroscopic signals from energy dispersive X-ray spectroscopy (EDS), electron energy loss spectroscopy (EELS) or energy filtered TEM (EFTEM) can also be used to obtain 3D mapping of composition and local elemental concentrations [106], local valence state [107], electronic [108] and optical [109] properties. Figure 1.12a,b show two studies by EDS tomography of Au-Ag nanorings and nanocubes, in which the 3D elemental distribution and concentration are retrieved. [106], [110] Figure 1.12c shows EELS tomography of a ceria nanoparticle in which the particle surface is predominantly in the Ce^{3+} state, compared to the Ce^{4+} core. [108] Figure 1.12d shows the iron distribution in a core-shell iron oxide particle reconstructed based on EELS tomography. [111] The morphology of an iron-based catalyst nanoparticle on top of a multiwall carbon nanotube (CNT) was revealed by a 3D iron elemental map using EFTEM tomography, as shown in Figure 1.12e. [112] However, it has to be considered that a high electron dose is often needed for analytical ET compared to conventional (S)TEM tomography, which can lead to structural and morphological changes caused by electron beam damage. Nevertheless, rapid advances in hardware coupled with data handling capabilities and reconstruction algorithms has brought good possibilities to acquire high quality spectrum imaging ET with reduced total electron dose. For example, the development of silicon drift EDS detector (SDD) and in-column configuration close to the TEM specimen has greatly improved the ability to perform EDS spectral imaging for a wider range of specimen tilt angles with reasonable acquisition time. Improvements in EELS spectrometers, including image filter system, and cameras as well as direct pixelated electron detectors can shorten the acquisition time and reduce the electron dose for EELS and EFTEM ET.

Although mapping elemental concentrations directly theoretically satisfies the projection requirement (see section 2.5.1), two factors need to be taken into account for reliable quantitative EELS tomography:

(i) Influence of multiple inelastic scattering becomes significant and the apparent elemental signal may actually begin to fall when the sample thickness is larger than the inelastic mean free path, so that the core-loss signal from such specimens (or at some high tilt angle) will no longer satisfy the projection requirement;

(ii) Complications might arise in crystalline specimens due to the strong diffraction contrast and anisotropic materials due to the remarkable response deviation with tilt for STEM-EELS.
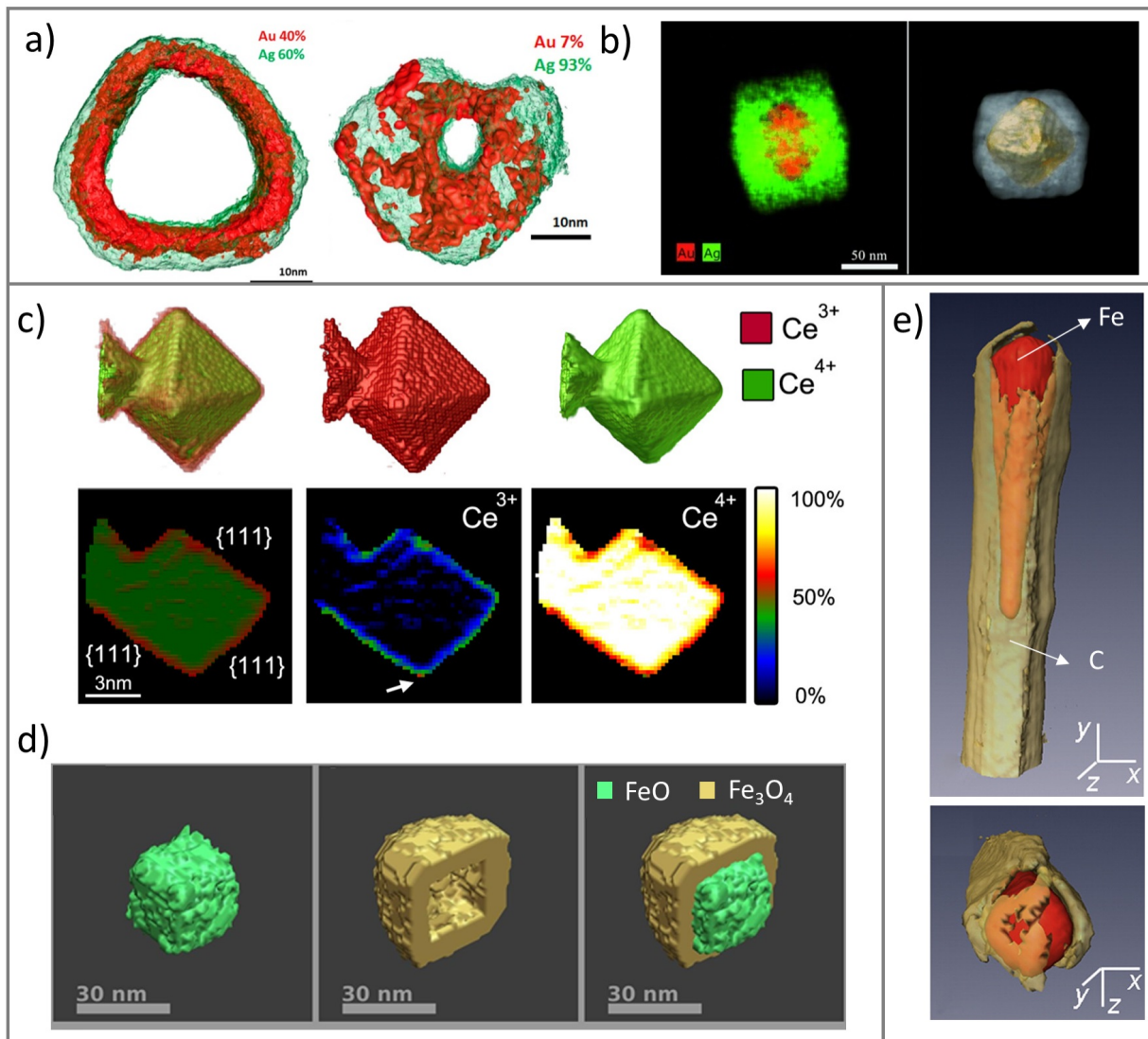
Figure 1.12: EDS tomography of (a) Au-Ag bimetallic nanorings with different Au-Ag ratios [106], and (b) Au@Ag nanocube [110]. EELS tomography of (c) valence state mapping of a ceria nanoparticle [108] and (d) changes in Fe valency in a FeO/Fe₃O₄ nanocube [111]. EFTEM tomography of (e) elemental mapping of an iron-filled multiwalled carbon nanotube [112].

One major consideration for EDS tomography is detector shadowing by the sample holder and the bars of the TEM grid during tilting. Shadowing of X-ray detectors will cause intensity variations as a function of tilt angle (Figure 1.13d) and will lead to artifacts within the tomographic reconstructions. A phantom simulation demonstrated the influence of intensity variations due to the shadowing effects for the reconstruction (Figure 1.13a-c). Both reconstructions show streaking and elongation artifacts. However, the reconstruction based on varying intensities caused by shadowing effects also show noticeable inconsistencies in the reconstructed intensities, as indicated by the white arrows in Figure 1.13c, where the intensity of the outer ring is reduced in the sections corresponding to low angle projections with lower signals. To compensate detector shadowing and reduce the variations at different tilt angles, one way is to acquire all spectra using a constant time and

normalization of the total counts prior the reconstruction. [113] Another way is to adjust the acquisition time at each tilt angle to achieve a constant total X-ray signal for each projection (Figure 1.13e, f). This allows for the maximum tolerable electron dose to be optimally distributed over all projections or can be used to minimize the total acquisition time. Another challenge for quantitative EDS tomography is X-ray adsorption, which can be corrected/refined either in data pre-processing by using e.g., Cliff-Lorimer [114] and ζ-factor methods [115], or during the iterative reconstruction process [116].
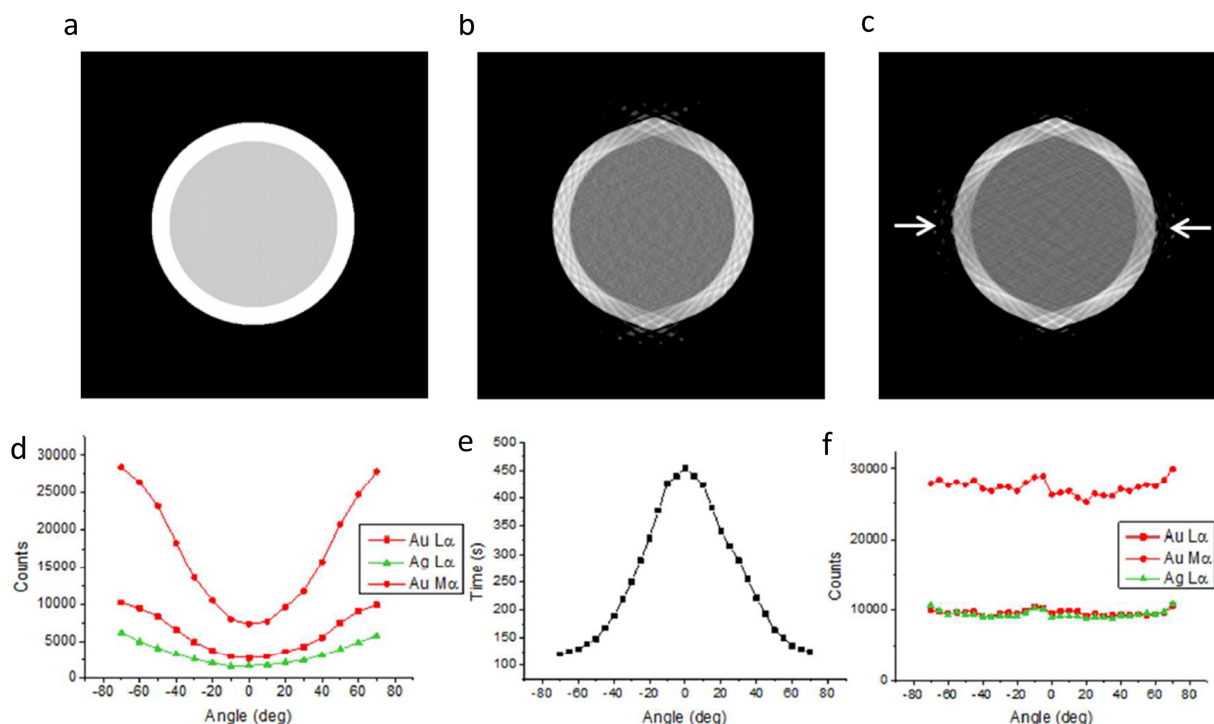
Figure 1.13: (a-c) phantom simulation of artifacts associated with variations in projection intensities due to detector shadowing: (a) a 2D phantom, (b) the object reconstructed using 15 simulated projections with an increment of 10° and a tilt range of $\pm70°$, each with the same total intensity, and (c) the same object reconstructed from the same tilt conditions while the total intensity for each projection varies in a similar way to the shadowing variations, adapted from [117]. (d-f) Time-varied acquisition scheme for recording tomographic STEM-EDS data, adapted from [106].

1.4.4. Fast tomography

Using conventional (S)TEM tomography normally takes a long time to acquire one tilt series, whether it is acquired manually or with automation software, typically around one hour. When combined with spectroscopic techniques, additional data needs to be acquired at every tilt angle, leading to an increased acquisition time of several hours or even more than 10 hours. Though this approach is sufficient for ex-situ analysis of samples stable under electron beam irradiation, the long acquisition time hinders observation of dynamic processes, especially for beam sensitive specimens and during in situ experiments. To solve these problems, a new technique called fast ET, which reduces the acquisition time to a few minutes or even less than one minute per tilt series, has been proposed recently. [118], [119] Both TEM and STEM mode can be used for the fast ET data acquisition and two approaches have been reported depending on the way of holder tilting. The first approach is continuous fast ET (CFET), where the projections are acquired continuously during tilting of

the holder while focusing and tracking of the object is performed manually. However, the continuous tilting of the holder inevitably causes mechanical movement of the goniometer during the data acquisition, thus resulting in blurring artifacts in TEM mode and scanning distortions seen as streaking artifacts in STEM mode. [119] These artifacts can be circumvented by using another approach, incremental fast ET (IFET), where the sample is rapidly tilted between consecutive tilting angles, allowing for a predefined relaxation time to stabilize the holder at a certain tilt angle, while continuously acquiring projection images. In this case, only the projections acquired when the holder is stabilized are used for further reconstruction, leading to a better-quality reconstruction compared to that from the CFET method. [119]
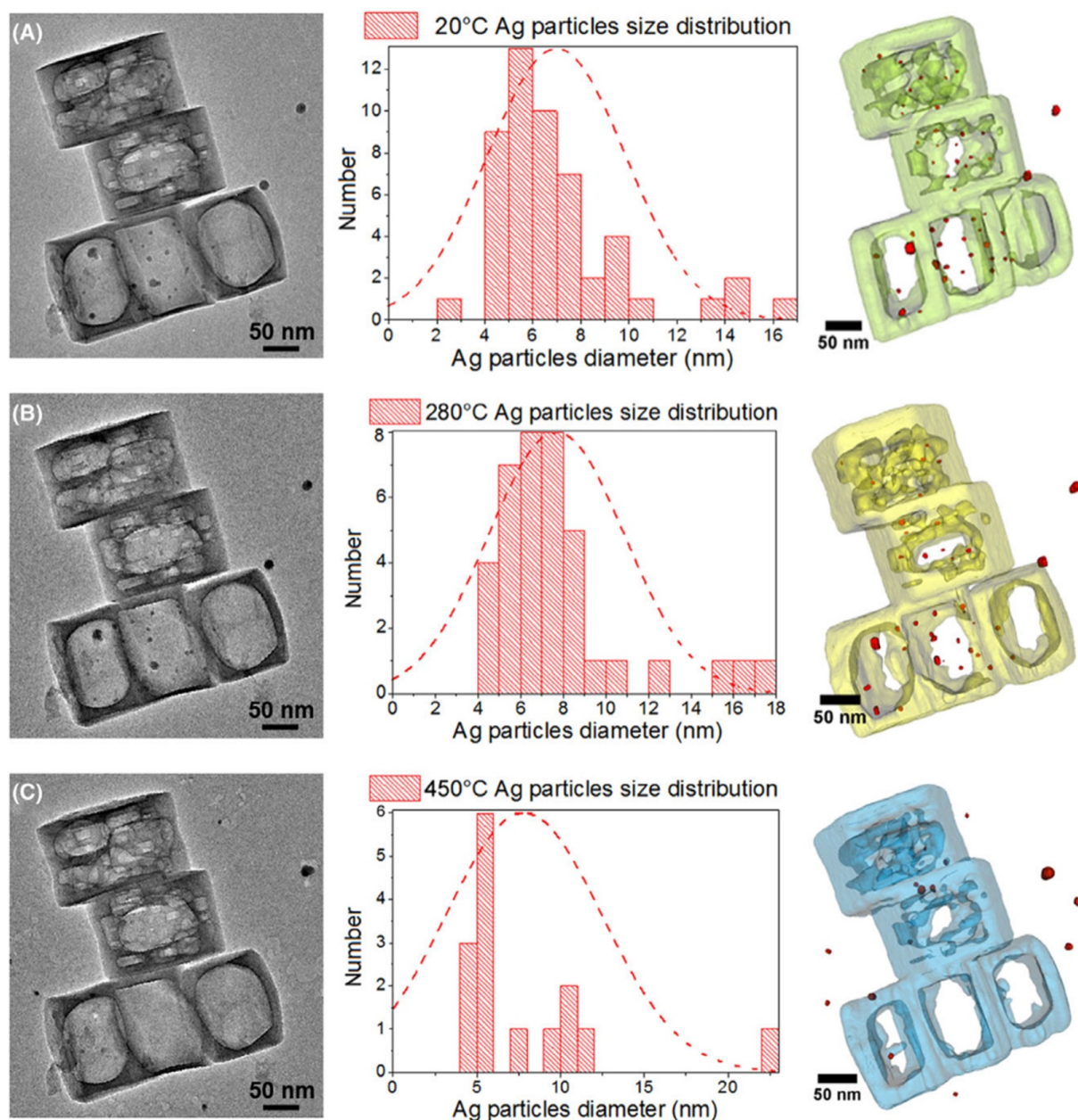
Figure 1.14: Calcination study by operando electron tomography of the same silicalite-1 hollow zeolites containing Ag NPs at (A) 20°C in high vacuum, (B) 280°C and (C) 450°C under a 1.8 mbar of O_2, adapted from [120].

Various works have shown the powerful ability of fast ET for delivering valuable insights in material science, either by revealing the 3D structure of beam sensitive materials or following the structural evolution during dynamic processes. Koneti and co-workers succeeded in imaging a polymer nanocomposite by making use of BF-IFET with a total acquisition time of 200s and a tilt range of 140°. [119] The first fast operando ET experiments of nanocatalysts was performed by Roiban and co-workers, in which the in situ calcination of silica zeolites encaging silver nanoparticles was studied using the BF-CFET approach. [121] As shown in Figure 1.14, three tomographic series with a tilt range of -25° to 42° were acquired within $\sim$2 min at 20°C in high vacuum, at 280 and 450°C at 1.8 mbar of O_2. Based on the 3D reconstructions of the catalysts and the statistical analysis of Ag NPs, the ripening and location change of Ag particles can be observed. In a series of works from the Electron Microscopy for Materials Science group at the University of Antwerp, fast ET in HAADF-STEM mode was used for in situ visualizations of heat-induced morphological transformation on crystalline NPs, e.g. highly anisotropic Au nanostars [121], AuPd octopods [122] and alloying in Au@Ag@SiO$_2$ NPs with various shapes [123].

1.4.5. Summary of characterization methods for mesoporous materials

Table 1.1 summarizes a comparison of the discussed characterization methods for mesoporous materials. From the above introduction of the main characterization techniques and the characteristics of mesoporous materials, it is clear that all of them are able to extract basic pore information such as pore size and distribution, pore volume, etc. Although the bulk techniques (gas adsorption, MIP and SAXS) allow to a certain extent quantification of the structure of mesoporous materials over a wide range of scales, the determination of

Table 1.1.: Summary of common characterization techniques used in mesoporous materials

	Gas adsorption	Mercury intrusion porosity	Small-angel X-ray scattering	Electron tomography
Information type	Surface area, pore volume, pore size & distribution	Pore volume, pore size & distribution	Surface area, pore size & distribution	Surface area, pore volume, shape, pore size & distribution, connectivity
Pore size range	Micro-, meso- and macro- pores	Meso- and macro-pores	Micro-, meso- and macro- pores	Meso- and macro-pores
Pore shape assumption	Yes	Yes	Yes	No
Advantages	Measurement for wide range of scales	Measurement for wide range of scales	Measurement for wide range of scales; can measure open, closed pores and solid	Can measure open, closed pores and solid; 3d pore /wall geometry and topology
Disadvantages	Can measure only open pores	Can measure only open pores	Complicate data fitting; no pore volume information	Local measurement; rely on reconstruction & segmentation
Sample damage	No	Yes	No	Depending on the samples

pore size relies on an assumption of a simplified pore shape (cylindrical or slit-like pores), which might cause inaccurate results for complex pore systems. Due to the technical limitations, both gas adsorption and MIP methods have no access to closed pores and cannot probe the solid/wall structure. ET evaluates the pore structure based on a reconstructed 3D tomographic volume without prior assumption of the pore model, resulting in high resolution real pore information especially for irregular mesopore materials. Based on the segmentation, quantitative analysis can be performed both on pore and solid structures. More importantly,

geometrical information about the average pore/wall size and the statistical distribution of the pore/wall size can be obtained by using e.g. CLD analysis and topological information about pore/wall tortuosities and pore/wall coordination numbers can be also achieved after skeletonization. The skeletonization technique was used for the quantitative analysis of all pore structures in this thesis.

1.5. State of the art of electron tomography

While ET has shown a promising ability for 3D characterization of mesoporous materials, a quantitative and accurate interpretation of the solid/void network from the ET results is still challenging due to constraints during tilt-series acquisition such as the missing wedge, limited sampling, signal-to-noise ratio of the camera or detector as well as reconstruction artifacts introduced by alignment errors and reconstruction algorithms. To solved such problems and improve the fidelity of the segmentation and thus the quantification of mesoporous structures, many efforts mainly including advanced reconstruction algorithms and experimental data sampling have been made.

From an algorithmic aspect, one approach to improve the quality of the reconstruction is by using advanced image processing, such as denoising [124] and enhancing the local contrast [12], or by introducing constraints during the reconstruction such as using a modified SIRT. The additional constrains can be a mask highlighting the object to be reconstructed [125] or by simultaneously minimizing projection differences and regularization object constraints e.g. in TVM based algorithms [126], [127]. The segmentation can also be integrated into iterative reconstruction procedures. For example, watershed segmentation has been combined with SIRT reconstruction with the prior knowledge that there exist many local regions of void space [128]. For a sample consisting of just a few a priori known components, each with uniform density, it is well known that DART can directly result in a segmented 3D structure [129]. More details about the reconstruction algorithms will be described in Chapter 2. However, an objective and comprehensive assessment of the effectiveness of different algorithms and approaches for a quantitative analysis of mesoporous materials is still limited and difficult in experimental practice. To get accurate reconstructions and evaluate the specific features for porous materials, a thorough survey of the dependence on different acquisition conditions is needed to optimize the acquisition and reconstruction methods and to judge the reliability of the obtained structure and depending properties.

On the other hand, filling in the missing information caused by a limited experimental tilt range has been regarded as the fundamental solution for solving the missing wedge problem. Methods for partial reduction of the missing wedge experimentally include dual-axis tomography, where the specimen is tilted along two orthogonal axes so that the missing volume is reduced to a missing pyramid [130], [131], or using conical tilt tomography where the specimen is first tilted to the maximum angle and then rotated in small increments until completing a 360° turn, such that missing volume is reduced to a missing cone [132]. However, the complicate operation and difficult tilt series alignment have limited their application in electron tomography. Alternatively, a new type of on-axis rotation holder equipped with a needle shape tip makes it possible to achieve full-range tilting ($\pm 90°$) without too much extra work compared to conventional single tilt tomography. It has been the most popular way for solving the missing wedge problem experimentally in recent years. Unlike conventional single tilt holders using TEM grids, sample preparation, especially for fine powder samples, is still the biggest challenge for full tilt tomography. Similar to atom probe tomography (APT) [133], specimens for full tilt tomography are required to be mounted on a needle/rod shaped tip. This usually requires reshaping the sample in a focus ion beam (FIB) instrument. So far, not many methods can be found in the literature for specimen preparation for powder samples to perform the full tilt tomography. There are limited examples such as dispersing nanoparticles in solution and dropping them onto a modified tip [134], [135], using carbon

nanofibers as bridge to carry a powder specimen on a holder tip [136] and the so-called 'stamp' method that enables in situ transfer of a single particle from a suitable substrate onto a tailored tip within a SEM/FIB instrument equipped with a suitable micromanipulator [137], [138]. However, these methods still suffer from either shadowing problems or do not allow selecting ultra-small nanoparticles. Therefore, a more facile and reliable preparation method, which can achieve precise picking of selected nanoparticles that is more or less insensitive to the tip size so that the selected particles are completely visible in all TEM projections, would be of great interest for many electron tomography applications.

1.6. Motivation of thesis

As mentioned in section 1.1, a reliable qualitative and quantitative 3D characterization of mesoporous materials plays a key role in understanding the structure-property relationship for various applications and further development of novel advanced materials. Using electron tomography, high quality 3D structural information at the nanoscale can be obtained for complex mesoporous materials. However, a reliable quantitative interpretation of ET results (reconstruction and segmentation) regarding the key features of porous structures is still far from straightforward and challenging because of various constraints and imperfections during data acquisition and reconstruction procedures. To solve these problems, two different approaches are usually considered: development of advanced reconstruction algorithms and improved experimental data sampling approaches.

From an algorithm aspect, the most popular method to reconstruct under sampled data is using prior knowledge about the specimen, providing a way to make an informed guess about the missing information, e.g. TVM and DART. Although several works have been performed to compare these algorithms based on either experimental data or phantom studies, [139], [140] an objective and comprehensive assessment of the effectiveness of different algorithms and their reliability for a quantitative analysis of porous materials is still limited. In particular for application to mesoporous materials, an analysis based on a simple evaluation of misclassified voxels and average residual errors using a model structure is not enough. It is of great importance to evaluate the reconstruction algorithms considering the adjustable parameters, experimental conditions, and errors due to imperfect alignment looking at pore size, shape and connectivity as critical structural quantities, which are directly related to the properties of the porous material. To get accurate reconstructions and to evaluate these specific features for porous materials, an analysis of the dependence on different acquisition conditions, such as noise level, tilt-range and number of projections as well as the reconstruction and segmentation parameters is necessary to optimize the acquisition and reconstruction methods and to judge the reliability of the obtained structure and depending properties. In contrast to real experimental datasets without a known ground truth, assessment of reconstruction algorithms based on simulated tilt-series from artificial phantom structures with selected, representative pore structures allows to provide useful insights on how to effectively measure specific features for mesoporous materials.

In addition, an on-axis rotation holder equipped with a needle shaped tip makes it possible to achieve full-range tilting ($\pm 90°$) without too much additional work compared to conventional single tilt tomography. This so-called 360° ET or full-range ET has been the most popular way for solving missing the wedge problem experimentally in recent years. However, unlike conventional single tilt holders using TEM grids, sample preparation especially for fine powders is still a big challenge for 360° ET as specimens are required to be mounted on a needle/rod shaped tip.

The aim of the work presented in this thesis is to explore new methods to improve the fidelity of tomographic reconstructions for mesoporous materials, both in terms of reconstruction algorithm and experimental aspects, and apply them to real catalytic systems.

Prior to introducing and discussing the results, a brief introduction to electron microscopy is provided in Chapter 2 including the general microscope setup, TEM and STEM imaging. Electron tomography is introduced in more detail as this is the main method used in this thesis. This includes the working principles and fundamentals, the experimental workflow, reconstruction algorithms, segmentation as well as quantitative analysis.

As mentioned above, a comprehensive evaluation of the fidelity of different reconstruction algorithms with limited data for a quantitative analysis of mesoporous materials is of great importance. To determine the influence of data constraints as well as the selected parameters for each reconstruction algorithm using mesoporous features, effective simulations based on ground truth are required. In Chapter 3, the reconstruction reliability of the three main-stream algorithms SIRT, TVM and DART was systematically investigated for different imperfect (realistic) conditions for mesoporous materials based on a set of artificial phantoms mimicking real mesoporous materials. The influence of different acquisition and reconstruction parameters on the reconstructed 3D volume and the quantitative analysis of pore features is discussed. Skeleton analysis and diffusion simulations are used to evaluate the quality of the corresponding reconstructions using the original phantom as ground truth. The aim is to provide a practical guideline for optimizing acquisition and reconstruction parameters and how to evaluate the accuracy when describing the mesoporous structure.

Given the difficulty in sample preparation for 360° ET, Chapter 4 shows a new preparation method that enables transfer of a selected individual nanoparticle or a few separated nanoparticles by cutting a piece of carbon film supporting the specimen and mounting them on a full range tomography holder tip with the help of an easily prepared sharp tungsten tip using FIB. The application of this new method is demonstrated by performing 360° ET on a hollow Pt/TiO_2 catalyst showing high quality reconstruction without missing wedge artifacts.

As one specific example for the application of electron tomography for mesoporous materials, Chapter 5 shows the identification of the differences in the structure of Pd/CMK3 catalysts used in batch and fixed bed reactors for formic acid decomposition. Quantitative analysis of the tomographic data of the fresh and used catalysts enables precise tracking of the evolution of the active metal particles inside the mesopores and on the external surface. The observed structural differences are considered to be the reason for the different catalytic performance in terms of activity and stability during formic acid decomposition.

In addition to the results discussed in chapters 3-5, electron tomography has been applied to solve a large number of 3D structures of mesoporous materials, supporting fundamental research in catalysis, hydrogen storage and battery. This has resulted in 16 additional scientific publications generated as part of my PhD thesis in the publication list at the end of this thesis.
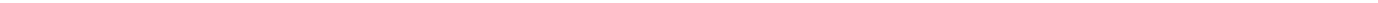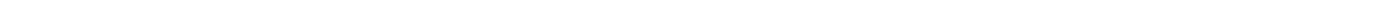
2. Electron Tomography

This chapter provides a brief introduction of electron microscopy, the basic mathematical foundation of electron tomography and its workflow including data acquisition, tilt series alignment, reconstruction and post processing. Among them, the limitations (missing wedge) of data acquisition by conventional single tilt holder and the resulting artifacts for reconstruction from various algorithms are discussed.

2.1. A brief history

Advanced (S)TEM imaging as well as spectroscopic techniques enable the characterization of nanomaterials, from morphological imaging at the low micron level down to the atomic scale, providing both structural and chemical information. However, most TEM based techniques only provide 2D projections of the real 3D objects, which is often not sufficient and may even lead to an incorrect understanding of the nature of nanomaterials. Therefore, a 3D characterization method is necessary in many cases. Electron tomography is such a technique using a series of 2D projections obtained at different tilt angles to reconstruct the 3D morphology of complex materials.

The term "tomography" is derived from two ancient greek words: $\tau\sigma\mu\sigma\varsigma$ (tomos) meaning to cut or section, and $\gamma\rho\acute{\alpha}\varphi\varepsilon$ (graphein) meaning to write. Tomography concerns the visualization of slices through objects. The mathematical foundations for tomography were first developed by the Austrian mathematician Johann Radon in 1917, who proposed the so-called Radon transform. [141], [142] Further development in this field came after more than forty years, when the physicist Allan MacLeod Cormack formulated some of the mathematical principles for an implementation of x-ray tomographic reconstruction for medical use in 1963. [143] Since then, the use and development of tomography scanners for medical imaging proliferated. In 1971, Godfrey Hounsfield who works at Electric and Musical Industries (EMI) validated Cormack's work by building a prototype CT scanner. [144] For their contribution to medicine, Cormack and Hounsfield shared the Nobel Prize in Physiology in 1979.

In electron microscopy, the first examples for 3D reconstructions using TEM were published in 1968 in three seminal papers. The first paper from De Rosier and Klug determined the 3D structure of the tail of the bacteriophage T4 with helical symmetry (Figure 2.1) from only one single projection. [145] This work is actually an example using electron crystallography, in which diffraction patterns/high-resolution images are acquired from biological objects, to extract the "average" molecule or unit cell of an object by a number of optical and computer methods. Due to the contribution to the development of crystallographic electron microscopy and to the study of the structure of biologically important nucleic acid-protein complexes, Klug won the Nobel Prize in Chemistry in 1982. The second paper from Hoppe and coworkers showed how asymmetric objects can be reconstructed from a sufficient number of projections. [146] This method is well known as single-particle analysis and widely applied for biological samples. The third paper from Hart and coworkers offered a means to determine 3D structures of low-contrast biological specimens at high

resolution using an average re-projection calculated from a tilt series of images. [147] These attempts are considered as the starting point for the development of electron tomography. This technique remained in the field of life science until 1988 when Spontak et al. first used it in materials science to visualize 3D polymer microstructures. [148] However, its popularity has increased only in the last decades due to the introduction of novel tomographic imaging modes, automation of microscope control, new reconstruction algorithms and the increased speed and ease of computation. [79] The first example of modern electron tomography for materials science was published in 2000 by of Koster and co-workers in Utrecht, who used bright field TEM tomography to reconstruct porous zeolites [84] and later in 2001 and 2003 by Weyland and Midgley [149], [150], which present the catalysis work based on STEM tomography and the development of Z-contrast and EFTEM tomography.
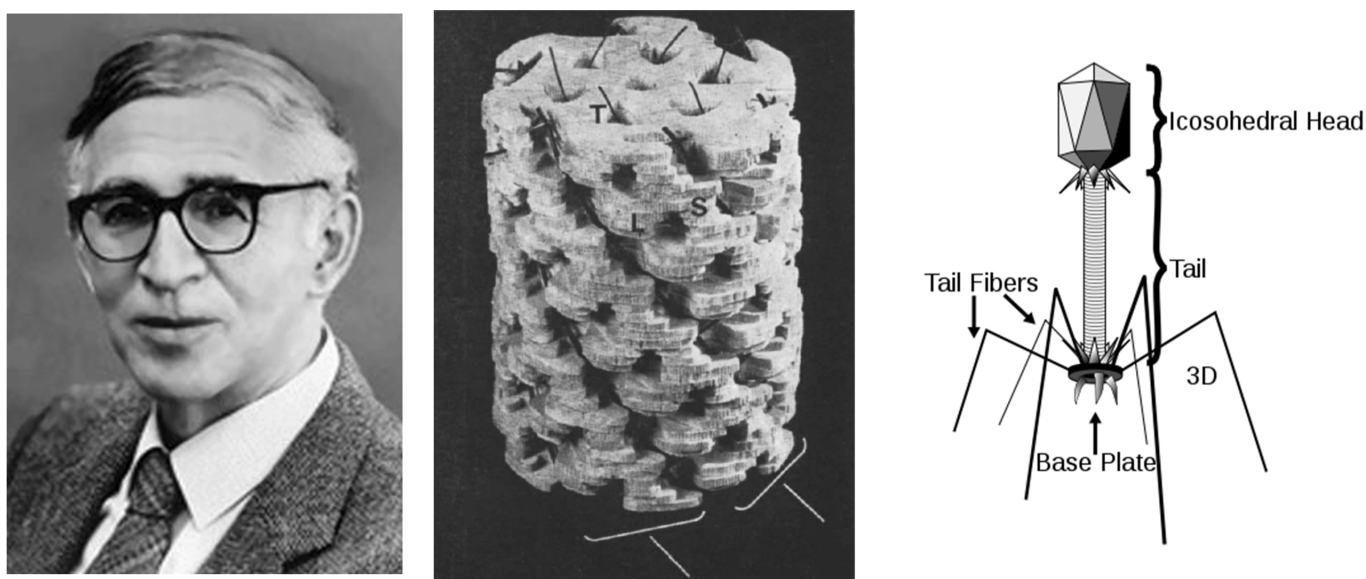
Figure 2.1: Aaron Klug and his work on 3D reconstruction of the structure of the tail of bacteriophage T4 in 1968, reproduced from [145].

2.2. Introduction to electron microscopy (EM)

The basis for electron microscopy is an electron microscope with a basic setup analogous to an optical microscope, consisting of an electron source and a system of lenses used to illuminate a specific part of the sample and to magnify images of the projected samples. The signals for imaging are generated from the interaction of the electron beam with the specimen. One advantage of using an electron beam is the short wavelength in the pm range, which enables to achieve high-resolution imaging down to the sub-Ångstrom level. Another advantage is that negatively charged electrons can be focused easily by electromagnetic lenses. In this section, the two main types of electron microscopes, transmission electron microscopes and scanning electron microscopes will be introduced and the signal generation will be briefly discussed.

2.2.1. Electron-matter interaction

When an incident electron beam hits a specimen, a large amount of information can be gained, as shown in Figure 2.2a. For the electrons that go through the specimen, besides the directly transmitted part that suffers no detectable interaction with the specimen, they are either scattered elastically or inelastically depending on whether there is an energy loss during the Coulomb interaction. This results in a non-uniform distribution of electrons emerging from the exit surface of the specimen that contains structural, chemical and other information about the specimen. Given the wave nature of the electrons, the scattered electrons can be divided into coherent and incoherent depending on the phase change. Elastic scattering occurs when there is no loss of energy of the incident electrons, meaning that the wavelength is maintained, but the travel direction might be changed due to scattering. As shown in Figure 2.2b, low-angle elastic scattering ($< 3°$) occurs when the incident electron interacts with the electron cloud of the specimen. These coherently scattered electrons can be used to analyze the crystal structure as they result in an electron diffraction pattern. High-angle scattering ($>3°$) mainly occurs when the incident beam interacts with the nucleus by Rutherford scattering with the scattering probability roughly proportional to the atomic number (Z) of the element squared. This high-angle, forward scattering can be used to form so called Z-contrast images, where the image contrast is not (too strongly) affected by the orientation of the specimen, providing high quality, linear intensity projections of the scattering power of the object. In some cases when the incident electrons hit the nucleus directly, the scattering angle can be larger than $90°$. These backscattered electrons (BSE) are usually used for the imaging in SEM.
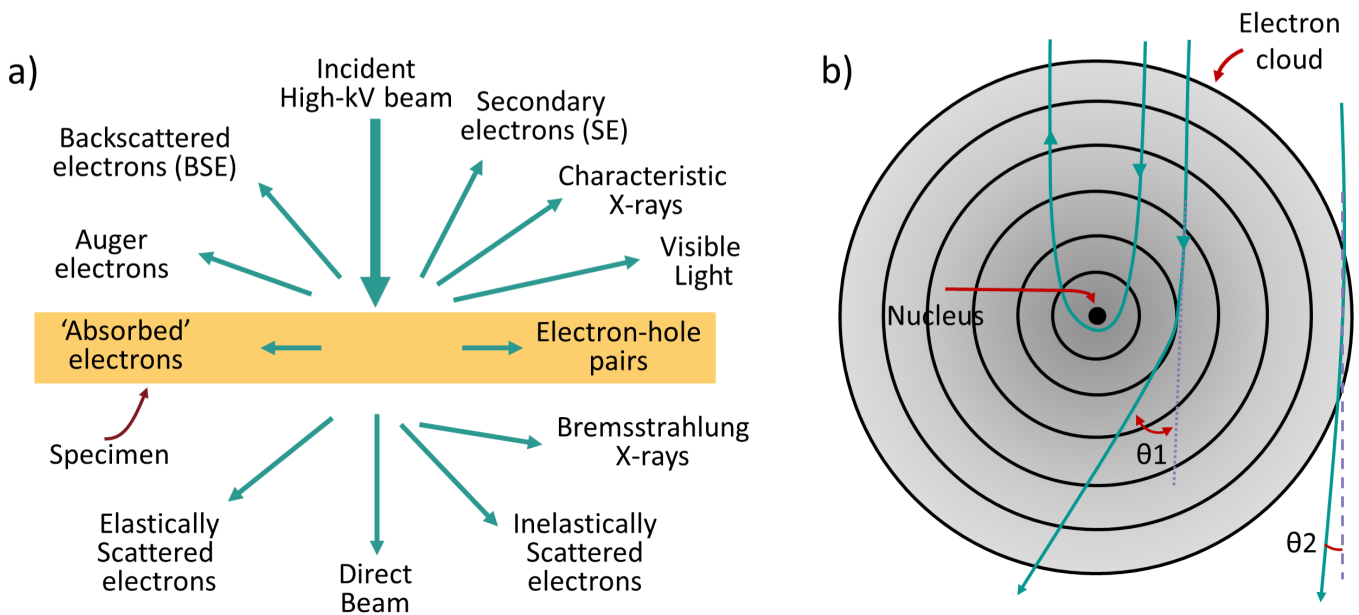
Figure 2.2: (a) Signals generated from the interaction between electrons and a thin specimen; (b) schematic of electron scattering by a single atom, adopted from [151].

In the case of inelastic scattering, the incident electron transfers energy to the specimen, generating a range of signals, such as characteristic X-rays, secondary electrons (SE), cathodoluminescence (CL), Auger electrons, plasmons and phonons. The energy lost from the primary electron can be used in EELS, which enables to identify the composition, bonding/valence state, the structure, the free-electron density, the band gap and the thickness of the specimen. The generated signals can also be exploited to characterize the materials. Considering the situation in a single atom, for example, when a high-energy incident electron

knocks out an inner-shell electron, this atom is ionized to an excited state and will return to a lower unoccupied state by filling in the hole with an outer-shell electron. This process will be accompanied by the emission of either a photon (X-ray) or an Auger electron. As both the emitted X-ray and Auger electrons are characteristic for each type of atom, they can be used for qualitative and semi-quantitative analysis of elements in EDS and Auger electron spectroscopy.

2.2.2. TEM setup

The optical setup of a TEM can be seen in Figure 2.3, from top to bottom it includes an electron source (gun), a condenser system, objective lenses and a projection system as the main optical components. Two types of electron sources including thermionic (LaB_6) and field-emission sources (Schottky/cold FEG) are commonly used to generate an electron beam either by heating or applying a high electric potential. The condenser
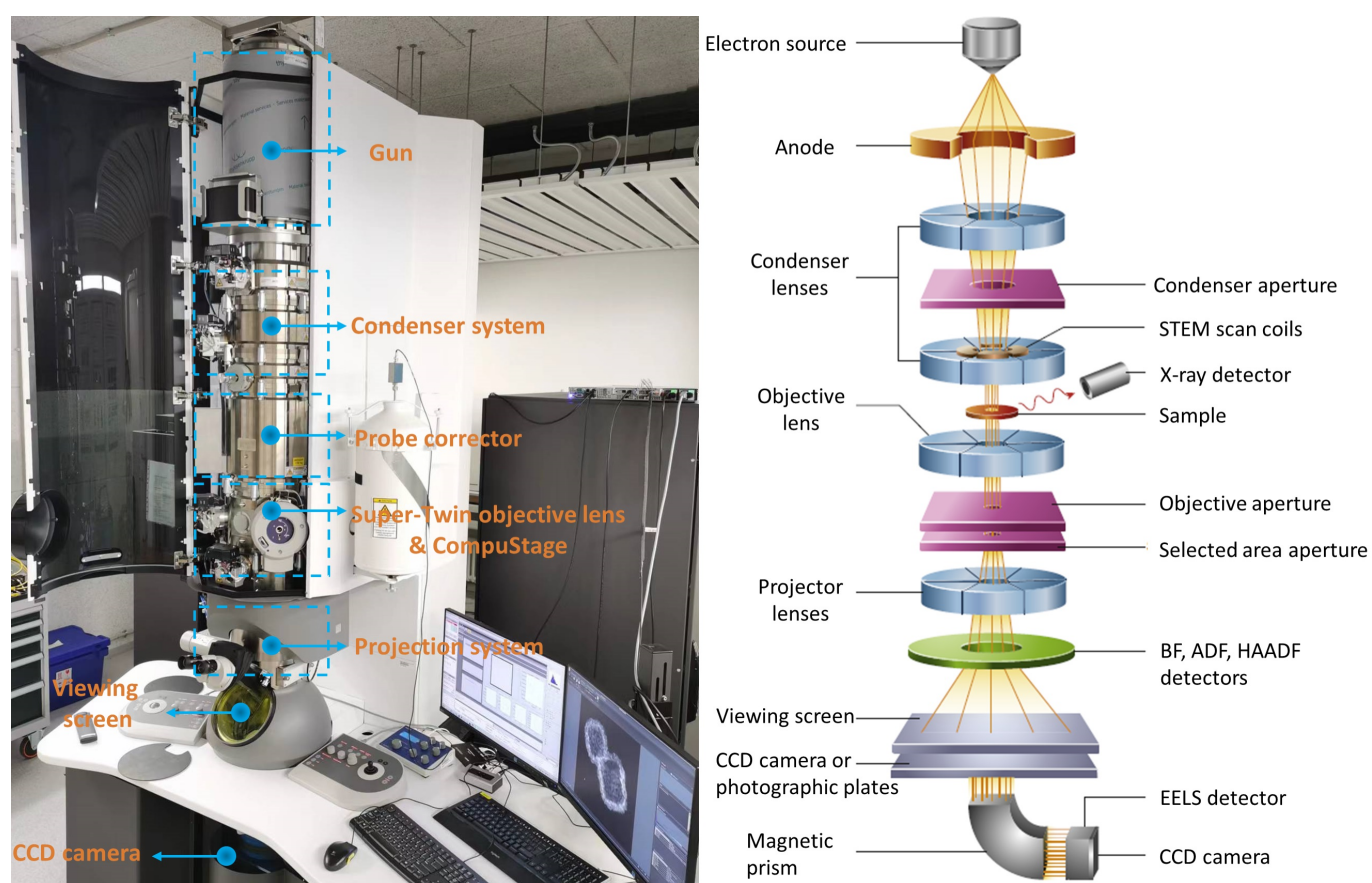
Figure 2.3: (left) Representation of optical components in an advanced TEM equipped with probe corrector (a Themis 300 used in this thesis), and (right) schematic diagram of TEM illumination, adopted from [152].

system often consists of three electromagnetic lenses and apertures in modern TEMs, which are used to adjust the intensity, illuminated area and convergence angle of the electron beam on the specimen. An advantage of using an aperture is improving the coherence of the electron beam as all the high angle electrons are blocked and only the electrons close to the optical axis are allowed to pass. Below the three-condenser system, a mini condenser lens is added and joined with the upper objective lens, enables switch between TEM and STEM mode. After passing through the upper part of the objective system, the electron beam hits the specimen and

generates the signals mentioned in section 2.2.1, that can be used for imaging, spectroscopy and diffraction. A first magnified image is formed at the intermediate image plane and a diffraction pattern at the back focus plane (BFP) of the objective lens. After further magnified by the projection system, they can be viewed with a camera or on the viewing screen. However, the electromagnetic lenses are not perfect and often suffer from spherical aberration (Cs), chromatic aberration (Cc) and astigmatism, decreasing the resolution of the final image. These problems can be partially compensated by Cs (image/probe), Cc correctors and stigmators in advanced TEM.

2.2.3. Imaging modes of TEM

The three imaging modes commonly used in a TEM are diffraction mode, imaging mode and STEM mode. In both imaging and diffraction modes, a parallel beam formed by the condenser system is used to illuminate the region of interest (ROI) of the specimen. After interacting with the specimen, the transmitted electrons (scattered and unscattered) are focused by the objective lens, forming an image at the intermediate image plane and a diffraction pattern at the BFP of the objective lens. Operation in imaging and diffraction mode can be switched by tuning the strength of the intermediate lens to focus on the intermediate image plane
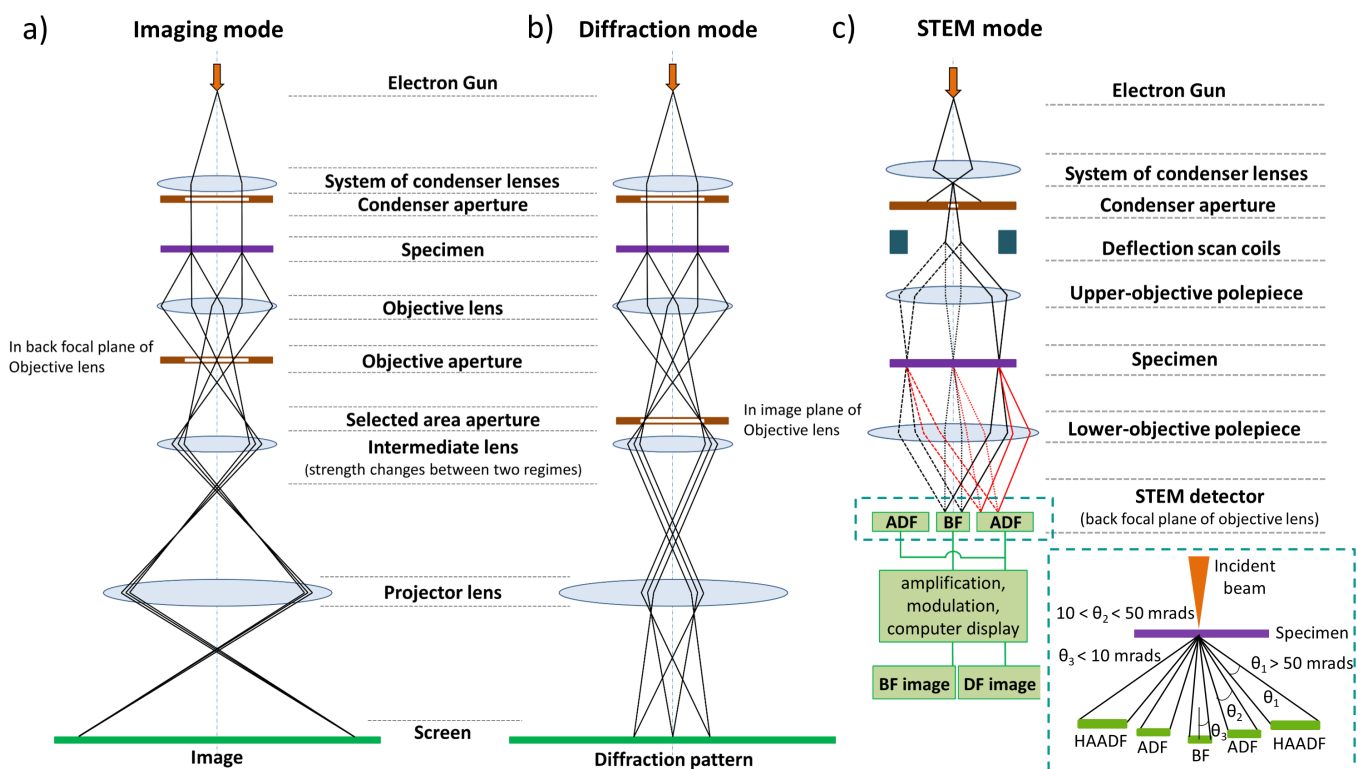
Figure 2.4: Schematic representation of the beam path in imaging, diffraction and STEM mode in a TEM, reproduced from [153].

for imaging or the BFP for diffraction (Figure 2.4a,b). In imaging mode, BF and dark field (DF) images can be obtained separately by selecting the unscattered (direct) beam or a scattered beam for imaging. The BF images originates from two types of amplitude contrast: mass-thickness contrast and diffraction contrast. As its name implies, mass-thickness contrast depends on the mass (related to the atomic number Z and density) and thickness of the specimen, with higher Z and thicker regions scattering more electrons, thus reducing the

intensity of the direct beam and causing these regions to appear darker in the image. Mass–thickness contrast dominates mainly for non–crystalline materials while diffraction contrast is more important for crystalline specimens, where the intensity of the BF image highly depends on the orientation of the crystal and the diffracted beams excited and blocked by an objective aperture. In a DF image, only the regions of crystals where the chosen diffracted beams are excited will appear bright.

Rather than using a parallel beam as introduced above, a finely focused probe produced by the condenser system is used to scan parallel to the optical axis across the sample using the double deflection scan coils in STEM mode (Figure 2.4c). During scanning, the electrons transmitted with different scattering angles are collected by various detectors. For example, the direct beam or low-angle scattered electrons (< 10 mrad) are collected by a BF detector to form a BF-STEM image with information similar to BF-TEM images. The higher scattered electrons (10-50 mrad) are collected by an angular dark field (ADF) detector and the resultant ADF image is complementary to a DF-TEM image with an aperture corresponding to the ADF detector shape. To collect the electrons scattered to higher angles (> 50 mrad), a HAADF detector is used. Such high-scattered electrons are dominated by Rutherford scattering and thermally diffuse scattering, with the intensity roughly proportional the atomic number Z squared and the sample thickness. In addition to imaging, STEM is also commonly combined with analytical techniques such as EDS and EELS to provide the corresponding information on the specimen.

2.2.4. Scanning electron microscopy and focus ion beam systems

Scanning electron microscopy (SEM) is a frequently used technique for studying the surface of bulk materials. Analogous to STEM imaging, SEM uses a fine electron beam (typical with an energy between 0.2 - 30 keV) focused by the condenser system to scan across the specimen surface using pairs of scanning coils. The signals
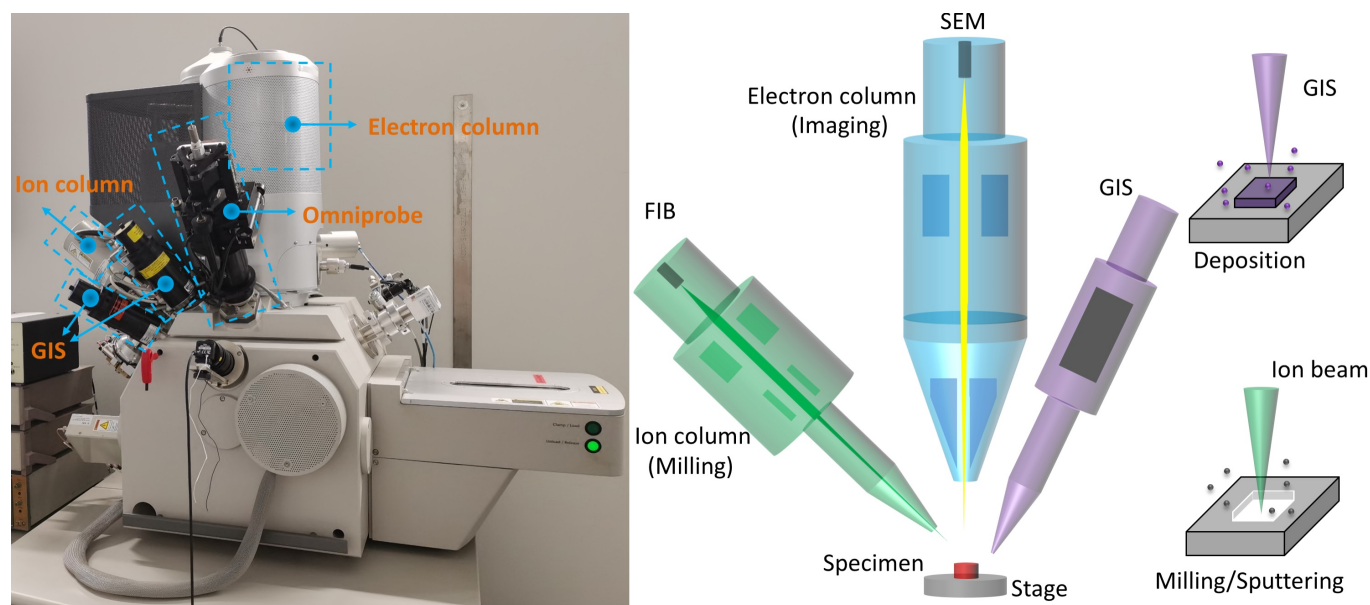
Figure 2.5: Image of a Dual-beam FIB and schematic representation of the main optical components (FEI Strata 400 S used in this thesis).

used for SEM imaging are typically the secondary electrons, back-scattered electrons and characteristic X-rays, making it possible to measure the surface structure and composition of the specimen. A FIB system uses setup

resembling a SEM but with a focused ion beam (typically Ga$^+$) instead of electrons, allowing for imaging at low beam currents and structuring the sample surface at high beam currents. With a built-in micromanipulator, the ROI of the specimen can be extracted precisely by in situ lift-out and attach to a typical TEM half grid after cutting a section of the sample free. Combining SEM and FIB in a single instrument, both imaging and nanofabrication can be achieved (Figure 2.5). In such a dual-beam system, a gas injection system (GIS) is usually employed for selective deposition of materials, e.g. Pt or carbon on the sample surface to protect the surface and enabling nanoscale welding, e.g. to connect to micromanipulator for in situ lift-out of TEM samples. This technique is widely used to prepare TEM lamella from bulk materials. [154]–[156]

2.3. Mathematical foundation of tomographic image reconstruction

The Radon transform

The Radon transform R describes the projection process by mapping a 2D function *f(x,y)* in real space by line integrals *f* along all possible lines *L*:

$$Rf = \int_L f(x,y)ds \tag{2.1}$$
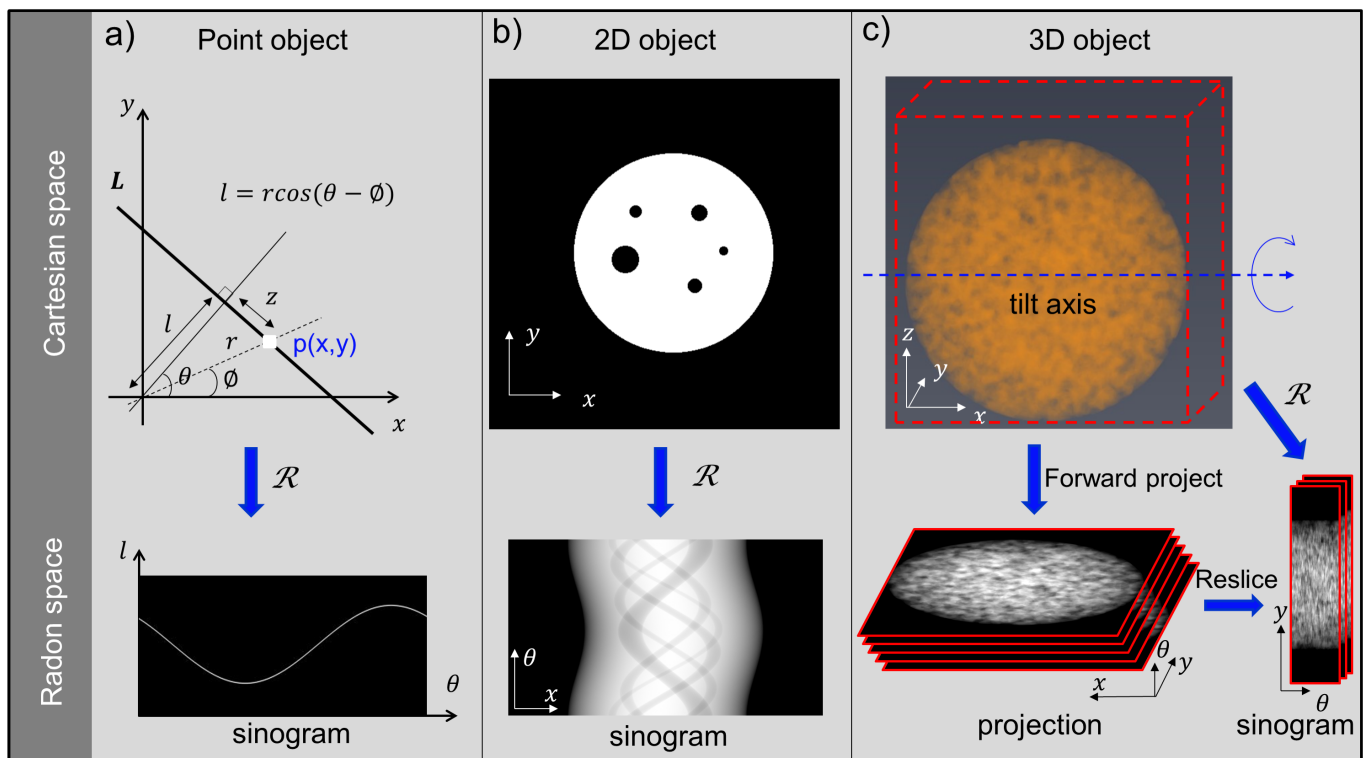
Figure 2.6: Illumination of the Radon transform of (a) point, (b) 2D and (c) 3D object.

As shown in Figure 2.6a, a given point object $p(x, y)$ in Cartesian space can be described using polar coordinates (r, ϕ) as $r = \sqrt{(x^2 + y^2)}$, $\phi = tan^{-1}(y/x)$. Suppose that this point object is projected (Radon transformed) along the projection direction *L* for all tilt angles θ (the angle between the horizontal and

projection direction), the distance between its corresponding position in projection plane and coordinate origin can then be calculated as $l = r cos(\theta - \phi)$, resulting in a sine wave. That is why the Radon space image is often termed as a 'sinogram'. The Radon transform of a 2D object is a linear projection of all points. In other words, the projections of an object along the tilt angles θ are the sum of sine waves. Thus, the Radon transform bridges the real space object and its projections in Radon space when the projection requirement (detailed explanation in section 2.5.1) is fulfilled, which implies the possibility that the real space structure can be recovered from the Radon domain by an inversion of the Radon transform. However, the sampling of the object by projections is in practice discrete and the tilt-range might be limited, so that the inverse Radon transform is not uniquely solvable. Reconstruction from a limited number of projections is usually used to yield an adequate approximation to the original object. Experimentally, after tomographic data acquisition of a 3D object (Figure 2.6c), a sinogram (bottom right) can be built by slicing the aligned projection stack perpendicular to the tilt axis (bottom left). Each sinogram slice allows to compute a 2D reconstruction corresponding to one section of the final volume. At the end, the 3D structure is built by stacking the reconstructed 2D sections corresponding to their original sequence.

2.4. Electron tomography workflow

Typically, a complete workflow for tomographic analysis includes tilt series acquisition, alignment, reconstruction and 3D visualization, as shown in Figure 2.7, potentially follow by further quantification of the 3D model. More details for each step can be found in section 2.5-2.8.

3D object   **Tilt series**   **Tomogram**   **3D Model**

ACQUISITION   **ALIGNMENT & RECONSTRUCTION**   **POST PROCESSING & INTERPRETATION**
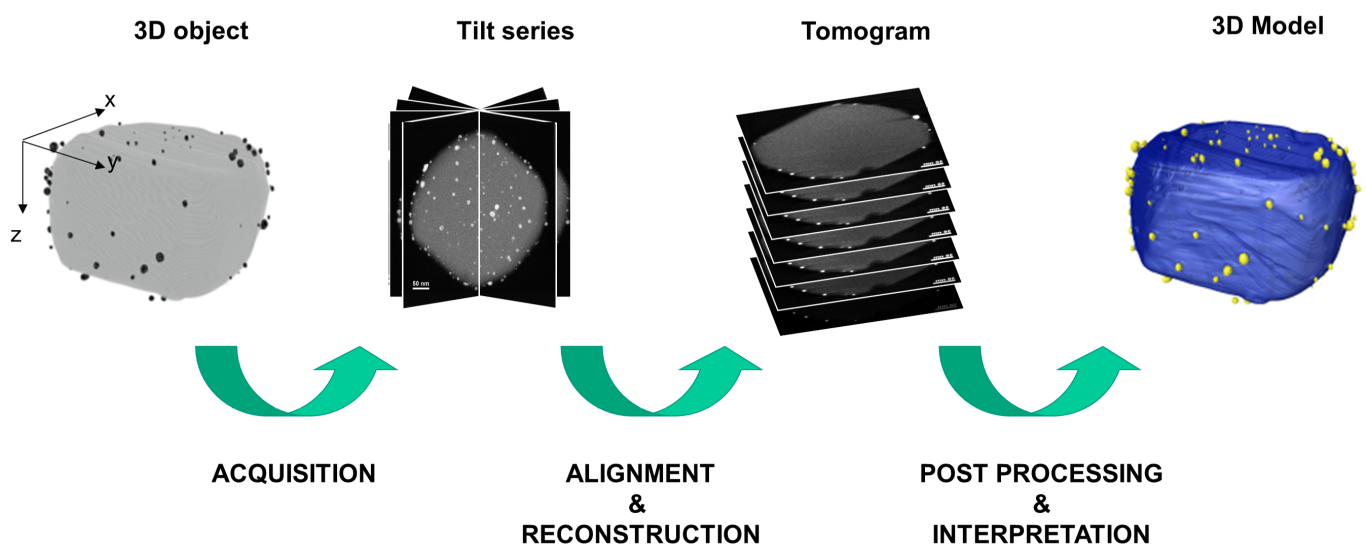
Figure 2.7: Schematic representation of a tomographic reconstruction: 1) acquisition of projection images at different tilt-angles, 2) alignment and reconstruction, 3) post processing and visualization, (figure courtesy of C. Kübel).

2.5. Data acquisition

2.5.1. Projection requirement

One key issue that needs to be considered before data acquisition is the 'projection requirement', which originated from Radon in 1917 [141] and was extended by Hawkers in 1992. [157] It states that the projected signal for electron tomography must be a strict monotonic function of a physical property of the sample under investigation, e.g. density, thickness, magnetic or electrical properties. In reality, slight variations from the projection requirement can be tolerated, where proper tomographic reconstructions can still be obtained. [158] However, research on electron tomography indicates that immediately interpretable signals that meet the projection requirement are far simpler to handle than those that do not. [159] Therefore, choosing a suitable imaging mode based on the sample properties to fulfill the projection requirement is important for tomographic experiments.

2.5.2. Imaging modes in ET

Among various electron microscopy techniques, BF-TEM and HAADF-STEM are nowadays the two standard imaging modes used in electron tomography. For many years, BF-TEM was used for biological specimens, since they are often non-crystalline and thin, weakly scattering objects. [160] For these samples, mass-thickness is the main contribution to image formation, which approximately obeys the projection requirement. For strongly scattering crystalline specimens, diffraction contrast dominates the BF-TEM images, which is very sensitive to the orientation of the sample. In addition, Fresnel contrast that depends on the defocus also contributes to BF-TEM imaging. This will break the projection criterion, limiting its application for many materials. In contrast, HAADF-STEM imaging, has become the most widely utilized technique for ET in materials science. [149] The motivation for collecting HAADF signals lies in the fact that contributions to the image from Bragg scattering is minimized at high detection angles with a large angular integration range. The signal intensity varies monotonically with the thickness of the specimen and the atomic number as long the sample is sufficiently thin. Moreover, the HAADF signal is approximately proportional to the square of the atomic number (Z^2), making it sensitive to compositional variations in the material. With this high contrast and improved visibility, HAADF-STEM has proven to be particularly effective for 3D imaging of buried nanoparticles [161] and catalysts in light supports [101], [162].

2.5.3. Projection geometry

Single-tilt

A typical tilt-series for data acquisition in ET can be obtained by tilting the ROI with respect to the electron beam. This can be performed easily using a single tilt tomography holder (Figure 2.8c). Considering the influence of beam damage to the specimens, data acquisition usually uses tilt increments of 1° to 5°. However, several factors such as the limited objective lens pole piece gap and shadowing by the grid or the TEM holder restricts the maximum tilt-range that can be achieved. In addition, the specimen geometry also plays a significant role limiting the tilt range. For instance, the projected thickness increases with tilt angle for slab-like specimens (Figure 2.8a), and only a small fraction of sample is in focus at high tilt angles. An other issue is that parts of the sample outside the field of view at 0° tilt can contribute to the image at high tilt angles and overlap with the ROI. Theses problems can be solved by using rod-like specimens (Figure 2.8b),

where there is no increase in projected thickness with tilt, no overlap problem, and the whole specimen can be kept at a constant focus for all tilt angles. Considering the limitations mentioned above, a typical tilt range in single tilt-axis tomography is around $\pm 70°$, which will result in the so-called missing wedge problem. More details about the missing wedge problem will be provided in section 2.7.1.
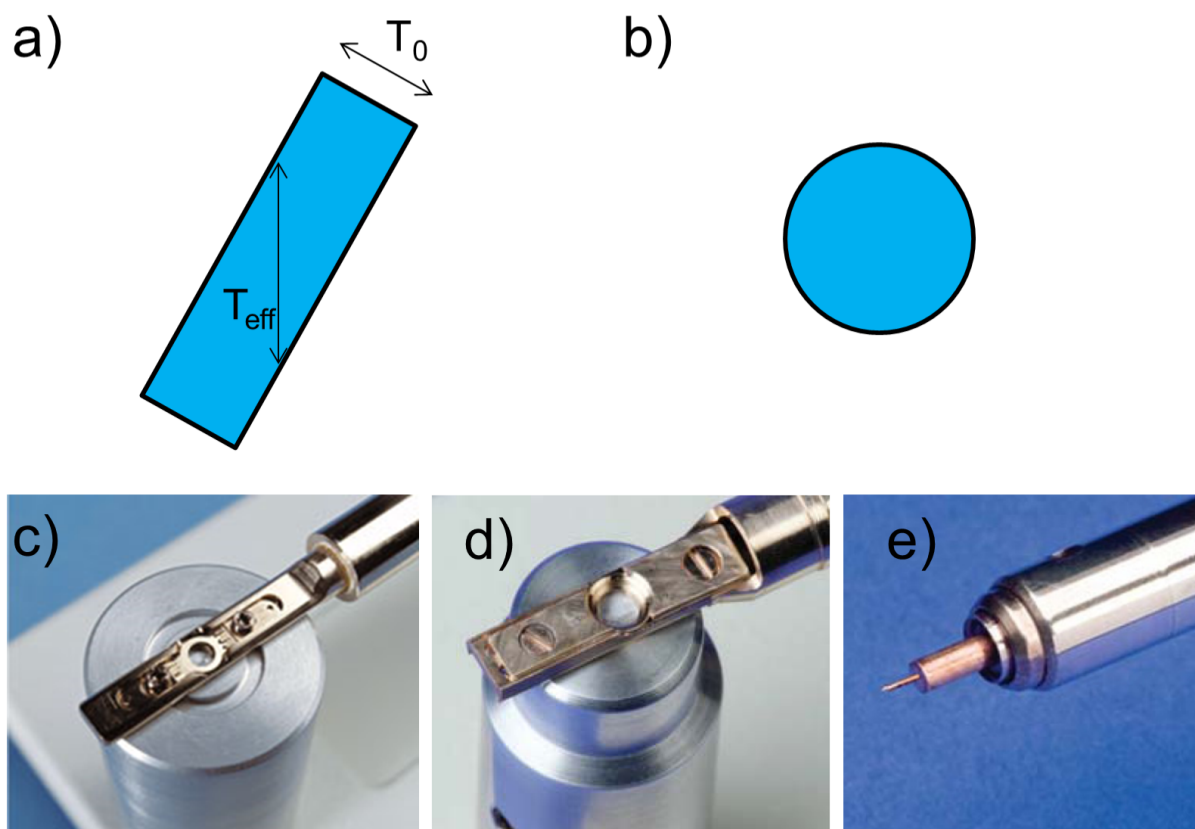
Figure 2.8: Specimen geometry: (a) slab-like specimen, (b) rod-like specimen and images of standard Fischione (c) single tilt holder, (d) double tilt holder and (e) on-axis tomography holder.

Double-tilt and 360° holder

To overcome the missing wedge problem to some extent, an improved tilt scheme can be used to acquire data around two perpendicular tilt axes with a dual-axis tomography holder (Figure 2.8d), which reduces the missing wedge to a missing pyramid. [131] However, the more complicated operation and tilt-series alignment for this technique limit its application. In recent years, an on-axis rotation holder (Figure 2.8e) has been introduced to enable acquisition of tilt series over a full 180° range for rod-like samples and achieve reconstructions without typical missing wedge artifacts. The biggest challenge in this technique is the sample preparation, as specimens are required to be mounted on a needle shaped tip. While some approaches have been reported using a FIB instrument to extract and mill the specimen into a needle geometry, [163], [164] FIB based methods are not suitable for nanoparticles and other fine powders.

2.5.4. Resolution

The resolution of the reconstruction in conventional ET can be estimated using the Crowther criterion. [165] Assuming perfect alignment, the resolution along the tilt axis (X) only depends on the resolution of the input image. However, for the Y direction, which is perpendicular to the tilt axis X and the optical axis (Z), the resolution is limited by the sampling rate and the dimension of the material, as shown in formula 2-2:

$$d_y = \pi \frac{D}{N} \tag{2.2}$$

where D is the diameter of the reconstructed object and N is the number of projections. In the direction parallel to electron beam, the resolution is further reduced due to the missing wedge [152], which can be approximated by multiplying the resolution in the Y direction by an elongation factor (e_{yz}). This can be expressed as:

$$d_z = d_y \cdot e_{yz} \text{ with } e_{yz} = \sqrt{\frac{\alpha + \sin\alpha \cdot \cos\alpha}{\alpha - \sin\alpha \cdot \cos\alpha}} \tag{2.3}$$

where α is the maximum tilt angle, directly determining the value of e_{yz}. For a typical tilt range of $\pm 75°$, e_{yz} is around 1.2 and increasing for a reduced tilt range. This results in an anisotropic resolution depending on the orientation, which causes elongation artifacts to appear along Z direction or so-called missing wedge direction. Nevertheless, the Crowther criterion only provides a rough resolution estimate, which is valid at the outer diameter of the reconstructed volume. In practice, typically a higher resolution can be obtained when some constraints are introduced during the reconstruction (as seen in section 2.7).

2.5.5. Implementation of data acquisition

The acquisition of a tomographic tilt series is straightforward and mainly includes four steps as seen in Figure 2.9. The first step is tilting the sample into the desired orientation with a preset tilt interval. As there are always small shifts in x, y and z direction between two successive tilt projections, the shift in x and y direction can be tracked by cross-correlation and compensated by an image shift in TEM mode and beam shift in STEM mode. The object of interest is refocused before the full image is acquired. Then the sample is tilted to the next tilt angle and the previous steps are repeated.
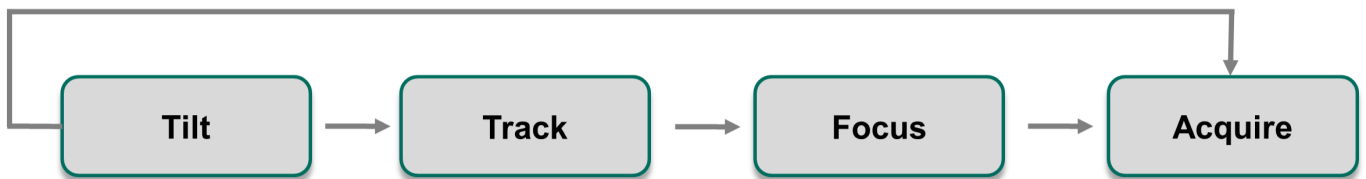
Figure 2.9: Workflow for tomographic data acquisition.

In practice, the data acquisition can be performed either manually or automatically. Compared to the tedious manual acquisition, which highly depends on the operator, the automatic procedure not only eases the acquisition process, but also reduce the total dose on the sample by incorporating a predefined holder calibration file. The purpose of the holder calibration is to measure a set of predictable lateral (x, y) and vertical (defocus/z) shifts at a series of tilt angles in advance and use these values as a coarse compensation to the mostly reproducible mechanical imperfections for a specific TEM stage for the experimental data acquisition.

This facilitates tracking of the object in the field of view after each tilt, thus reducing the time and beam exposure in relocating the region of interest. Another benefit of automated acquisition is the possibility of integrating dynamic focusing for STEM tomography, which compensates for the focus differences encountered in a slab-shaped sample at high tilt angles, thus ensuring that different parts of the sample at different height are at reasonably well focus in every frame. Nevertheless, dynamic focusing does not help with the problem of focus spread in thick samples. In this case, increasing the focal depth of STEM is of great importance. This can be achieved by reducing the convergence angle using a weaker condenser lens or a smaller C2 aperture to increase the depth of focus.

2.6. Tilt-series alignment

As the projected images of a tilt series are recorded only with shift correction during tracking by cross-correlation, small uncompensated shifts in any direction between two successive projections are inevitable. In addition to image shift, other factors that lead to the misalignment of tilt series should be also considered. For instance, the imperfect rotation axis and magnification changes caused by an imperfect optical system sensitive to focus changes, and slight deviations of tilt angles because of an imperfect mechanical control of the stage. To ensure a high quality 3D reconstruction, the acquired tilt series must be aligned to a common coordinate system corresponding to a tilt around a well-defined axis with sub-pixel accuracy. The most commonly used methods for alignment in electron tomography including cross-correlation, center of mass and fiducial marker tracking methods will be introduced in this section.

2.6.1. Cross-correlation

The basic purpose of the cross-correlation function (CCF) is to determine the XY shifts between every two consecutive images (I_A, I_B) of the tilt series. CCF provides an output image whose maximum intensity peak indicates the shift required to bring the features from the two similar images into best coincidence, which can be calculated as:

$$CCF_r = \sum I_{A_{r+r'}} \cdot I_{B_{r'}} = F^{-1} \left[F\left(I_A\right) \cdot F\left(I_B\right)^* \right] \tag{2.4}$$

where F and F^{-1} correspond to the Fourier transform and inverse Fourier transform. Figure 2.10a-c shows an example for a real application in ET. One problem for this method is a quite broad CCF peak is usually obtained when calculating the CCF from two images directly. This is worse when dealing with low-contrast images or noisy images, in which the identical signal is not dominating and the cross-correlation peak might be indistinct. To improve the shift measurement, one or more filtering processes are often used to enhance or reduce the influence of certain features in the images. As shown in Figure 2.10d-f, a much sharper cross-correlation peak can be achieved by using a high bandpass filter. Nevertheless, the cross-correlation match will never be exact as the projected view of the specimen is similar but not identical for successive tilts. This may become more critical for slab-like and thicker specimens, where additional features are brought into the field of view. Foreshortening of features in projection at successively higher tilts can be significant in these specimens. In this case, a linear stretch ($1/cos\theta$) perpendicular to the tilt axis is needed, which enables recovery of the spatial correspondence between successive projections. [159], [166]

Another problem of this method is the cumulative error. When aligning a tilt series by cross-correlation, the projections are aligned one by one, i.e., the actual projection is aligned using the previous projection as

reference. Then the aligned second projection will be used as a new reference to align the next projection and so on. The consequence of this is that, small subpixel misalignment errors occurring between each set of projections, are building up to a significant error over the tilt series. In addition, variations in the tilt-axis orientation, tilt angle and magnification cannot be compensated by cross-correlation alignment.
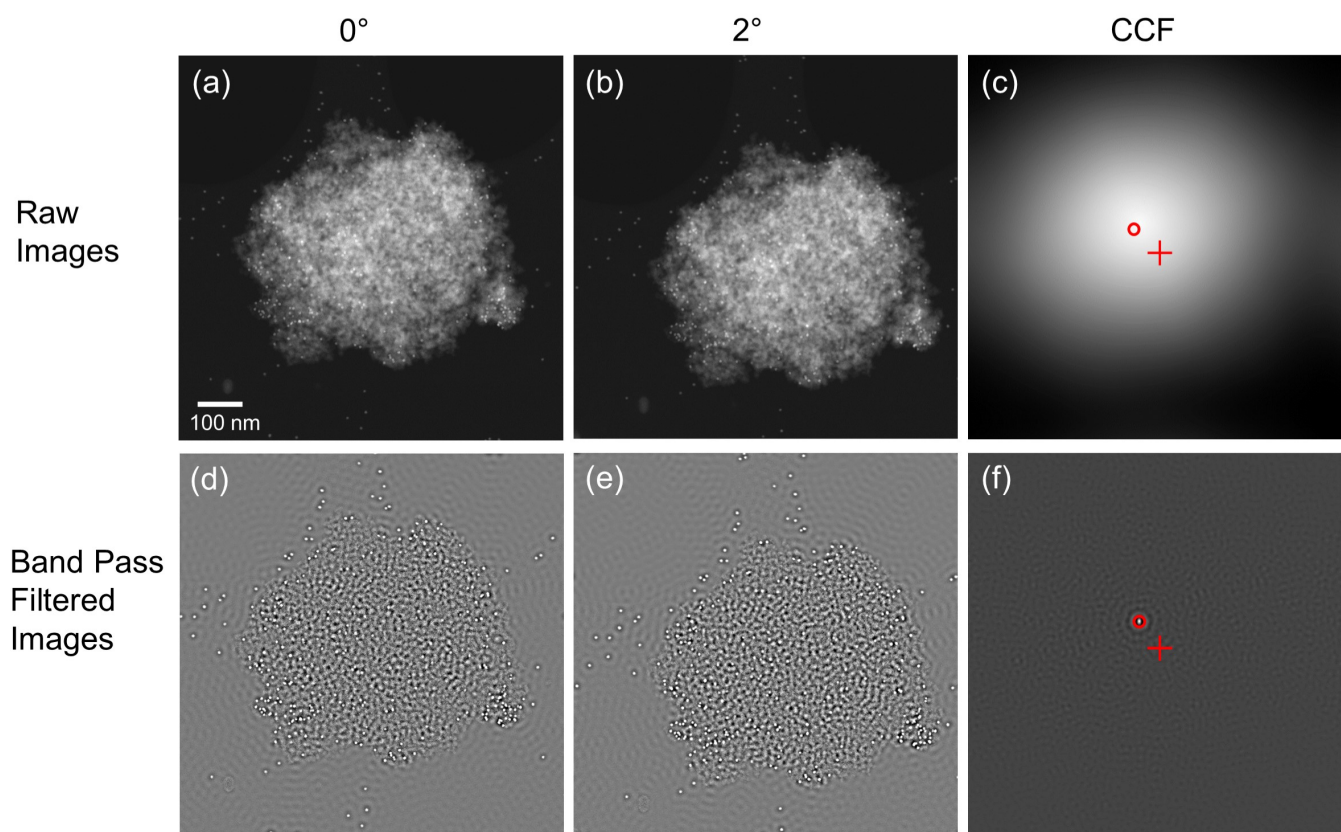
Figure 2.10: Determining the relative shift between two tilt series images by cross-correlation. (a,b) Successive tilt series images and (c) the corresponding cross-correlation indicating their relative shift. (d,e) Band pass filtering of the images to yield (f) a sharper cross-correlation peak.

2.6.2. Tilt axis adjustment

As the cross-correlation only aligns the image shift in lateral and vertical direction, the identification of the position and orientation of the tilt axis has to be performed manually. As an example, artifacts caused by tilt axis misalignment for on a HAADF-STEM tilt series of gold dog-bone nanoparticles can be seen in Figure 2.11. [159] When the tilt axis is correctly positioned, all reconstructed particles show a high symmetry and roughly round shape in cross-section (depending on the effect of missing wedge), regardless of their spatial location in the reconstructed volume (Figure 2.11b). However, an incorrect tilt axis angle will introduce 'banana' artifacts in opposite directions at the top and bottom of reconstructed slices while the reconstruction of the central slice remains correct, as indicated schematically in the lower right corner in Figure 2.11c. Similarly, a lateral shift of the tilt axis will also cause 'banana' artifacts in a common direction in all reconstructed slices (Figure 2.11d). Thus, the misaligned tilt axis can be adjusted easily by minimizing these 'banana' artifacts.
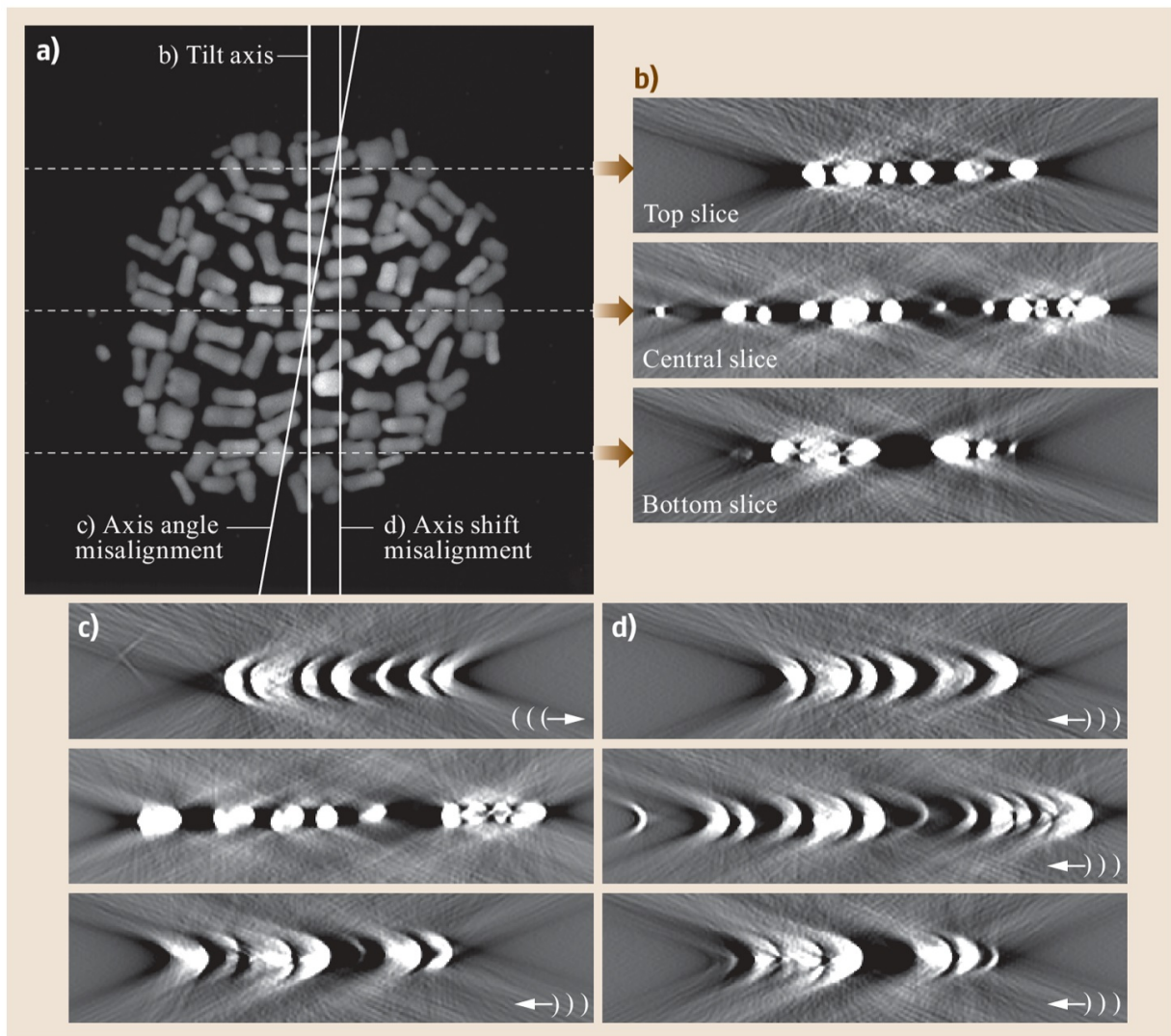
Figure 2.11: Tilt axis alignment by minimization of arcing artifacts based on a HAADF-STEM tomographic series of gold dog-bone nanoparticles, adapted from [159].

2.6.3. Fiducial marker tracking

An alternative to cross-correlation is the fiducial marker tracking method, in which fiducial markers (often colloidal gold particles, which are assumed to be immobile with respect to the specimen structure) are added to the specimen. Figure 2.12b-h shows Au particles distributed randomly on the sample in all projections. These markers can be easily tracked in the images due to their high contrast. In practice, the tracking procedure mainly involves three steps, as illustrated in Figure 2.12a:

(i) 20-30 markers are usually selected and the positions of these markers are tracked throughout the whole tilt series. This process can be carried out automatically after an initial cross-correlation alignment of the tilt-series;

(ii) The 3D position of each marker is estimated and used to predict the corresponding 2D projected positions in all views of the tilt series;

(iii) The alignment of the tilt series is refined by minimizing the difference between the experimental marker positions and the calculated positions.

This process is iteratively repeated to refine the alignment of all the projections. During the refinement process, it is also possible to correct to a certain extent for image distortions, tilt axis orientation, inaccuracies of the tilt angle, magnification variations, beam tilt and sample shrinkage, yielding an overall alignment with average residual errors at the sub-pixel level. Therefore, the fiducial marker-based alignment procedure is superior to the cross-correlation for obtaining an accurate alignment of the projected images.
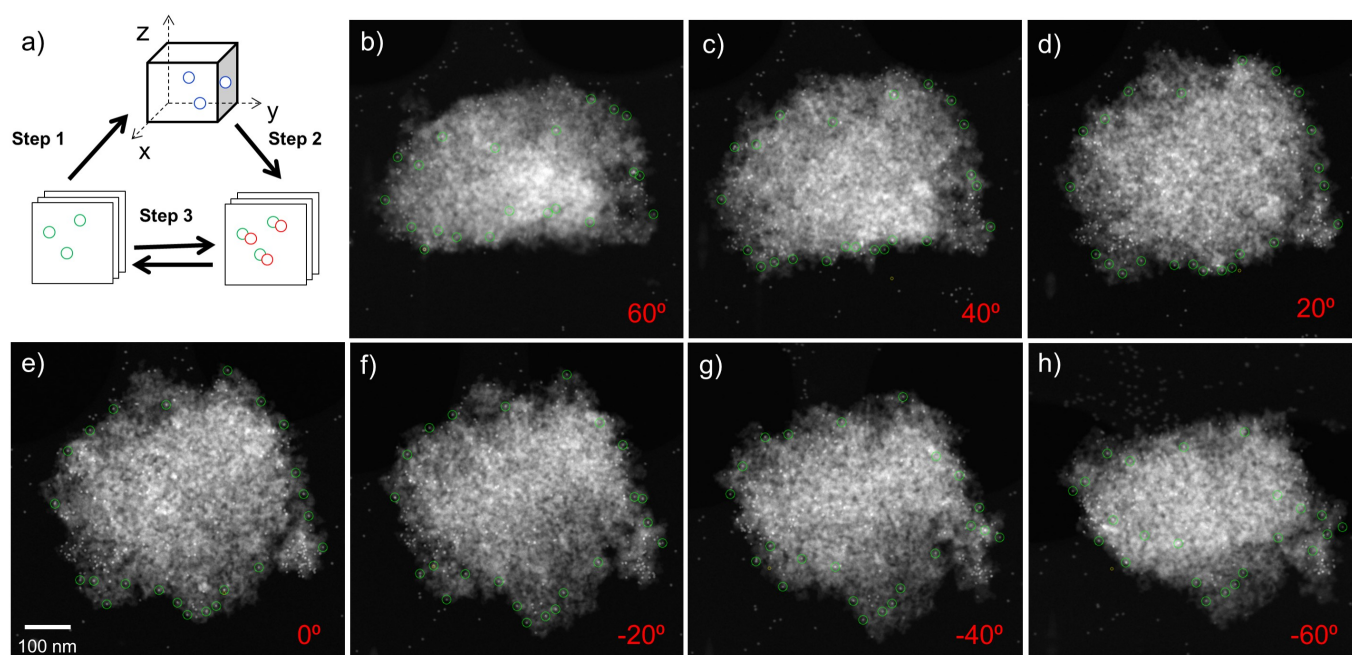
Figure 2.12: Illustration of alignment by fiducial marker tracking method.

Other alignment approaches such as center of mass (CM) and common line are also used, especially in atomic-scale ET. [167]–[169] The CM method assumes that the position of the center of mass is the same in all projections when tilting the object. In practice, the tilt series can be aligned to the common axis by shifting all projections so that their center of mass is located at the same position. The idea of common line alignment comes from the Fourier slice theorem, where the Fourier transform of all projections will intersect on a single line along the tilt axis for a single tilt tomographic series in Fourier space. In real space, this means that if the measured 2D projection images were further projected onto the tilt axis to obtain one dimensional (1D) profiles, they all should be exactly the same. By using cross-correlation, all 1D projected curves can be aligned together along the tilt axis. Is has to be noted that the common line method cannot align the tilt series along the direction perpendicular to the tilt axis. Unlike cross-correlation, both CM and common line methods align all the projections based on one common image as reference rather than aligning the projections one by one, thus avoiding the problem of accumulative error and thus potentially give rise to higher alignment accuracy. However, one common problem for both methods is their sensitivity to the background and noise, so proper background subtraction and denoising should be done prior to the alignment. In addition, similar to the cross-correlation method, these two methods only allow the alignment of spatial image shifts, further steps are needed for tilt axis alignment and it is not possible to compensate for other alignment error sources.

2.7. Reconstruction algorithms

Various reconstruction algorithms have been applied in ET, among them three mainstream classes are introduced in this thesis: (weighted) back projection, conventional iterative reconstruction methods such as algebraic Reconstruction Technique (ART) and SIRT, and advanced iterative reconstruction methods using prior knowledge like TVM and DART. To better understand reconstruction artifacts caused from constrained sampling, a brief introduction to the Fourier/Central slice theorem will also be provided in this section.

2.7.1. Fourier/Central slice theorem and missing wedge

The Fourier/central slice theorem was introduced for tomography by Bracewell in 1956 [170], which states that the Fourier transform of a 2D projection at an angle θ is a central section through the Fourier space of the 3D object at the same angle. As shown in Figure 2.13a, recording projections at various tilt angles is then equivalent to sampling 3D Fourier space at the corresponding angles. Therefore, a limited tilt range during the acquisition results in a missing wedge of information in the 3D Fourier space. In addition, the discrete angular increment will result in a higher sampling density at low spatial frequencies compared to high spatial frequencies (Figure 2.13b), resulting in a blurring of the reconstruction.
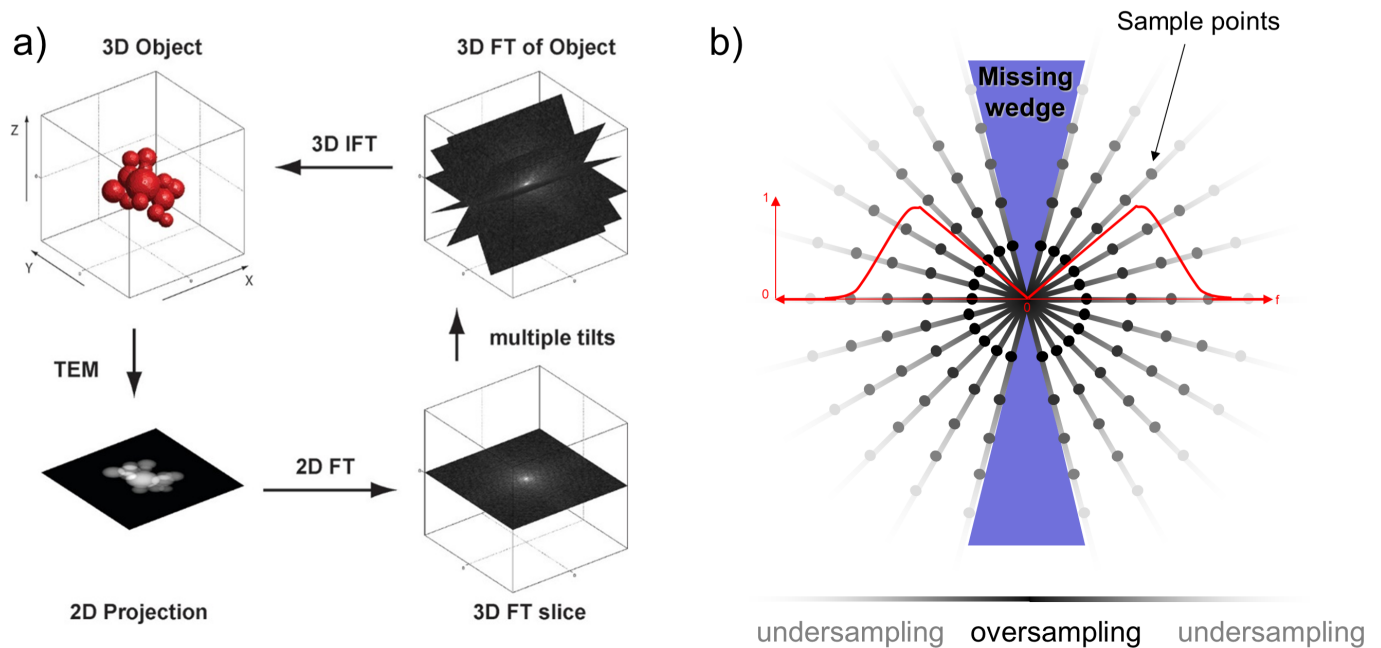
Figure 2.13: Schematic representation of (a) Fourier slice theorem from Friedrich et al. [171] and (b) missing wedge from limited angular sampling (figure courtesy of C. Kübel)

.

2.7.2. Backprojection

Backprojection (BP) is the process of propagating each projection along the projection direction back. Figure 2.14a-e shows BP reconstructions of a KIT logo from various projections. By backpropagating an infinite

number of projections, the summation of the back projected rays in the reconstruction space will generate the original object. However, the number of projections in a real experiment is limited. According to the Fourier slice theory (Figure 2.13), the Fourier domain of the object is sampled in such a way that the low frequencies are sampled much more densely than the high frequencies. The more severe undersampling for higher spatial frequencies causes the reconstruction to appear blurred, especially edges (Figure 2.14e).
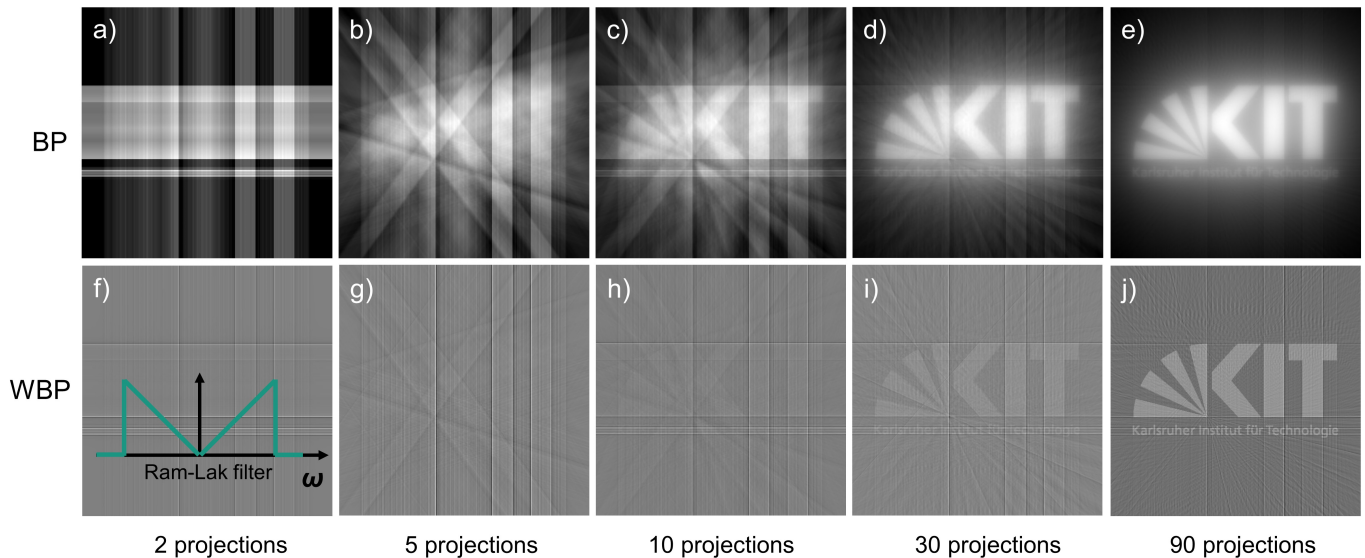
Figure 2.14: (a-e) Backprojection and (f-j) weighted backprojection reconstructions using Ram-Lak filter of the KIT logo from various projections within a tilt range of $\pm 90°$.

To partially overcome this problem, a proper filter like a Ram-Lak filter (inset in Figure 2.14f) can be applied to the projections in the Fourier domain. This is so-called weighted back projection (WBP), in which the low frequencies will be suppressed, thus avoiding overly blurred back projected reconstructions. To start a WBP reconstruction, the raw projections are Fourier transformed using FFT method. The resulting transformed image is then filtered by multiplying with a Ram-Lak filter to reduce the low frequencies and enhance the high frequencies. Typically, there is also a cut-off defined above which all frequencies are set to zero to reduce noise. After the filtering, the previous transformed image is inversely Fourier transformed to a new set of projections, which will be used as input for the BP to obtain the final reconstruction. Figure 2.14f-j shows the WBP reconstructions of the same KIT logo from various projections. With a sufficient number of projections, the reconstructed image preserves sharp edges much better compared to BP. This method is still widely used nowadays especially in computed tomography or even electron tomography because of the simple principle and fast reconstruction. Nevertheless, it should be noted that using a filter during the WBP reconstruction can induce artifacts in the reconstruction. More details will be discussed in the next section.

2.7.3. Iterative methods

Another approach in ET is the application of iterative algorithms using additional constraints, which aim to find the best match between experimental projected images and forward projection images from the reconstructed tomogram, by refining the reconstructed object iteratively. According to the Radon transform, the projection process in tomography can be expressed as a linear operator W that maps the object function $x \in R^n$ to the projection vector $p \in R^n$:

$$\boldsymbol{W}x = p \tag{2.5}$$

which can be expressed as:

$$\begin{pmatrix} w_{1,1} & & w_{1,n} \\ \vdots & \cdots & \vdots \\ w_{m,1} & & w_{m,n} \end{pmatrix} \begin{pmatrix} x_1 \\ \vdots \\ x_n \end{pmatrix} = \begin{pmatrix} p_1 \\ \vdots \\ p_m \end{pmatrix} \tag{2.6}$$

where $n = k^2$ represents the size of reconstructed object (here an example of a 2D object) and $m = k \times h$ corresponds to the total size of projection data with the number of projection angles of h. $W \in R^{m \times n}$ is the projection matrix, in which each row represents the projection operator for a single ray at a given projection angle and each row of p represents the corresponding projection data. The problem of reconstructing the object is equivalent to finding $x \in R^n$ for a given projection matrix W and measured projection data p such that $Wx = p$ is fulfilled. In practice, this problem is underdetermined as $m < n$ in most cases, and the projection data often contains noise or other errors. In this case, a solution is to seek the minimum of $\|\boldsymbol{W}x - p\|$ with some vector norm, e.g. l_2-norm ($\|y\|_2^2 = \sum_{i=0}^{n-1} y_i^2$ for $y \in R^n$), using iterative methods:

$$x^* = \operatorname*{argmin}_x \|p - \boldsymbol{W}x\|_2^2 \tag{2.7}$$

Algebraic Reconstruction Technique

The principle used by ART is rather straightforward and was proposed by Kaczmarz in 1937 [172] and then introduced to the field of ET by Gordon, Bender and Herman in 1970 [173]. A simple example in which a 2D matrix with four unknown pixels was reconstructed by three projections can be seen in Figure 2.15, where the iterative procedure includes three steps:

(i) Make an initial guess for the solution, typically with all pixels set to zero;

(ii) Compute the weighted difference between projections and guess along a certain projection ray. For the first row in Figure 2.15a, the weighted difference is (7-0)/2=3.5;

(iii) Update the reconstructed matrix by adding the weighted difference to the previous values of the corresponding pixel hit by the projection ray.

Therefore, each pixel in the first row should be 0+3.5 = 3.5, as shown in Figure 2.15b. With the same procedure, all the pixels are updated iteratively, so that a refined 2D matrix can be retrieved. In a real reconstruction of a tomographic dataset from a tilt range of $\pm 70°$, typically, 70-140 projections (depending on the tilt step) with a size of 1024×1024 are used, the reconstruction is usually carried out iteratively. However, this method is quite sensitive to noise and is not guaranteed to converge.
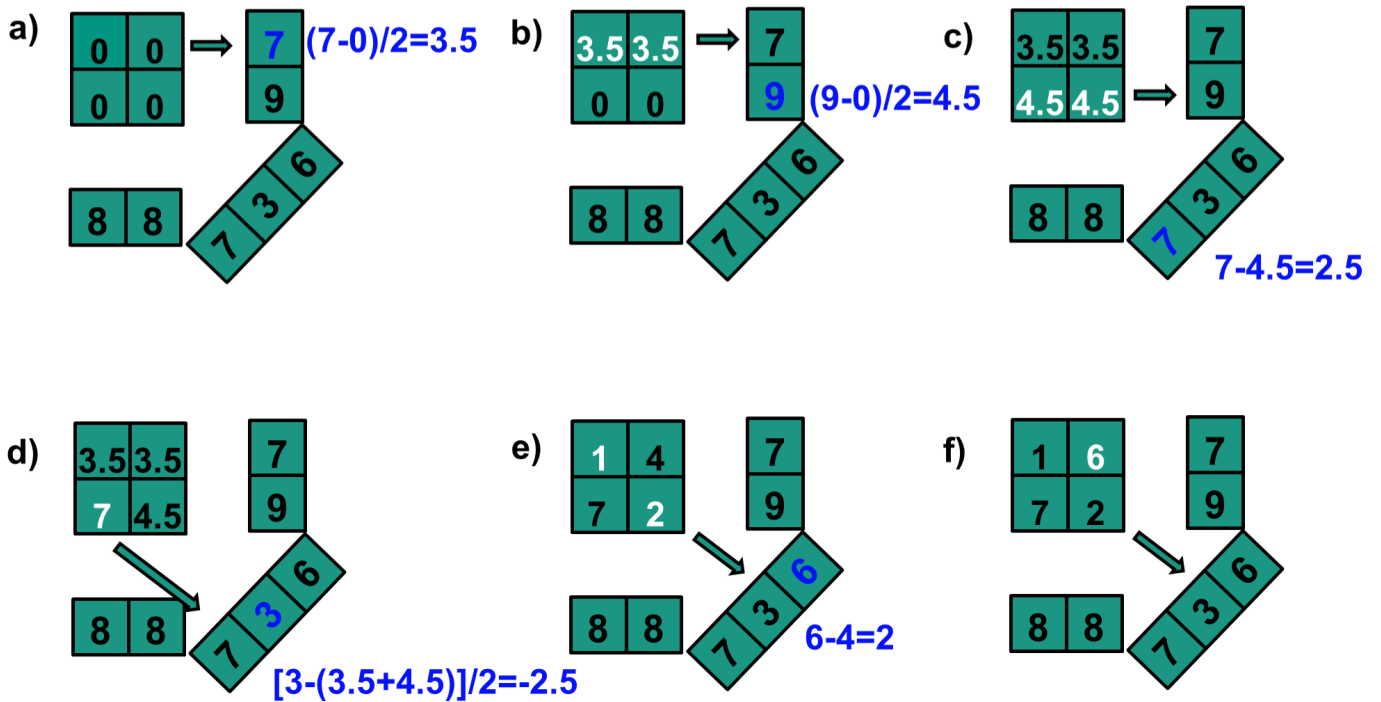
Figure 2.15: Illustration of ART reconstruction for a simple 2D matrix with four unknown pixels from three projections.

Simultaneous Iterative Reconstruction Technique

One year after the introduction of ART for ET, Gilbert suggested a modified approach which is widely known as SIRT. [174] As its name implies, SIRT is an iterative method that updates the reconstruction using all the available projection data simultaneously, making it less sensitive to noise than ART. More specifically, SIRT converges with sufficient iterations in the absence of noise. Figure 2.16 shows the workflow for this technique. Starting from an initial reconstruction obtained by e.g. WBP, the obtained reconstruction is re-projected along the original experimental tilt angles, resulting in a set of new computed projections. These computed projections are either subtracted from the measured projections (additive SIRT) or the experimental projections are divided by the computed projections (multiplicative SIRT). The resulting difference projections are back projected to get a difference reconstruction. Then the current reconstruction is updated by adding/multiplying the difference reconstruction. This process is repeated until a certain iteration number is reached.

However, it is not true that better reconstructions are obtained with an increasing number of iterations. It has been found that in the presence of noise, the results tend to be a better approximation of the 3D structure of the studied object after a few iterations, but above a certain number of iterations the resemblance starts to deteriorate, even though the match between the experimental and the re-projected images can be maintained or even improved. This problem occurs when there is a high noise level in the experimental projections, where the noise in the original experimental data is averaged during the iterations between forward- and back-projections.
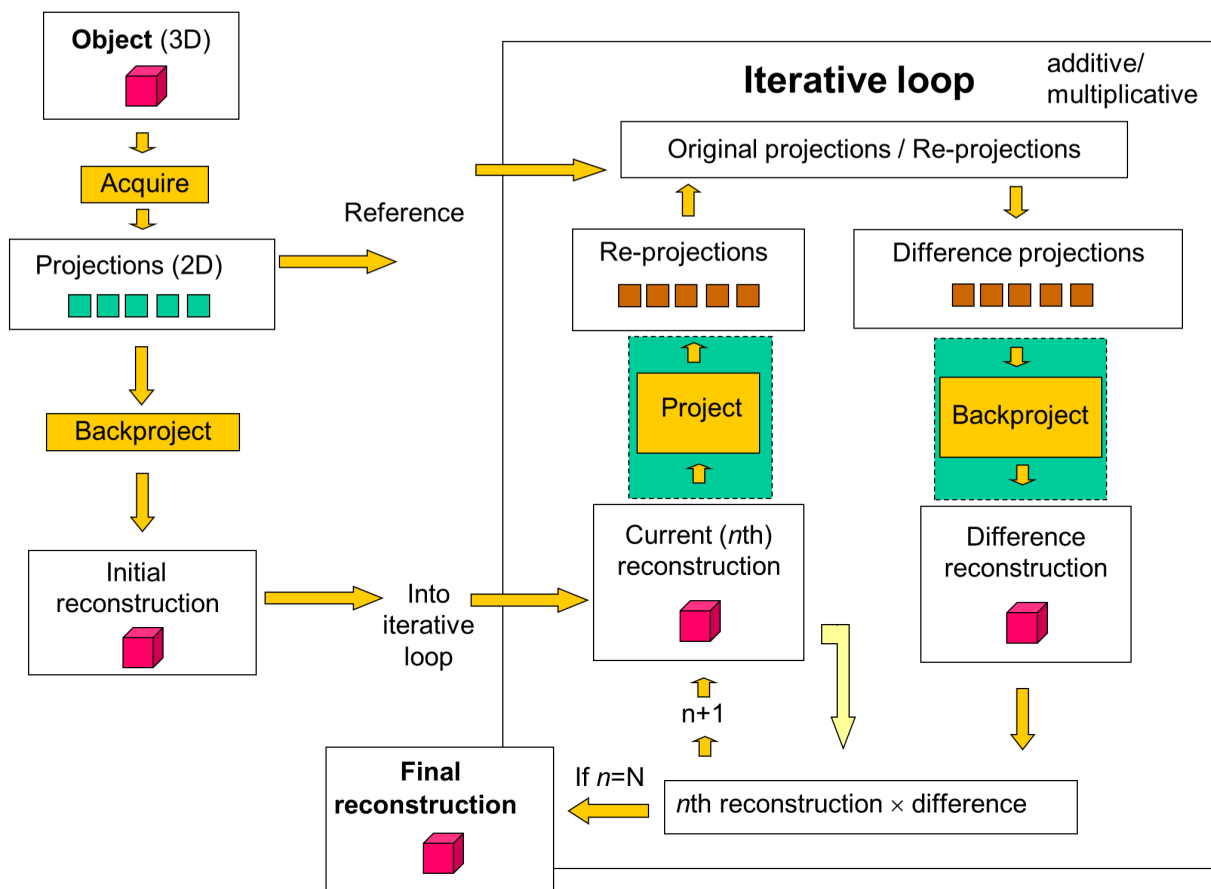
Figure 2.16: The flow chart for SIRT (figure courtesy of P. Midgley from University of Cambridge).

Figure 2.17 shows a comparison of WBP and SIRT reconstruction from a full tilt range with 91 projections. The Ram-Lak filter using during WBP reconstruction introduces strong artifacts for the intensities, as visible in Figure 2.17b, where the intensity of the vacuum area around the KIT logo is almost identical to the intensity of the logo. This will become a serious problem especially for imaging specimens with low- and high-density
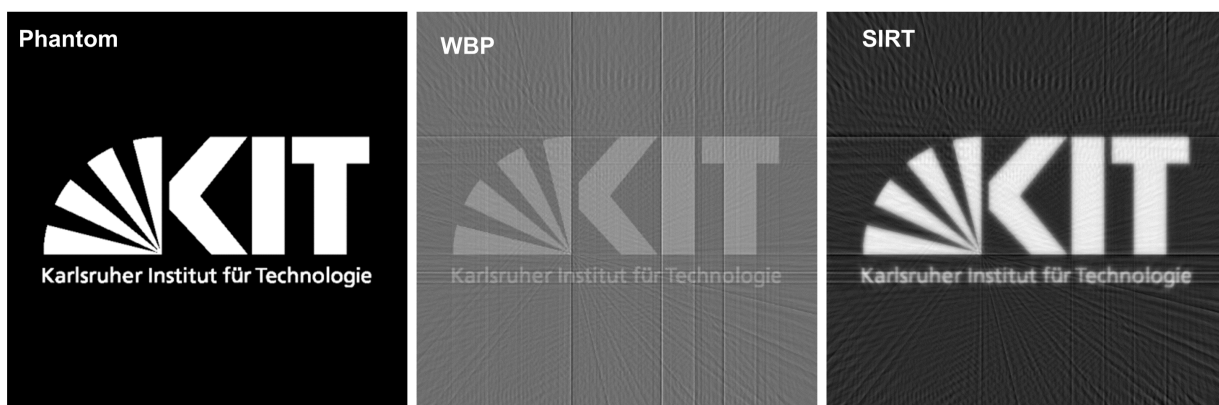
Figure 2.17: Comparison of the reconstruction of the KIT logo using WBP and SIRT methods.

components. In the SIRT reconstruction of the same data, the contrast is better preserved. However, clear

streaking artifacts which are caused by the discrete sampling can be seen in both reconstructions.

The missing wedge problem caused by the limited tilt range is another challenge for SIRT. Figure 2.18 showed SIRT reconstruction from a set of series of the TU Darmstadt logo with different tilt ranges and a tilt step of $2°$. For the tilt range of $\pm90°$, meaning no missing wedge, all the detailed features can be reconstructed perfectly when ignoring the streaking artifacts. With a reduced tilt range (sever) elongation artifacts appear and some features are missing in the missing wedge direction. This problem will strongly affect the accuracy of the reconstruction especially for some small features, e.g. isolated pores or embedded particles. As single tilt ET with limited tilt range is still the routine technique in material science, alternative approaches that are able to reduce or even solve the missing wedge problem remain avidly sought after.
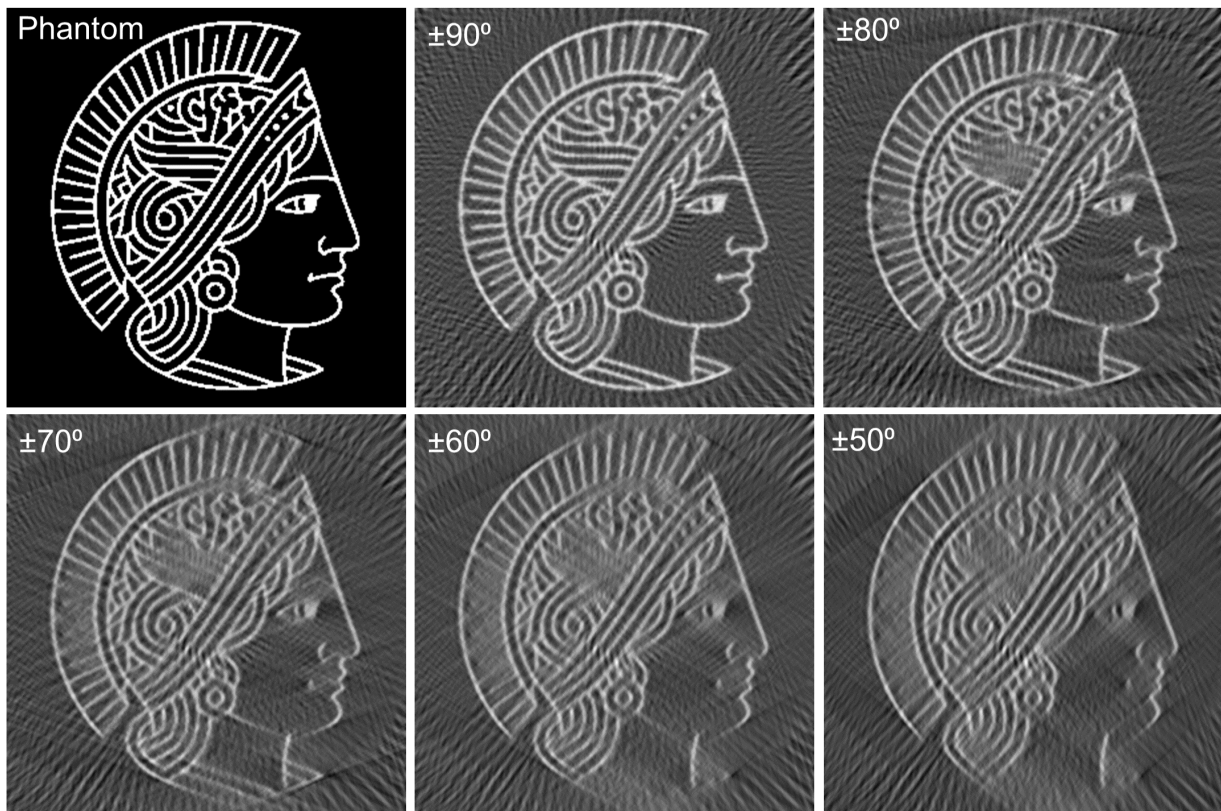
Figure 2.18: Evaluation of the SIRT reconstruction for the missing wedge problem using the TU Darmstadt logo.

2.7.4. Advanced iterative algorithms using prior knowledge

With the improved computation power and the development of new mathematical methods, advanced algorithms have been proposed in ET by incorporating prior assumptions on the measured objects.

Total variation minimization

TVM is based on compressed sensing image processing methods, which aims to exploit the knowledge that the reconstructed object has a sparse representation. Sparse means that most of the elements are zero in a system. For example, although the image in Figure 2.19a is not sparse due to the existence of many non-zero pixels, the image in Figure 2.19b shows that the gradient is sparse. As most continuous areas have the same intensity, the corresponding gradient is zero. In nanostructured materials consisting of finite components, it

is often reasonable to assume that the gradient of the object is sparse. A convenient way to implement this sparsity in a tomographic reconstruction is by simultaneously minimizing the projection difference between the reconstructed object and the original projections and the total variation of the reconstructed object:

$$x^* = \underset{x}{\mathrm{argmin}} \left[TV(x) + \frac{\mu}{2} \| p - \boldsymbol{W}x \|_2^2 \right] \tag{2.8}$$

where TV is the total variation computed as the norm of the discrete gradient of the reconstructed object and μ is a regularization parameter. This parameter penalizes the TV with the difference between the measured projection p and the reconstructed projection $\boldsymbol{W}x$, where a large μ leads to a result closer to a SIRT reconstruction with high frequency details while a small μ will suppress noise, thus choosing a proper μ is of great importance to obtain a reasonable reconstruction. The influence of μ on the reconstruction is shown in Figure 2.19c-e. An underestimation of μ leads to a reconstruction in which noise is suppressed, while high frequency details of the reconstruction are wiped out as well. A large value of μ leads to a result that resembles a SIRT reconstruction, in which both missing wedge artifacts and noise are observed in the resulting reconstruction.
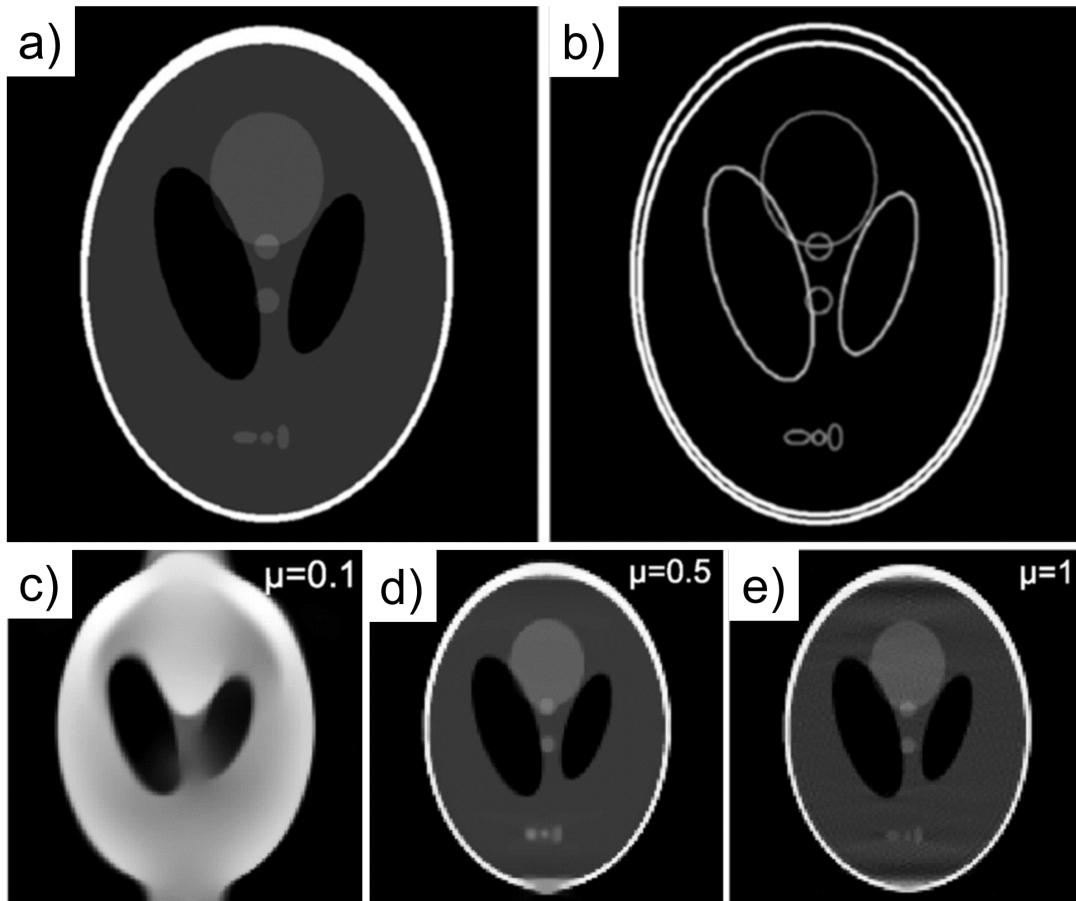
Figure 2.19: (a) Shepp-logan phantom object, (b) gradient image of this phantom and (c-e) influence of the regularization parameter μ on the quality of the reconstruction by TVM from a tilt range of $\pm 70°$ with an increment of $2°$, reproduced from [127].

Figure 2.20 shows a comparison of TVM and SIRT for PbSe–CdSe core shell nanoparticles. Figure c

and d are two corresponding slices in xy plane. Both SIRT and TVM perform well in the xy plane (the projection direction), while it is clear that the SIRT reconstruction is more elongated in comparison to the TVM reconstruction in the xz plane (the missing wedge direction). An additional advantage of the TVM reconstruction is that, after the minimization of the gradient, the reconstruction shows better signal to noise ratio, resulting an easier segmentation for quantitative analysis.
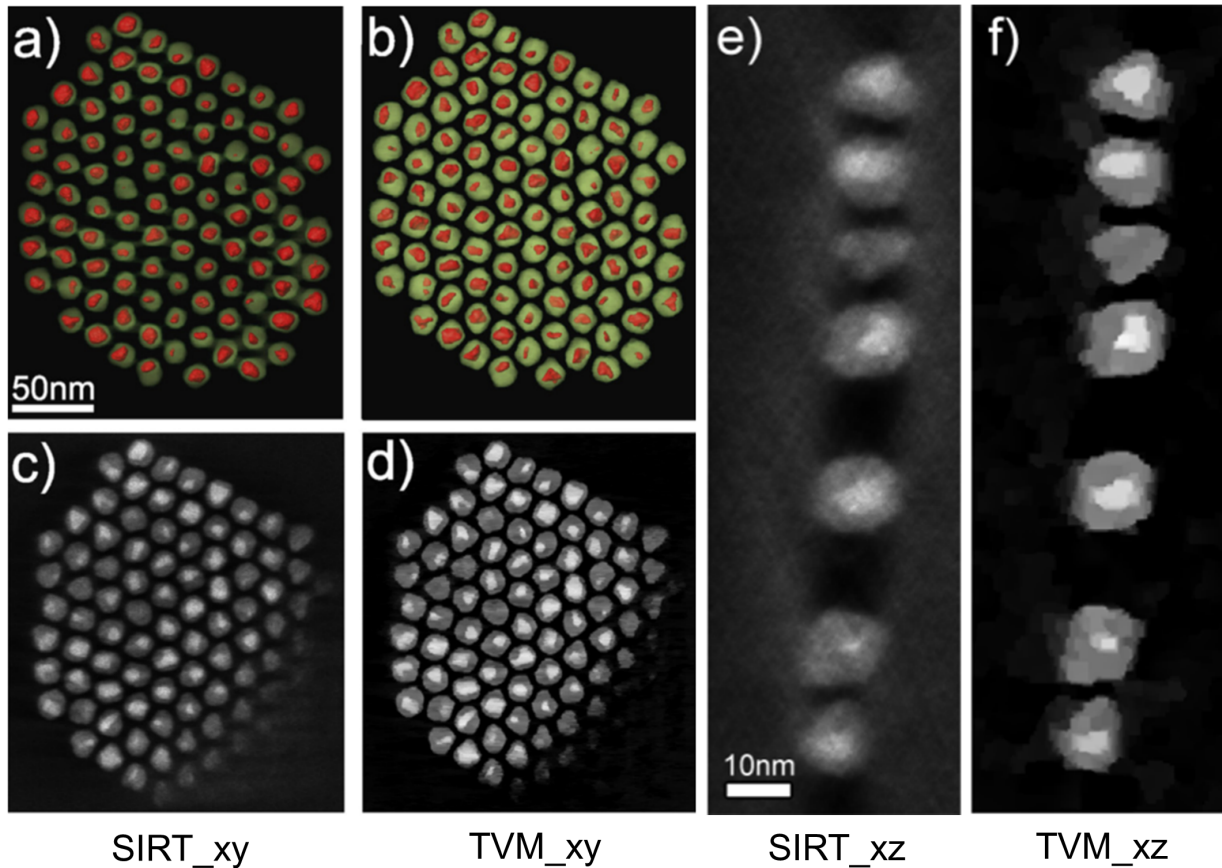
Figure 2.20: SIRT and TVM reconstructions of the PbSe–CdSe core shell nanoparticles. (a,b) show a voltex visualization of the SIRT and the TVM reconstruction. Orthoslices of the SIRT and TVM reconstruction in (c,d) xy plane and (e,f) xz plane, reproduced from [127].

Discrete algebraic reconstruction technique (DART)

Another algorithm that incorporates prior knowledge is DART, which assumes that the unknown object consists of a small number (i.e., two to five) of different materials, each corresponding to a certain gray level in the reconstruction. [129] Such prior knowledge is valid for a wide range of tomography applications, such as porous materials, which normally have only two components: material and pores. A simple workflow for DART is schematically illustrated in Figure 2.21, in which a 2D binary image is supposed to be reconstructed from some available projections and two gray levels for this model image are known in advance, either black or white. The DART algorithm starts from an initial reconstruction, by e.g. WBP or SIRT, followed by an initial segmentation based on preset grey levels to obtain a binary image. Based on this segmentation, one can see that the pixels in interior of the object as well as in the background that has a certain distance from the boundary have the correct gray level. The next step is to identify all the boundary and non-boundary pixels. All non-boundary pixels are assigned with their corresponding grey levels, in the current case either white or black. Afterwards another reconstruction is performed, but only boundary pixels are allowed to be

updated. In this way a new reconstruction where the non-boundary pixels are kept at the original value and some boundary pixels change their grey levels can be obtained. This process is repeated iteratively until the expected number of iterations are achieved. In practice, for some systems with small features, instead of only updating the boundary pixels, a certain percentage of randomly selected non-boundary pixels could also be updated so that small features will not be washed out during the initial iterations. In addition, smoothing or positive constraint can be also introduced during the reconstruction to improve the signal to noise ratio and reliability.
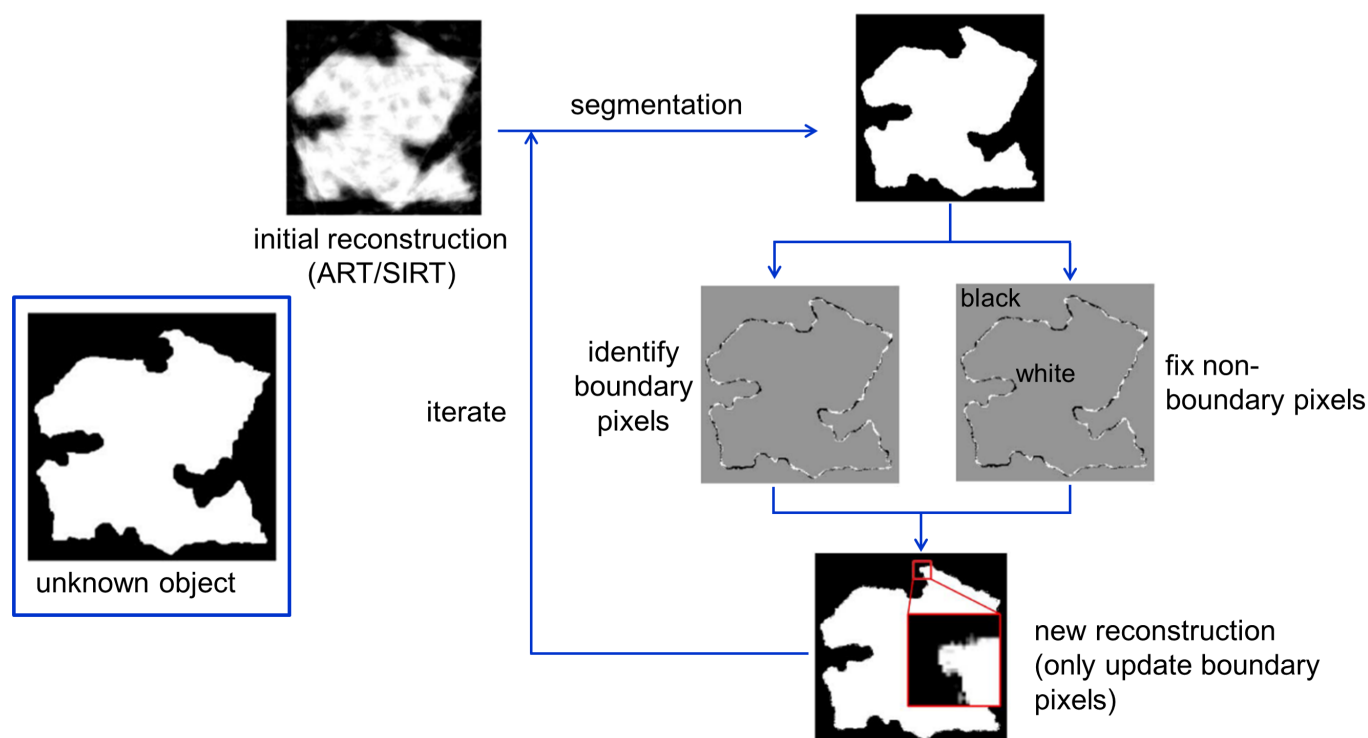
Figure 2.21: The flow chart of DART, reproduced from [129].

Figure 2.22 shows a comparison of SIRT, TVM and DART reconstructions of Au nanoparticles, where it can be seen that a reasonable accuracy of the particle shape can be obtained by all three reconstruction algorithms in xy direction, while elongation along the missing wedge direction present in the SIRT reconstruction is largely removed with TVM and DART. From the isosurface rendering, it appears that the small Au particles (encircled in Figure 2.22a-c) are reconstructed well from TVM and DART reconstructions, while they cannot be observed in the SIRT reconstruction. Compared to SIRT, TVM promotes broadly homogeneous intensity in the nanoparticles and sharp boundaries by using a total variation regularization. However, intensity variations in the nanoparticles caused by residual diffraction contrast in the original projection can be observed in both SIRT and TVM reconstruction. Such intensity variations in the nanoparticles do not appear in the DART reconstruction due to the specific characteristic of the algorithm. One slight problem for the DART algorithm in this study is that, the residual diffraction contrast that is present in the projections may hamper the correct estimation of the boundaries as it breaks the purely thickness dependence of the signal, leading to small artifacts as indicated by a white arrow in Figure 2.22i.

Given all reconstruction methods mentioned above, a considerable advantage of DART is that the reconstructed structures are segmented during the reconstruction process, as they are assigned to a particular grey value for each component. This is quite helpful and able to avoid the risk of artifacts introduction by

further segmentation for a quantitative analysis, especially for porous materials, which mainly focuses on the measurement of pore size distribution, pore length, tortuosity, etc.
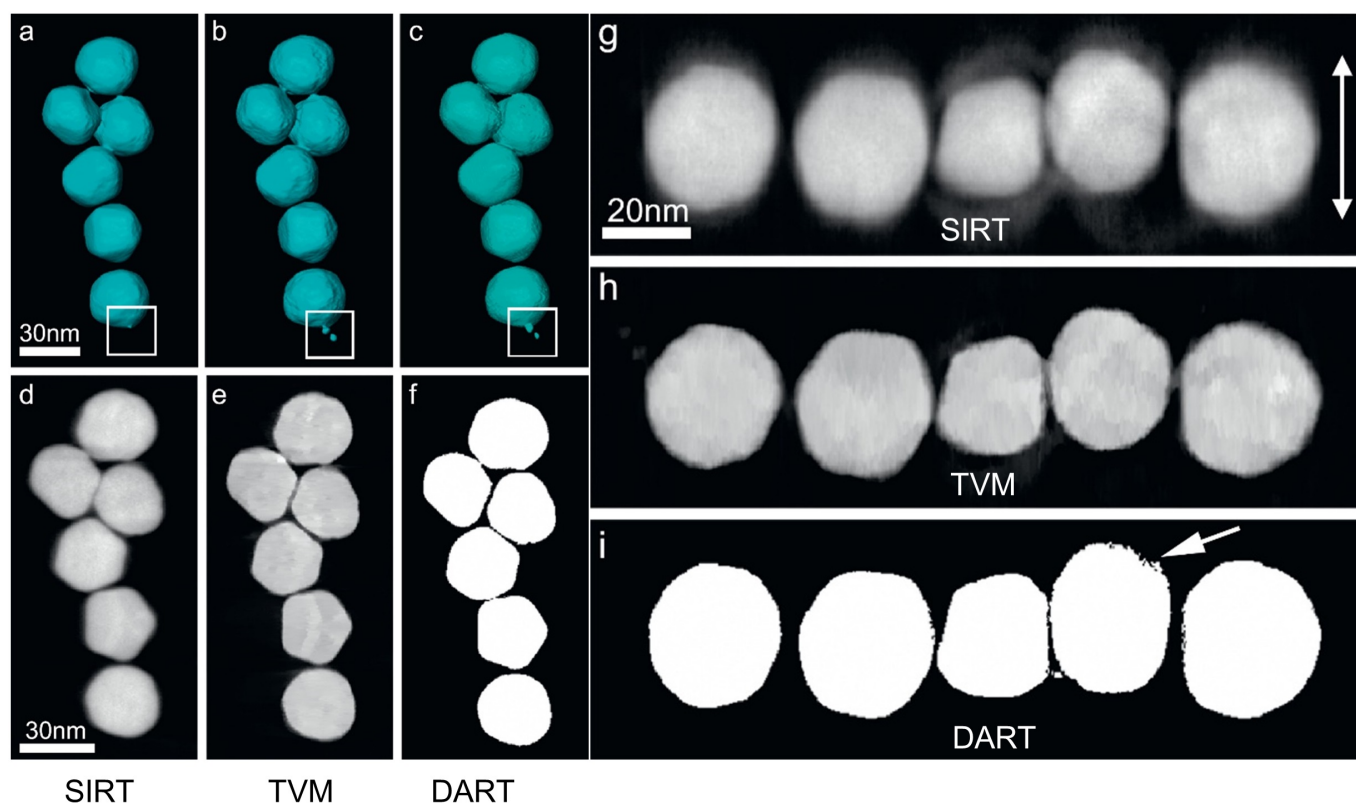
Figure 2.22: Comparison of SIRT reconstruction, TVM reconstruction and DART reconstruction of a series of Au nanoparticles in (a-f) xy direction and (g-i) xz direction, reproduced from [139].

2.7.5. Other reconstruction algorithms

In addition to the reconstruction methods mentioned above, other methods and algorithms such as single-particle reconstruction [175], generalized Fourier iterative reconstruction (GENFIRE) [176], Bayesian reconstruction [177], etc., also show promising reconstruction abilities for specific types of materials and imaging conditions. For example, single-particle method, a reconstruction technique that has been well documented in biological science based on sufficient number projections of identical particles recorded at different viewing angles, has been used to determine the 3D structure of particularly stable atomic clusters and nanoparticles, such as Au_{68} [178] and Pt NPs [175]. The GENFIRE algorithm is an iterative technique that incorporates interpolation and physical constraints between real and reciprocal space, and has been mainly reported for atomic-resolution reconstructions of crystalline nanoparticles. [179], [180] Bayesian approaches are another tomographic reconstruction technique using prior information (e.g. intensity) of the target object during the reconstruction to suppress noise, while it suffers either from over-smoothing effects or staircase effects when distinguishing edges from noise. [181] With the rapid development of computational power and the rise of artificial intelligence, machine learning based techniques have also been used for tomographic reconstructions in recent years. [182], [183] These approaches will not be considered in this thesis. Given the mesoporous materials of interest, especially for those with a narrow pore size (e.g. ~ 5 nm) in this thesis, an accurate quantitative analysis of the pore structures is always pursued. This requires the algorithm to be able to

maintain good fidelity of the final reconstruction during denoising in the reconstruction process. Therefore, this thesis did not focus on algorithms such as GENFIRE and Bayesian reconstruction, instead, the efficiency and reliability of three commonly used reconstruction algorithms (SIRT, TVM and DART) are evaluated.

2.8. Post processing

2.8.1. Segmentation

For mesoporous materials, the extraction of quantitative information on the pore network such as pore size, pore length, tortuosity and connectivity from tomographic reconstruction, requires segmentation. Various segmentation methods have been reported for tomographic data [184]–[186], with 'simple' thresholding approaches, either global or local thresholding, being most widely used. Methods for threshold selection fall broadly into two categories: threshold estimates solely based on the reconstructed tomogram or examined using projection data. The first group tries to define thresholds based on the histogram of the reconstructed volume such as Otsu's clustering method [187] or k-mean clustering methods [188]. These methods work well if the contrast between two materials is sufficiently large. In the case of mesoporous materials such as carbon and silica, which are widely used in heterogeneous catalysis, the grey levels of materials and pores overlap considerably in the reconstructed tomogram. In particular, for the well-established reconstruction approaches such as WBP and SIRT, there is a significant grey level overlap because the reconstructed intensities strongly depend on the local neighborhood and structure in the projections. For example, the reconstructed intensities of small metallic nanoparticles in a HAADF-STEM tomogram are lower than the intensities of the large support particle due to the systematic errors related to the reconstruction algorithms. [189] Similarly, the reconstructed intensity of isolated small pores is higher compared to the intensity of large pores, resulting in great challenges for accurate segmentation by histogram-based thresholding methods. Another segmentation method called projection distance minimization (PDM) was proposed by Batenburg et al. [190]. The main idea of this method is to use the tomographic projection data to determine optimal threshold values by minimizing the difference between the forward projection of the segmented image and the measured projection data. From various simulation experiments, it has been demonstrated that this method yields superior results compared to classical thresholding algorithms. However, PDM does not solve the inherent problem of the intensity dependence on different pore sizes and connectivities since it simply results in the best overall compromise between over- and under- segmentation of different pore sizes. Further research by J. Batenburg and coworkers revealed that the segmentation can be improved using local thresholding based on PDM compared to global thresholding, in particular, when the initial reconstruction contains artifacts. [191] Although PDM based methods succeed in an optimized threshold selection, the final segmentation still strongly relies on the reliability of the initial reconstruction, which limits its application.

2.8.2. 3D visualization

The most direct and simplest way of visualizing 3D image data is an orthoslice, which is taken orthogonally to the primary reconstruction axes and the intensity often represents a physical property of the material, e.g. density (Figure 2.23a). Based on these 2D slices, some direct impression of the morphology inside the measured materials, e.g. disordered/ordered pores, size and distribution can be readily obtained. This visualization method is particularly useful e.g. for supported catalysts to identify whether nanoparticles are located inside or outside of the support. Alternatively, a 3D visualization of the reconstructed volume can be achieved in

e.g. Avizo software (Thermo Fisher Scientific). For instance, shaded and classical texture-based volume rendering (VRT) technique in the volren module enables a direct 3D visualization with customized colors and transparency with virtual lighting effects for better rendering of complex spatial structures and enhancing fine details, as shown in Figure 2.23b. Another visualization method volume rendering or voxel projection is analogous to the original projection process on the microscope, visualizing the intensity distribution through a reconstruction volume by computing a projection through the volume (Figure 2.23c). Based on the segmented volume, surface rendering creates a 3D surface representing the boundaries between different materials or phases by computing a triangular approximation of the interfaces. This module is usually applied by combining a smoothing operation to enhance the recognizable surface morphology, as shown in Figure 2.23d.
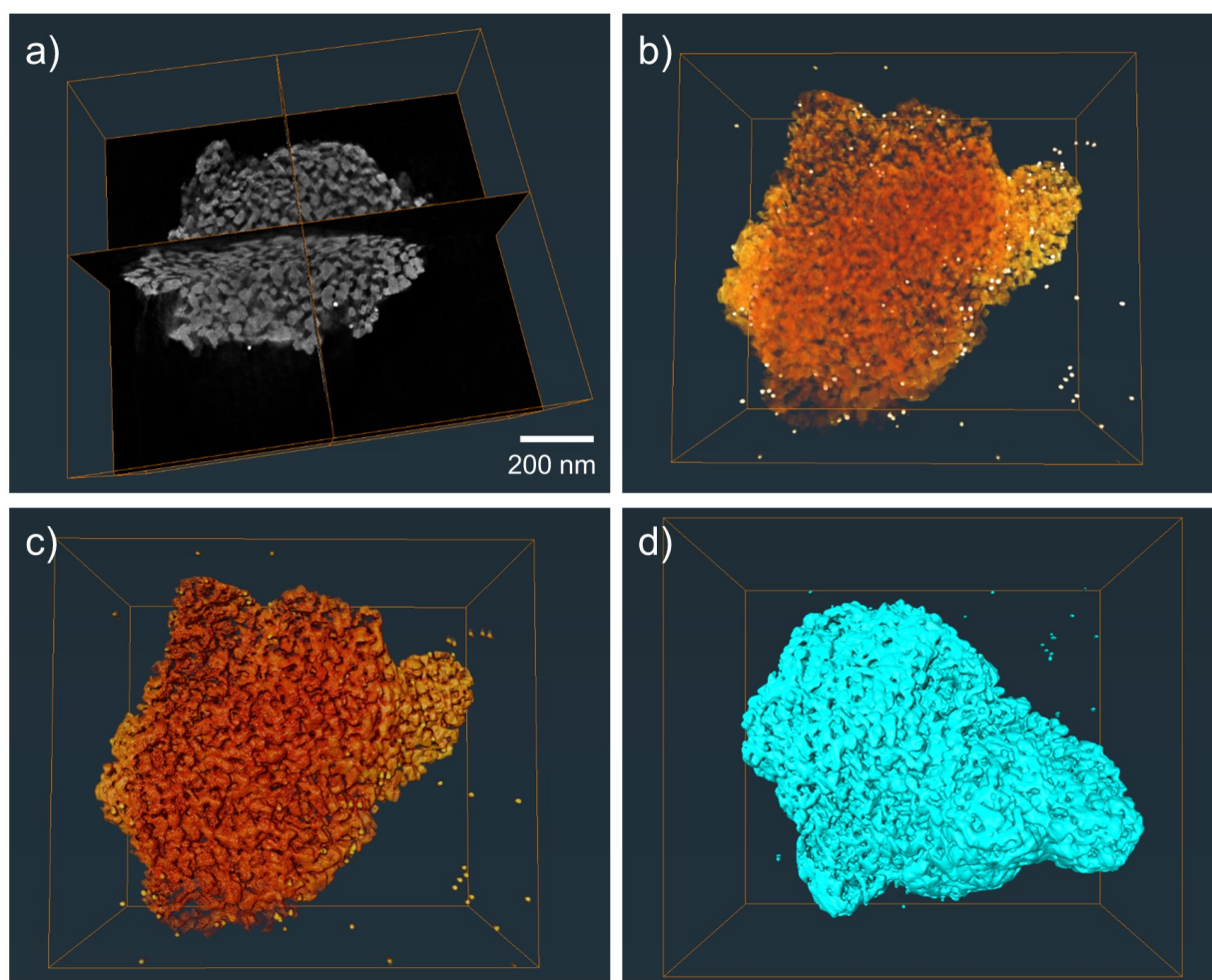
Figure 2.23: Various 3D visualization modes of porous CeO_2 in avizo software: (a) orthoslice; (b) volren by VRT technique; (c) volume rendering and (d) generate surface with a Gaussian filter kernel of 5.

2.8.3. Quantification

As mentioned in section 1.3, the average measure of the pore structure and pore volume from bulk techniques relies on standard pore models. Alternative methods to locally extract quantitative information from disordered porous structures are necessary to complement the bulk measurements. This can be achieved by using image

analysis such as skeleton analysis and CLD analysis based on the segmented 3D reconstruction from ET. With the segmented volume, the transport properties inside the mesoporous space can also be investigated using diffusion simulations.

Skeleton analysis

Skeleton analysis is a powerful technique for porous materials by extracting quantified structural features like pore diameter, pore length, coordination number and tortuosity based on the 3D segmented volume. [12], [81] To start the skeletonization, a distance map is first calculated based on the segmented volume, in which the value of each voxel is set equal to the distance to the nearest border voxel. This is used to guide the thinning procedure and provide an estimate of the thickness (radius) of the solid/pore space. Afterwards, a thinning procedure removes voxel by voxel from the segmented object until only a string of connected voxels remains. In this way, the pore space is reduced to a branch-node network, while both the geometrical and topological information are preserved (Figure 2.24). As the branch-node network has recorded the information including the distance to the nearest boundary (thickness/radius) at each voxel, branching or endpoints of the network and the number of voxels along the skeleton, the basic statistics about the pore structure features can then be computed. For example, the mean radius of each individual pore was calculated as the average radius along each skeleton segment. The pore length was obtained from the flow path between two adjacent skeleton nodes. The pore coordination number was determined by counting the number of individual branches sharing a common node, and the tortuosity was defined as the ratio of actual flow path length to the Euclidian distance between the two ends of the flow path.

Chord length distributions analysis

As shown in Figure 2.24, CLD analysis, also known as mean path length distributions, starts from a certain amount of seed points that are randomly placed within the solid/pore space. Then vectors from each seed point are projected in angularly equi-spaced directions until they hit a phase boundary. The chord lengths are calculated as the sum of the absolute lengths of pairs of opposed vectors. In most cases, the chords probe a single pore, while some chords also probe adjacent pores. The CLD analysis therefore reveals information about the local (pore level) and short-range (a few pores) heterogeneity. Based on the calculated chord length, a chord length distribution is plotted and can be fitted with a k-Γ function [192]:

$$f\left(l_{\text{chord}}\right) = \frac{k^k}{\Gamma(k)} \frac{l_{\text{chord}}^{k-1}}{\mu^k} \exp\left(-\frac{k \cdot l_{\text{chord}}}{\mu}\right) \tag{2.9}$$

where l_{chord} denotes the chord length, $\Gamma(k)$ is the gamma function, μ is a first-moment parameter corresponding to the mean chord length of the investigated phase, and k is a second moment parameter related to the statistical dispersion defined by μ and the standard deviation of the distribution: $k = \mu^2/\sigma^2$. The higher the k-value, the more homogeneous is the respective phase, i.e., the more homogenous is the morphology over a length scale of a few pores.
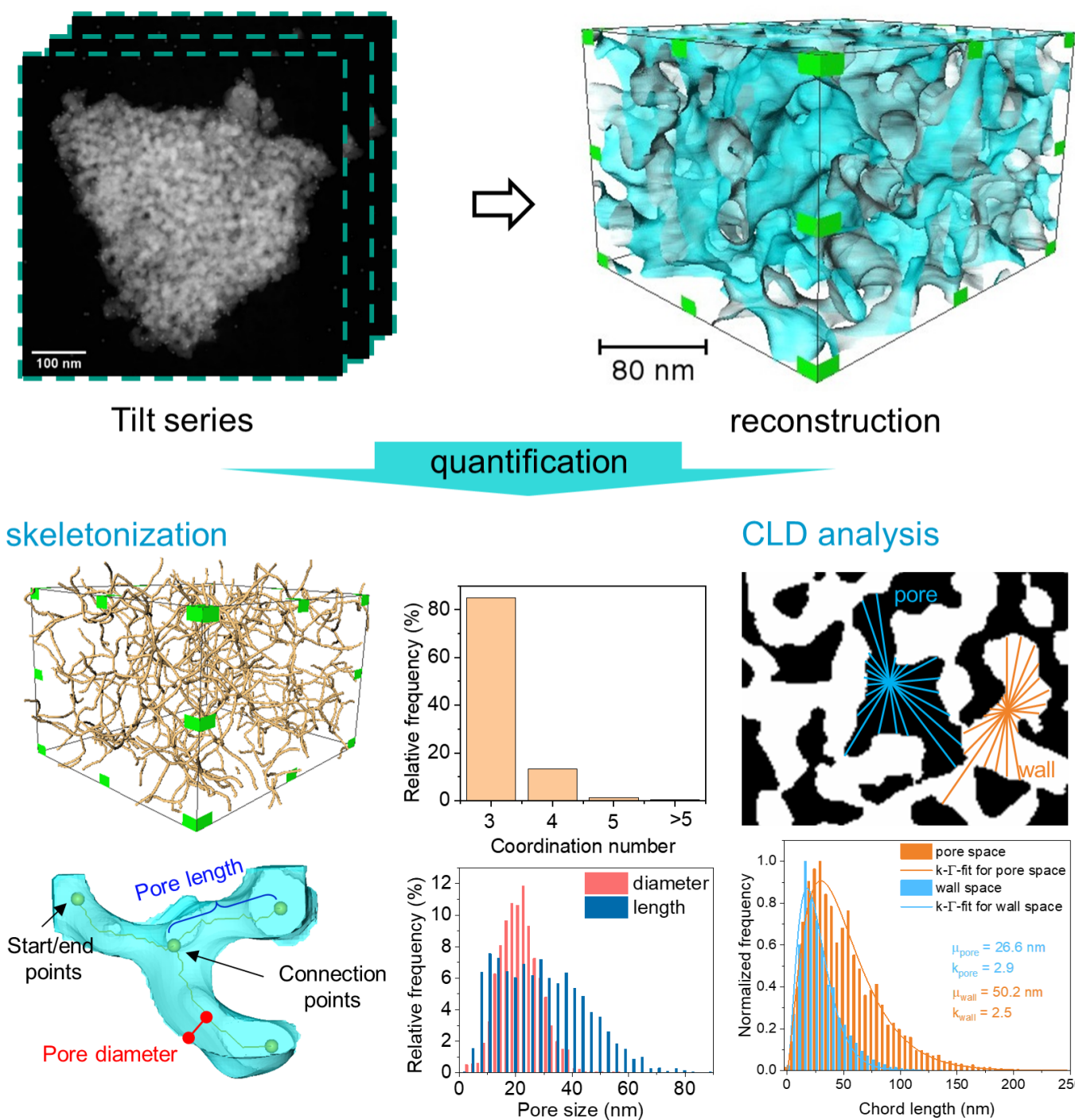
Figure 2.24: Schematic illustration of the quantitative analysis of porous materials by skeletonization and CLD analysis.

Diffusion simulation

Both skeleton and CLD analysis are able to extract structural features of pores. However, the average geometrical quantification of the structure of mesoporous materials obtained by these methods might not be sufficient. For example, for application in heterogenous catalysis and gas separation, transport properties are essential to understand gas and liquid diffusion in a 3D porous network, one of the most important aspects

for catalytic/separation performance. Based on the segmented tomographic data, morphology-transport relationships of mesoporous structures can be investigated using diffusion simulations, as mentioned in section 1.4.1. Typically, the simulation was performed in the spherical porous particles using a random-walk approach, where a large number N of passive, i.e., nonadsorbing and nonreacting tracer particles were initially (at t = 0) distributed randomly and uniformly throughout the entire pore space of the particles. Then, each tracer was iteratively displaced within the pore space due to random (Brownian) motion. The displacement Δr of every tracer during a time step Δt was calculated from a Gaussian distribution with zero mean and standard deviation $(2D_m\Delta t)^{1/2}$ along each Cartesian coordinate, where D_m is the molecular diffusion coefficient in free space. The value of Δt was chosen such that the average diffusive displacement at each iteration does not exceed half the voxel size. A multiple-rejection boundary condition was realized at the pore walls. If a tracer leaves the particle, its random-walk stopped. The amount of tracers $N(t)$ remaining inside the particle was recorded after each time step. The effective diffusion coefficient D_{eff} was determined from the best fit of the simulated *N(t)*-values to the analytical model for emptying an ideal sphere by diffusion: [193]

$$\frac{N(t)}{N(t=0)} = \frac{6}{\pi^2} \sum_{n=1}^{\infty} \left[\frac{1}{n^2} \exp\left(-n^2\pi^2 \frac{D_{\text{eff}}t}{r_{\text{p}}^2} \right) \right] \tag{2.10}$$

where r_p denotes the particle radius.

2.9. Equipment and software used in this thesis

2.9.1. Transmission electron microscopy

A Themis 300 TEM equipped with a Schottky FEG, a probe corrector and a Super-X EDS detector was used to acquire the experimental data for chapters 4 and 5. This microscope was operated at 300 kV and the data analysis was performed using Velox software. To increase the depth of field, a small convergence angle of around 8 mrad was used either by selecting a small C2 aperture or using a weaker condenser lens. The spot size of C1 was set to 4-8, resulting in a beam current ranging from 50-100 pA and a probe diameter of around 180 pm after the aberration correction. For the acquisition of tomographic data, HAADF-STEM tilt series were collected using the Xplore3D software (Thermo Fisher Scientific) with auto focus and tracking before acquisition. Conventional ET was performed using a Fischione 2020 tomography holder. To ensure a sufficient tilt range, particles located at the center region of the grid windows not blocked by other neighboring particles were commonly selected, thus a typical tilt range greater than $\pm 70°$ could be achieved. For the 360° ET, a Fischione 2050 on-axis rotation tomography holder was used. Sample preparation and parameters for ET measurements are described in the corresponding experimental chapters.

2.9.2. Dual beam focus ion beam - scanning electron microscopy

A FEI Strata 400 S equipped with a Schottky FEG electron source and a Gallium liquid metal ion source was used for the sample preparation of 360° ET in chapter 4. This dual-beam FIB-SEM system was equipped with an Omniprobe 200 manipulator with independent x,y,z motion, a flip stage, and a gas injection system with Pt, C and W precursors. The high tension used for SEM imaging was 5 kV and the range for FIB was between 2 kV - 30 kV. Detailed parameters about the electron and ion beam currents used for milling and Pt deposition are described in chapter 4.

2.9.3. IMOD

Alignment of the tilt series was performed in IMOD (version 4.7) using colloidal Au particles as fiducial markers. Typically, a coarse aligned stack was initially produced by cross-correlation calculation for the original tilt series in the 'coarse alignment complete' module. Then around 20 fiducial markers (supported metal particles or colloidal Au particles) in one projection were manually selected as starting seeds in the 'seed model' module, followed by a combination procedure of automatic and manual tracking so that the corresponding beads in all projections were marked through the 'fix fiducial model' module. The resulting fiducial model was used to calculate the alignment error and the beads with large residual error were corrected iteratively using 'edit fiducial model' module. It is worth noting that, although this correction process can be performed automatically, manual correction is sometimes necessary due to the inaccurate calculation of some beads. To reduce alignment artifacts in the reconstruction, a residual error smaller than 0.7 pixels is usually pursued for the final alignment.

2.9.4. ASTRA toolbox

The SIRT and DART reconstructions in chapter 3 and chapter 5 were performed using the ASTRA toolbox [194] in Matlab. The simulation work with the largest dimension of 512×512×512 in chapter 3 was performed on a Windows Server (2012 R2) equipped with a Tesla K40c graphics card. The reconstructions in chapter 5 with a dimension of 1024×1024×1024 were performed on a Windows Server (2019) equipped with a NVIDIA Quadro RTX 8000 graphics card.

SIRT

It is well known that the SIRT convergence is poor for noisy data and the final reconstruction depends on the number of iterations used for the reconstruction. To clarify the relationship between the number of iterations and the reconstructions in chapter 3, series of iterations were tested for three different noise levels with a positive constraint. The reconstructed tomograms were further filtered by convolution with an adjustable filter kernel and radius prior to segmentation. The threshold used for segmentation was estimated by PDM method [190] until the relative number of misclassified pixels (rNMP) was at a minimum compared to the phantom reference.

DART

As introduced in section 2.7.3, the DART reconstruction starts from an initial reconstruction and a threshold is selected for each material class present and applied to segment the reconstruction based on prior knowledge of grey levels. To reduce noise effects, a certain percentage of random pixels (depends on the random probability r) and a smoothing process can be included. In this thesis, a SIRT reconstruction was used as input for DART and a convolution filter controlled by a smoothing kernel k and smoothing radius b is applied to improve the signal to noise ratio during the reconstruction. After the initial SIRT reconstruction with a preset number of iterations was calculated, the main loop for DART was repeated a certain number of times and then SIRT with another preset number of iterations was included for each iteration to ensure convergence. The initial grey levels were set based on a rough estimation of the intensity of each component in the SIRT reconstruction. The initial threshold was set to the average value of the grey levels. In the simulation work in chapter 3, the grey levels and threshold used for segmentation in each loop were optimized by PDM while other parameters r, k and b were not changed between iterations. These three parameters were optimized by minimizing the rNMP using the phantom as reference.

2.9.5. TVAL3 package

The TVM reconstructions in chapter 3 were implemented using the TVAL3 package in Matlab with an isotropic TV/L2+ model, which was provided by Li et al. [195], [196] The algorithm is based on the total variation regularization model and uses the augmented Lagrangian method (ALM) and the alternating direction method (ADM) to find a solution in an iterative process. This iteration scheme stops when the average difference between two successive reconstructions becomes smaller than a predefined tolerance value. The mathematical model can be written as follows:

$$\min_{u \in \boldsymbol{R}^{n^2}} \sum_i \|D_i u\|_2 + \frac{\mu}{2} \|Au - b\|_2^2, \quad \text{s.t. } u \geq 0 \tag{2.11}$$

while this function is not convex and not straightforward to be minimized, w_i can be defined as a set of constraints to obtain a differentiable objective function from u:

$$\min_{u \in \boldsymbol{R}^{n^2}} \sum_i \|w_i\|_2 + \frac{\mu}{2} \|Au - b\|_2^2, \quad \text{s.t. } D_i u = w_i \tag{2.12}$$

which can be transformed into the corresponding augmented Lagrangian problem:

$$\min_{w_i, u} \sum_i \|w_i\|_2 - \sigma^\top (D_i u - w_i) + \frac{\beta}{2} \|D_i u - w_i\|_2^2 + \frac{\mu}{2} \|Au - b\|_2^2 \tag{2.13}$$

where $u \in R^{n^2}$ is the reconstructed image with a size of $n \times n$, $D_i u$ is the discrete gradient vector of u at position i; $b \in R^{mn}$ is the sinogram of u with $m(m < n)$ projections in the tilt series; $A \in R^{n^2 \times mn}$ is the projection matrix; and σ is the Lagrange multiplier. Two parameters need to be considered for this algorithm including the primary penalty parameter μ and a secondary penalty parameter β. Here, μ penalizes the difference between the measured sinogram b and the reconstructed sinogram Au, where a large μ leads to a result closer to a SIRT reconstruction with high frequency details while a small μ will suppress noise. β is the weighting factor of the squared l_2-norm term containing the gradient ($D_i u$). It controls the smoothing level of the solution, thus stronger smoothing can be achieved by using a larger β to filter image details and increase the presence of constant intensity regions (patches or stripes) in the reconstructed volume. [126] For each reconstruction, both μ and β were tested in the range of 2^1 to 2^{13} in order to enhance the signal to noise ratio for the final reconstruction. To ensure convergence, a maximum iteration of 300 was used and the tolerance value was set to 10^{-3}. The threshold for the segmentation was estimated using the PDM algorithm analogous to the SIRT post processing.

2.9.6. Inspect3D

The SIRT reconstructions in chapter 4 were performed using the Inspect 3D software (v4.4, Thermo Fisher Scientific) with 100 iterations for each tomogram. This commercial software is more user friendly and can be used to analyze larger datasets ($2048 \times 2048 \times 2048$ number of projections), which is limited in the ASTRA toolbox using the same computer.

2.9.7. Avizo

3D visualization including orthoslices, volume and surface rendering, as well as the skeletonization analysis in this thesis were performed using Avizo 2020.2 (Thermo Fisher Scientific). In the 3D phantom study in chapter 3, all quantified structural features were calculated based on the skeleton analysis using the Auto Skeleton module. The initial segmentation was first refined by removing unconnected and small islands with a diameter smaller than 3 voxels, which are caused by reconstruction artifacts. Then a skeletonization procedure was performed to reduce the pore space to a branch-node network (Skeleton). All branches shorter than 2 voxels were removed and not assigned as side branches. This is reasonable to allow for a certain pore diameter variation along the main branch thereby improving the reliability of the quantification. Afterwards, the basic statistics were computed using the Trace Correlation Lines module. Details for the calculation of each pore feature can be seen in section 2.8.3.

2.9.8. Diffusion simulation

The 3D diffusive mass transport simulations presented in chapter 3 were done by the research partners, Dr. Dzmitry Hlushkou and Prof. Ulrich Tallarek at Philipps-Universität Marburg. The simulation was performed using a random-walk approach, where 10^6 passive tracer particles were used. In addition to point-like tracers (i.e., the tracer diameter is 0), finite-size tracers with different diameters, ranging from 1 to 4 voxels (with one-voxel increment) were also used to simulate the transport properties. It is worth noting that the entire void space of the porous particles can be reached by point-like tracers, while the accessible void space for finite-size tracers is smaller due to their steric interactions with the solid pore walls. Thus, the accessible porosity ε_a for tracers with a given diameter was defined as the volume fraction of the spherical particles that is actually accessible for the center of the tracers.

3. Quantitative Analysis of Mesoporous Structures by Electron Tomography: A Phantom Study

3.1. Introduction

ET has attracted significant attention for a quantitative analysis of mesoporous materials, especially for complex disordered pore structures, as no prior assumptions on the pore shape are needed, which is normally inevitable when using traditional bulk characterization techniques. However, a quantitative interpretation of ET results is still far from straightforward and an accurate quantification of the pore space is challenging because of constraints during tilt-series acquisition such as missing wedge and limited sampling as well as reconstruction artifacts introduced by alignment errors and the reconstruction algorithm. In addition, to extract quantitative information on the pore network such as pore size, pore length, tortuosity and connectivity from a tomographic reconstruction, segmentation is essential. Although significant efforts have been dedicated to improve the fidelity of the segmentation for mesoporous materials [12], [124]–[128], an objective and comprehensive assessment of the accuracy of different algorithms and approaches for a quantitative analysis of mesoporous materials is still limited, in particular, an analysis beyond a simple evaluation of misclassified voxels and average residual errors looking more towards applications. In addition to the pore size distribution, one important property of mesoporous materials is their connectivity and constrictivity, which affects transportation properties in applications like catalysis. To get accurate reconstructions and evaluate these specific features for porous materials, an analysis of the dependence on different acquisition conditions, such as noise level, tilt-range and increment as well as the reconstruction and segmentation parameters is needed to optimize the acquisition and reconstruction methods and to judge the reliability of the obtained structure and depending properties.

In this chapter, a set of 2D and 3D binary images with various pore features was created as test structures. These test structures were used to assess the fidelity of the three main-stream algorithms SIRT, TVM and DART for mesoporous materials for different imperfect (realistic) tilt-series based on a set of phantom simulations. The effect of these reconstruction approaches on the pore morphology quantification is discussed with respect to pore size, pore length, tortuosity and connectivity as well as differences in diffusion properties based on a 3D phantom study. For each algorithm, different reconstruction and segmentation parameters were evaluated and optimized using the phantom as ground truth. Moreover, the effect of the initial reconstruction for a DART reconstruction is discussed. It showed that DART outperforms the other two methods in reliably revealing small pores and narrow channels, especially when the number of projections is strongly constrained. The accurate segmented reconstruction from DART makes it possible to achieve reliable quantification of pores

structure, which in turn leads to reliable evaluation of effective diffusion coefficients. In addition, the influence of different acquisition and reconstruction parameters on the reconstructed 3D volume and the quantitative analysis of pore features is discussed. This work aims to provide a practical guide for optimizing acquisition and reconstruction parameters and how to evaluate the accuracy when describing the mesoporous structure.

3.2. Methods

SIRT and DART reconstructions in this work were implemented using the ASTRA toolbox in Matlab [194]. TVM reconstructions were implemented using the TVAL3 package in Matlab with an isotropic TV/L2+ model [195], [196]. In the 3D phantom study, all quantified structural features including pore diameter, pore length, coordination number and tortuosity were calculated based on the skeleton analysis performed in Avizo (version 2020.2, Thermo Fisher Scientific). All segmentation results were evaluated using the minimum rNMP as a common global analysis criterion. The rNMP value is defined as the number of pixels that were misclassified (with respect to the reference), both for the pores and the material, reported as percentage of the total number of pixels. The detailed parameters for reconstruction and quantification have been described in Chapter 2.

3.3. Results and discussion

3.3.1. Noise effects

Noise in STEM images has been extensively studied. [197], [198] Considering the characteristics of the image acquisition process in STEM using a HAADF detector, where the electrons arriving at the detector can be modelled as a Poisson process in case of low counts, while further additive noise from the detector and electronic circuits can be modelled as a Gaussian process. Together the noise in HAADF-STEM images can be modelled as:

$$\text{Y} = \alpha \text{Z} + \text{E} \text{ with } \begin{cases} \text{Z} \sim P\left(\frac{\text{X}^0}{\alpha}\right) \\ \text{E} \sim N\left(\mu, \sigma^2\right) \end{cases} \tag{3.1}$$

where α is the gain of the detector and μ corresponds to a detector offset; Z and E are two independent variables following a Poisson and a Gaussian distribution; σ is the standard deviation of E; X^0 is the true signal without noise.

To mimic the real experimental conditions with noise effects, the parameters describing the Poisson-Gaussian noise were estimated using a Themis 300 microscope, operated at 300 kV. As Gaussian noise is signal-independent, it can be estimated directly from images in regions not containing any sample (e.g. regions corresponding to vacuum in STEM). According to equation 3.1, the noise model corresponds to pure Gaussian noise when $\alpha = 0$. For instance, Figure 3.1a shows a HAADF-STEM image acquired in a vacuum region with a gain of 0 and offset of 42.3% (a typical parameter used in real experiments), where the intensity histogram shows a standard Gaussian distribution. The parameters μ and σ for the Gaussian noise can be obtained from the mean and standard deviation fitting a Gaussian function of the curve.

Estimation of the Poisson noise is more complicated as it is a signal-dependent noise and factors that might affect the signal collected by the HAADF detector need to be considered. Figure 3.1b shows the dependence of
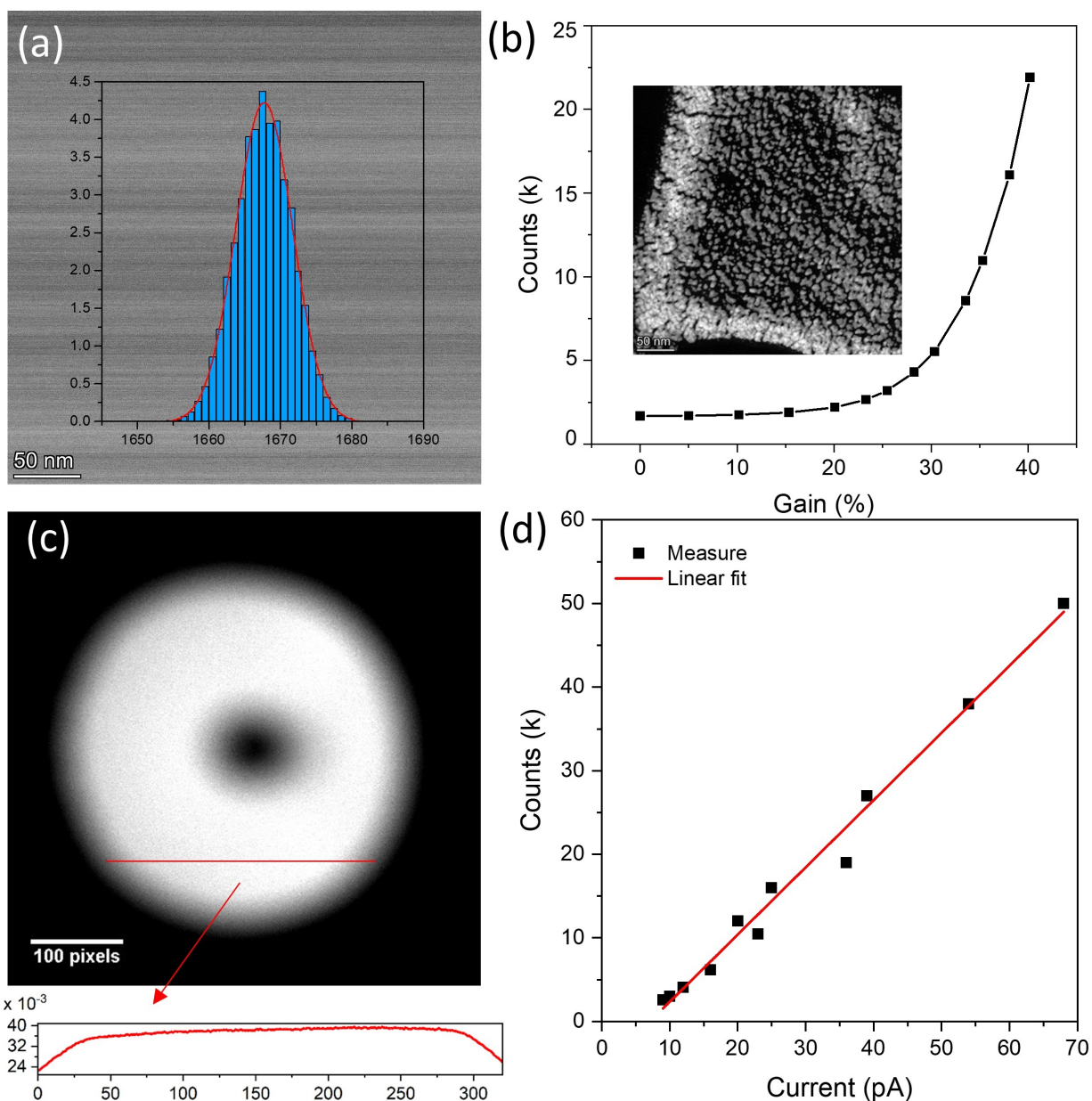
Figure 3.1: Estimation of Poisson-Gaussian noise using a Themis 300 microscope: (a) HAADF-STEM image acquired from vacuum region and the corresponding intensity histogram, (b) the intensity of a cross crating Au sample as a function of the gain setting, (c) HAADF-STEM vacuum signal acquired in image mode at large defocus with the electron beam scanning across the HAADF detector and (d) linear relationship between image counts and beam current at a dwell time of 5 μs and a gain setting of 30.7%.

the counts on the gain setting for a cross-crating Au sample, resulting in an increasing intensity in the STEM images. Therefore, an accurate estimate of the real number of electrons on the detector is needed. For this purpose, an HAADF-STEM image in image mode (diffraction has been deactivated) at a given dwell time t_i in a vacuum region was acquired. With this setup, electrons are converged to a probe and hit the detector directly, so that the bright region in Figure 3.1c reflects the shape of the HAADF detector. The image was acquired at large defocus to reduce damage to the detector. Based on this image, the apparent average counts

can be determined. The current has been recorded directly from the present screen current I_{im}, allowing a rough estimation of the number of electrons (N_i) for each pixel:

$$N_i = I_{im} \times t_i \times C \qquad (3.2)$$

where C corresponds the elementary charge (1C = 6.241×10^{18}e). Thus, the correlation of the counts in a HAADF-STEM image to the real number of electrons on the detector is obtained. Figure 3.1d shows the resulting linear relationship between counts and current at a dwell time of 5 μs and a gain setting of 30.7%. In a typical HAADF-STEM tomographic data acquisition in a Themis 300 microscope operated at 300 kV, the measured counts are mainly in the range of 5k-50k, depending on the current, camera length and gain setting, corresponding to a real number of electrons in the range of 400-2000. Comparable noise levels were used for the simulations in this work. Alternatively, several methods have been developed to estimate the amount of mixed Poisson-Gaussian noise only based on STEM images, such as a linear regression based method [199], variance stabilizing transforms [200] and expectation-maximization method [201].

To investigate noise effects on the reconstruction of small pores, a 400×400 pixel phantom of spherical pores with different diameters (5, 10, 15 and 20 pixels) as shown in Figure 3.11a was created . Based on the sinogram from 71/91 projections with a tilt step of 2° corresponding to a tilt angle range of ±70°/±90°, a mixture of Poisson and Gaussian noise was added where the Poisson noise ratio per pixel was varied from 4×10^2 up to 4×10^6 and the standard deviation of the Gaussian noise was $\sigma = 0.01$. The Gaussian noise was kept the same for all simulations in this work. The Matlab code for the introduction of Poisson-Gaussian noise to the true signal is shown in Figure 3.2.

```
% scale sinogram to [0,1]
sinogram = sinogram./max(sinogram(:));
% parameters setting
std = 0.01^2;              % standard deviation for gaussian noise
counts = 1.6e03;          % mean counts for poisson noise;
% create poissson noise
sinogram = poissrnd(max(0, counts*sinogram))/counts;
% add gaussian noise
sinogram = sinogram+sqrt(std)*randn(size(sinogram));
```

Figure 3.2: MATLAB code for Poisson-Gaussian noise introducing to a sinogram.

Tests with different noise levels were performed for each reconstruction algorithm to get an overall impression of the effect of noise on the final reconstruction. Figure 3.3 shows the simulated sinograms with three different noise levels and the corresponding rNMP as a function of iterations for the SIRT-based segmentation when no filter is used during the reconstruction. It is clear that the SIRT reconstruction converged after around 100 iterations and the rNMP does not change further for noise free or moderate noisy data (1600 counts), while the reconstruction does not converge and becomes worse after 50 iterations for high noise data (400 counts). However, many falsely segmented voxels can be corrected by applying a convolution filter prior to segmentation. Figure 3.4 shows that the final segmentation will also converge with increased iterations even for high noisy data if a suitable filter is applied.
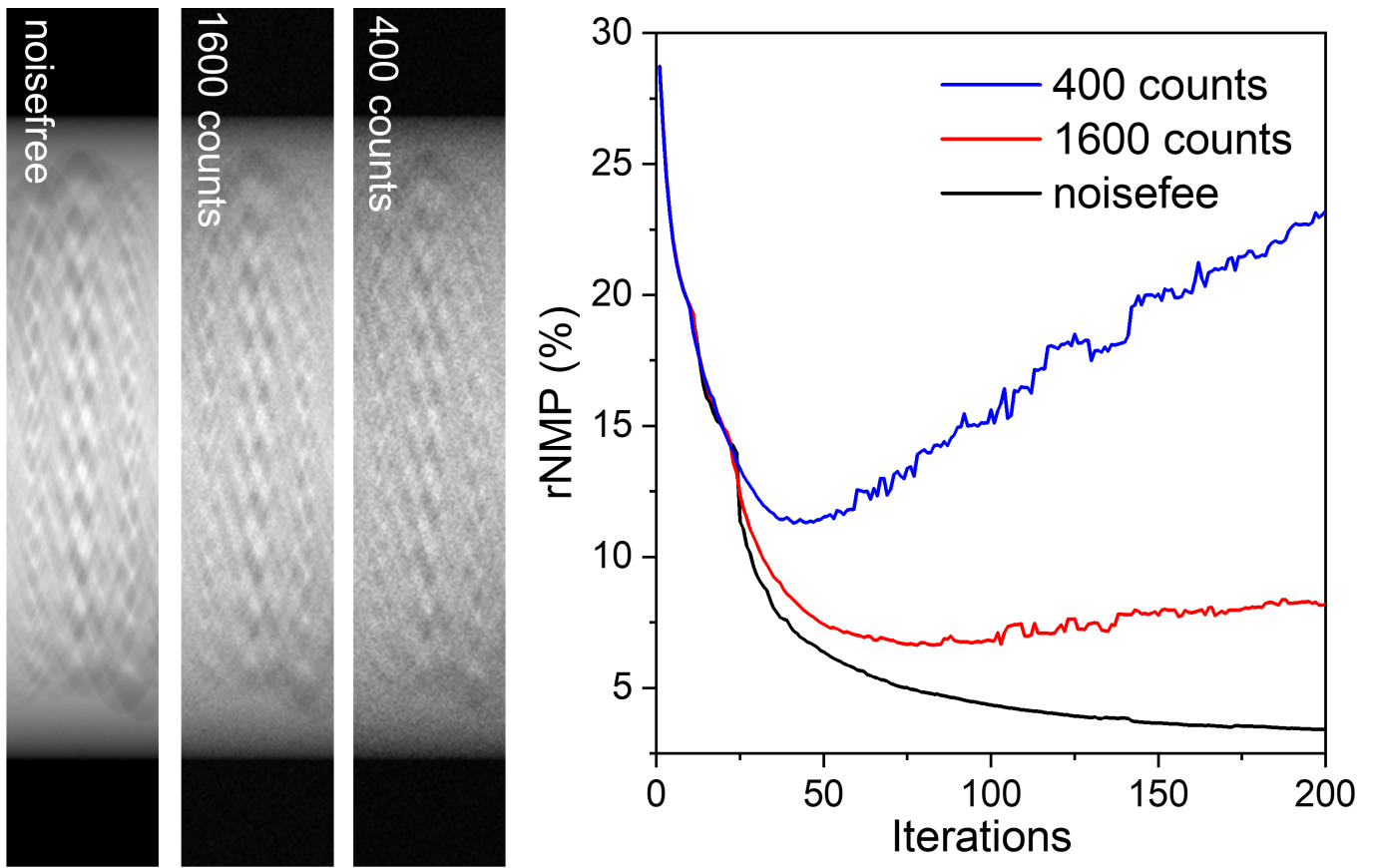
Figure 3.3: Simulated sinograms for the phantom in Figure 3.11a with three different noise levels and the corresponding rNMP as a function of iterations from a segmented_SIRT reconstruction. For each noise level, no filter was used during the reconstruction. The tilt range is $\pm70°$ with an increment of $2°$.
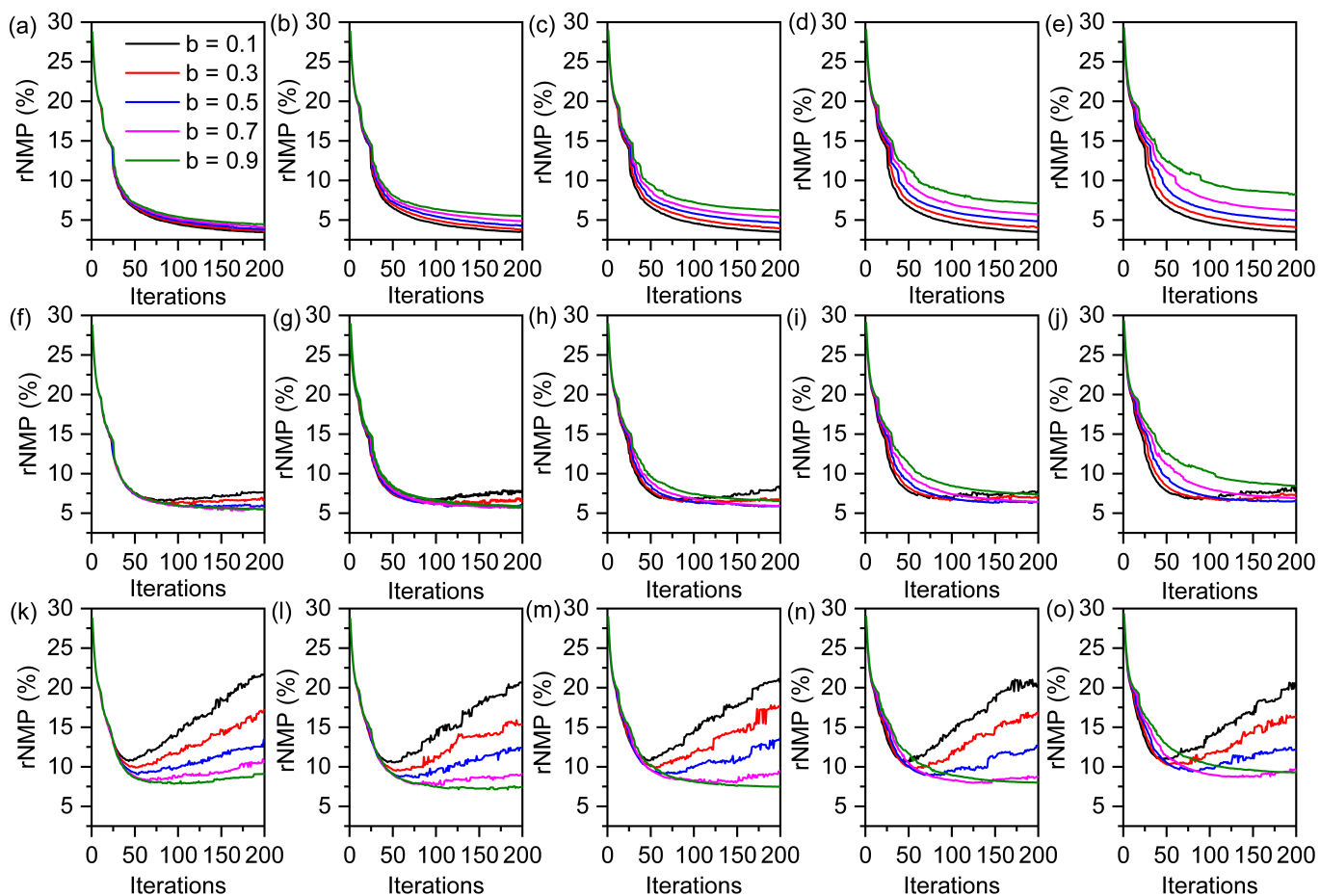
Figure 3.4: rNMP as a function of iterations at three different noise levels: (a-e) noise free, (f-j) 1600 counts and (k-o) 400 counts from a segmented_SIRT reconstruction. For each noise level, a convolution filter with various filter kernel and radius b were used during the reconstruction (from column 1 to 5: the corresponding kernels are 1 to 5). The dimension of the filter matrix w is determined by the kernel: $w = 2 \times kernel + 1$. The central value of the matrix is $1 - b$, while all the other values are equal to $b/(w^2 - 1)$. The tilt range is $\pm 70°$ with an increment of $2°$.

The reconstruction error in TVM using μ and β combinations covering a wide range of 2^1-2^{13} is shown in Figure 3.5. As expected, large μ values lead to high quality reconstructions for noise free datasets. This is easily understood via equation 2.11, as large μ controls the main weighting of the l_2 term, yielding similar results to SIRT. Nevertheless, the additional constraint in TVM leads to smaller rNMP values compared to SIRT. With the noise level increasing, smaller μ values are more favorable. In this case, β has a large influence on the reconstruction and a smaller value for β is more favorable. These findings are consistent with the work of López-Haro et al., who exploited an automated procedure for optimization the two parameters (μ and β) to analyze carbon-based porous materials using TVM. [126]
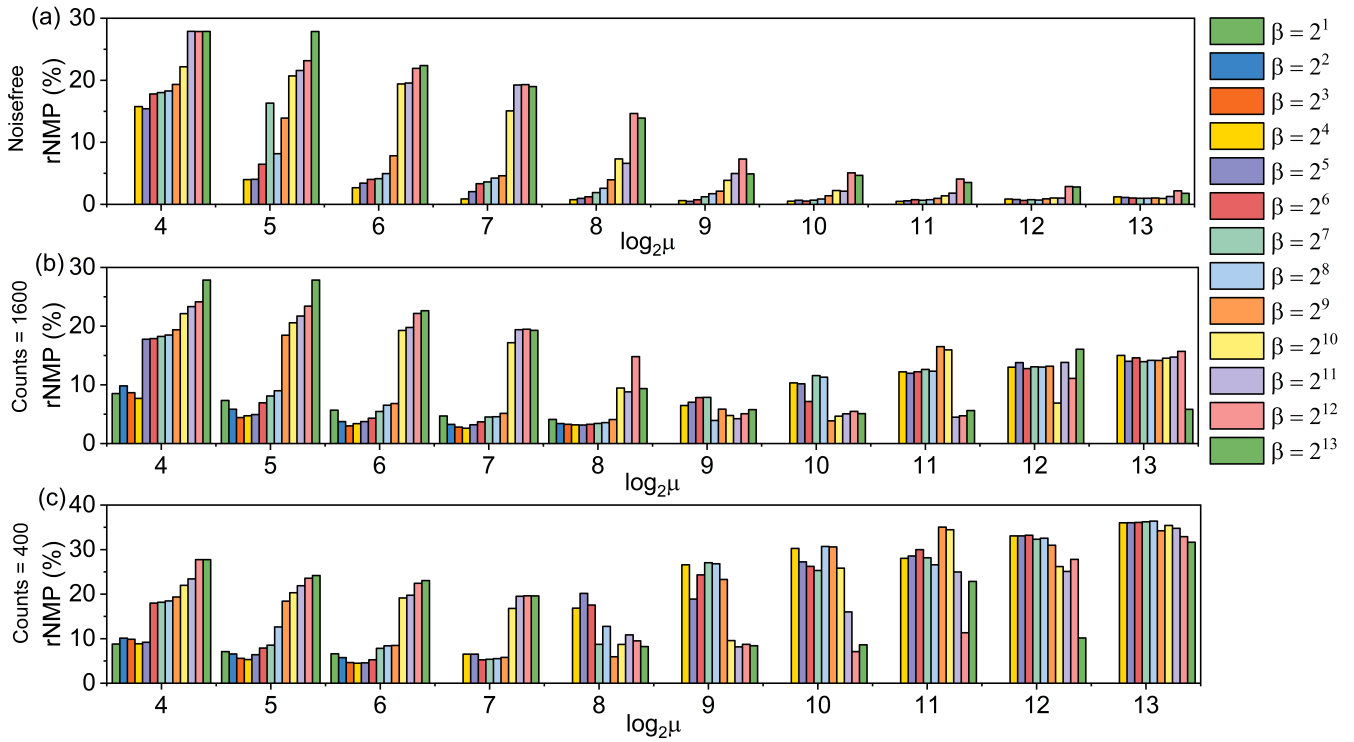
Figure 3.5: rNMP as a function of μ and β at three different noise level: (a) noise free, (b) 1600 counts and (c) 400 counts from a segmented_TVM reconstruction. The tilt range is $\pm 70°$ with an increment of $2°$.

Noise effects on choosing the parameters for DART were also evaluated. Figure 3.6 to Figure 3.8 show the rNMP as a function of iterations, random probability r, smoothing kernel k and smoothing radius b at different noise levels in a DART reconstruction. It is obvious that mild filtering (small k and b) and small r yield more accurate reconstructions for noise free/moderate-noisy data, fitting to the results of Batenburg and coworkers [129]. In their work, the two smoothing parameters stay fixed, while r is varied to minimize noise. However, the iterations will not converge without a strong smoothing even when a large r is used for noisy data. In this case, stronger smoothing (larger k and b) combined with a moderate r will yield more accurate results for these structures (Figure 3.8).
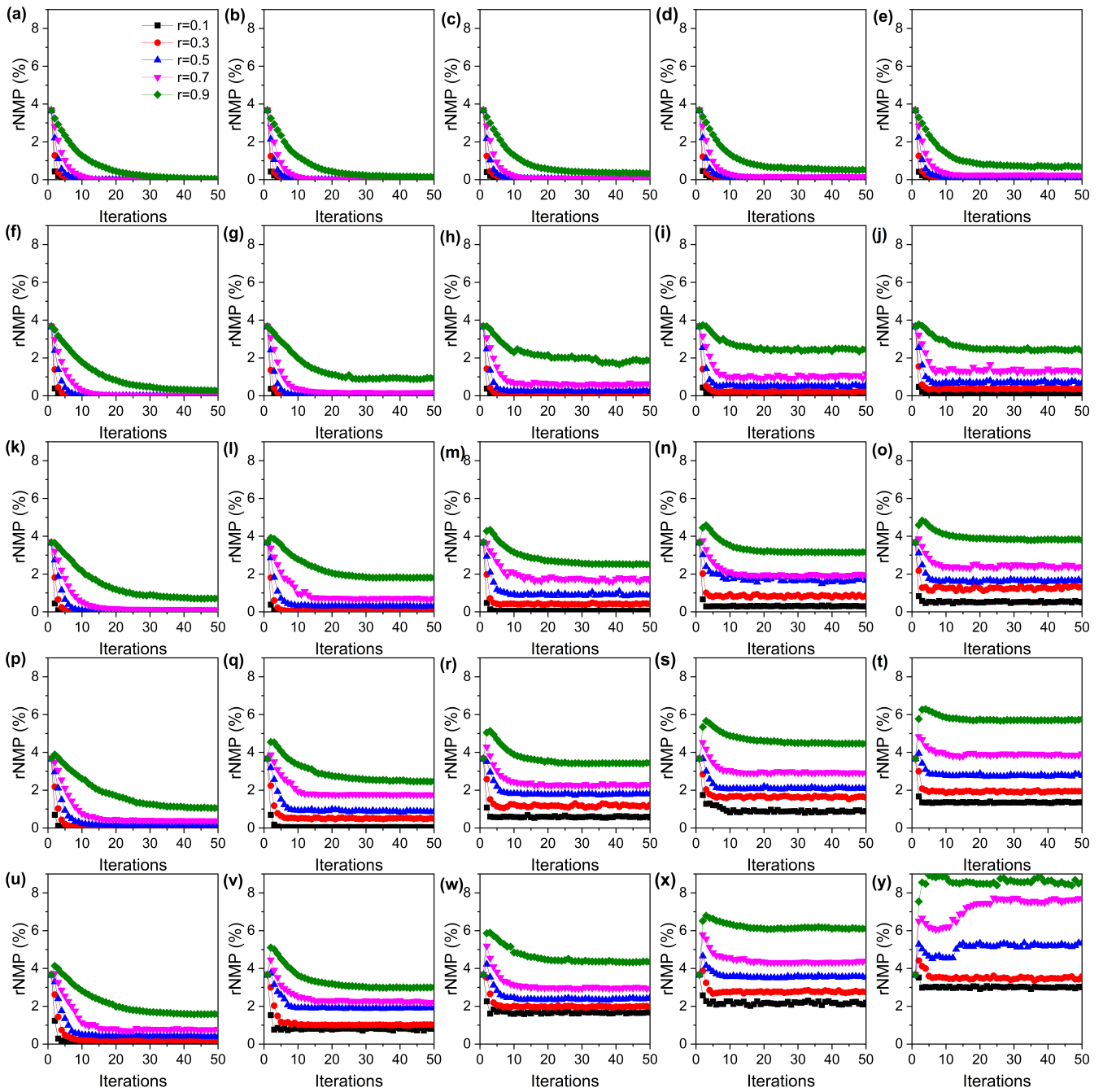
Figure 3.6: rNMP as a function of iterations at different random probability r, smoothing radius: (a-e) b=0.1, (f-j) b=0.3, (k-o) b=0.5, (p-t) b=0.7 and (u-y) b=0.9, and smoothing kernel (from column 1 to 5: the corresponding kernels are 1 to 5) in DART reconstructions based on noise free tilt series. The tilt range is $\pm70°$ with an increment of $2°$.
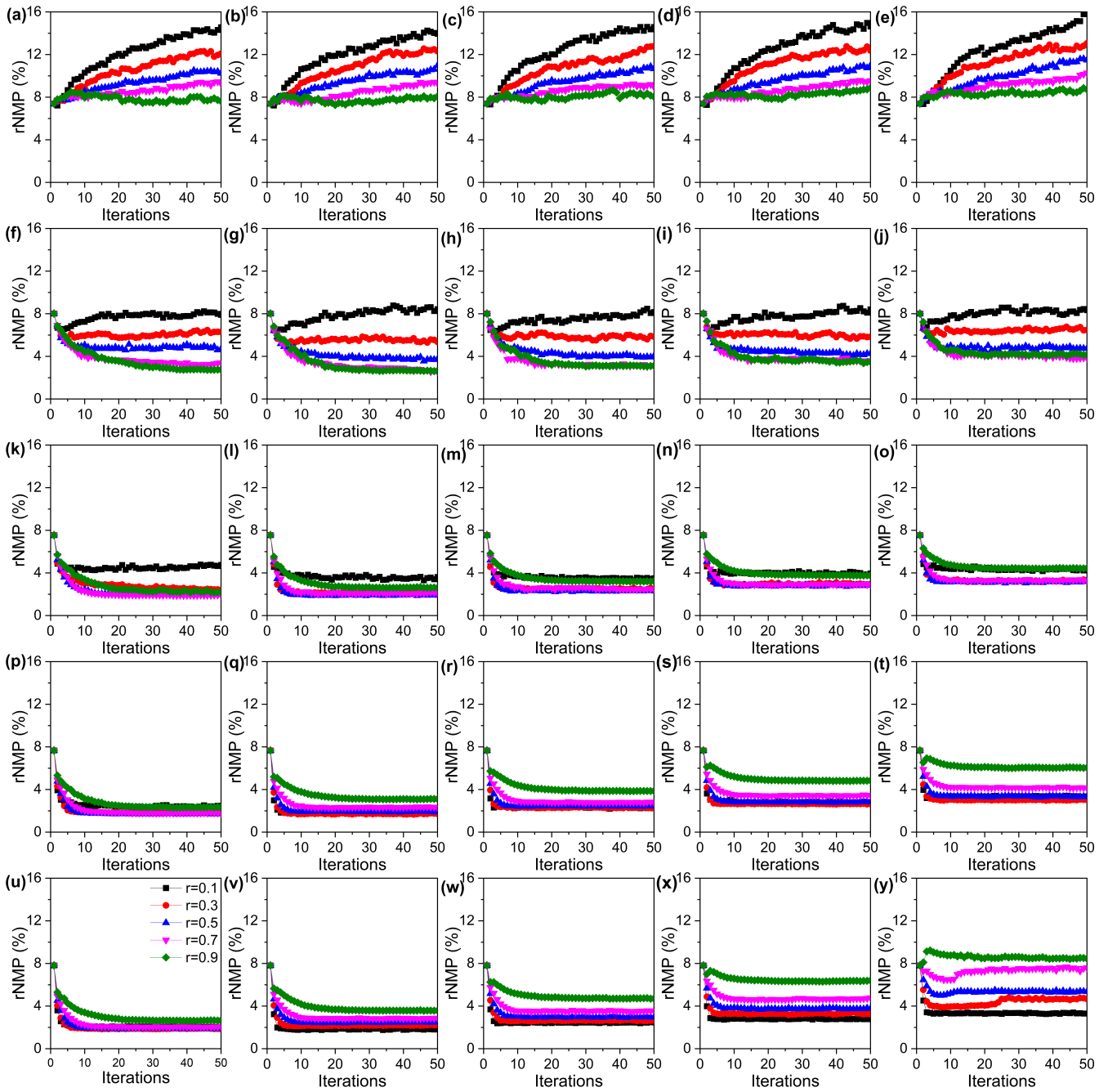
Figure 3.7: rNMP as a function of iterations at different random probability r, smoothing radius: (a-e) b=0.1, (f-j) b=0.3, (k-o) b=0.5, (p-t) b=0.7 and (u-y) b=0.9, and smoothing kernel (from column 1 to 5: the corresponding kernels are 1 to 5) in DART reconstructions based on noisy tilt series (1600 counts). The tilt range is $\pm70°$ with an increment of $2°$.
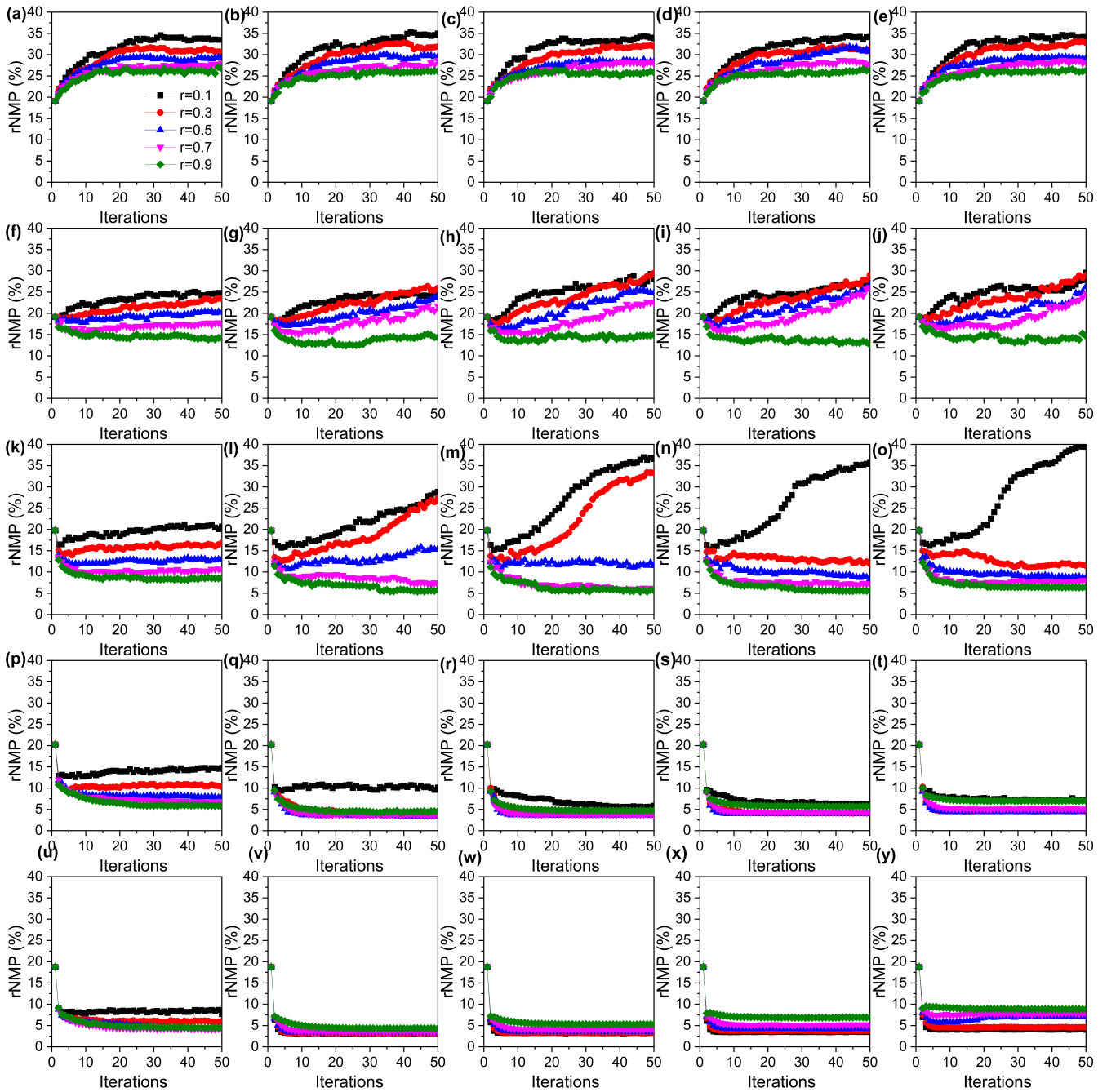
Figure 3.8: rNMP as a function of iterations at different random probability r, smoothing radius: (a-e) b=0.1, (f-j)b=0.3, (k-o) b=0.5, (p-t) b=0.7 and (u-y) b=0.9, and smoothing kernel (from column 1 to 5: the corresponding kernels are 1 to 5) in DART reconstructions based on noisy tilt series (400 counts). The tilt range is $\pm70°$ with an increment of $2°$.

To evaluate the effect of the initial reconstruction on the DART convergence and results, a 2D phantom (1024×1024 pixels) with a complicated disordered pore structure (Figure 3.9a) was used to simulate the DART reconstruction from 1D projections. The rNMP values were calculated as a function of the number of iterations in DART starting from three different initial reconstructions including an all-zero image, a SIRT

reconstruction and a TVM reconstruction, as shown in Figure 3.9b. During the DART reconstruction, the main loop was iterated 50 times followed by 150 iterations for SIRT. A probability of 0.1 was used to re-evaluate random pixels and a convolution filter with kernel 1 and radius 0.9 was used for smoothing the reconstruction before further segmentation. It is surprising that the rNMP converged to similar values after 20 iterations despite the huge difference of the three initial reconstructions. A more reliable initial reconstruction e.g. reconstruction by TVM, only leads to faster convergence in DART, while it has little influence on the final reconstruction after sufficient iterations.
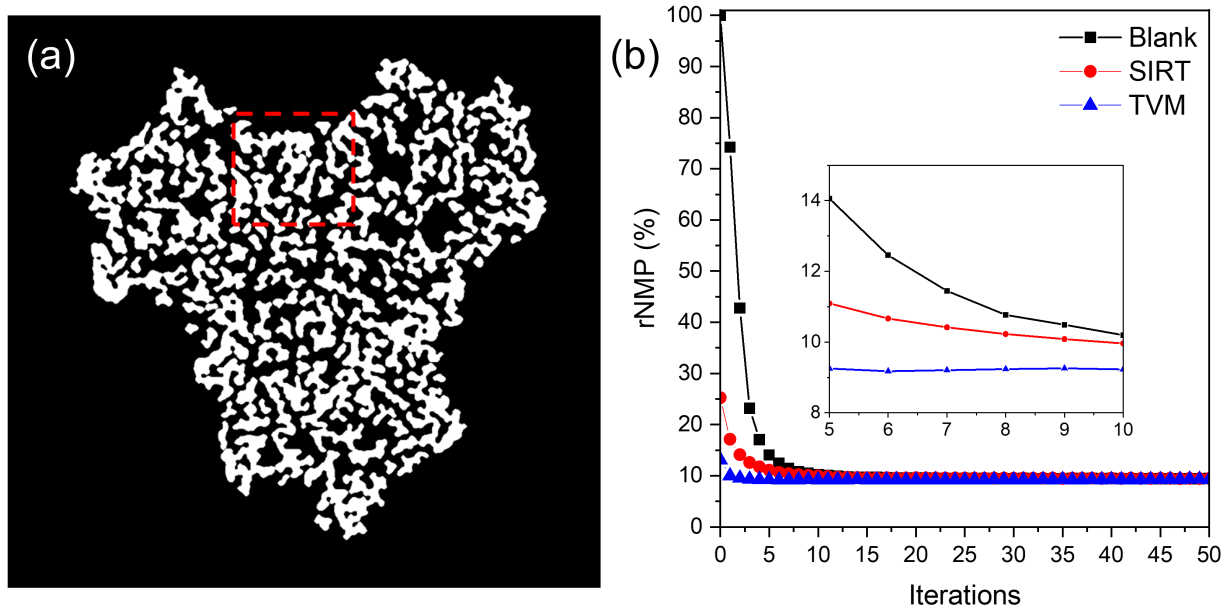
Figure 3.9: (a) 2d phantom for the test the influence of the starting structure on the DART reconstruction. (b) rNMP as a function of the number of iterations for DART from three initial reconstructions with a tilt range of $\pm 70°$ with an increment of $2°$. The number of counts for the Poisson noise is 1600 and the standard deviation for the Gaussian noise $\sigma = 0.01$.

A more revealing comparison is presented in Figure 3.10, which shows the reconstruction after different iterations for the different initial reconstructions in DART. When using a blank image as input for the DART reconstruction, a very rough image is produced after the first segmentation (1 iteration, Figure 3.10a), resulting in a rNMP value of 75%. The reconstruction became more and more reliable with increasing number of iterations until it does not change anymore after a sufficient number of iterations. The reason why the DART algorithm can succeed without an initial reconstruction depends on the possibility for a certain percentage of random pixels (10% in this case) to change their classification at each iteration. With sufficient iteration time (as long as the random probability is not 0), basically all the pixels have a chance to be adjusted. When starting from a SIRT reconstruction as the initial reconstruction, a rough reconstruction is already produced after the first iteration (Figure 3.10e) and the final reconstruction converges after around 10 iterations (Figure 3.10g). A quite reliable reconstruction was obtained already after the first iteration when using a TVM reconstruction as initial reconstruction and the final result quickly converge after around five iterations. This finding shows that the image quality of the original tilt series, which is highly affected by noise and the consistence of the alignment, instead of the initial reconstruction is the key factor to get the most reliable results, because for each iteration the improvement in the reconstruction is solely based on the difference between the back-projected images and the experimental projections. Appropriate smoothing at each iteration is also important in order to suppress noise so that convergence is ensured without washing out small structural features of interests.

Other smoothing methods during the iteration or some advance segmentation methods like local thresholding may be also helpful to improve the final reconstruction.
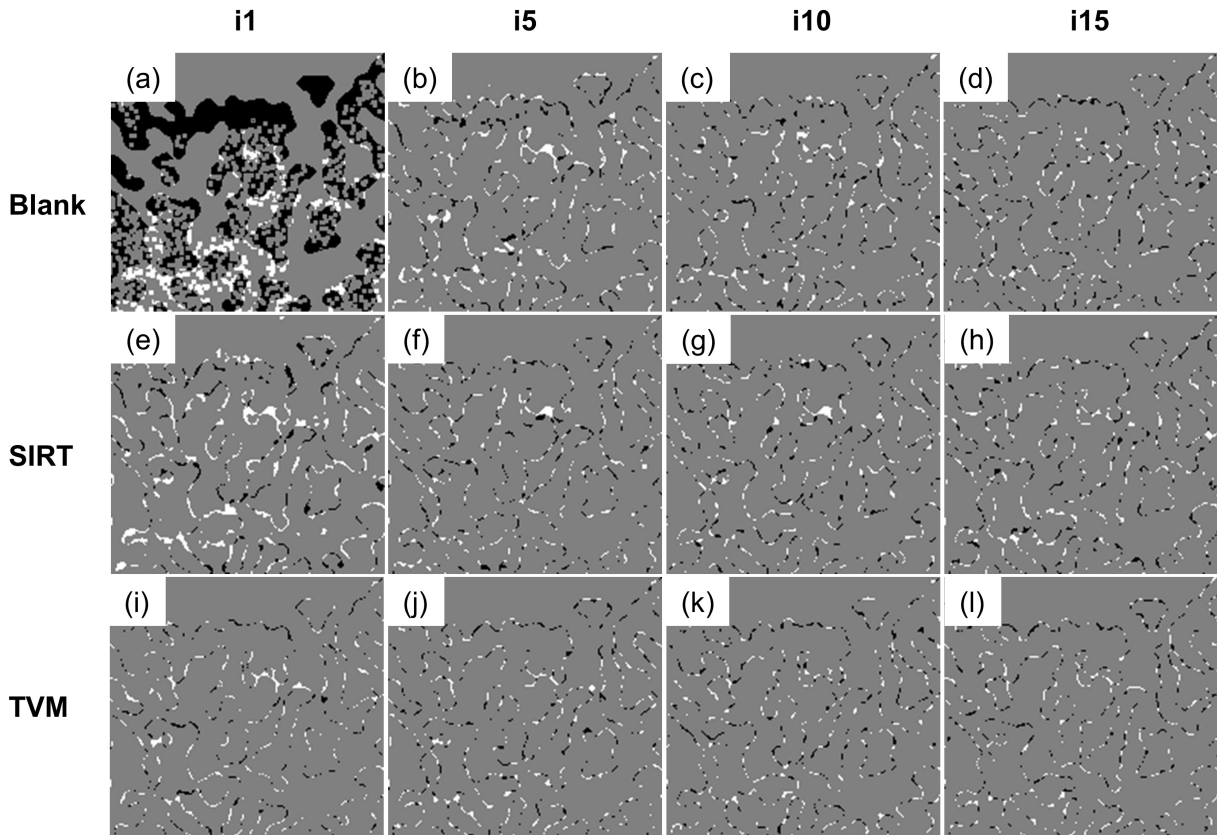
Figure 3.10: Misclassified pixels of blank (a-e), SIRT (f-j) and TVM (k-o) as initial input in DART compared to the original phantom (highlighted in Figure 3.9a) after different iterations: (column 1) 1, (column 2) 5, (column 3) 10 and (column 4) 15.

Figure 3.11b shows that the three reconstruction algorithms behave similarly with the full tilt range of $\pm 90°$ for all noise levels tested with a higher noise level (lower number of counts) resulting in larger rNMP. It is clear that SIRT is more sensitive to noise compared to TVM and DART for a tilt range of $\pm 70°$, as can be seen from Figure 3.11c. At a fairly high noise level (400 counts), the rNMP from SIRT is 7.2%, 1.6 times as high as TVM (4.5%) and more than twice as high as DART (3.1%). Even at a fairly low noise level (4e-6 counts), the rNMP from SIRT is 4.2%, more than three times that of TVM (1.3%) and almost eight times as high as with DART (0.5%). These results show the superior performance of TVM and DART for the reconstruction of noisy data, especially with a typical missing wedge.

For a better visualization of the reconstruction quality, segmentation results based on the three reconstruction methods for 400 counts are shown in Figure 3.12. Both SIRT and DART can recover the smallest pores accurately when there is no missing wedge, while all pores with a diameter of 5 pixels disappeared from the segmented TVM reconstruction. This is due to the large penalty parameter μ, which causes strong smoothing of the final reconstruction but results in the lowest rNMP value. For the reconstructions from data with missing wedge (Figure 3.12d-f), both SIRT and TVM show clearly elongation artifacts in the vertical direction and artificial pores at random places are observed for segmented_SIRT, while elongation artifacts are highly reduced and most small pores are correctly recovered by DART. A comparison of the segmentation results

based on a lower noise level (1600 counts) is shown in Figure 3.13, where more accurate reconstructions were obtained by all three algorithms.
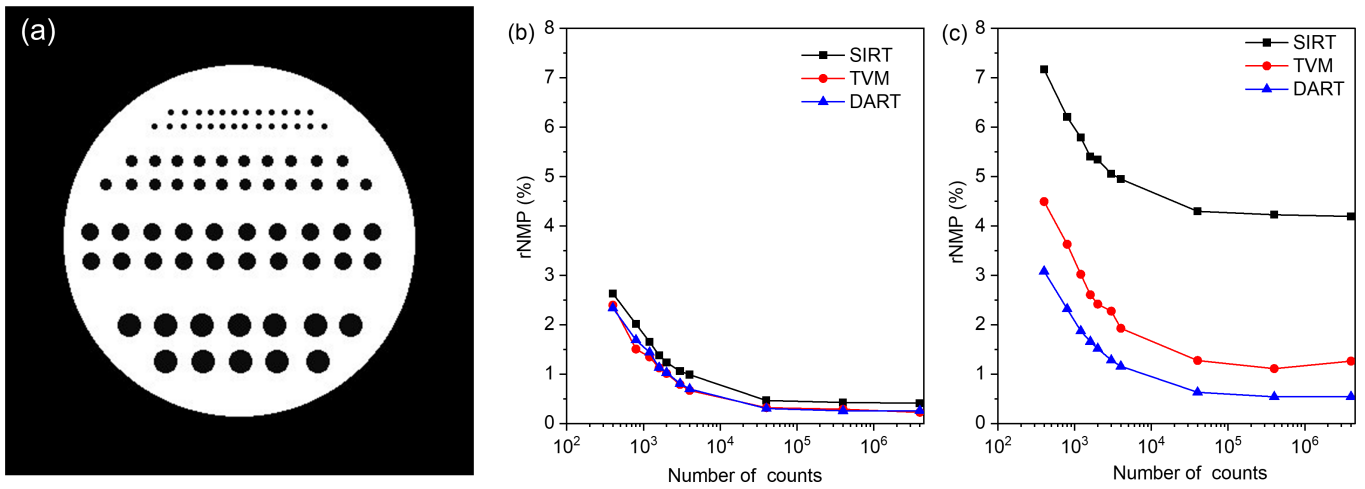
Figure 3.11: (a) 2D phantom with spherical pore with different sizes, rNMP as a function of the number of counts for the tested three reconstructions at a tilt range of (b) ±90° and (c) ±70° with an increment of 2°.
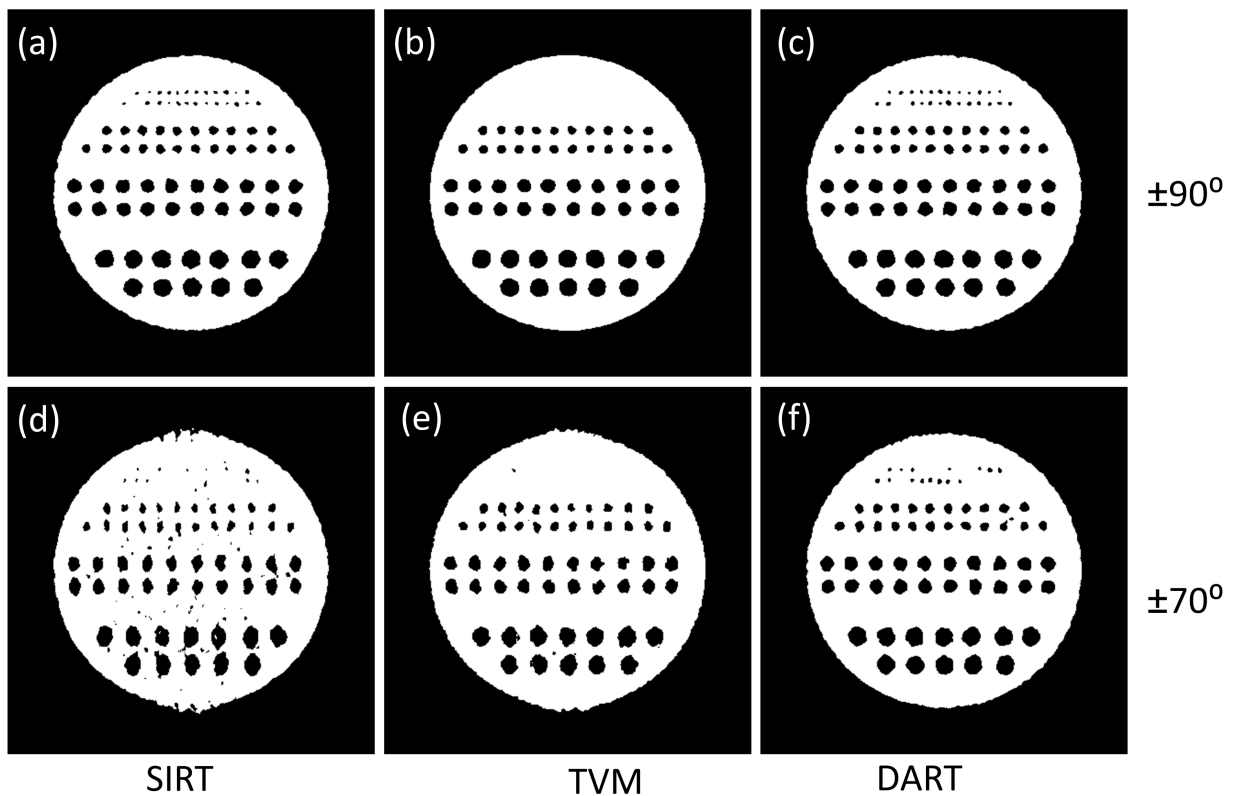
Figure 3.12: Comparison of SIRT (a,d), TVM (b,e) and DART (c,f) reconstructions including noise effects with a tilt range of (a-c) ±90° and (d-f) ±70°. The number of counts for the Poisson noise is 400.
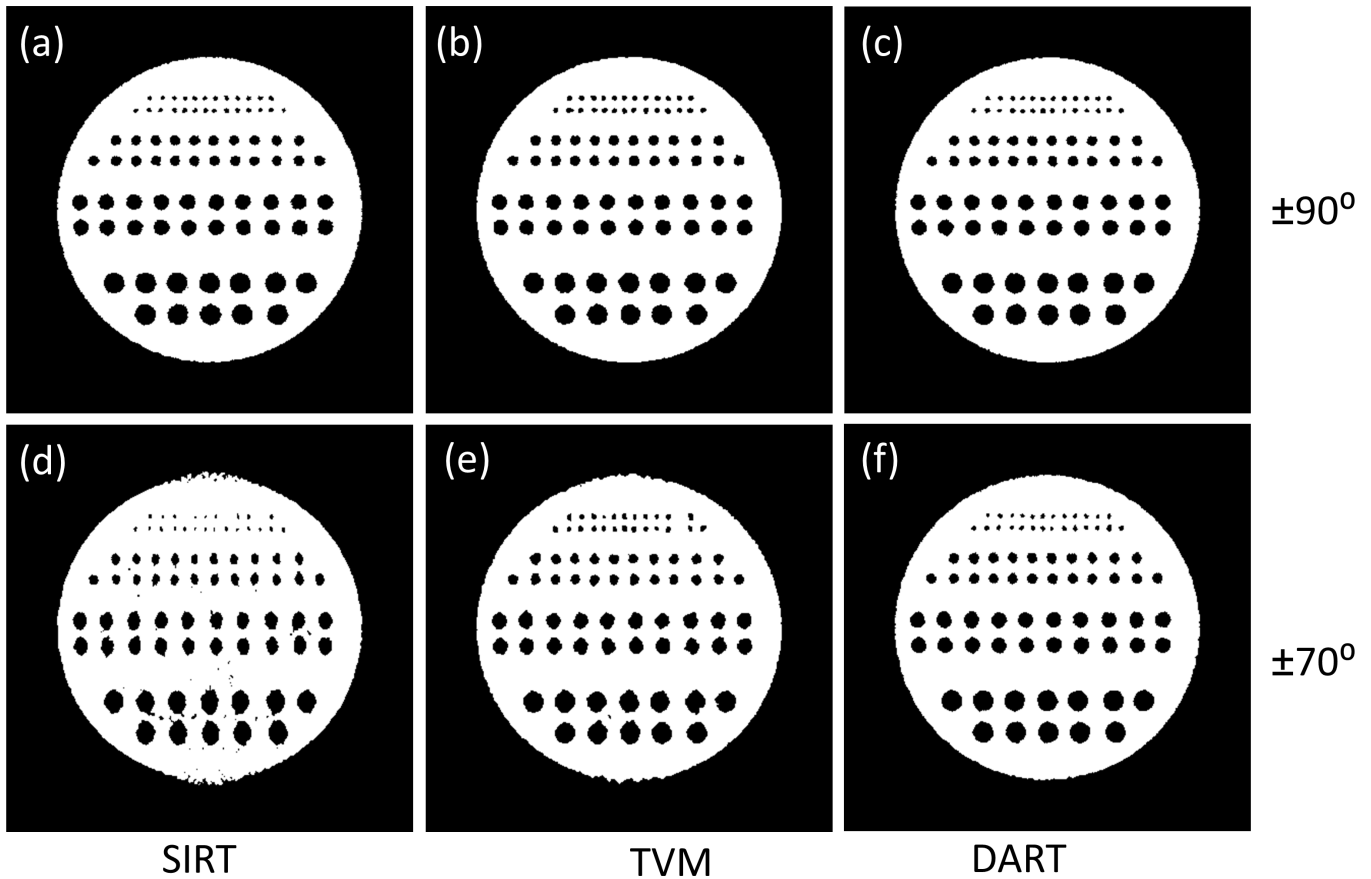
Figure 3.13: Comparison of SIRT (a,d), TVM (b,e) and DART (c,f) reconstructions including noise effects with a tilt range of (a-c) $\pm 90°$ and (d-f) $\pm 70°$. The number of counts for the Poisson noise is 1600.

3.3.2. Effect of missing wedge

In this section, a 2D phantom (600×600 pixels) with an artificial pore structure (Figure 3.14a) was used to investigate the efficiency of different reconstruction methods in revealing the pore connectivity from various tilt series with different missing wedges. The phantom was designed to include three small pores, 6-8 pixels wide (green arrows) connected channels in the horizontal direction, 10-20 pixels wide (red circles) narrow necks between pores and disconnected channels, 10-15 pixels wide for solid separation of the pores (blue triangles) as well as some other randomly distributed pores. Using this phantom, an error estimate of the statistical variations based on 10 reconstructions for each algorithm and two noise levels was first calculated to ensure repeatability, as shown in Figure 3.14d,e.

Figure 3.14b,c shows the rNMP as a function of the tilt range without and with noise, indicating that DART is the most promising reconstruction method in case of the presence of a missing wedge. The rNMP of DART is 0 even for a tilt range as low as $\pm 50°$, when there is no noise present, resulting in a fully accurate reconstruction of the raw phantom, far superior to SIRT and TVM with a corresponding rNMP of 13.3% and 4.6%. At moderate noise levels (1600 counts), DART still keeps an excellent accuracy with small rNMP values for the same tilt range. A comparison of the segmentation results in Figure 3.15 clearly shows that the pore connectivity was recovered accurately by DART for a tilt range of $\pm 50°$ without and with moderate noise. Strong elongation artifacts in the vertical direction can be seen for the SIRT segmentation and the area of

narrow pore channels were mistakenly segmented so that the connected channels were misclassified to be broken and vice versa, as shown in Figure 3.15a,d. Although elongation caused by the missing wedge was less prominent in the TVM reconstructions compared to SIRT, most narrow channels were not recovered correctly as showed in Figure 3.15b,e.
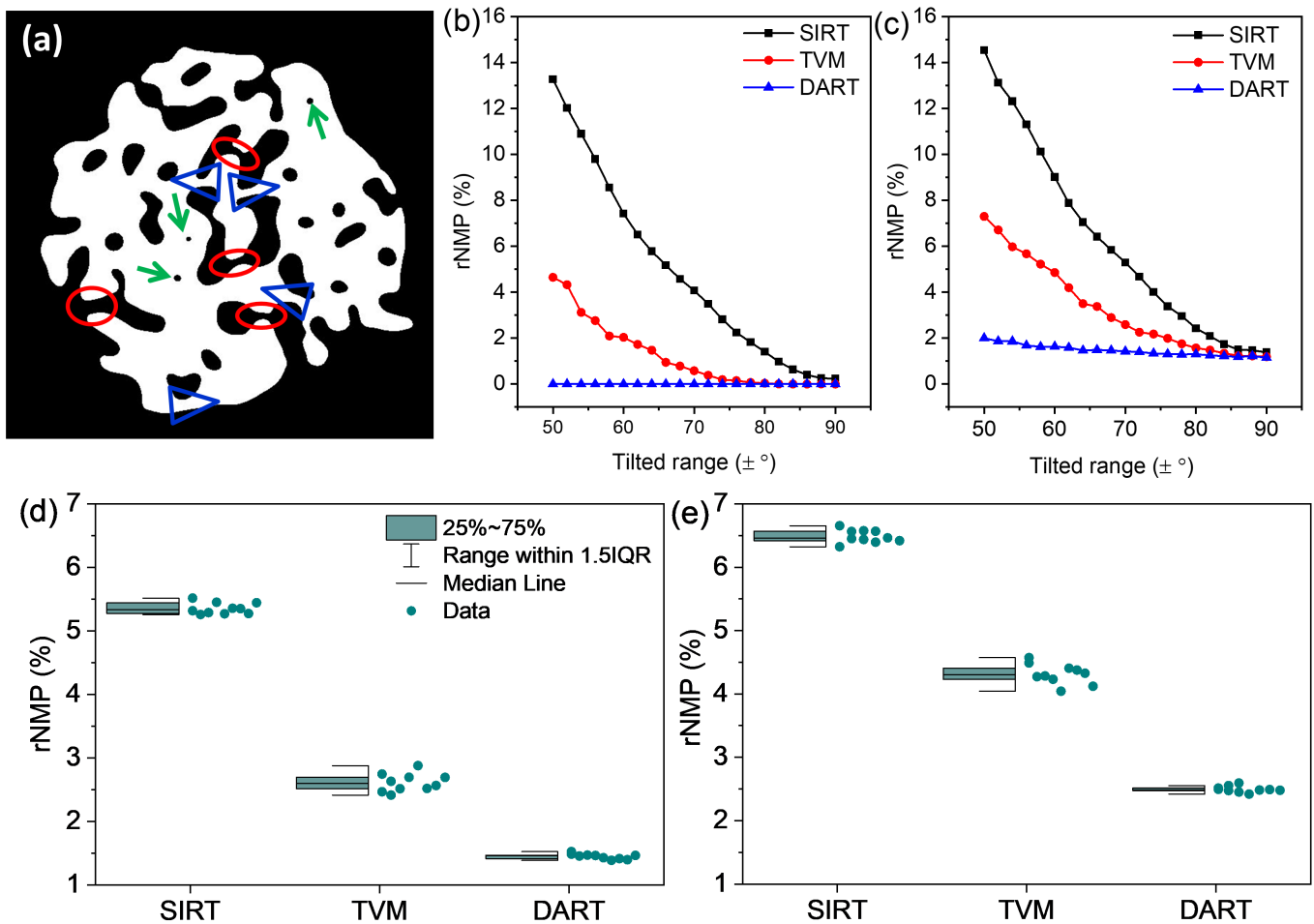
Figure 3.14: (a) 2d phantom for missing wedge experiments: rNMP as a function of the tilt range for three reconstructions at 1600 counts (b) without noise and (c) with noise; An error estimate of the statistical variations based on 10 reconstructions for each algorithm and two noise levels: (d) 1600 counts and (e) 400 counts.
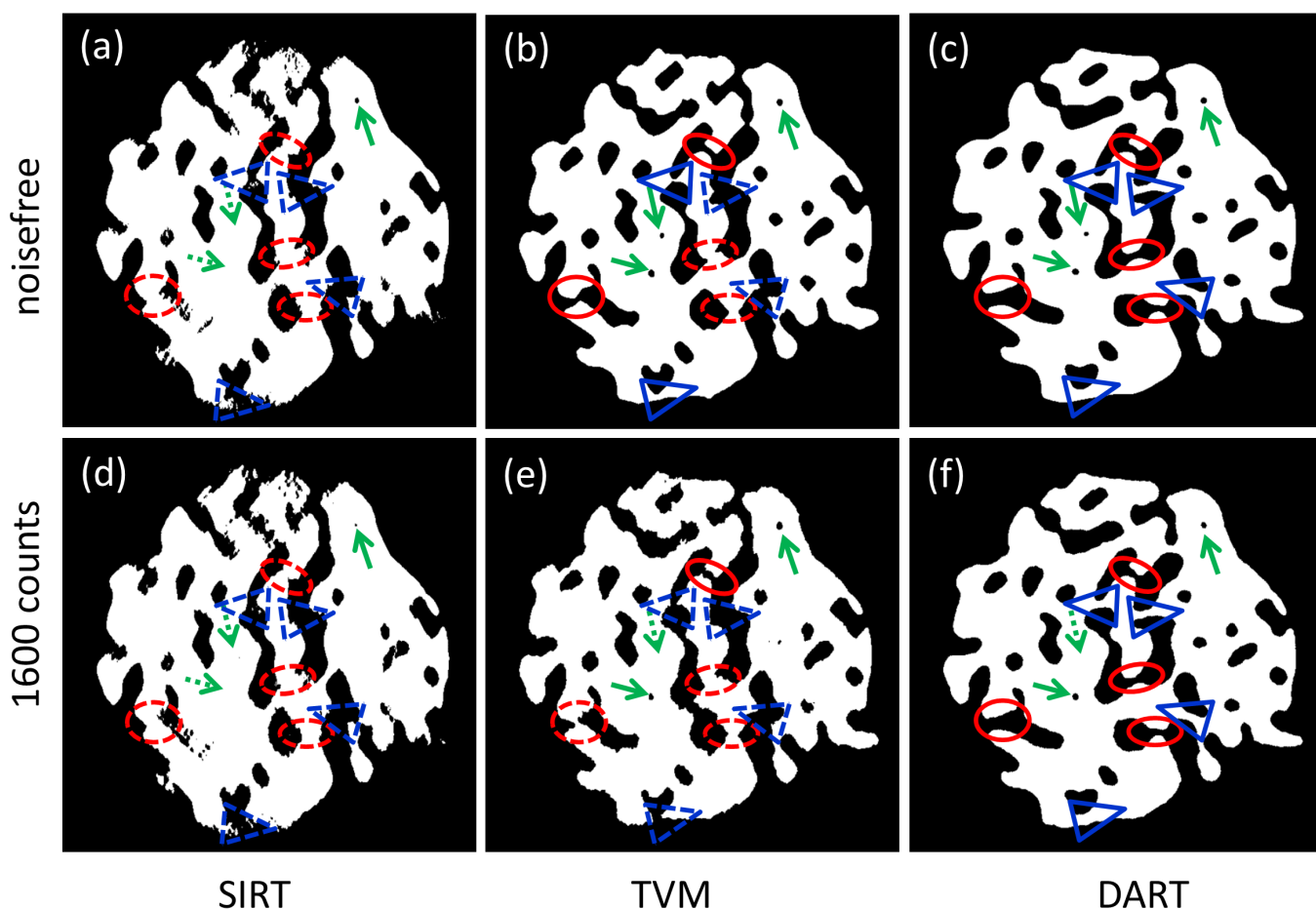
Figure 3.15: Comparison of SIRT (a,d), TVM (b,e) and DART (a,f) reconstructions including missing wedge effects (a-c) without noise and (d-f) with noise. Here, the tilted range was $\pm 50°$, the solid and dashed lines represent correct and wrong reconstruction features.

3.3.3. Number of projections

Classically, the more projections are used for a reconstruction, the higher resolution can be achieved, which can be estimated for example using the Crowther criterion [202]. However, many mesoporous materials, e.g. silica or carbon are not stable under the electron beam and a compromise has to be made between dose and number of projections. It is necessary to consider the influence of reducing the number of projections on the final reconstruction reliability. Here, ten different tilt increments are used to investigate the influence of the angular sampling scheme for the same phantom with narrow bottlenecks shown in Figure 3.14a with and without noise.

Figure 3.16 shows the rNMP as a function of tilt increment ranging from $1°$ to $10°$ without and with noise for SIRT, TVM and DART reconstructions. Here, a tilt range of $\pm 70°$ was used to sample the projections and 1600 counts for the Poisson noise was used for the tilt series with noise. The results show that DART again yields more accurate reconstructions than TVM and SIRT, both with and without noise. The rNMP for DART with an increment of $3°$ in the presence of noise is 1.7%, around half compared with TVM (3.1%) and

less than one third compared to SIRT (5.9%). TVM is comparable with DART for increments of 5° and less without noise (Figure 3.16a).
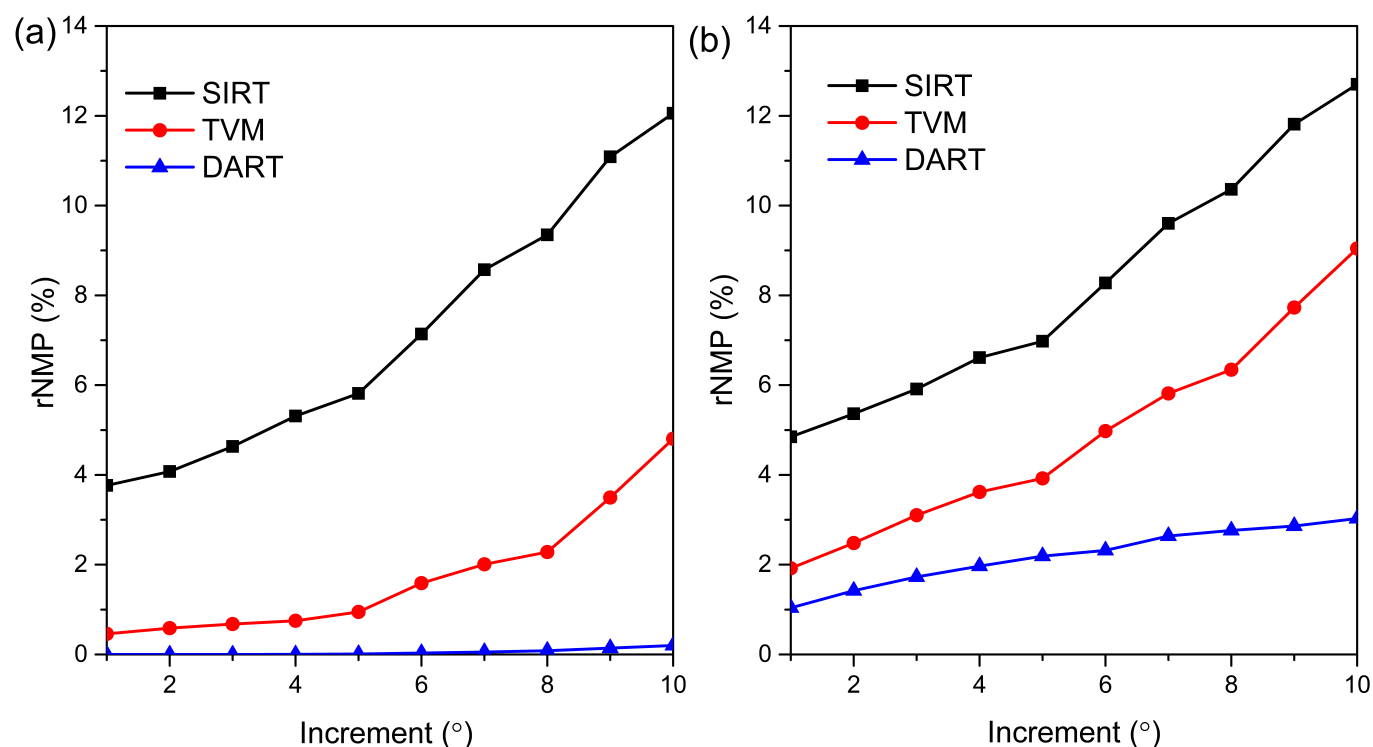
Figure 3.16: Influence of the number of projections on the 3D reconstruction: rNMP as a function of the tilt increment for SIRT, TVM and DART (a) without noise, (b) with noise (1600 counts). The tilt range is ±70°.

As an illustration of the reconstruction accuracy of the pore connectivity, Figure 3.17 shows the segmentation results based on SIRT, TVM and DART with an increment of 3°, a typical experimental tilt step for data acquisition. Again, all pore connections were accurately recovered by DART both with noise free and moderate-noise data, with only two of the isolated pores disappearing for the noisy data. TVM also performed fairly well for noise free data, while the reconstruction of narrow channels was unsatisfactory for noisy data. However, SIRT failed to reconstruct most narrow channels even for noise free data. A comparison of the segmented results with a more extreme tilt increment of 10° can be seen in Figure 3.18, where both SIRT and TVM lose almost all connections for narrow channels, while DART was still able to yield reasonably accurate reconstructions. Such superior performance of DART for the reconstruction of tilt series with large tilt steps would be helpful for in situ investigation or beam-sensitive specimens by reducing the data acquisition time and dose.
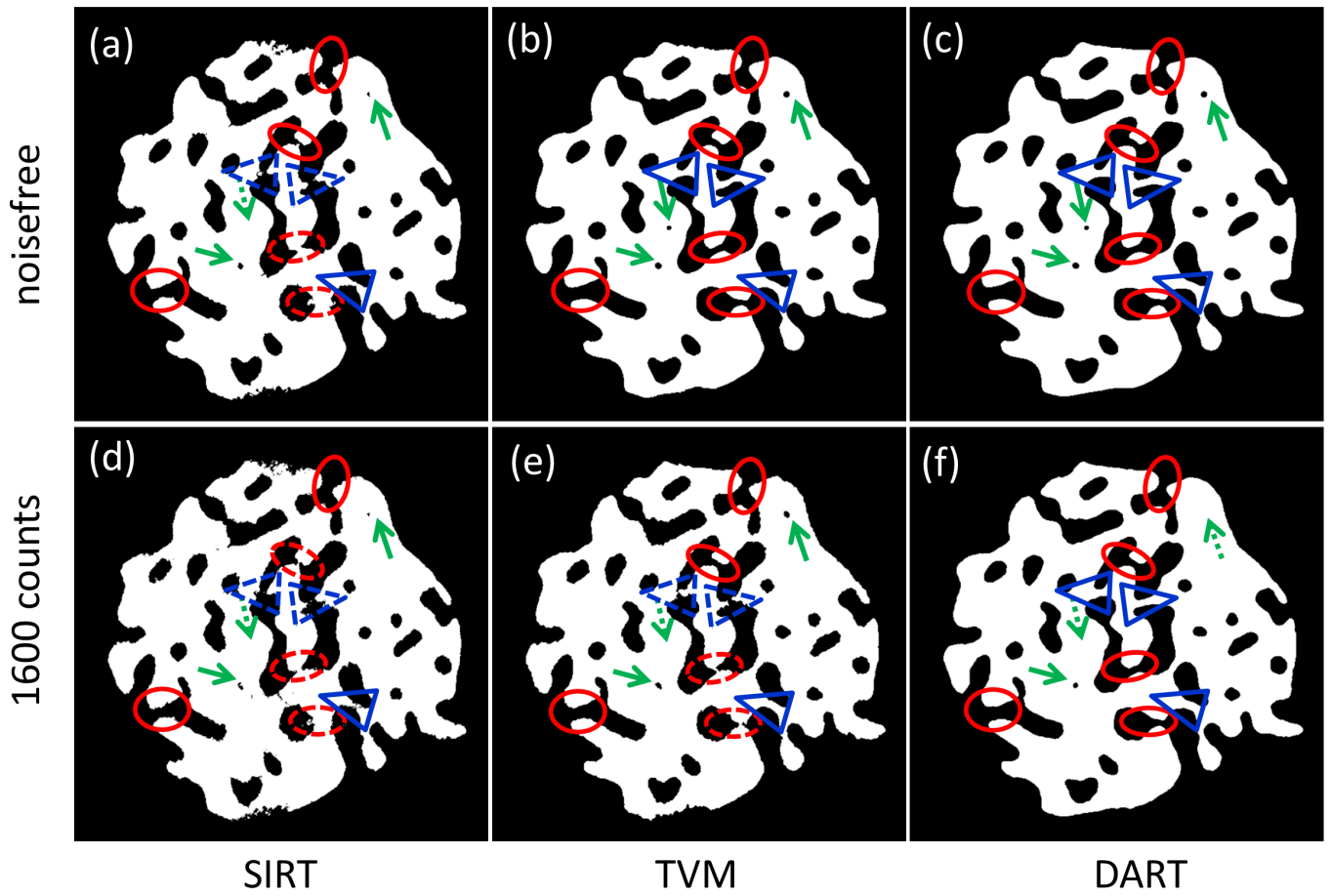
Figure 3.17: Comparison of segmented reconstructions without noise (a-c) and with noise (d-f) for a tilt increment of 3° based on SIRT (a,d), TVM (b,e) and DART (c,f) reconstructions. The solid and dashed lines represent correct and wrong reconstruction of narrow pores/walls. The tilt range is ±70°.
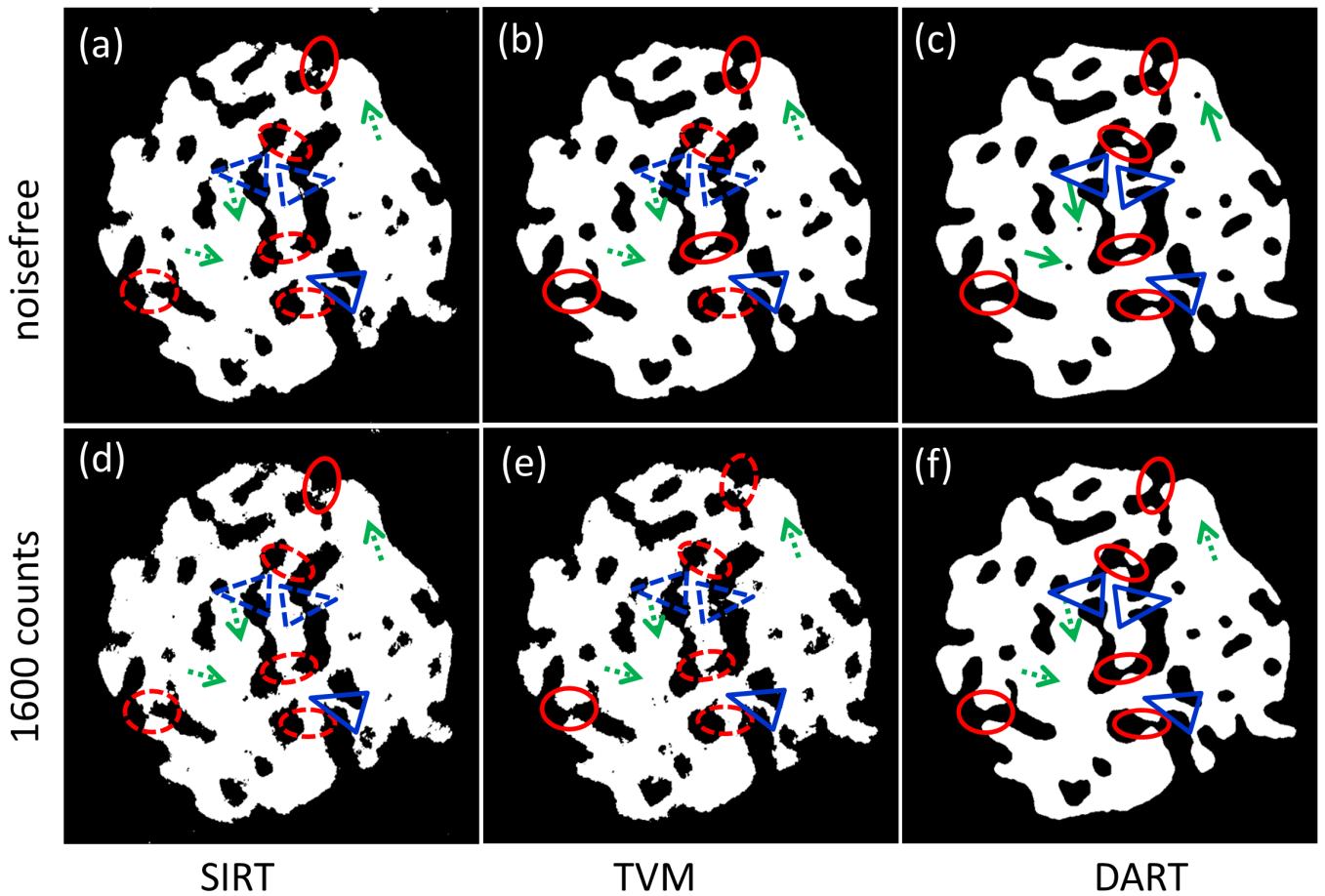
Figure 3.18: Comparison of segmentation without noise (row 1) and with noise (row 2) at tilt step of 10° from: SIRT-based segmentation (column 1), TVM-based segmentation (column 2) and DART (column 3). The solid and dashed lines represent correct and wrong reconstruction. The tilt range is ±70°.

To exclude the influence of the missing wedge, the same simulations with different tilt increments covering the full tilt range (±90°) was performed and the results are shown in Figure 3.19-Figure 3.21. The three algorithms show similar and excellent performance for the reconstructions of pore structures at small tilt increments of less than 3°, while DART is clearly superior for higher tilt increments (>5°). These results show again the promising ability of DART for the reconstruction of pore structures from tilt series with a limited number of projections.
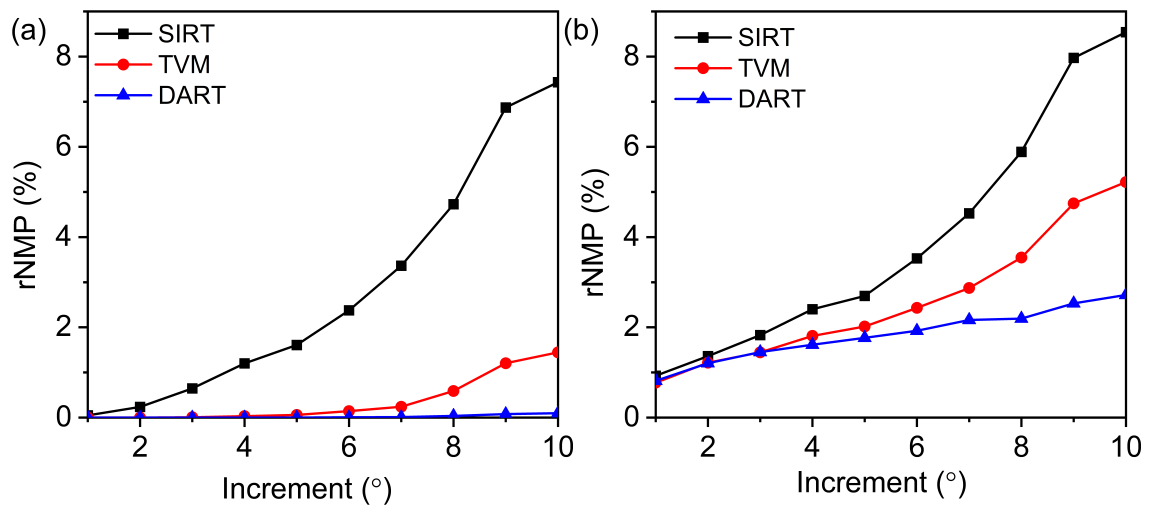
Figure 3.19: Influence of the number of projections on the 3D reconstruction: rNMP as a function of the tilt increment for SIRT, TVM and DART (a) without noise, (b) with noise (1600 counts). The tilt range is $\pm 90°$.
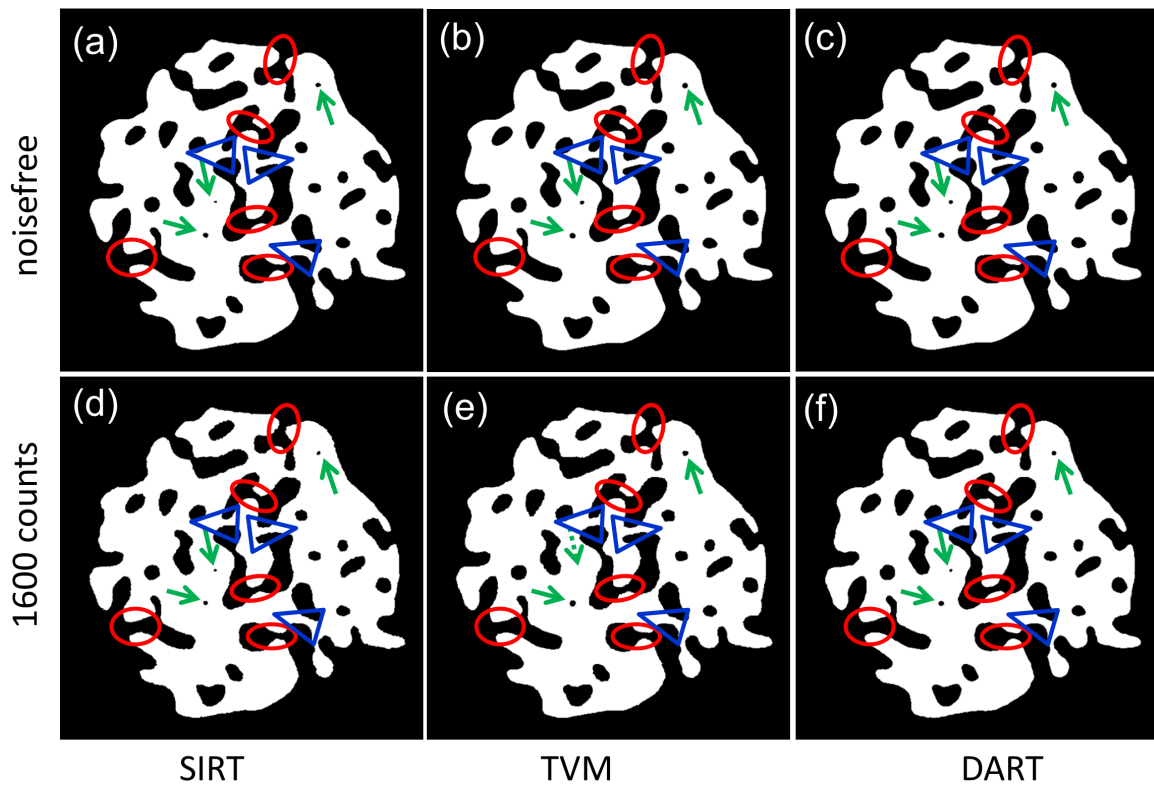
Figure 3.20: Comparison of segmentation without noise (row 1) and with noise (row 2) with a tilt increment of 3°: SIRT-based segmentation (column 1), TVM-based segmentation (column 2) and DART (column 3). The solid and dashed lines represent correct and wrong reconstructed pores. The tilt range is $\pm 90°$.
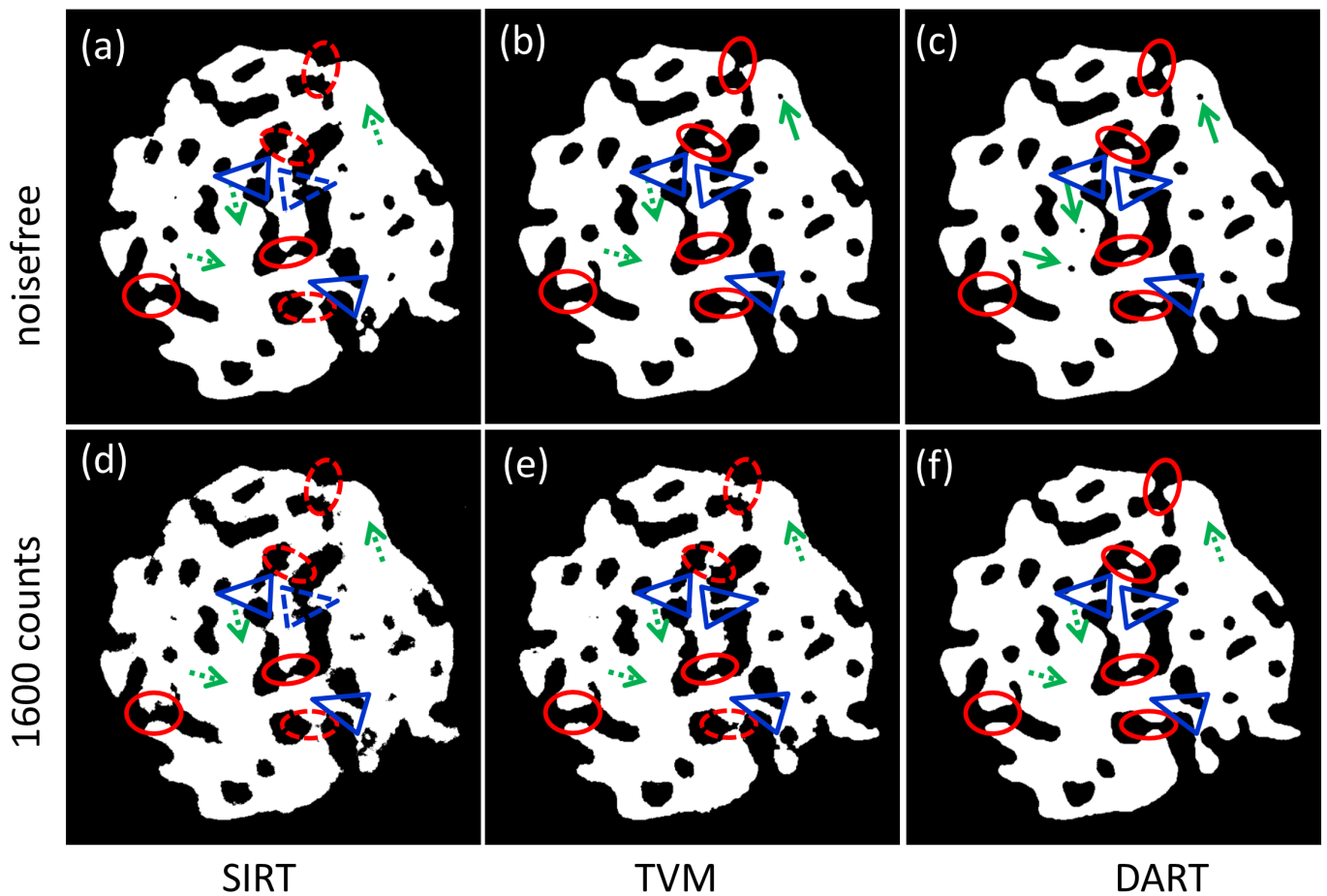
Figure 3.21: Comparison of segmentation without noise (row 1) and with noise (row 2) with a tilt increment of 10°: SIRT-based segmentation (column 1), TVM-based segmentation (column 2) and DART (column 3). The solid and dashed lines represent correct and wrong reconstructed pores. The tilt range is ±90°.

3.3.4. 3D model simulation

To test the influence of the reconstruction quality for a quantitative analysis of 3D pore features, a 3D phantom of 512×512×512 voxels with an irregular pore structure was created as shown in Figure 3.22. The matlab code for the model creation is presented in Figure 3.23. In total, 71 forward projections were simulated covering a tilt range of ±70° with an increment of 2°, which is typically used for tomographic data acquisition in a TEM. To make the simulation realistic, Poisson noise with a mean number of counts of 1600 combined with an additive Gaussian noise with a standard deviation of $\sigma = 0.01$ was added to the projections and each of the projected images was misaligned by 0.4±0.2 pixel on average in either direction to mimic the inevitable residual alignment error for experimentally acquired projected images. The resulting projections were used as the input for SIRT, TVM and DART reconstructions.
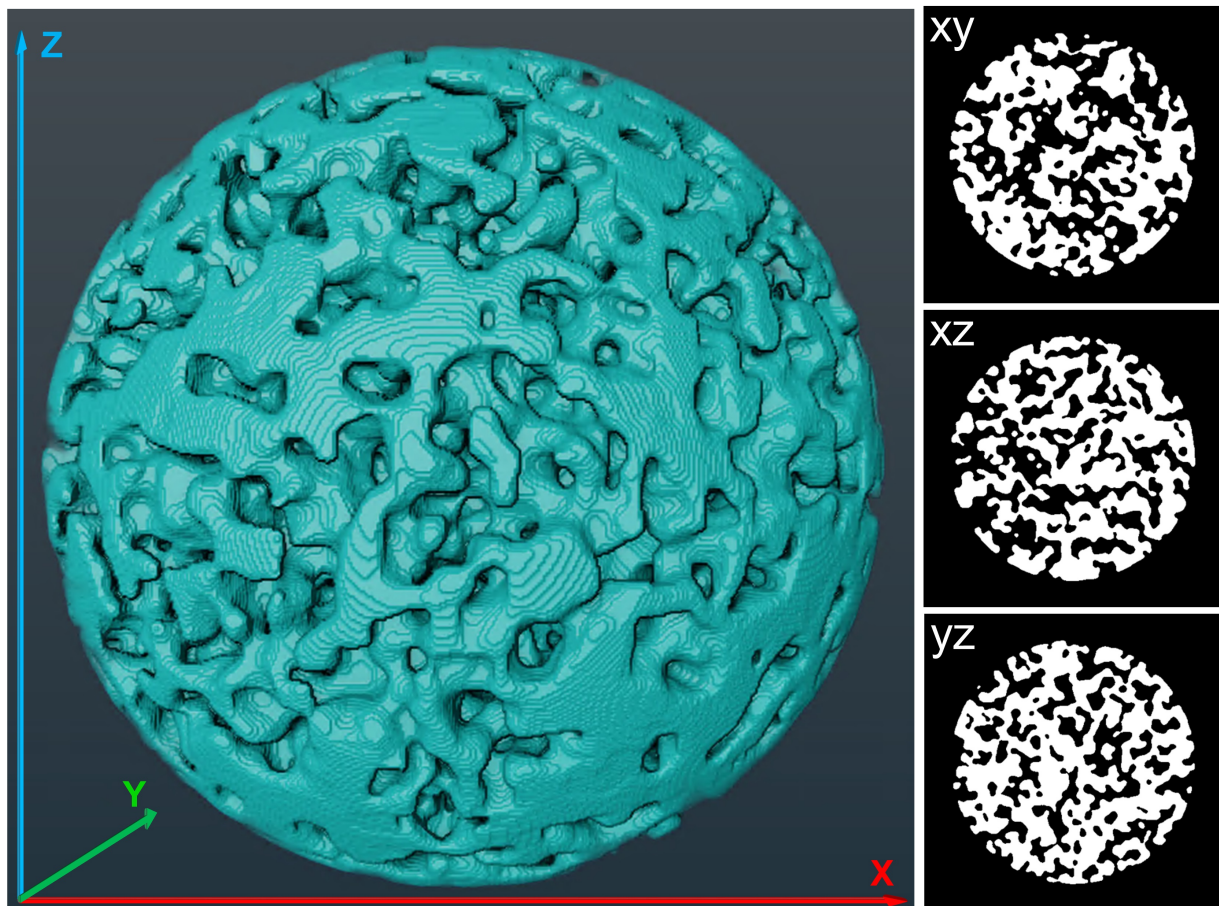
Figure 3.22: 3D phantom and corresponding representative slices along the xy, xz and yz planes.

```
% 3d model creation with disordered pores
s = 512;  % size of phantom
a = rand(s,s,s); % create a 3d matrix with random noise
model = double(imbinarize(a)); % binary the created matrix
model = medfilt3(model,[5,5,5]); % median filter
% create a spherical mask
x = -255.5:255.5; y = -255.5:255.5; z = -255.5:255.5;
[X,Y,Z] = meshgrid(x,y,z);
mask = (X.^2+Y.^2+Z.^2<=220^2);
mask = double(mask);
model(mask==0)=0;
model = double(model);
```

Figure 3.23: MATLAB code for the creation of a 3d phantom with disordered pores.

Representative slices after reconstruction and segmentation based on SIRT, TVM and DART are shown in Figure 3.24. It is clear that the SIRT reconstruction and corresponding segmentation images suffer from obvious missing wedge artifacts, which is mostly visible in the xz slices, resulting in a false reconstruction of the pore connectivity as highlighted by red circles in the segmented structure in Figure 3.24 (column 2). Artifacts caused by the missing wedge are reduced to some extend in the TVM reconstruction compared to SIRT, but most narrow connected pores are still falsely segmented as disconnected (Figure 3.24, column 4). In contrast, the reconstruction was greatly improved by DART, which suppresses the missing wedge artifacts and keeps the correct pore connectivity (Figure 3.24, column 5). These results indicate that DART is the most promising of the three algorithms for porous materials, consistent with the analysis of the 2D simulations.
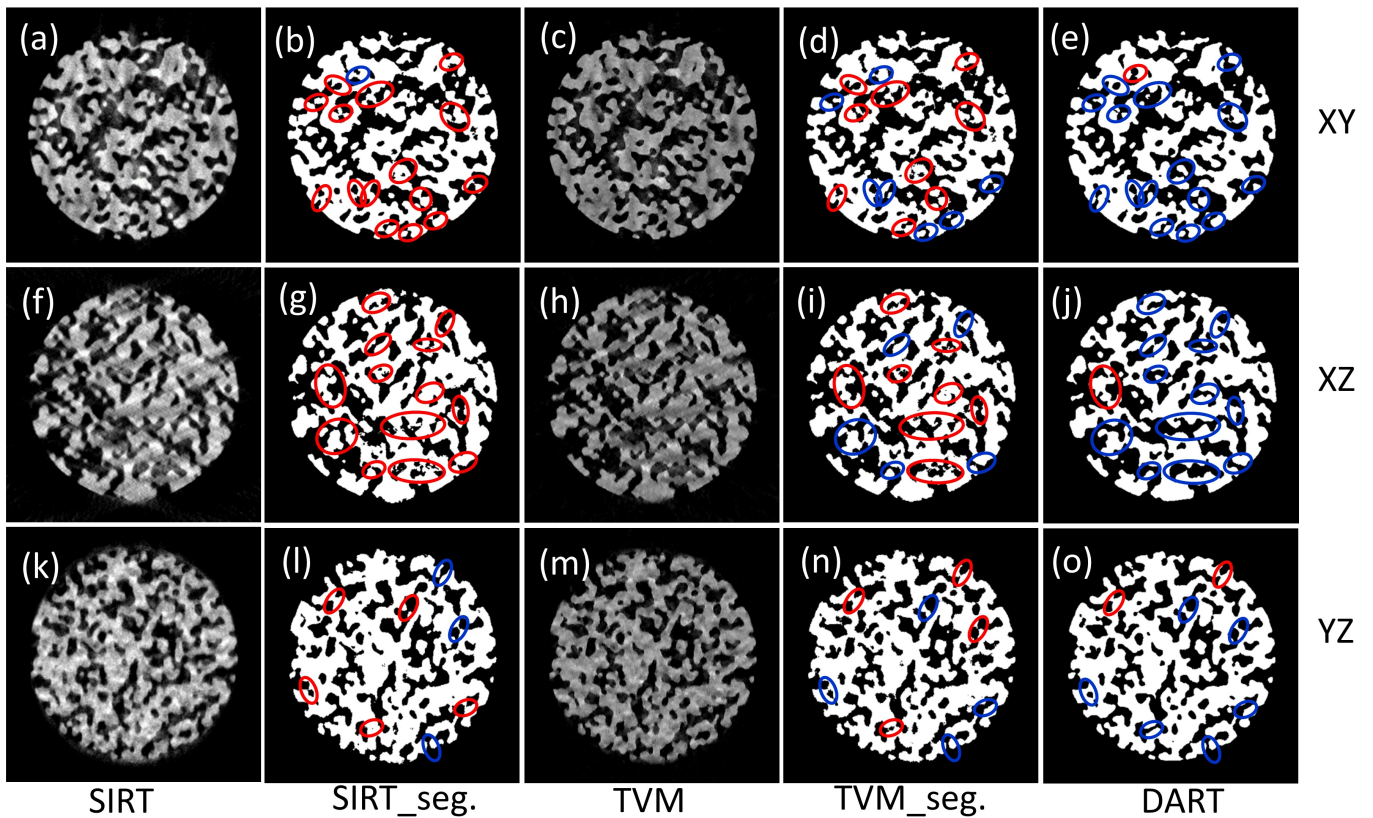
Figure 3.24: Representative slices of SIRT reconstruction (a,f,k), SIRT-based segmentation (b,g,l), TVM reconstruction (c,h,m), TVM-based segmentation (d,i,n) and DART (e,j,o) along the xy (a-e), xz (f-j) and yz (k-o) planes. Narrow channels are highlighted by red circles in case the connectivity has been altered by the reconstruction and in blue if it has been correctly reconstructed.

Figure 3.25 shows 2D slices and 3D surface rendering of the misclassified voxels for a SIRT-, TVM-based segmentation and DART. For the creation of the surface rendering, the segmented volumes were filtered by Gaussian smoothing with kernel size of 2. Compared to the SIRT- (11.2%) and TVM-based (9.8%) segmentation, which exhibit large continuous areas of misclassified voxels, the misclassified voxels produced by DART (6.4%) are more randomly distributed and mostly located as single pixels at the boundaries between pores and solid. Therefore, the recovery of the pore network topology is less affected by the randomly distributed misclassified voxels, even though the number of misclassified pixels in DART is only reduced by about a factor of 1.5/2 compared to TVM/SIRT.

	SIRT	TVM	DART
rNMP (%)	11.17	9.79	6.42
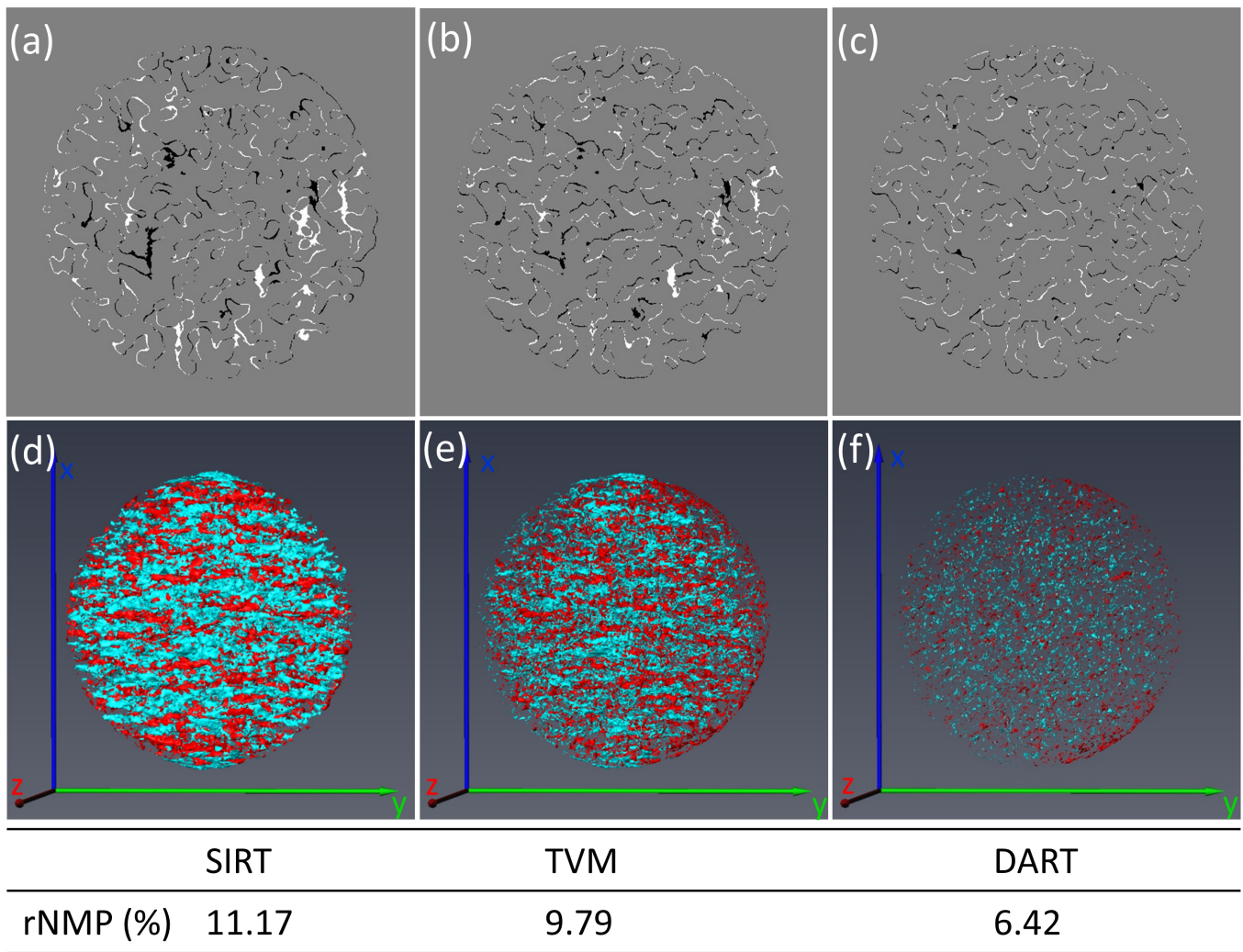
Figure 3.25: Representative slices (a-c) and 3D surface rendering (d-f) of misclassified voxels from (a,d) a SIRT-based segmentation, (b,e) a TVM-based segmentation and (c,f) DART compared with the original phantom. The simulation parameter include: tilt range of $\pm 70°$ with a tilt increment of $2°$, the number of counts for the Poisson noise is 1600, each of the projection images was misaligned by 0.4 ± 0.2 pixel on average in either direction). The black and white pixels in figure a-c represent the false positive (overestimated) and negative (underestimated) values. Blue and red in figure d-f correspond to the white and black voxels, respectively.

Skeleton analysis was used to quantify the 3D wall/solid morphology of the segmented reconstructions. Significant features related to the geometry and topology of the wall network such as mean radius, wall length and interconnectivity are summarized in Figure 3.26 and Table 3.1. The wall radius distribution shows a higher percentage of walls with a diameter below 5 voxels in the segmented SIRT and TVM volumes, thereby resulting in a smaller mean wall radius (Table 3.1) compared to the phantom volume. Similarly, the smaller average wall length of the SIRT- and TVM-based segmentations was caused by the higher percentage of chord length below 10 voxels. This error in the smaller wall size distribution for the SIRT and TVM reconstructions comes from the large amount of isolated small wall islands caused by mistakenly breaking the wall connectivity as shown in Figure 3.25. The average reconstructed intensity of the pores/walls varies noticeably in different parts of the particle, rendering a global segmentation difficult. This leads to inaccurate segmentation of the SIRT and TVM reconstructions although optimized global thresholds were calculated by

PDM. The inaccurate segmentation also causes deviations of two important topology parameters, the branch tortuosity (Figure 3.26c) and the coordination number of the branch-node network (Figure 3.26d). The most reliable quantification results come from DART, which resulted in errors of only 0.45%, 0.78%, 0 and 0.4% for the average values of wall length, mean radius, tortuosity and wall volume. Despite a global threshold used during the DART reconstruction, with the iterative update of the boundary pixels, local features were refined so that the segmented 3D reconstruction is very closed to the original phantom structure (Figure 3.24, Figure 3.25).
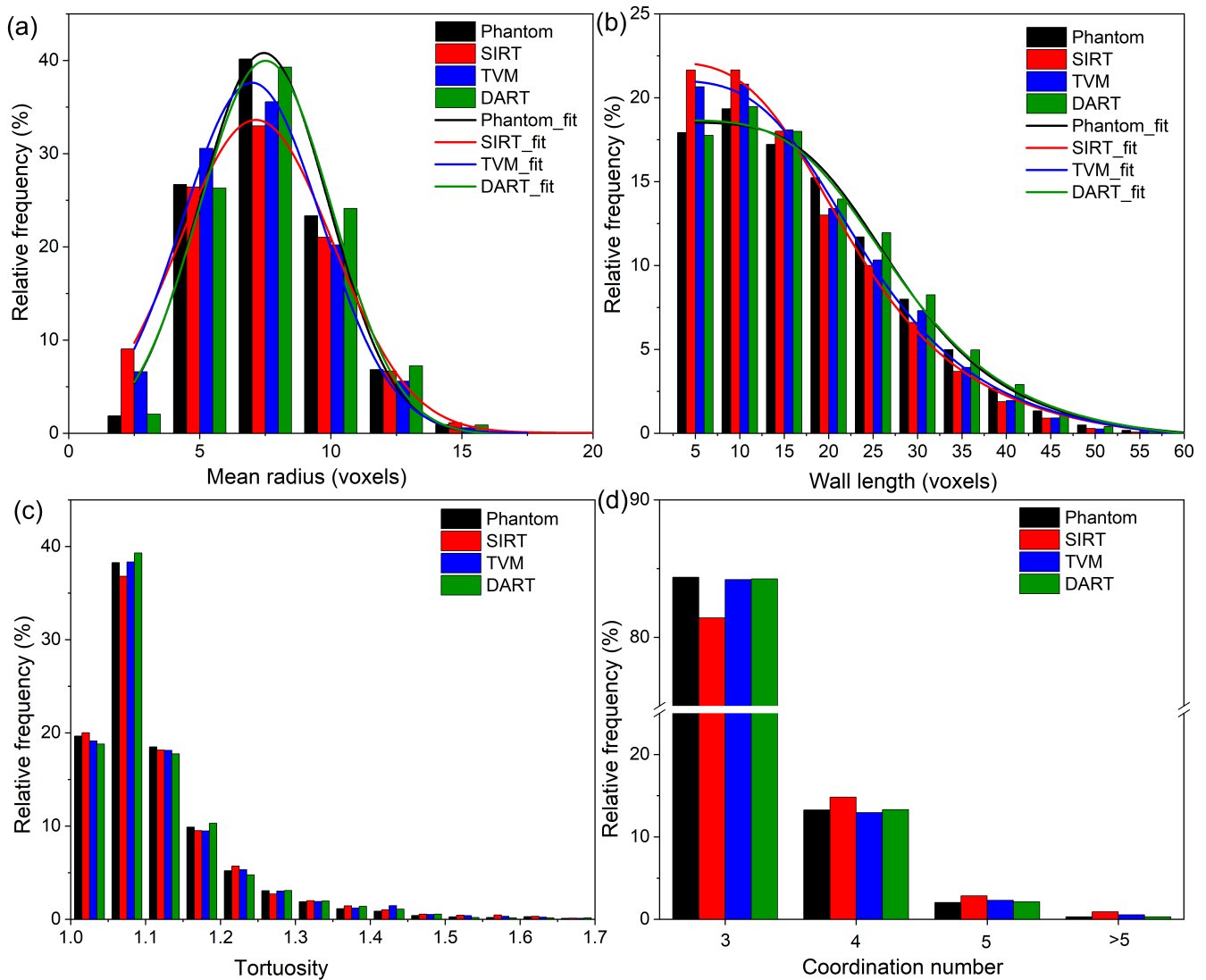
Figure 3.26: (a) Mean radius (b) wall length (c) tortuosity and (d) coordination number distribution from a skeleton analysis of the SIRT- and TVM-based segmentation and the DART reconstruction.

Table 3.1.: Quantification of the wall structure based on a skeleton analysis of the 3D phantom and reconstructions.

	Wall length (voxels)	Mean Radius (voxels)	Tortuosity	Wall Volume (10^6 voxels^3)
Phantom	17.7 ± 10.5	7.7 ± 2.3	1.10 ± 0.11	20.1
SIRT	16.0 ± 9.9	7.4 ± 2.7	1.12 ± 0.26	21.8
TVM	16.3 ± 10.1	7.3 ± 2.5	1.14 ± 0.42	19.7
DART	17.6 ± 10.5	7.8 ± 2.4	1.10 ± 0.12	20.2

[1] Note: the standard deviation represents the homogeneity of the material but not the accuracy of the measurement.

To further investigate the effect of the different algorithms on the reconstructed volume and the properties of mesoporous materials, transport properties were analyzed based on diffusion simulations [11], [89], [203], which represent one of the most important aspects for catalytic performance. Given the significant effect of the two penalty parameters μ and β for the final TVM reconstruction, a slight adjustment of these two parameters was performed manually to improve the signal to noise ratio at the expense of sacrificing the minimum of rNMP. As shown in Figure 3.27a, the parameter pair of $\mu = 11$ and $\beta = 5$ result in a minimum rNMP. However, the resulting reconstruction shows a fairly rough surface. A reconstruction with a smaller $\mu = 10$ and larger $\beta = 9$ yielded a larger rNMP value (12.3%) but a smoother surface (Figure 3.27b). This is
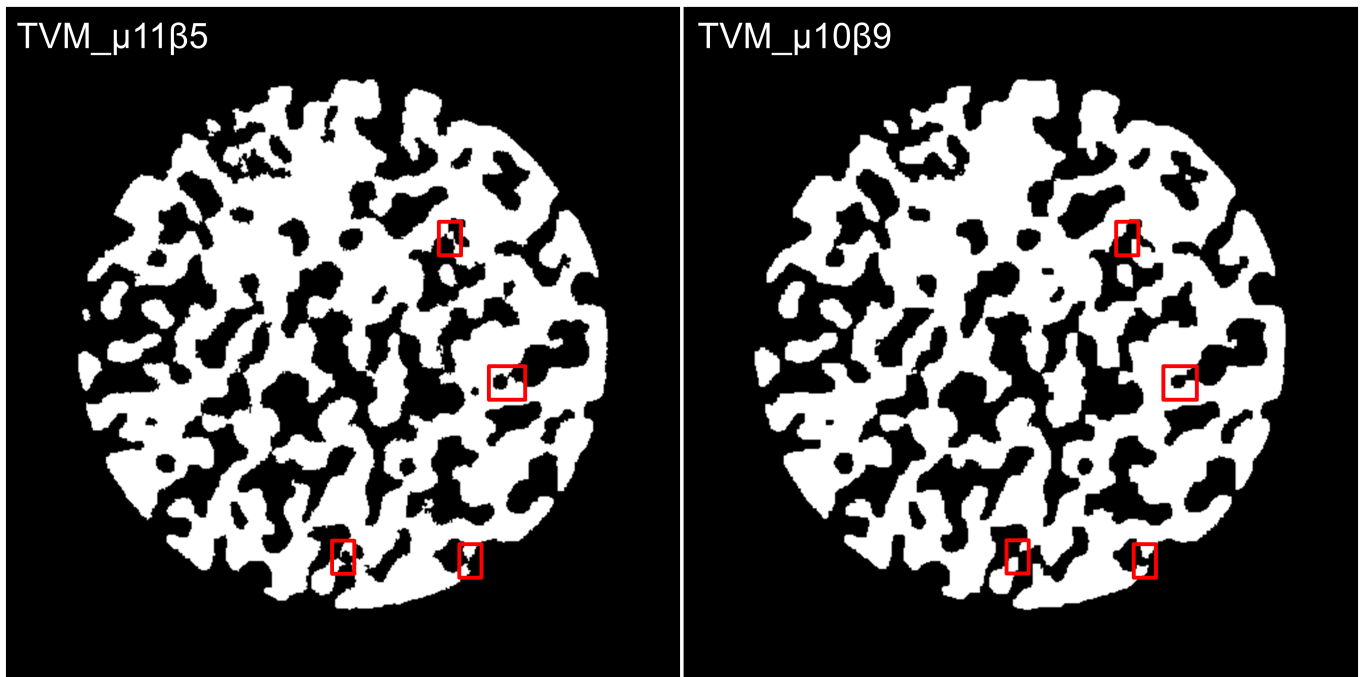
Figure 3.27: Representative slices of a TVM-based segmentation of reconstruction with different penalty parameters μ and β. The effect of surface roughness resulting in narrow pore channels is highlighted by red squares.

expected since μ penalizes the difference between the measured and reconstructed sinograms and a large μ leads to a result closer to a SIRT reconstruction, while β controls the smoothing level and a large β leads

stronger smoothing as described in section 2.9.5. When focusing on the narrow pore channels in these two TVM-based segmentations, it was found that some channels were narrowed or even blocked by the rough surface. This morphological deviation caused by surface roughness plays a key role for the transportation properties, which will be discussed later in more detail.
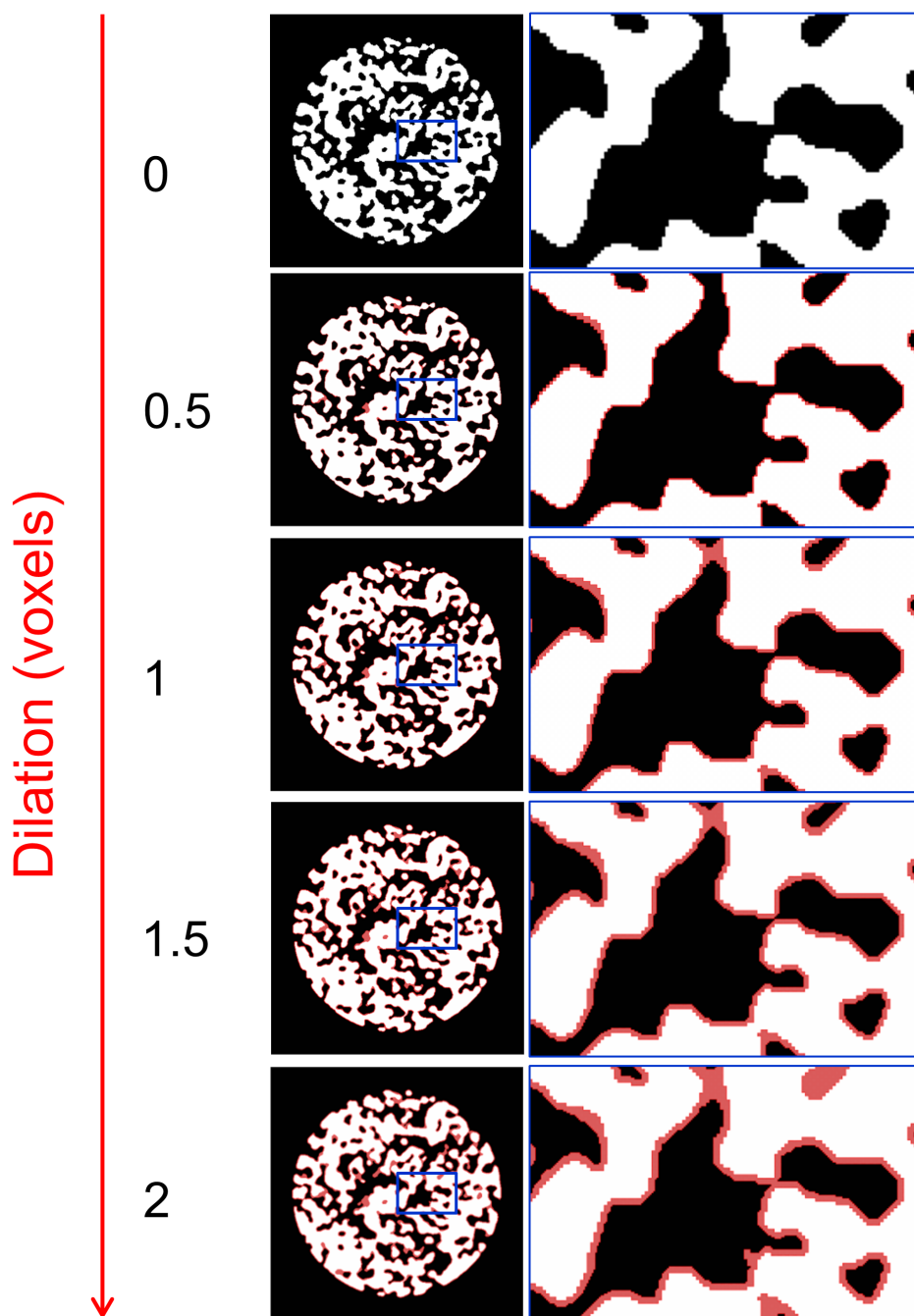
Figure 3.28: Representative slices of the 3d phantom before and after dilation by 0.5-2 voxels. The entire pore space is accessible for pointlike tracers, i.e., when dilating 0 voxel. In contrast, the accessible pore space is significantly reduced for finite-size tracers.

The diffusion properties were simulated for a set of point-like and finite-size tracers. The point-like tracers (tracer diameter is 0) have access to the entire pore space inside the 3D volume without steric interaction with the walls. However, not all pores are accessible for finite-size tracers due to steric effect, depending on the size of the object diffusing inside the pores. Some pores become "closed" due to the bottle-neck effect for finite-sized objects. The effective porosity is represented by the accessible instead of the geometric pore volume and the topology of the accessible pore network depends on the tracer size. The topological deviations of the pore space for finite-size tracers due to steric effects can be represented by dilating the solid space with the diameter $d_{tracer}/2$, since the pore space accessible to the center of a finite-size tracer becomes identical to the pore space accessible to a point-like tracer if the pore diameter is reduced by d_{tracer}. [11] The reduction of the accessible pore space for a set of spherical tracer particles with diameters of 1, 2, 3, and 4 voxels for the 3d phantom is shown in Figure 3.28, where narrow constrictions become inaccessible ('blocked') with increasing tracer size.

Figure 3.29 shows the dependence of accessible porosity on the tracer diameter and the differences in accessible porosity compared to the phantom reference. It is clear that the accessible porosity decreases monotonously with the tracer size for all reconstructions(Figure 3.28). However, the different reconstructions show noticeable differences in the relative accessible porosity compared to phantom. For point-like tracers, the accessible porosity mainly reflects the overall pore volume. However, for finite size tracers, the accessible porosity is sensitive to the local pore network structure. In case of SIRT and TVM_$\mu11\beta5$, the deviations from the phantom reference increase with increasing tracer diameter, presumably due to roughness introduced during the reconstruction as discussed below for the diffusion behavior. For TVM_$\mu10\beta9$, the deviations in
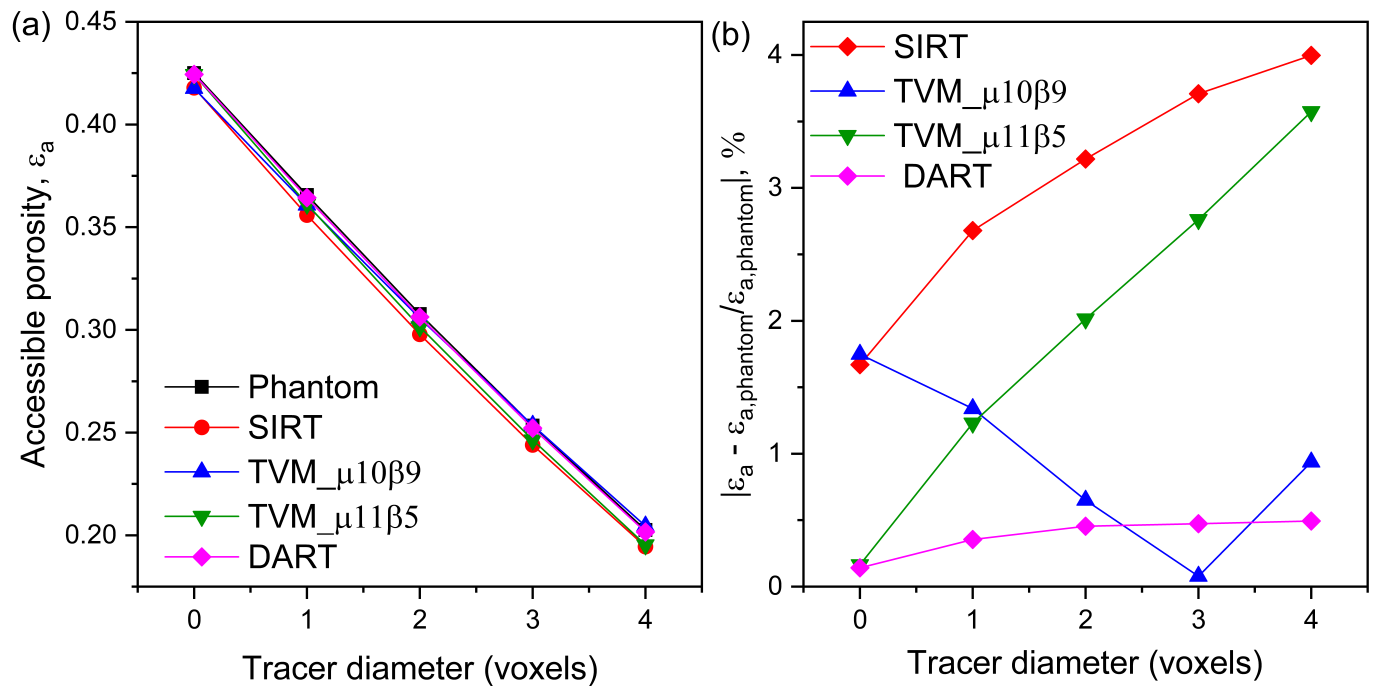
Figure 3.29: (a) Accessible porosity and (b) relative accessible porosity (using the phantom as reference) calculated from SIRT-, TVM-based segmentations and DART as a function of tracer diameter.

accessible porosity for point-like tracers are comparable to SIRT, fitting to their rNMP values (11.2% SIRT and 12.3% TVM_$\mu10\beta9$). With the stronger smoothing during the TVM_$\mu10\beta9$ reconstruction, the increasing tracer size does not lead to an increased difference in accessible pore volume (Figure 3.27). Overall, the smallest difference and dependence on tracer size was observed for the DART reconstruction, where deviations

of less than 0.5% were found for all tracer sizes, indicating the most reliable reconstruction not only for the pore space but also for pore network.

Similarly, a monotonic decrease in effective diffusion coefficient (D_{eff}) can be seen with increasing tracer size in Figure 3.30a. It can be seen that the D_{eff} determined from DART was closest to the ground truth of the phantom, whereas SIRT and the two TVM reconstructions deviated more. The difference between the reconstructions becomes clear when looking at the ratio of the effective diffusion constant D_{eff} for the phantom compared to the different reconstructions in Figure 3.30b. For point-like tracers the difference of the segmented SIRT and TVM reconstructions compared with the phantom is 5% and 2.6%. With increasing tracer diameter, the relative difference of the SIRT-based segmentation increases continuously. This increasing discrepancy is mainly due to reconstruction errors affecting the local pore connectivity, as shown in Figure 3.25a,d. Interestingly, the transport properties determined from the two TVM-based segmentations are noticeably different. The relative diffusion coefficients of TVM_$\mu11\beta5$ increase with increasing tracer diameter, similar to the diffusion behavior of the SIRT reconstructions, while the relative error of the diffusion coefficients for TVM_$\mu10\beta9$ is fairly constant regardless of tracer size. This difference is due to the aforementioned morphological deviation due to the surface roughness. As a rough surface leads to local size reductions of the pores, which become particularly important for small pores and necks between pores (Figure 3.27), this results in the diffusion rates of large tracers to be more hindered due to surface roughness introduced during
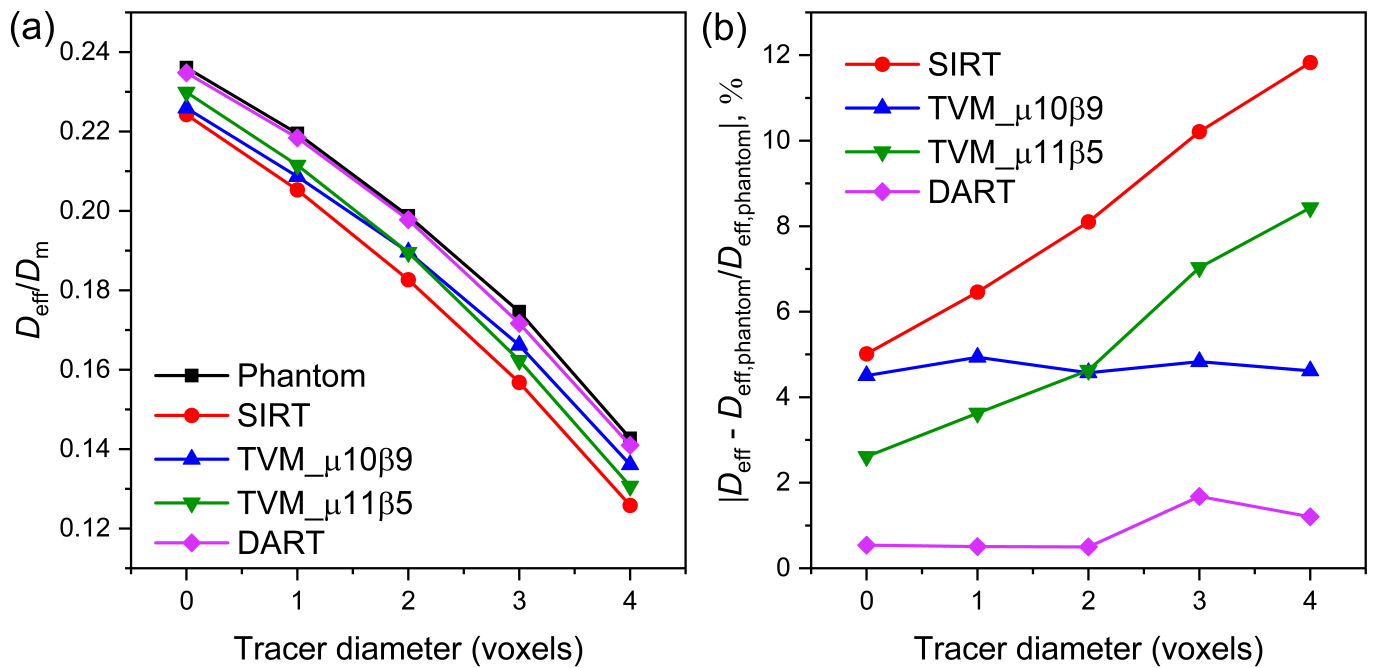
Figure 3.30: (a) Effective diffusion coefficients and (b) relative effective coefficients (using the phantom as reference) calculated from SIRT-, TVM-based segmentations and DART as a function of tracer diameter.

reconstruction. The larger β in the TVM_$\mu10\beta9$ reduces this surface roughness and therefore results in a better representation of the diffusion behavior in this reconstruction. In addition, the accessible porosity and the effective diffusion coefficient show a slightly different behavior suggesting, that the TVM_$\mu10\beta9$ reconstruction introduced some topological differences. As could already be seen in the accessible porosity, the DART reconstruction is much less affected by the tracer size. This is expected from the morphology (Figure 3.25c,f) and skeletonization (Figure 3.26) results, where the DART reconstruction resembles the phantom structure the most and retrieves accurately most of the pore connectivity with only small local variations.

The transport properties discussed above are based on the overall reconstructed volume, a directional dependence of the diffusion properties has not been considered. However, it has been demonstrated that missing wedge artifacts have an impact on the reconstruction quality in the different directions, resulting in a noticeable anisotropy of the diffusion coefficient along the three main directions of the volume. This anisotropy is strongly reduced in the DART reconstruction compared to SIRT. [12] However, as this has been addressed previously, the anisotropy is not considered here.

3.3.5. Parameter optimization for DART reconstruction

It has been shown that the parameters used for the different algorithms can significantly affect the reconstruction and segmentation (Figure 3.3 to Figure 3.8). To explore the fundamental influence a parameter optimization has for different models is thus another point of interest for practical application without knowl-
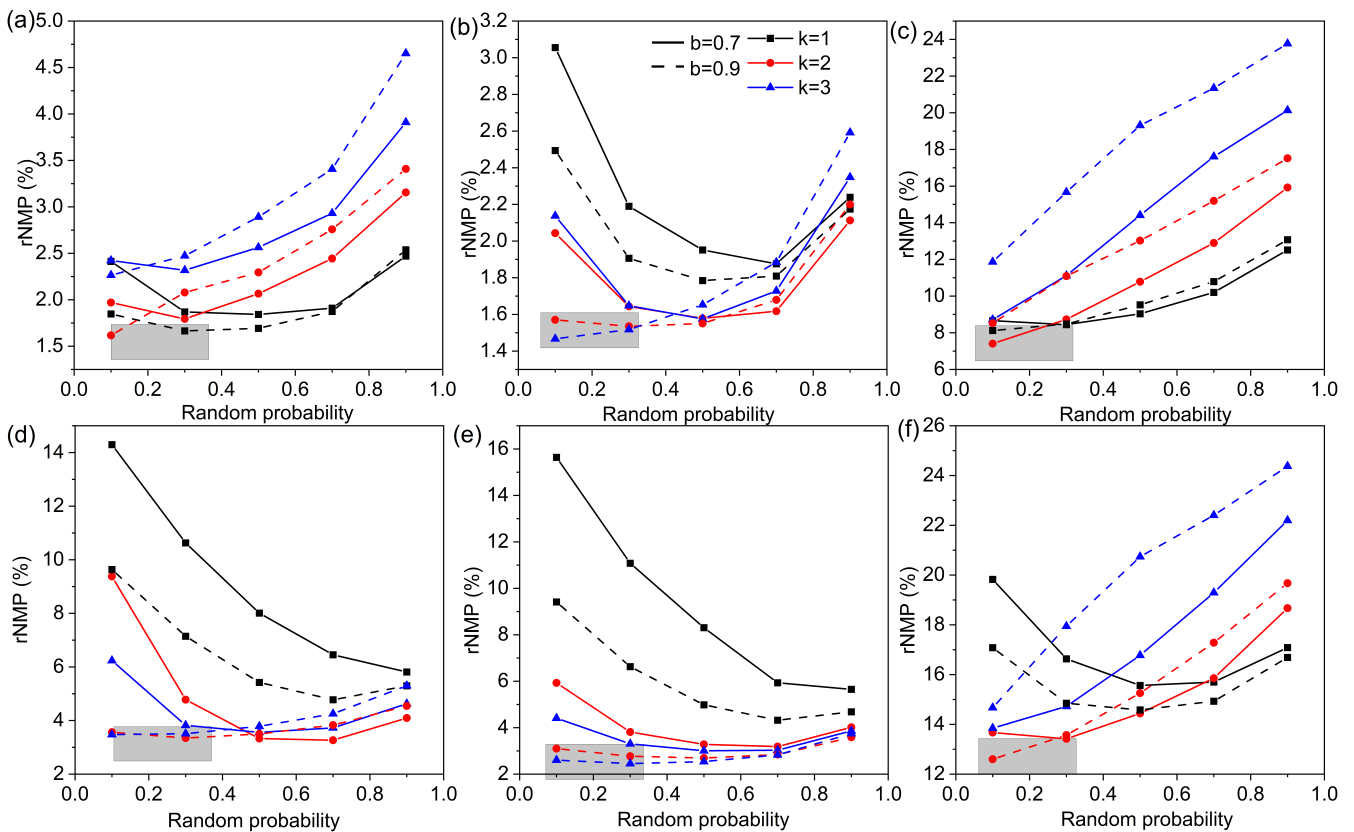
Figure 3.31: rNMP as a function of random probability, smoothing kernel k and smoothing radius b for three different 2d phantoms (a,d) the phantom in Figure 3.11a, (b,e) the phantom in Figure 3.14a and (c,f) the phantom in Figure 3.9a for different Poisson noise levels: (a-c) 1600 counts and (d-f) 400 counts in the DART reconstruction.

edge of the ground truth. As DART is superior to SIRT and TVM for the reconstruction of mesoporous structures, the evaluation of the parameter optimization was focused on the DART algorithm. Figure 3.31 shows the dependence of rNMP on a variety of parameters for three 2D phantoms with significantly different pore structures at two noise levels for the DART reconstruction. Although the effect of the parameter varies for different phantoms, the optimal parameters for comparable noise levels turn out to be in a similar range.

As indicated in the highlighted region of Figure 3.31, the lowest rNMP of all models is always achieved by a random probability ranging from 0.1 to 0.3, regardless of noise level. Given the noise level, the high-noise models (Figure 3.31d-f) show the least rNMP with a smoothing kernel of 2 or 3 and a smoothing radius of 0.9. In contrast, a smaller smoothing kernel of 1 or 2 is preferred with the same smoothing radius of 0.9 for moderate-noise levels in case of disordered pore structures (Figure 3.31b-c). Overall, this behavior reflects the fundamental role of the different parameters and most likely this observation can be extended to experimental studies with similar structures, if the noise in the raw data can be evaluated.

3.4. Conclusion

In this work, the tomographic reconstruction accuracy achievable by three commonly used algorithms (SIRT, TVM, DART) has been evaluated for mesoporous materials considering the most critical parameters for tilt series acquisition such as noise, missing wedge and number of projections based on a series of 2D and 3D phantom simulations, which also included realistic misalignment effects. Parameters that have a strong influence on the final reconstruction have been surveyed for each algorithm and optimized by minimizing the relative number of classified pixels using the phantom as the ground truth. The 2D simulations have shown that the fidelity of the reconstruction of mesoporous structures strongly depends on data acquisition parameters such as tilt step and tilt range, noise level in the raw projections and the reconstruction approach used. However, structural features like pore shape and pore size variations also play an important role for the reconstruction. Large pores are always reconstructed more easily with high accuracy while a faithful reconstruction of small isolated pores with narrow channels between them is a challenge using classical algorithms (SIRT and TVM). The systematic error in the tomographic reconstruction is thus composed by the limits in data acquisition on the one hand and the influence of structural features of the measured object on the other hand. With this, a systematic parameter optimizing enables an objective evaluation of these three algorithms. In addition, although it is convenient to evaluate the reconstruction quality by the rNMP using the phantom as ground truth, this evaluation criterion is too simplified and does not necessarily represent the general systematic errors for parameters derived from the reconstruction. For example, the quantitative analysis of porous structures usually focuses on the geometry and topology of pores, where pore diameter, length, tortuosity and coordination numbers are measured from a segmented volume. In such cases, randomly distributed misclassified pixels are unlikely to have a substantial impact on the final statistical results.

One interesting finding for DART is its insensitivity to the initial reconstruction. A more reliable initial reconstruction only speeds up the convergence, but hardly improves the final reconstruction accuracy. The overall finding is that all three reconstruction algorithms provide a reasonable accuracy for the basic morphological description and the determination of diffusion properties of porous materials with systematic errors below 5% and, even in the presence of realistic noise, the errors are on the order of 10% or less. Nevertheless, there are significant differences between the reconstruction accuracy of the different algorithms. DART turned out to provide the most accurate reconstruction of the three algorithms with mainly slight randomly distributed errors in the reconstruction even in the presence of a typical missing wedge and realistic noise settings. In particular, small isolated pores and narrow channels are reconstructed well. SIRT- and TVM-based reconstructions result in segmented volumes with a noticeably higher rNMP and, moreover, these errors are not randomly distributed but tend to cluster leading to a breakup of structural features and a loss of small pores/necks and therefore have a stronger effect on the morphological and diffusion properties. In particular for extended tracers, the resulting surface roughness and additional blockages lead to increases in the error for diffusion rate estimates. An interesting point here is also that the structure with the lowest rNMP value does not necessarily lead to the best diffusion estimate for extended tracers.

Considering the practical application of electron tomography to solve experimental mesoporous structures without knowledge of the ground truth, a systematic reconstruction parameter analysis for DART, as the most promising algorithm, indicates that noise level and a rough estimate of the structural sizes are the most important aspects to define the best reconstruction parameters. Based on the modeling tests, the parameters should be transferable to experimental data sets suggesting that a similar accuracy in experimental work can be maintained as in the phantom investigations.

4. Precisely Picking Nanoparticles by „Nano-scalpel" for 360° Electron Tomography

This chapter is reorganized from 'X. Huang, Y. Tang, C. Kübel and D. Wang, Precisely picking nanoparticles by „Nano-scalpel" for 360° Electron Tomography' published in *Microscopy and Microanalysis* (DOI: https://doi.org/10.1017/S1431927622012247).

4.1. Introduction

Electron tomography has gained increasing attention for the 3D characterization of nanoparticles, but the missing wedge problem due to a limited tilt range is still a challenge for accurate reconstruction in most experimental transmission electron microscopy (TEM) setups. Many efforts have been tried to solve the missing wedge problem, falling roughly into two categories: advanced reconstruction algorithms and improved data sampling. The algorithmic aspects using prior knowledge of the specimen to make an informed guess at the missing information, such as TVM and DART, has been mentioned in Chapter 3. Advanced algorithms can in paint missing wedge artifacts to a certain extent but cannot recover the missing structural information completely.

360° ET provides an option to solve this problem fundamentally by tilting a needle-shaped specimen over the full range. In addition, even with advanced algorithms, the quality improves by using a full tilt series. However, sample preparation, especially for fine powders, is still challenging as the specimens are required to be mounted on a needle/rod shaped tip. Most reported works were using a FIB to extract and mill the specimen into a needle geometry [163], [165], which is not suitable for nanoparticles and other fine powders. Other methods such as dispersing nanoparticles in solution on a modified tip [134], [135] or using carbon nanofibers as bridge to connect powder specimens and holder tips [136] suffer from shadowing problem and are not suitable to select specific particles of interest. Another method the so-call 'stamp' method, [137], [138] enables in situ transfer of a single selected particle from a suitable substrate onto a tailored tip by using a SEM/FIB instrument equipped with a suitable micromanipulator. However, several shortcoming of this technique, such as the requirement of a special micromanipulator, risk of shadowing, inability to select ultrafine nanoparticles smaller than 10 nm and only one particle or particle assembly that can be attached to the tip each time, hamper its application. Therefore, a robust preparation method, which enables precise picking of selected nanoparticles, so that they are completely visible in TEM more or less independent of the tip size, is of great interest for many electron tomography applications.

In this work a new sample preparation method that enables the transfer of a selected individual nanoparticle or a few separated nanoparticles has been proposed. With a piece of carbon film, specimens can be mounted onto a full range tomography tip with the help of an easily prepared tungsten tip. Since the selected particles are left intact on the original carbon film and they are not attached to the tip directly, it allows picking ultrafine

nanoparticles without size limitation, avoiding the risk to damage the sample and making them accessible for full range electron tomography. This method is demonstrated by one example of Pt nanoparticles supported on a TiO$_2$ hollow cage support [204], which enhances the catalytic stability of the particles due to its special hollow structure. The hollow cage structure with a size of $\sim$100 nm is suitable to show the reconstruction improvement of the cage walls in the missing wedge direction. Such delicate material with fine structures was successfully prepared by this method, yielding a high quality tomographic reconstruction without missing wedge effects.

4.2. Preparation of tungsten tip

The tungsten tip was prepared using an electrochemical etching method, which has been proven to be an inexpensive, fast and reliable way to fabricate extremely sharp tips [205]–[207]. A simple setup for the etching equipment is shown in Figure 4.1. Typically, a 1 mm diameter tungsten wire (purchased from Agar scientific company) is dipped into a sodium hydroxide (NaOH) electrolyte and biased so that etching starts at the air/electrolyte interface and progresses into the immersed tungsten wire. The DC bias used in this work was around 8 V and a threshold current set to 0.2 A to control the drop off process. During the etching, necking occurs below the air/electrolyte interface and, when the weight of the wire below the neck exceeds the tensile strength of the thinnest part, the bottom piece drops off. Ibe et al. [208] showed the electrochemical reactions as follows:

$$\text{Cathode: } 6\,H_2O + 6\,e^- \longrightarrow 3\,H_2(g) + 6\,OH^- \tag{4.1}$$

$$\text{Anode: } W_{(s)} + 8\,OH^- \longrightarrow WO_4{}^{2-} + 4\,H_2O + 6\,e^- \tag{4.2}$$

$$\text{Overall: } W_{(s)} + 2\,OH^- + 2\,H_2O \longrightarrow WO_4{}^{2-} + 3\,H_2(g) \tag{4.3}$$
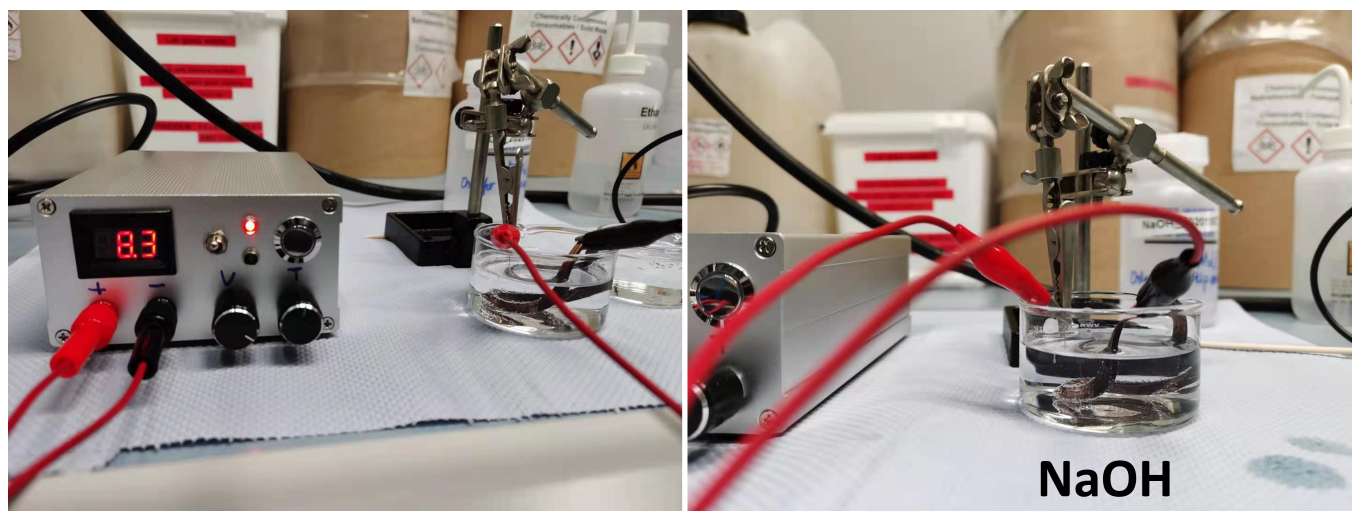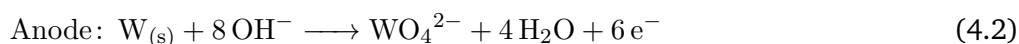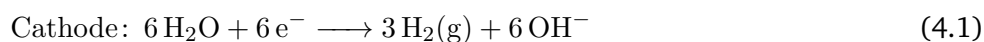
Figure 4.1: Tungsten tip preparation by electrochemical etching.

The whole process takes around half an hour. In this way, tips with a diameter of a few hundred nanometers can be prepared. In order to get even sharper and smaller tips, one can lift the tungsten wire a little bit from the electrolyte surface half way during etching, while there is still enough tungsten tip submerged into the

electrolyte so that the drop off can occur at the gradually thinner part. The resulting tips are shown in Figure 4.2, where the diameter of the etched tips can be reduced to a range of 30-200 nm.
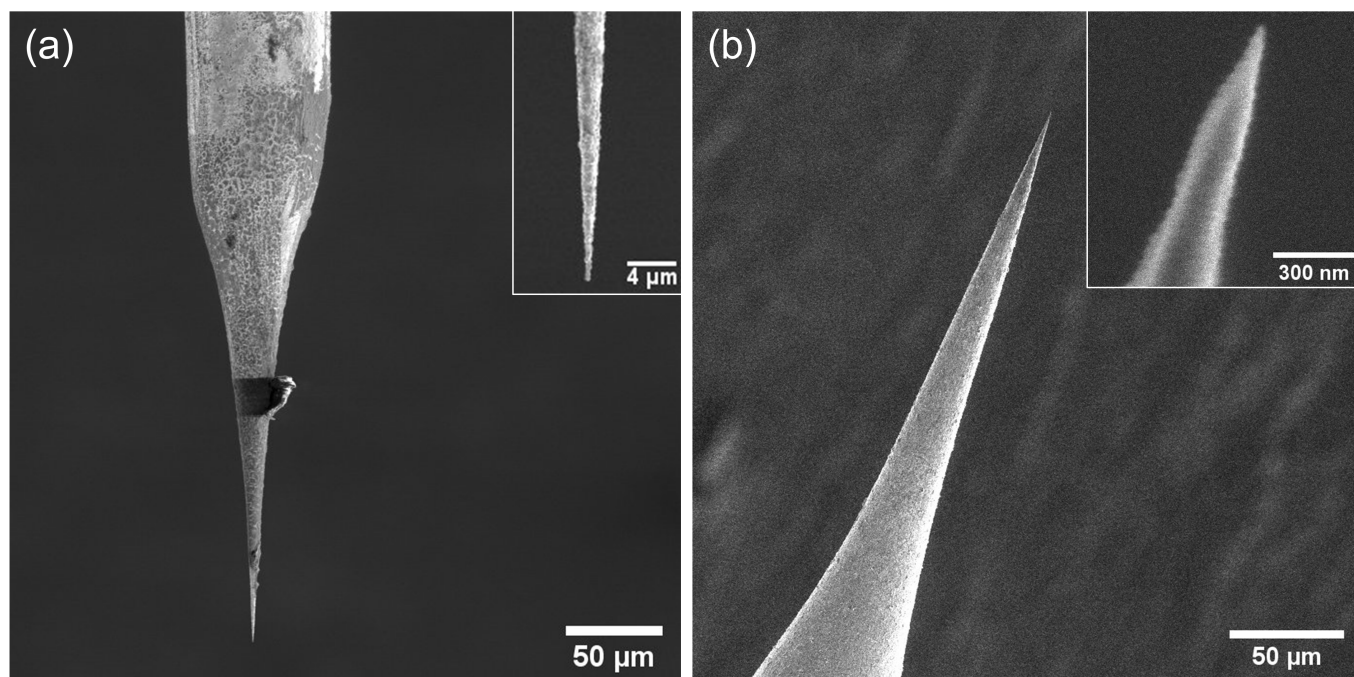
Figure 4.2: Scanning electron micrographs of etched tips.

4.3. Specimen selection

The dry Pt@ hollow TiO$_2$ powder was dispersed in ethanol and drop casted on carbon coated copper TEM grids (Quantifoil Micro Tools GmbH) with a supporting film thickness of 10-20 nm. Afterwards, the grid was kept under a warm lamp for 10 minutes to dry completely. Fiducial Au nanoparticles (6.5 nm diameter) were added to the grid from suspension and dried for another 30 min. The prepared grid was examined in a Themis 300 microscope (Thermo Fisher Scientific) and the ROI was determined and labeled by identifying the particles in TEM images at different magnifications, as shown as Figure 4.3. Using a so called "finder grid" is of great convenience for locating and labeling, though not necessary. This step can be also performed directly in an advanced SEM equipped with a STEM detector.
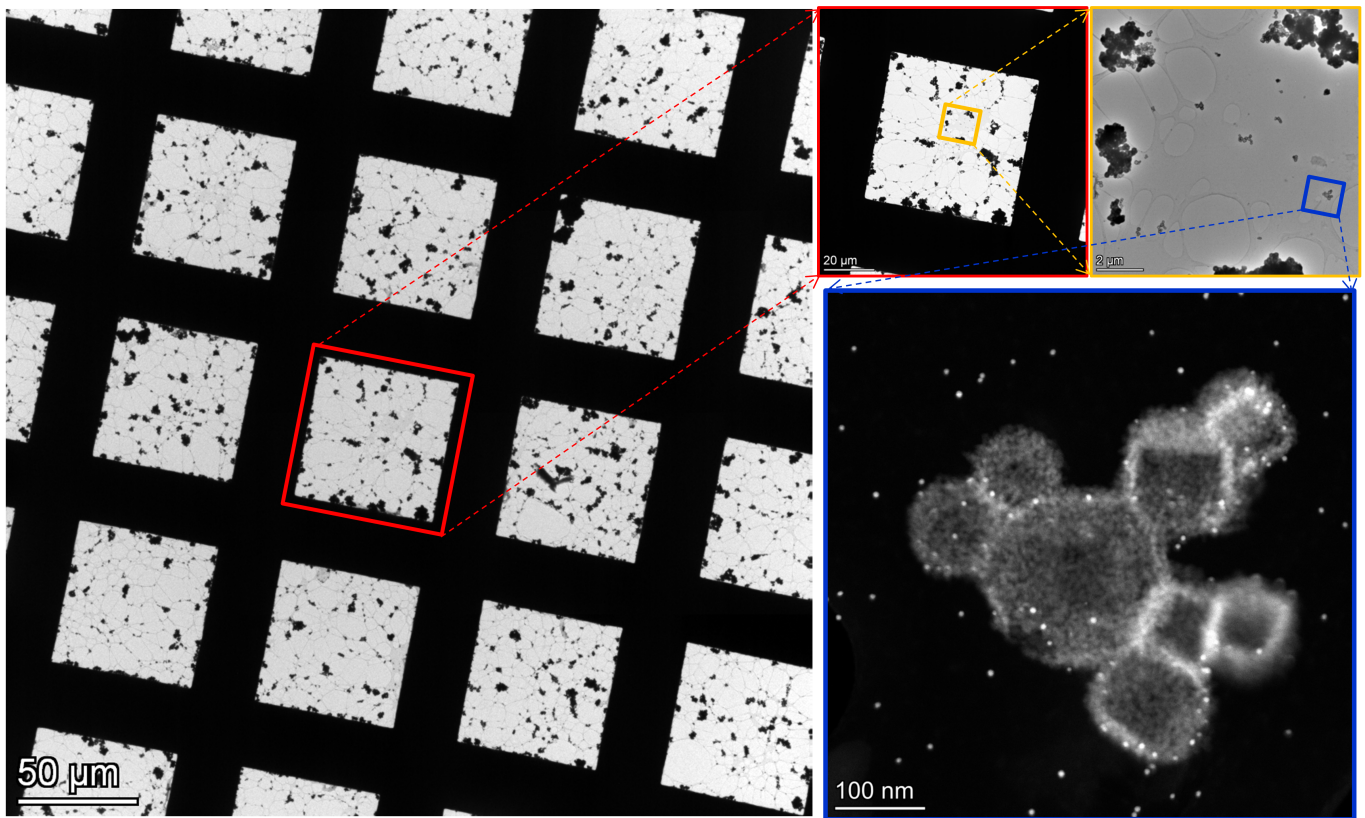
Figure 4.3: Region of interest selection from TEM.

4.4. Specimen transfer to 360° tomography tip

Once the ROI has been determined by TEM at sufficiently low magnification (e.g. ~130 x), it is easy to precisely navigate to the same location in the SEM. In this work, a dual-beam FIB (FEI Strata 400S) equipped with an OmniProbe 200 micromanipulator (Oxford Instruments) was used for the particle picking and in situ lift-out. The FIB is equipped with a GIS for Pt, C and W. All Pt contacts and the patches for welding the tungsten tip to the omniprobe and to the tomography tip were made by ion-beam-induced decomposition of a Pt metalorganic precursor (trimethyl(methylcyclopentadienyl)platinum: $C_5H_4CH_3Pt(CH_3)_3$) from the GIS system at 30 kV accelerating voltage with an ion-beam current of 0.92 nA. To reduce the electron/ion-beam-induced Pt contamination, both the electron and ion beams were switched off for a few minutes after Pt deposition until the residual Pt precursor gas molecules were fully pumped out and the chamber vacuum returned to a pressure lower than 10^{-6} mbar. The lowest ion-beam current of 1.5 pA at 30 kV was used for cutting the carbon film. To avoid ion beam damage, all scanning was preferentially performed using only the e-beam at 5 kV acceleration voltage and 98 pA current to track the sample and correct its drift.

Figure 4.4 shows the whole process of particle picking and mounting on a 360° tomography holder. First, a sharpened tungsten tip was welded to the omniprobe by Pt deposition at a position around 20 μm from the sharp tip. Afterwards, the tungsten tip was cut at the thicker part, around 30-40 μm from the top, by a high ion-beam current (2.8-21 nA), depending on the diameter of the tungsten tip typically in a few tens of seconds (Figure 4.4a). For instance, for a tungsten tip with a diameter of ~10 μm it typically takes around 5 minutes

to cut the tungsten tip using a 2.8 nA ion current or ∼20 s using a 21 nA current. Similarly, throughout this work, 10-20 s of ion-beam-induced Pt deposition was enough to weld the tungsten tip for reliable lift-out. The next step is to pick up nanoparticles from the TEM grid using the tungsten tip that has been attached to the micromanipulator. One important aspect is the positioning of the tungsten tip, the TEM grid and the 360° tomography holder tip in the FIB. A picture of the prepared FIB stage is shown in Figure 4.5.
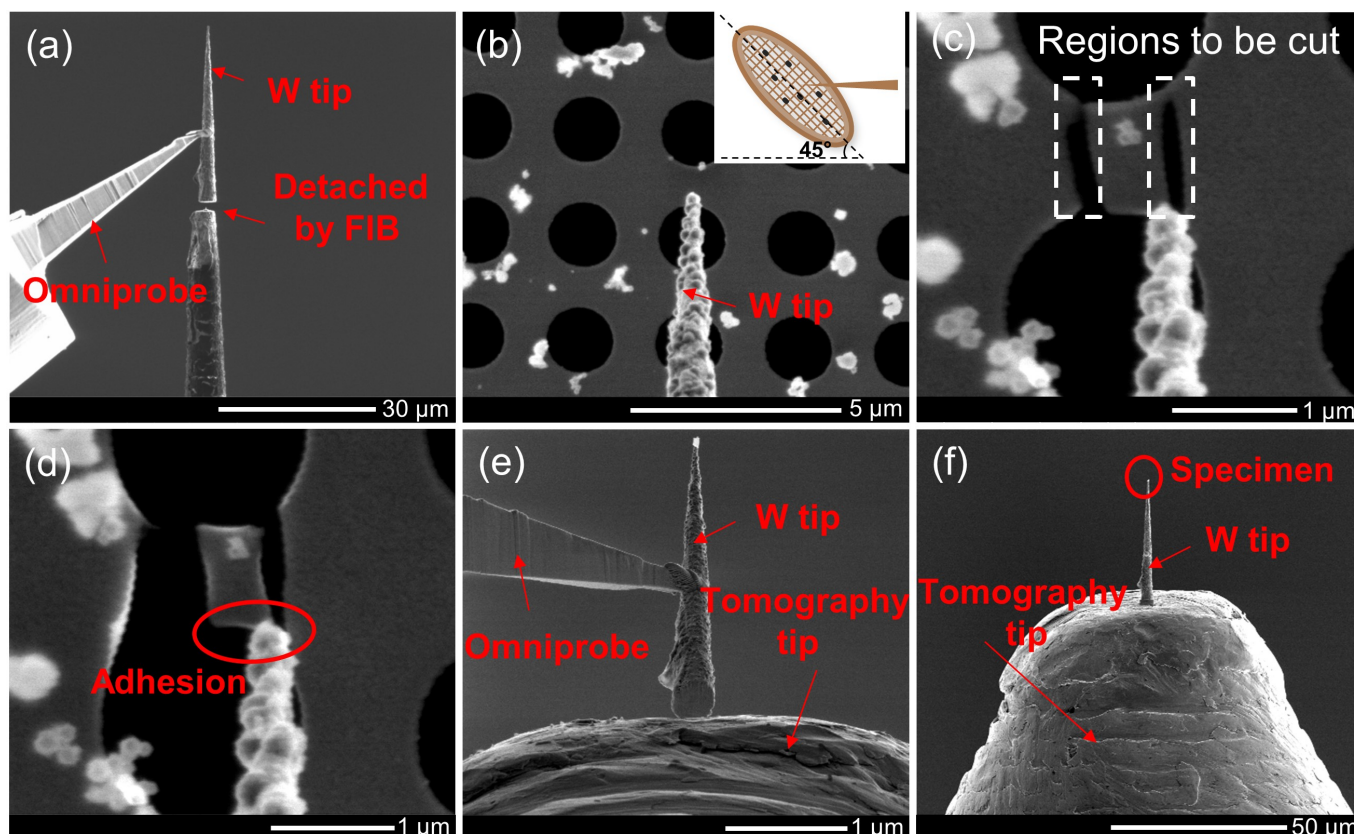
Figure 4.4: The processes of nanoparticle picking and mounting onto tomography holder tip in FIB.

Mounting of the tungsten tip to the manipulator was performed at 0 degree stage tilt (horizontal) and without changed during the following processes. To make sure the nanoparticle picking can be performed smoothly, it is better to approach the TEM grid with the tungsten tip at a certain angle, as shown in the inset of Figure 4.4b. This can be achieved by loading the TEM grids on a tilt holder at an angle of around 50°. Another advantage of leaving an angle between the tungsten tip and TEM grid is to avoid that the end of the tungsten tip touches the edge of the TEM grid, which will rip it off the manipulator.

The next step is cutting the carbon film. For holey or lacey carbon film, generally particles sitting close to the edge of a hole are preferred so that the tungsten tip can easily touch the edge of the carbon film and less cutting is needed. To ensure that the carbon film will not bend too much during the cutting process, the following approach was used before the tungsten tip was brought into contact with carbon film. Initially, two parallel cuts were made in the film. On one side, the two cuts went fully through the edge of the area of interest (lower edge in Figure 4.4c) and, on the other side, two corners were left intact to maintain the connection to the main film (upper edge in Figure 4.4c). Afterwards, the tungsten tip was approached smoothly by controlling the manipulator to attach the side where the carbon film was already free (Figure 4.4c). It is worth noting that the carbon film can be firmly adhered to the tungsten tip only through electrostatic forces
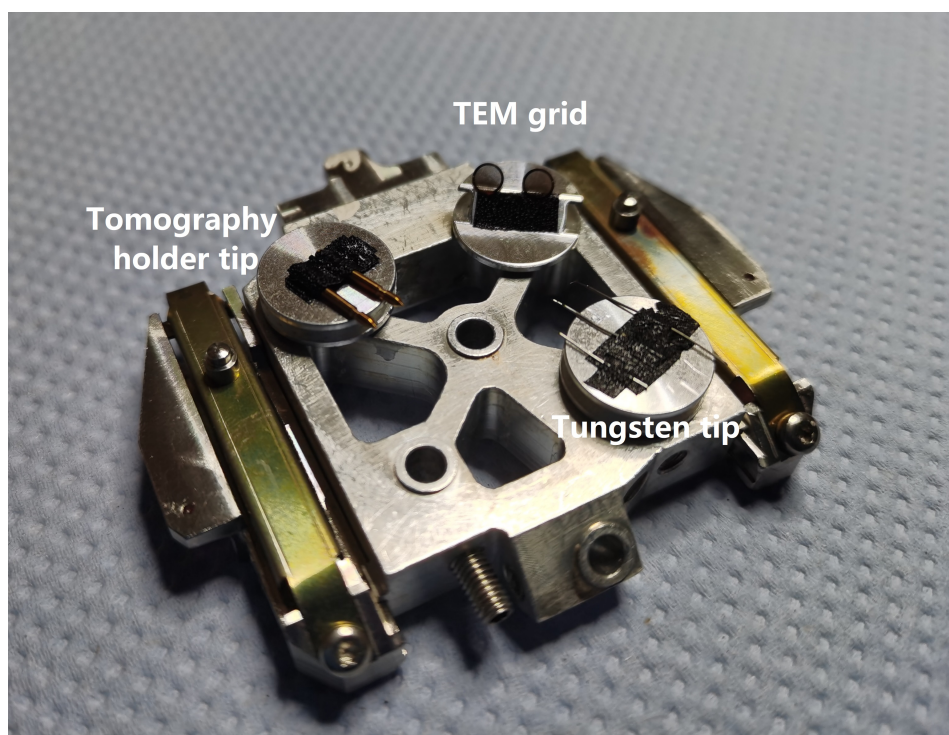
Figure 4.5: Initial FIB stage setup with tungsten tip, TEM grid and 360° tomography holder tip loaded on it.

without Pt deposition, which avoids Pt contamination. Right after the last cut freed the two corners, the film stayed completely flat, supported by the tungsten tip only through a small contact area (Figure 4.4d). Moreover, to reduce ion beam damage to the carbon film as well as to the nanoparticles, the entire transfer process was controlled only by using the electron beam, whereas the selected particles were never exposed to the ion beam. Limited dose of ion beam was only applied to the areas being cut (as highlighted in Figure 4.4c), which was kept at a certain distance from the particles. Different types of commercial TEM grids coated with carbon film were tested, including 100×400 mesh complete carbon film and 200 mesh holey carbon film with patterned holes from Quantifoil and 200 mesh lacey carbon film. All of these carbon films can be successfully cut without noticeable bending as shown in Figure 4.6.
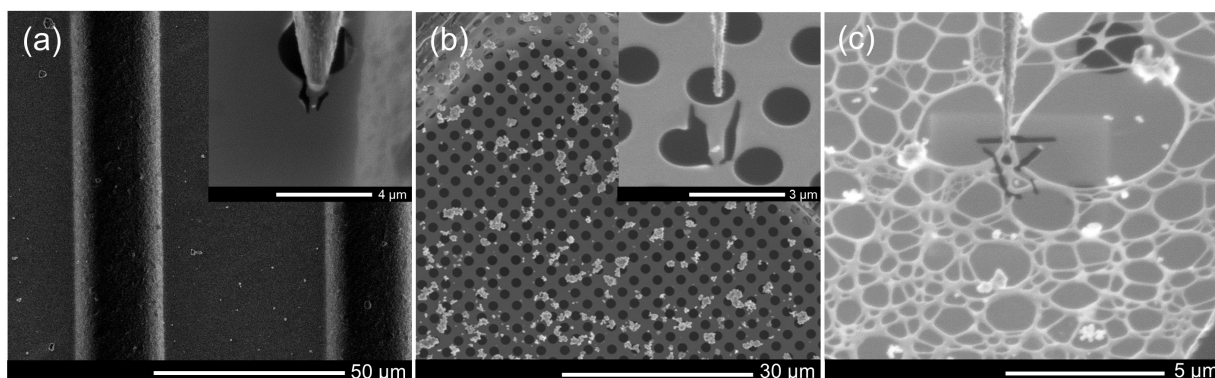
Figure 4.6: Three commercial TEM grids covered by different carbon films including (a) 100×400 mesh carbon film (thickness: 10-20 nm), (b) 200 mesh holey carbon film (thickness: ∼ 12 nm) with patterned holes and (c) 200 mesh lacey carbon film (thickness: ∼ 20 nm) with irregular holes.

After successful preparation procedure, a rectangular carbon film ($\sim 300 \times 500$ nm^2) with the nanoparticles of interest at the center was attached to the tungsten tip and cut free. The tungsten tip with the carbon film was subsequently transferred and welded onto the $360°$ tomography holder tip by depositing a few Pt patches with an ion-beam current of 0.46 nA (Figure 4.4e). One main advantage of leaving the W tip on the omniprobe during the transfer is a reduced Pt contamination on the carbon film, as there is sufficient distance between the wedding position and the carbon film for the ion-beam-induced Pt deposition. The last step is to release the micromanipulator by cutting the junction of Pt patches with an ion-beam current of 93 pA, resulting in a tungsten tip, holding a piece of carbon film with the nanoparticles of interest, sitting on the top of tomography holder tip (Figure 4.4f). This tip can then be transferred to the TEM for tomographic measurements with a full tilt range. The overall transfer procedure of particles from a TEM grid to a $360°$ ET holder tip using a FIB system is summarized schematically in Figure 4.7.
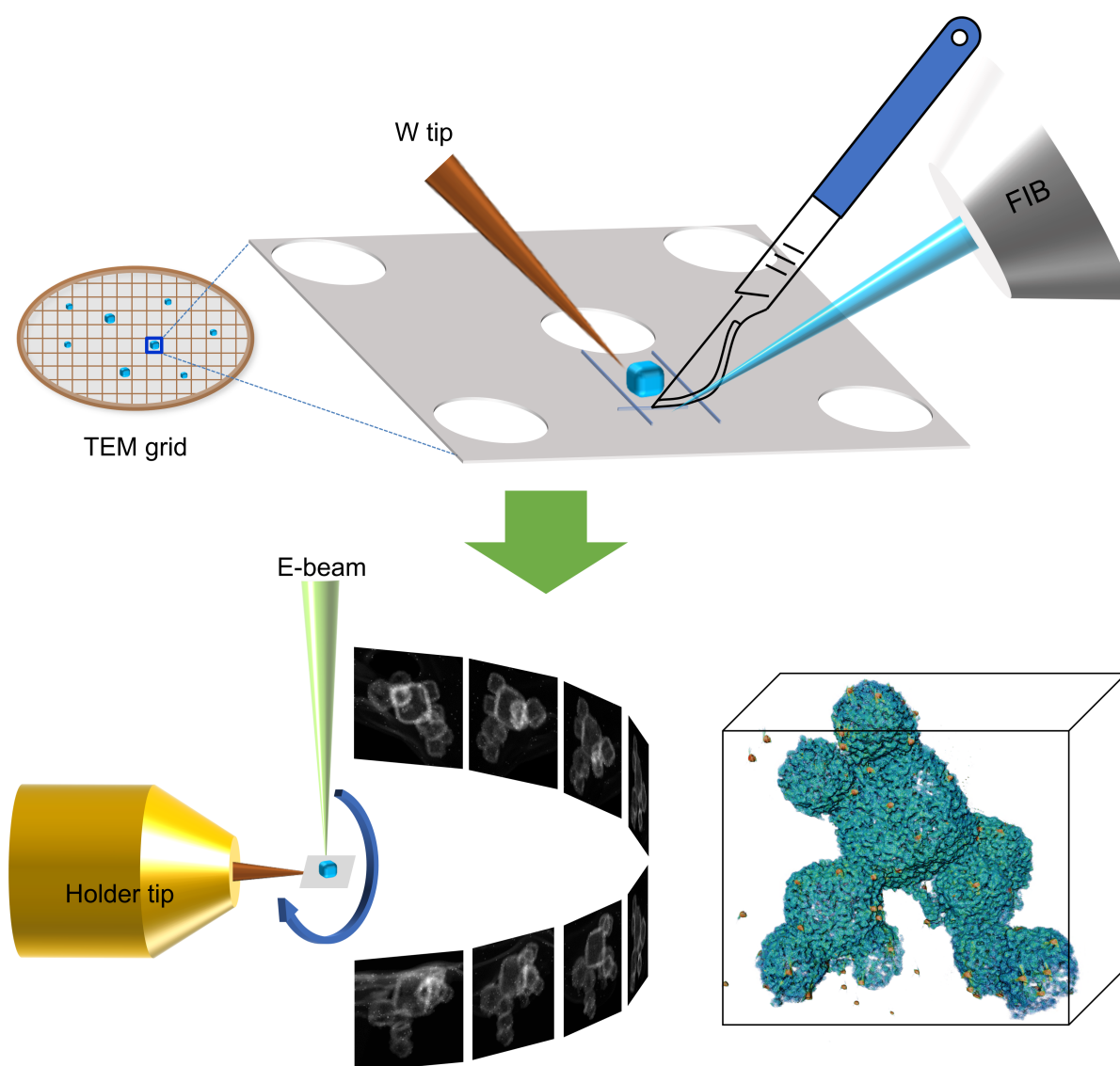
Figure 4.7: Schematic of particle pick up and amounting to a $360°$ ET holder tip using a FIB system.

Reviewing the overall process of the proposed method for particle picking, a number of advantages stand out immediately. First, no special manipulator is needed since the picking process can be implemented in a conventional FIB instrument compared to the reported 'stamping transfer' method [137]. Thus, it can be employed in any laboratory equipped with a standard FIB system. In addition, this method is fully compatible with conventional TEM sample preparation of powders as suitable particles or aggregates can be conveniently selected in TEM or SEM and the sample is then transferred to the W tip together with a piece of C film. Since a small piece of carbon film remains on the tungsten tip, not only single particles or aggregates can be precisely picked up, but a few particles suitably distributed can also be selected and measured at the same time. This is helpful especially for studies that focuses on the shape of anisotropic nanoparticles, whose properties depend on their specific anisotropic shape and the exposed surface facets [209], [210]. Moreover, the selected particles are sitting on the carbon film instead of touching the tip directly, avoiding any mechanical damage to the sample caused by a collision at the specimen and the tip. Such a "touching" might have significant influence on fragile materials such as porous materials since it could easily result in cracks caused by mechanical damage in addition to the intrinsic pores of the raw material. Another important advantage is the possibility of picking ultrafine nanoparticles. In principle, particles of any size seen on the carbon film can be selected.

One of the major concerns with this sample preparation method for 360° tomography is potential Pt contamination and additional electron and ion dose for sample searching and further FIB/SEM processing. With the optimized procedure, the carbon film with the selected sample was attached to the tungsten tip without using Pt deposition. Only afterwards, during the process of welding the tungsten tip to the 360° tomography needle, there is a minimal risk for Pt contamination to the area of interest. This contamination can be avoided using a sufficiently long tungsten tip (30-40 μm) to increase the distance between the sample and the welding region. EDS maps and the spectrum shown in Figure 4.8 were acquired from a sample area after finishing the preparation. It can be seen that the Pt signal is well below the detection limit. It is inevitable that extra electron dose is needed to determine the area of interest and to monitor the tungsten tip manipulation in the FIB. However, the electron dose is carefully controlled in the TEM by applying low current (<100 pA) and imaging at low magnification for searching. In the FIB/SEM, a similar electron beam current is used just enough for identifying and locating at a low accelerating voltage of 5 kV. Therefore, the extra dose is low compared to the total dose used for tilt-series imaging acquisition. For beam sensitive materials, consideration of the total dose in tilt series acquisition is in principle not different from conventional tomography with limited tilt-angle range. The dose for image acquisition, tracking and focusing throughout the tilt steps are still the critical aspects to be considered for reasonable dose control. Nevertheless, it is always recommended to reduce the beam exposure for such specimens to reduce beam damage as some of them, such as single layer graphene, are easily damaged by the ion beam even at very low beam currents. [211] It is also worth noting that, in the case where ionization is the main damage mechanism, the influence from a low voltage (such as 5kV) in the SEM is more critical compared to 300kV in the TEM.
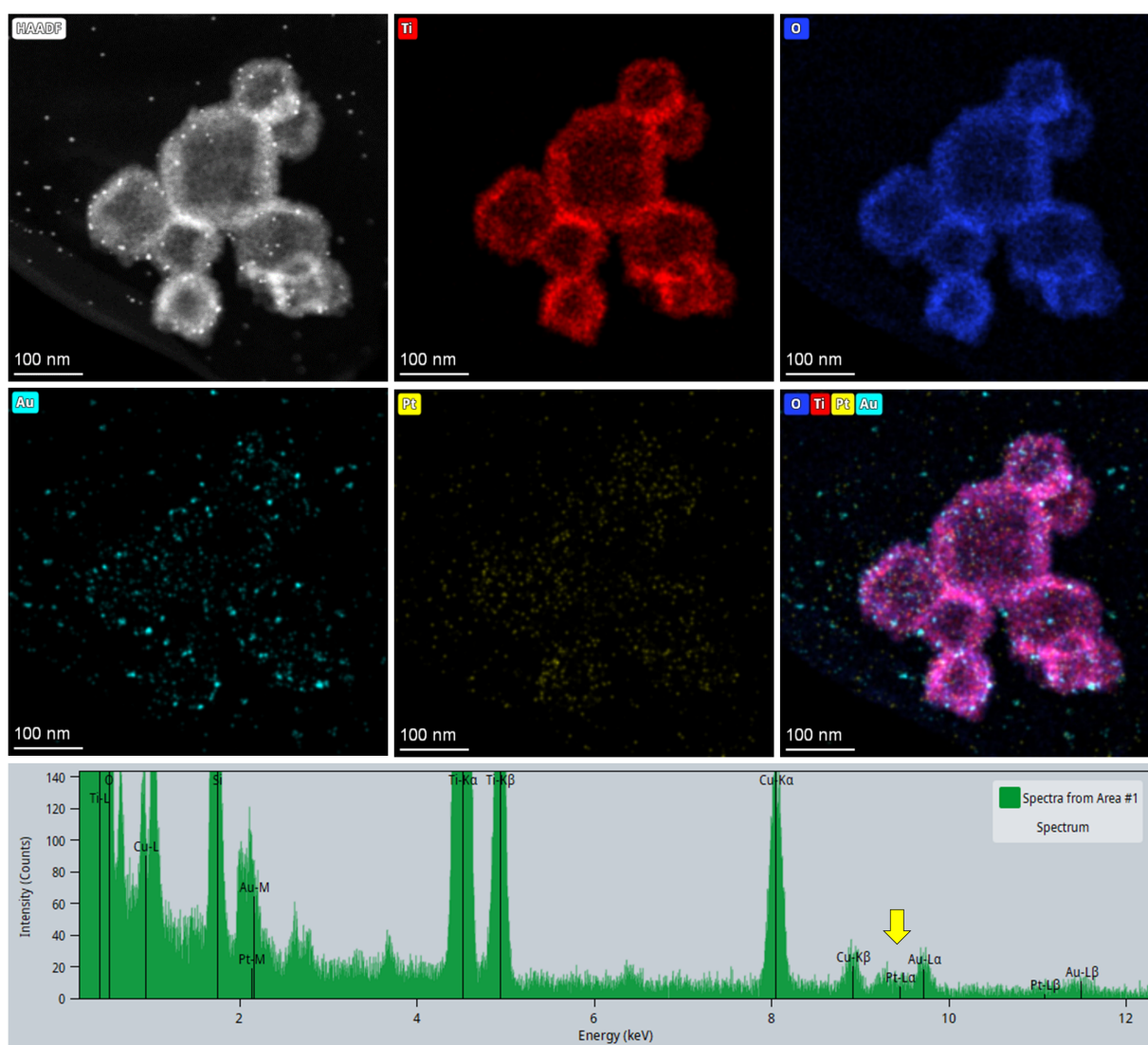
Figure 4.8: EDS maps and spectrum acquired from the sample area after finishing the preparation.

4.5. Electron tomographic measurement

The electron tomographic measurement was performed using a Fischione 2050 on-axis rotation tomography holder (E.A. Fischione Instruments, Inc., Export, PA, USA) on a Themis 300 TEM (Thermo Fisher Scientific) operated at an acceleration voltage of 300 kV in STEM mode. A semi-convergence angle of $\sim$8 mrad was used to provide sub-nanometer resolution while still keeping a relatively large focal depth. HAADF-STEM tilt series with image dimensions of 2048$\times$2048 pixels with a pixel size of 0.23 nm were collected using the Xplore3D software (Thermo Fisher Scientific) with auto focus and tracking before acquisition. At each projection, a STEM image was acquired with a dwell time of 6 μs and a total acquisition time of 27.8 s. The full-range tilt series was achieved by tilting the stage over a certain range in combination with a manual rotation of the holder by 90°. At both holder rotation positions, tilt series images were recorded with 2° interval from -50° to +50°, to avoid the imprecision of the manual holder rotation and to ensure full coverage of the angular range.

The two-tilt series were combined after removing one set of overlapped images and adding the angular offset, 90 degrees, between the two half series, leading to a full range tilt series consisting of 91 images. During tilt-series acquisition, no detectable morphological changes caused by electron beam damage were observed. Alignment of the tilt series was performed in IMOD [212] using the colloidal Au particles as fiducial markers. Before reconstruction, the aligned series was binned by two, resulting in a pixel size of 0.46 nm. Finally, the tomograms were reconstructed using the SIRT algorithm with 100 iterations implemented in Inspect 3D (v4.4, Thermo Fisher Scientific). 3D volume rendering was performed in Avizo 2020.2 (Thermo Fisher Scientific).
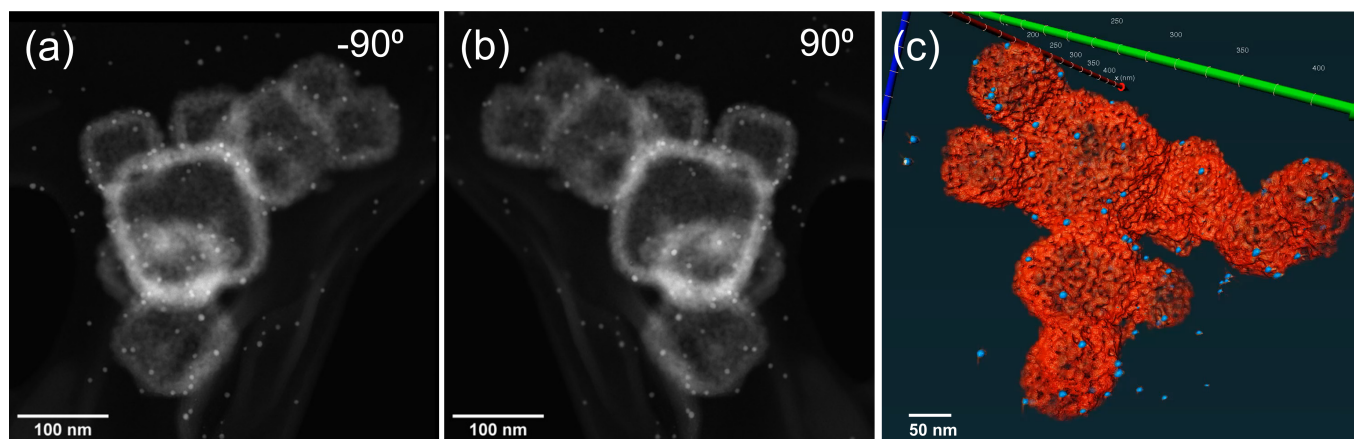
Figure 4.9: Projections at (a) -90°, (b) 90° and (c) volume rendering of the reconstructed Pt@hollow TiO$_2$

Figure 4.9 shows two projections taken at -90° and 90° tilt with the front and back view of some hollow cube-shaped particles and 3D volume rendering. Representative xy, xz, and yz slices of the reconstruction from the full tilt-range are shown in Figure 4.10a-c with the x-axis parallel to the tilt axis. The wall of the hollow nanocages can be clearly seen, which consists of an assembly of TiO$_2$ nanoparticles with diameters of around 10 nm, resulting in an interparticular space constituting an open 3D mesoporous network. From the slice in yz orientation (Figure 4.10c), no visible elongation artifacts caused by a missing wedge are observed, demonstrating the high-quality 3D reconstruction that has been achieved. For comparison, two reconstructions from limited tilt ranges of $\pm70°$ (Figure 4.10d-f) and $\pm60°$ (Figure 4.10g-i) from the same aligned series are shown. As expected, the reconstructed xy slices from these three reconstructions are fairly similar. However, the contrast from the limited tilt-range series is slightly weaker compared to the full tilt-range series even in the xy slices (Figure 4.10a,d,g). Moreover, the reconstruction quality was reduced in xz direction for the limited tilt-range series, where the particles were reconstructed with much lower intensity compared to the full tilt series and, the most severe problem is that some TiO$_2$ particles are hardly visible in the slices (Figure 4.10e,h) due to the missing wedge. Strong elongation artifacts caused by missing wedge are obvious in the yz slices for the limited tilt-range series as indicated by the red arrows (Figure 4.10f,i). The smaller the tilt-range, the stronger is the elongation artifacts. Not only the large hollow cubes were reconstructed with an artificial 'hexagonal' shape, but also the small TiO$_2$ nanoparticles are elongated in the z direction. The 3D interparticulate network is not accurately represented with the limited tilt-range, causing significant errors in a porosity evaluation of the mesoporous material, whereas the full-range tilt-series results in a high-quality 3D reconstruction.
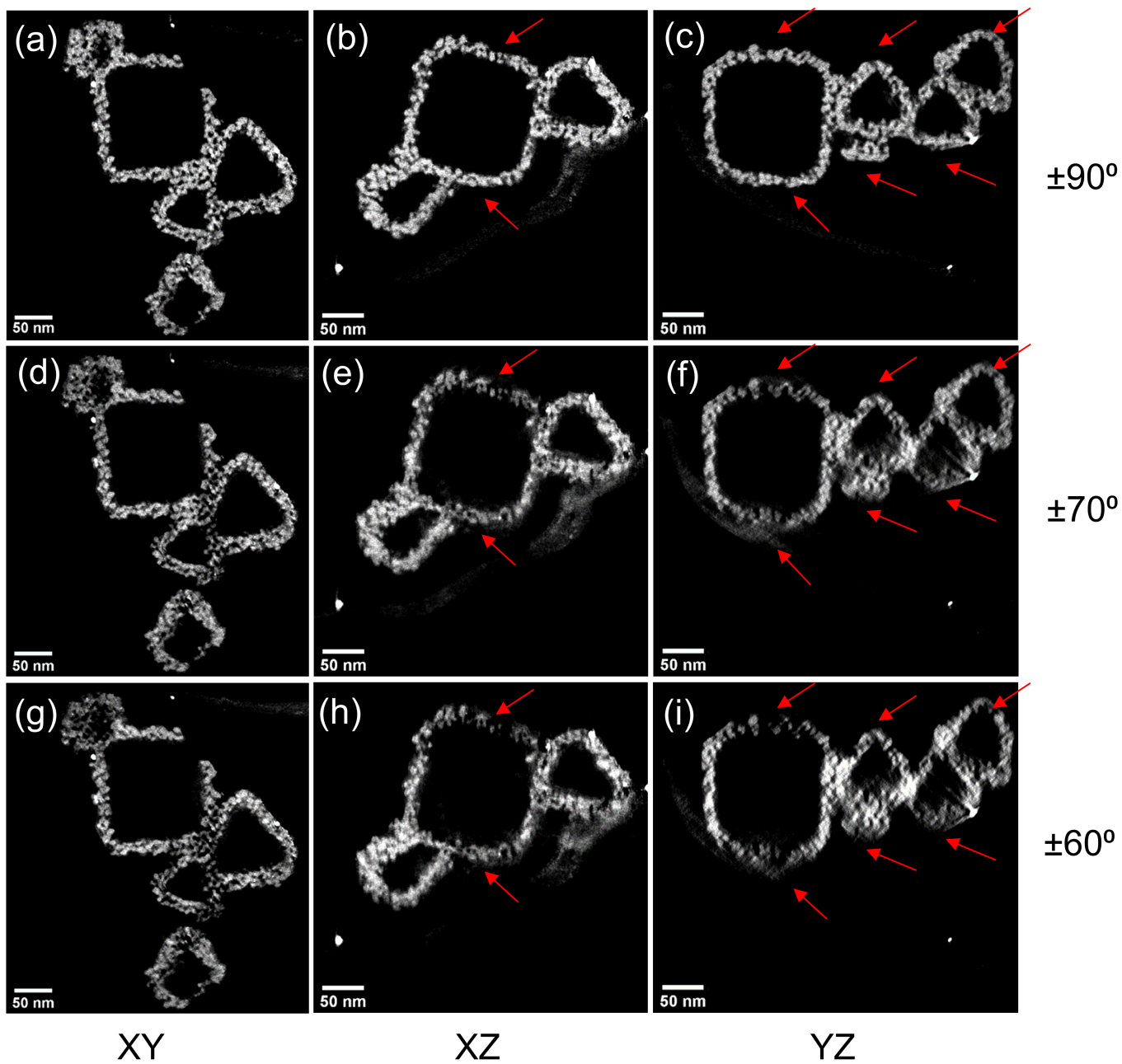
Figure 4.10: Representative slices for different tilt-ranges: (a-c) $\pm 90°$, (d-f) $\pm 70°$, (g-i) $\pm 60°$ at (column 1) xy, (column 2) xz and (column 3) yz orientations. Red arrows showed strong elongation artifacts for the reconstructions from $\pm 60°$ and $\pm 70°$ compared to $\pm 90°$.

4.6. Stability of the prepared specimen

As the piece of carbon film is adhered to the tungsten tip without Pt deposition, the stability of the film is critical point. To evaluate the film stability, two aspects need to be considered: the stability of the carbon film on the tungsten tip during/after the sample preparation and the stability of the carbon support and

the particles sitting on the film during data acquisition. Based on the observations, the carbon film remains on the tungsten needle for at least several weeks and even months after successful sample preparation. A comparison has been done by STEM imaging of the W tip, the carbon film and the sample particles directly after preparation and 11 months later, confirming the very stable form of the whole sample (Figure 4.11).
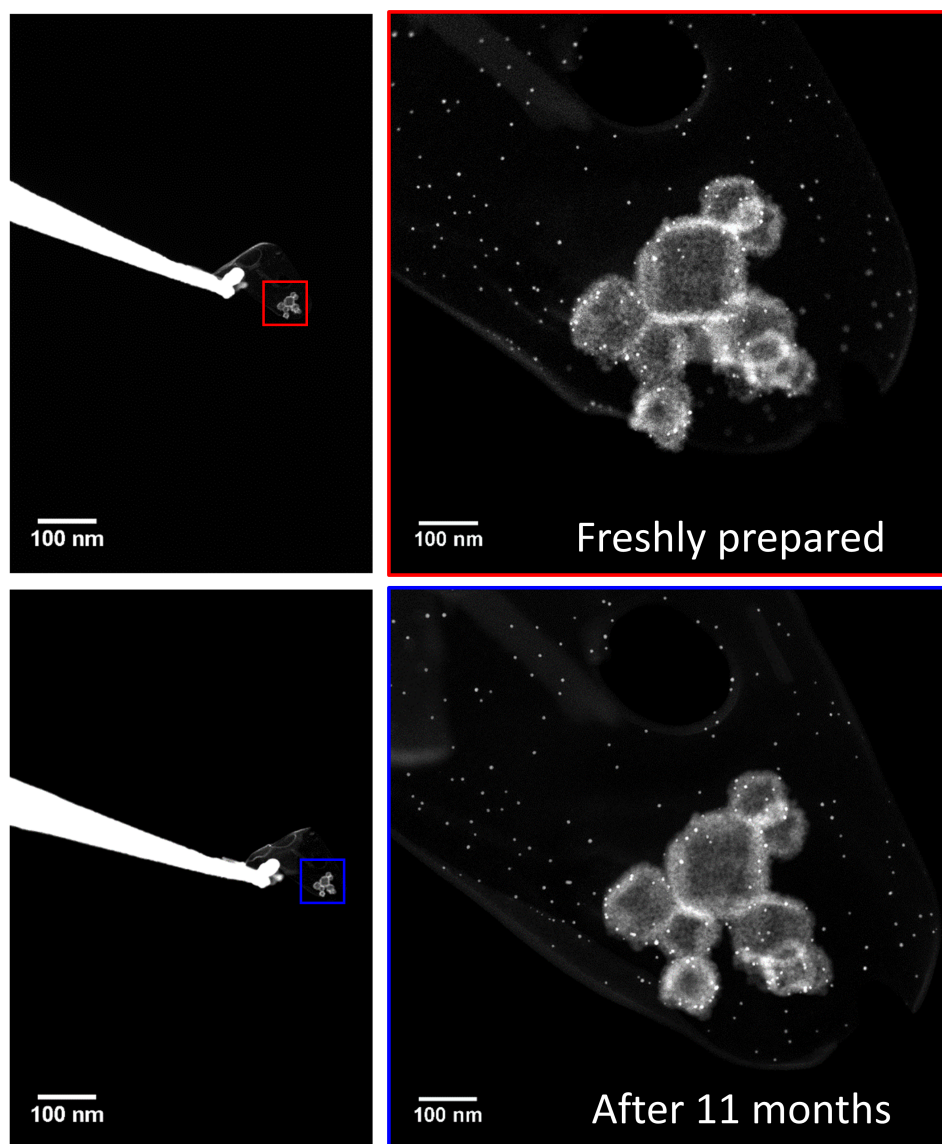
Figure 4.11: STEM images showing a stable sample by comparing the freshly prepared sample and after 11 months of storage.

The stability of the carbon film during tilting is critical as an unstable carbon film would lead to bending and movement during holder tilting, causing big challenges or even failure for the further projection alignment by conventional alignment methods, both marker-free or marker-based. Representative slices from the aligned sinogram are shown in Figure 4.12, in which well-aligned bright sine waves caused by the fiducial Au particles can be observed. The alignment was performed using Au particles as tracking markers, with optimization of adjustable parameters including rotation, tilt angles and magnification during the alignment, resulting a mean

residual alignment error of 0.7 pixels. The achieved good overall alignment demonstrates that the specimen sitting on the cut carbon piece keeps quite stable during the whole tilting process.
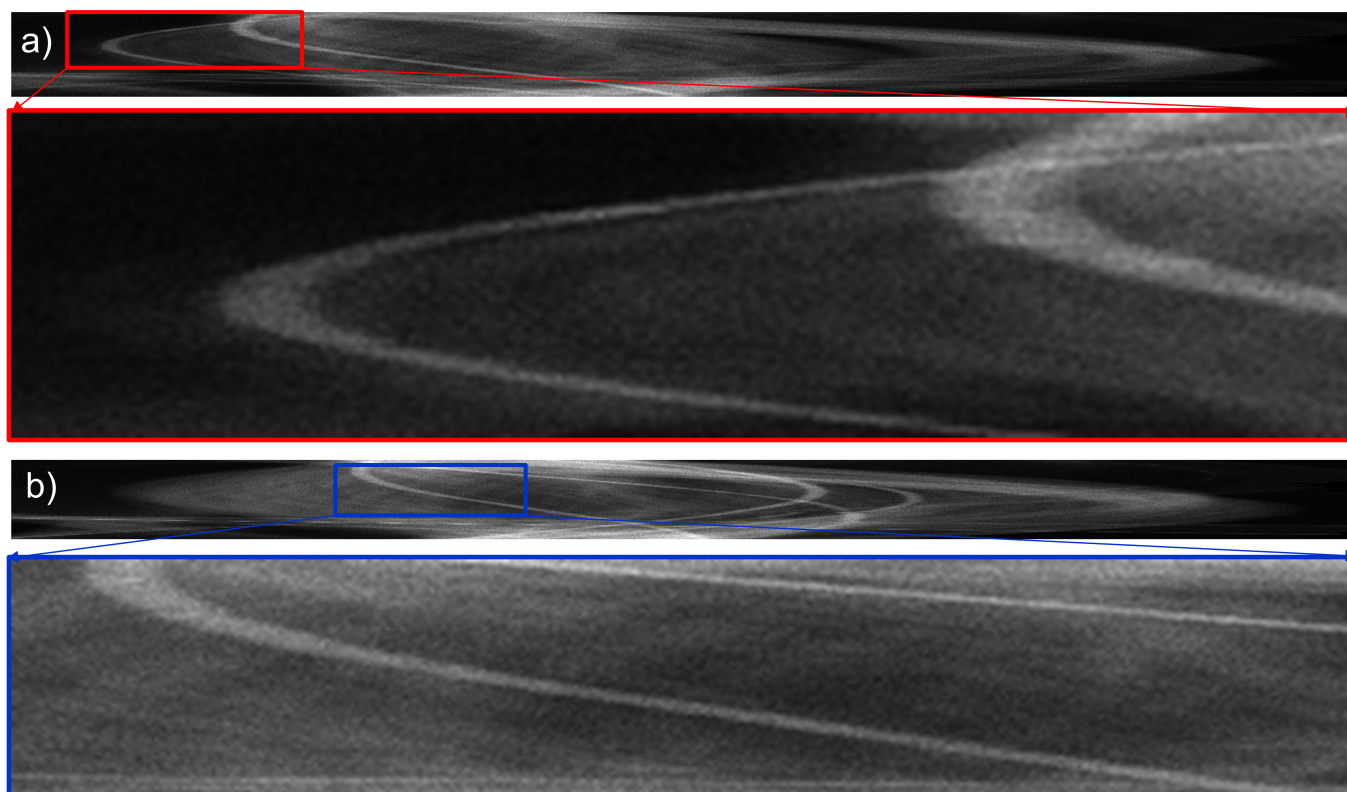
Figure 4.12: Representative slices from an aligned sinogram.

4.7. Conclusion

In this work, a new sample preparation method has been introduced that enables transfer of a selected individual nanoparticle or a few separated nanoparticles to a full-range electron tomography holder tip. This is achieved inside a standard FIB equipped with an omniprobe by employing a readily prepared tungsten tip. No other additional nano-manipulation setup is needed. A piece of carbon film supporting the specimen is adhered to the tungsten tip and both are transferred to the tomography holder tip. The carbon film is stable during the acquisition of the tilt series as proven by the excellent tilt-series alignment that could be achieved. Since the selected specimen is well placed on the original carbon film and not in direct contact with the tip or manipulator, this approach allows to select ultrafine nanoparticles without size limitation, avoiding the risk of sample damaging and making it fully visible for full-range electron tomography. As a proof of concept, the reconstruction results of Pt@hollow TiO$_2$ nanoparticles from a full tilt-range set of projections were presented, showing no missing wedge artifacts and overall improved quality compared to the reconstruction from limited tilt-series.

5. Understanding the Leaching Behavior of Pd@CMK3 Catalysts during Formic Acid Decomposition by Electron Tomography

In this chapter, electron tomography is applied to uncover leaching and redeposition phenomena at a Pd@CMK3 catalyst during formic acid (FA) decomposition in batch and fixed bed reactors. The 3D distribution of the Pd NPs on mesoporous carbon CMK3 support is determined by a quantitative tomographic analysis and the observed structure is discussed in terms of differences in the activity and stability during FA decomposition. This work has been submitted to *Nanoscale Advances* during the preparation of this thesis.

5.1. Introduction

Hydrogen, as a clean and reproducible carrier with high specific energy density, has been regarded as one of the most promising energy sources for the future due to the depletion of finite fossil fuels and increasing environmental issues such as climate change. [213], [214] One challenge for the application of hydrogen is its storage due to the nature of hydrogen. Typically, hydrogen is stored physically as highly pressurized hydrogen gas [215], liquid hydrogen [216] or constrained within porous networks, e.g. zeolites [217], porous carbon [218] and metal organic frameworks [219]. It can also be chemically stored and released via decomposition processes from compounds, such as water [220], ammonia borane [221] or formic acid [222]. The decomposition of FA has attracted increasing interest in the field of hydrogen storage due to various advantages, e.g. it is environmentally benign, has a high volumetric hydrogen content (4.4 wt.%) and the ability to release hydrogen under mild condition. [223] The thermodynamic properties at the decomposition pathways of FA under standard conditions can be seen below, where FA decomposition can proceed either via dehydrogenation to release hydrogen and carbon dioxide or dehydration producing carbon monoxide and water: [223]

$$\mathrm{HOOH} \longrightarrow \mathrm{H_2 + CO_2}, \Delta\mathrm{G}° = -32.9\,\mathrm{kJ\,mol^{-1}} \tag{5.1}$$

$$\mathrm{HOOH} \longrightarrow \mathrm{H_2O + CO}, \Delta\mathrm{G}° = -12.4\,\mathrm{kJ\,mol^{-1}} \tag{5.2}$$
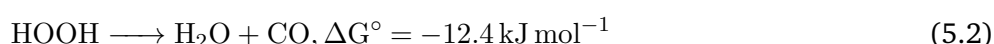
Pd is the most active monometallic transition metals for the decomposition of FA. [224] However, one major challenge for monometallic Pd catalysts in this system is deactivation, which is mainly due to active sites being blocked by poisoning species (such as CO) [225], metal particle sintering and leaching [226]. In addition to the weak interaction between active sites and the support, the leaching behaviour depends on the experimental setup. For example, it has been demonstrated that heterogenous catalysts exhibit different catalytic performances in batch and continuous flow reactors for a wide range of catalytic processes such

as hydrogenation and cross coupling, due to differences in metal leaching. [227]–[229] In a typical batch reactor, reactants including the catalyst are stirred under optimized conditions to accomplish the desired transformation, after which the catalyst can be easily retrieved for further utilization from the reaction mixture by a simple filtration step, as shown in Figure 5.1a. For a catalytic process accompanied by leaching, the concentration of the metal species in solution increases during the reaction, leading to the possibility of redeposition of the metal species on the solid support as all reactants, catalyst and products are constrained in a reactor with limited size, leading to a limited decrease of the metal concentration. [230] In a continuous flow process, the catalyst is placed in a packed-bed reactor (with typical packing materials such as silicon, glass, stainless steel, ceramics or polymers) and appropriate pumping systems are used to control the flow of the reaction mixture through the reactor. [231] As the reaction and separation of the catalyst from the reactants and products occur simultaneously (Figure 5.1b), further separation or filtration is not necessary in a fixed bed reactor. However, the continuous reaction stream might transport the active metal species away from the support, leading to significant metal leaching from the packed-bed reactor. [229]
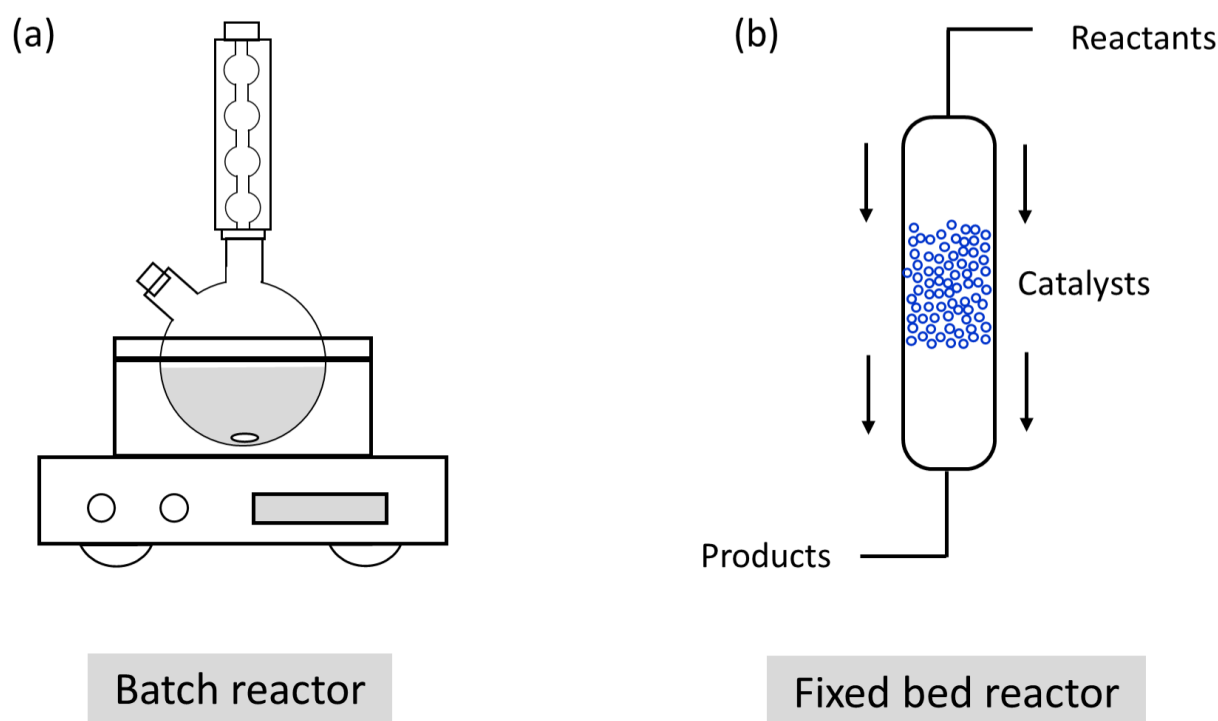
Figure 5.1: Schematic diagram of a typical lab-used batch and fixed bed reactor.

TEM has been extensively used to investigate the leaching/readsorption phenomena of supported catalysts in batch [232], [233] as well as continuous flow [234], [235] mode by comparing the particle size and shape of fresh and used catalysts. However, the typically obtained 2D information is not sufficient to reveal the details of the leaching process, especially for those catalysts supported on porous materials. For example, how does the leaching behavior of particles in interior pores and on the outside of the support differ and how to evaluate the redeposition of NPs and their preferred redeposition sites. As introduced in Chapter 1, examination of the location and distribution of NPs in 3D volume is possible using electron tomography. In this work, structural changes in a Pd@CMK3 catalyst during FA decomposition in batch and fixed bed reactors were studied and correlated with the leaching behavior. CMK3 is a commercially available ordered mesoporous carbon with a pore size of a few nanometer. Using Pd nanoparticles mainly constrained inside

the pores, we were able to track the overall evolution of their distribution, their particle size, and the loading after the catalytic reaction by electron tomography. In this way, it is possible to build a structure-performance relationship for improved design of more advanced catalysts.

5.2. Materials and experimental methods

5.2.1. Synthesis of Pd@CMK3 catalyst

Pd@CMK3 was synthesized by incipient wetness impregnation. Solid $K_2PdCl_4 \cdot 2\,H_2O$ (Aldrich, purity 99.99%) (0.094 mmol of Pd,) was dissolved in water. The correct amount of solution to completely fill all pores (based on the total pore volume calculated from N_2 adsorption analysis), was added to 1 g of porous carbon. The quantity of metal in the precursor solution was set to obtain a final metal loading of 1 wt.%. The produced material was filtered, redispersed in water and reduced with $NaBH_4$ (Pd/$NaBH_4$ molar ratio of 1/8). Afterwards, the catalyst was filtered and washed with 1 L of distilled H_2O and dried at 80°C for 4 h in air. The synthesis was done in the group of our collaborator Dr. Alberto Villa at the University of Milano.

5.2.2. Catalytic testing – batch reactor

Liquid-phase FA decomposition was carried out in a 100 mL two-neck round-bottom flask placed in a water/ethylene glycol bath with a magnetic stirrer and a reflux condenser. Typically, 10 mL of an aqueous solution of 0.5 M HCOOH was placed in the reactor and heated to a constant reaction temperature of 30°C. Once the solution reached the desired temperature, the required amount of Pd@CMK3 catalyst (formic acid/catalyst molar ratio of 2000/1) was added and the solution was stirred using a magnetic stirrer. Recycling tests were performed after 30 minutes of reaction, filtering the catalyst present in the solution without further treatment. Reproducibility tests were performed for every reaction repeating the test with the same catalyst three times. The catalytic testing was done in the group of our collaborator Dr. Alberto Villa at the University of Milano.

5.2.3. Catalytic testing – fixed bed reactor

Liquid-phase FA decomposition in a fixed bed reactor was tested with a bed length of 7 cm (50 mg Pd@CMK3 and 50 mg silica carbide). The bed was heated to a constant reaction temperature of 30°C. 0.5 M FA was inserted in the reactor with a flow of 0.1, 0.3 and 0.5 mL/min. Reproducibility tests were performed for every reaction repeating the test three times. The catalytic testing was done in the group of our collaborator Dr. Alberto Villa at the University of Milano.

5.2.4. Catalyst characterization

The Pd loading of Pd@CMK3 before and after the reaction was determined using an inductively coupled plasma atomic emission spectrometer (ICP-AES) and EDS analysis. HAADF-STEM imaging and EDS analysis were performed on a Themis 300 TEM (Thermo Fisher Scientific) operated at 300kV, equipped with a probe corrector and Super-X EDS detector. TEM samples were prepared by dispersing powder samples of the Pd@CMK3 catalyst on 100×400 mesh carbon coated copper grids (Quantifoil). Around 30 regions of interest of the same size were selected randomly and measured by EDS to evaluate the homogeneity of the Pd loading

under identical conditions for each catalyst. The mass fraction of Pd loading was calculated by fitting the L peak for Pd and K peak for carbon after background subtraction. The absorption correction for a sample thickness of 400 nm and density of 2.1 g/cm^3 were used. The Pd particle size distribution was estimated from HAADF-STEM images using the software tool ImageJ (National Institutes of Health) approximating the particles with an elliptical shape. The reported diameter of each particle is calculated as the average of the long and short axis. For each catalyst 500-700 Pd particles from 3-4 support particles were measured to obtained a good statistical representation. Electron tomography was performed using a Fischione 2020 tomography holder. HAADF-STEM tilt series with image dimensions of 2048×2048 pixels and a pixel size smaller than 0.5 nm were collected using the Xplore3D software (Thermo Fisher Scientific) with auto focus and tracking before acquisition. All tilt-series were collected over a tilt range of at least ∼70° with a tilt step of 2°. During tilt-series acquisition no detectable morphological changes caused by electron beam damage was observed. Alignment of the tilt series was performed in IMOD version 4.7 (University of Colorado) using supported Pd nanoparticles as fiducial markers with a mean residual alignment error smaller than 0.5 pixels. The aligned tilt series were reconstructed using the DART algorithm [129] within the ASTRA toolbox [194]. After an initial reconstruction with 150 iterations by SIRT [174], the main loop for DART was repeated 10 times and then SIRT with another 150 iterations was included for each iteration to ensure convergence. The grey levels used for segmentation were set based on a rough estimation of the intensity of each component based on the initial SIRT reconstruction. The initial threshold was set to the average value of the grey levels. During the DART reconstruction, the random probability was fixed to 0.3 and a 3×3 Gaussian filter was used to smooth the reprojected sinogram during each loop. The Pd loading (in wt.%) of each catalyst was also calculated based on the segmented volumes using the bulk density of metallic Pd (12.02 g/cm^3) and CMK3 carbon (2.1 g/cm^3). 3D visualization including volume and surface rendering was performed in Avizo 2020.2 (Thermo Fisher Scientific).

5.3. Determination of the 3D location of Pd NPs in a Pd/CMK3 catalysts

To identify the 3D location of Pd NPs, a similar but not identical procedure as reported by Wu et al. [101] was used. Based on the DART reconstruction, it is quite straightforward to extract the features of interests, e.g. carbon support and Pd NPs. However, as shown in Figure 5.2, it is difficult to determine the internal and external surface of the carbon support by simple edge detection due to the existence of a large number of pores inside the volume. Therefore, the segmented volume was dilated by certain number of voxels (depending on the pore size) using the 'grow' module in Avizo to expand the solid phase and reduce the pore space, thus filling all internal pores. The resulting volume was then eroded by the same number of voxels as used previously during dilation using the 'shrink' module. The resulting volume without pores was further eroded by certain number of voxels (depending on the pixel size) to provide a mask for the detection particles on the outer surface. This erosion step is essential to avoid recognizing the intensity gradient between metal particles and vacuum as carbon. In this case, Pd particles located outside the eroded mask are considered as particles on the external surface when they are in contact with vacuum. The other particles located inside the eroded mask are regarded as particles on internal pores. Thus, the Pd NPs located on the external surface of the support and the particles inside the pores were extracted separately and can be used for further statistical analysis such as the particle size and volume measurements, which will be discussed in section 5.6.
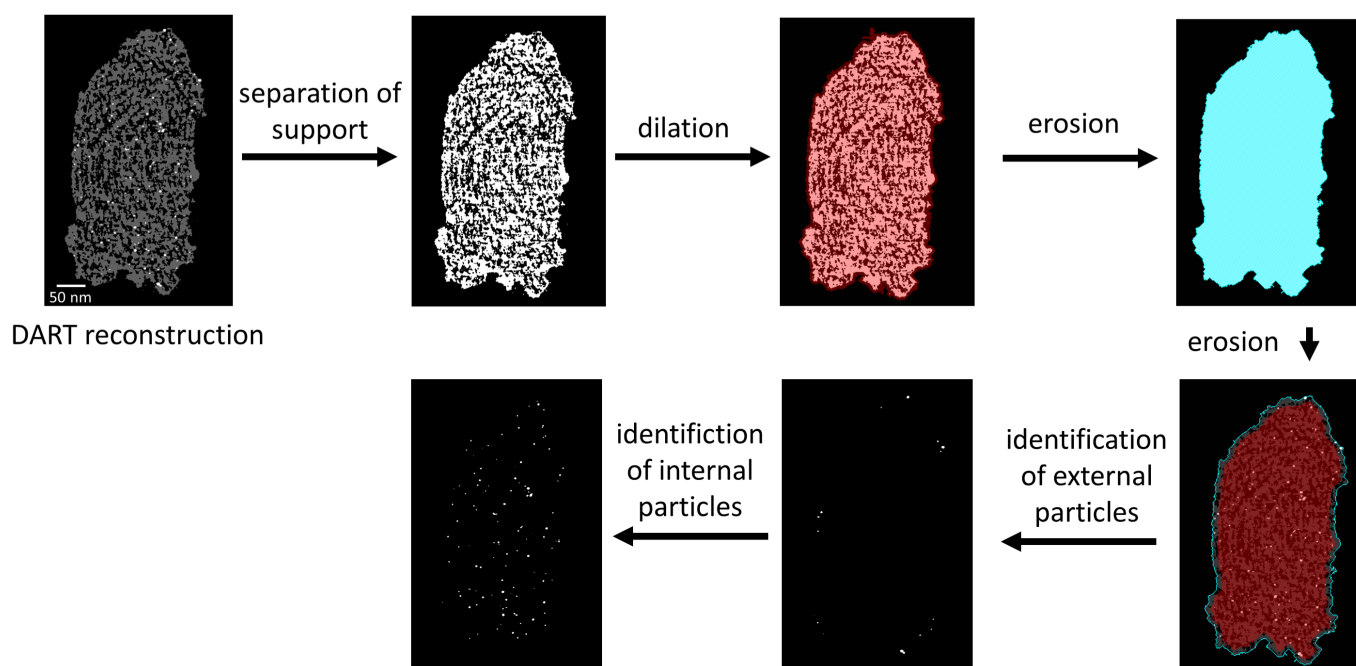
Figure 5.2: Workflow for the determination of the Pd location in a Pd@CMK3 catalysts in 3D.

5.4. Catalytic performance during FA decomposition

The Pd@CMK3 catalyst was tested for FA dehydrogenation in a batch reactor, as a model system for liquid orangic hydrogen carriers (LOHC) and compared with one of the best Pd-based monometallic catalyst present in literature i.e. 1% Pd@HHT [236]. As shown in Figure 5.3a, Pd@CMK3 shows an initial activity of 3261 h^{-1} (calculated after 5 minutes of reaction time as mol of reacted FA to total mol of metal per hour), which is more than 3 times higher compared to Pd@HHT (979 h^{-1}). Moreover, Pd@CMK3 showed a conversion of 67% after two hours of reaction time, around two times higher compared to Pd@HHT. The Pd@CMK3 catalyst was also tested over 5h of reaction time in the fixed bed reactor with three different flow rates, i.e. 0.1, 0.3 and 0.5 mL/min. Silica carbide was mixed to the catalyst (ratio of 1:1 by weight) in order to increase the length of the catalytic bed. From Figure 5.3b, it is clear that the catalyst reached a high conversion after 30 min of reaction time (61%) at a flow rate of 0.1 mL/min, around 20% higher compared to the batch reactor after the same reaction time. However, the catalyst is deactivated rapidly and the conversion decreased to only 21% after 2h of reaction time, around 3 times lower compared to the batch reactor (67%). A similar fast deactivation can be also seen for the higher flow rate of 0.3 mL/min (Figure 5.3b). The conversion reached only 8% after 30 min of reaction time for the flow rate of 0.5 mL/min and is deactivated further with increasing reaction time.

The catalyst stability was evaluated for the batch reactor using repeated catalytic testing. Both Pd@CMK3 and Pd@HHT catalysts were tested by filtering and reusing the catalyst without further treatment over 6 reaction runs. To compare the stability with a similar conversion, the stability test was performed on Pd@CMK3 after 30 minutes and on Pd@HHT after 2 hours of reaction time for the FA decomposition. While Pd@HHT rapidly deactivates (Figure 5.4a), Pd@CMK3 shows a more stable behaviour over 6 reaction cycles (Figure 5.4b). The stability difference can be attributed to the different support structures of these two catalysts. Compared to the Pd@HHT catalyst, where the Pd NPs are supported on the surface of high-heat treated carbon nanofibers (HHT) having a highly graphitized surface, the Pd NPs immobilized in the porous
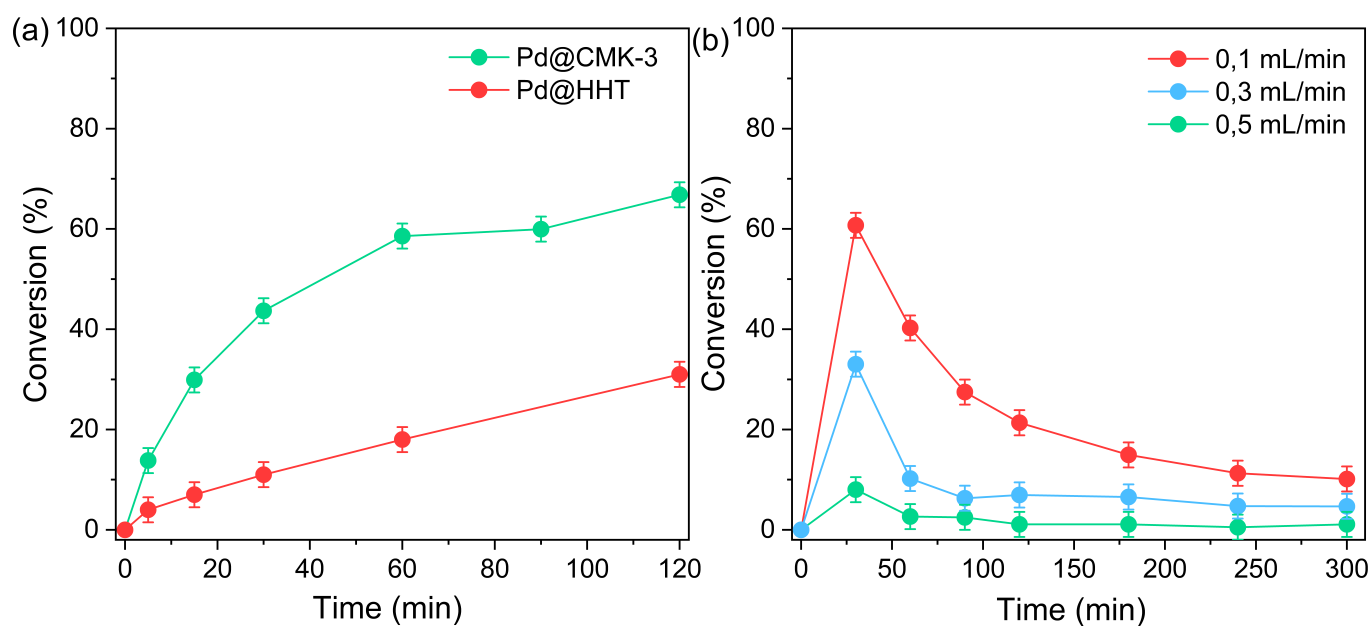
Figure 5.3: Catalytic performance of Pd@CMK3 and Pd@HHT (from [235]) during FA decomposition. (a) FA conversion as a function of reaction time on Pd@CMK3 and Pd@HHT catalysts in a batch reactor. (b) FA conversion as a function of reaction time for Pd@CMK3 in a fixed bed reactor using a flow of 0.1, 0.3 and 0.5 mL/min.
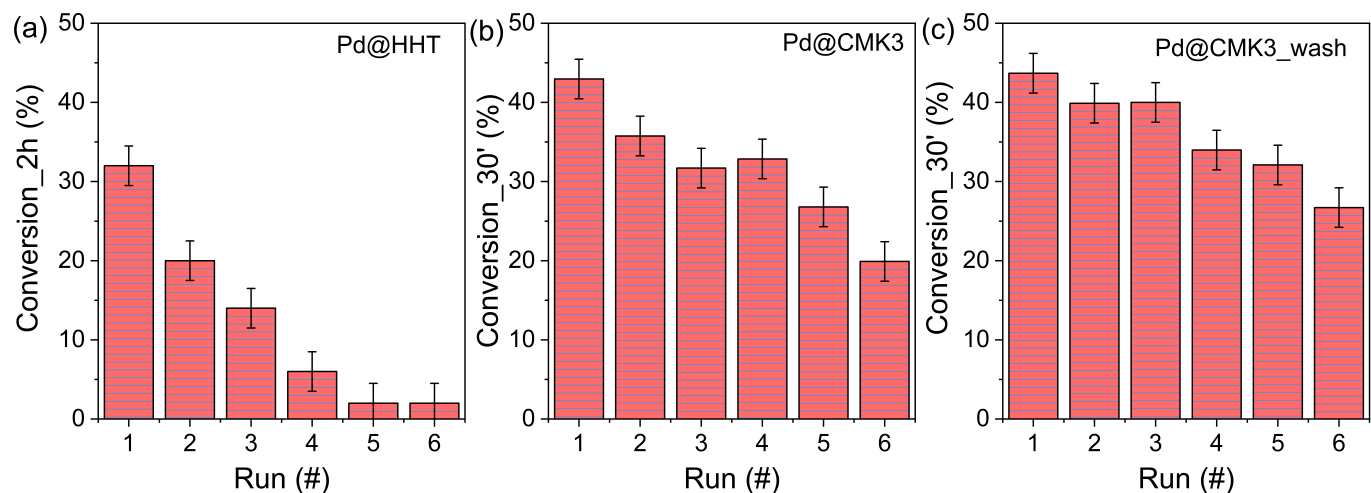
Figure 5.4: Stability test for (a) Pd@HHT after 2 hours of reaction for FA decomposition; (b) Pd@CMK3 after 30 minutes of reaction and (c) Pd@CMK3 after washing the catalyst in each cycle (the filtered material was placed in a beaker with 50 mL of water under vigorous stirring for 30 minutes) in a batch reactor with a similar initial conversion.

carbon support in Pd@CMK3 show the expected higher stability due to confinement effects. Such enhanced stability caused by confinement effects has been reported previously by various groups [10], [59].

5.5. 2D morphology and Pd loading of Pd@CMK3

To understand the different catalytic performance of Pd@CMK3 in the batch and fixed bed reactor, the fresh and used catalysts were characterized using STEM to assess the particle size distribution. Figure 5.5 shows STEM images of these three catalysts and histograms of their particle size distributions. It is clear that the Pd NPs in the fresh catalyst are fairly homogeneously dispersed on the support with an average particle size of 2.7 nm. The average particle size grows to 3.3 nm for both used catalysts after the reactions, indicating particle sintering or aggregation during FA decomposition. A small number of Pd NPs with a diameter larger than 5 nm can be found in both used samples, which was not present in the fresh sample (Figure 5.5d-f). This aggregation of active particles might be one reason for the catalyst deactivation. To unravel the dependence of the catalytic performance on the structural evolution, a more accurate analysis of the particle size by alternative techniques will be discussed later.
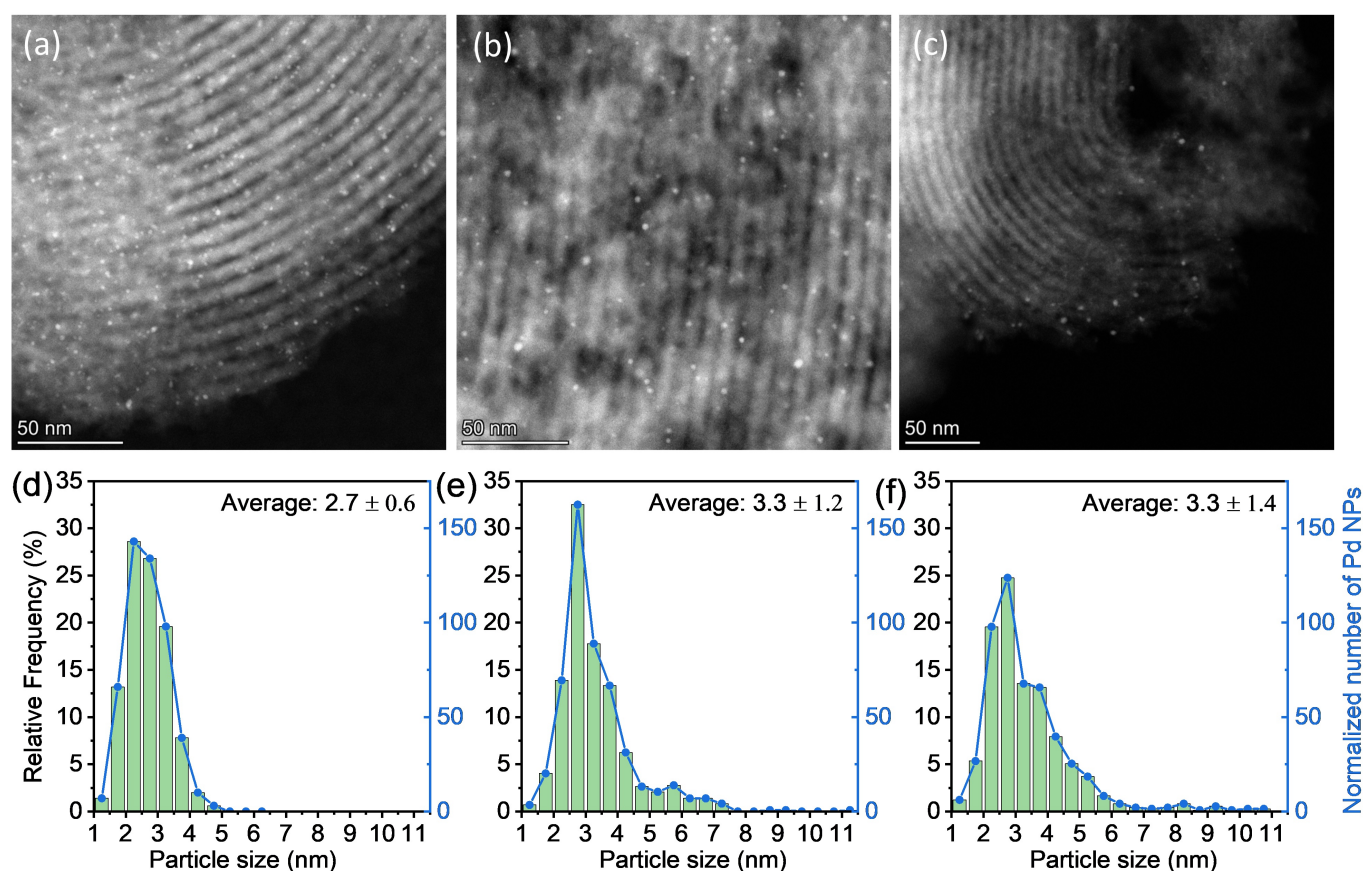
Figure 5.5: Representative STEM images of Pd@CMK3: (a) as-prepared state, (b) after FA decomposition in the batch reactor and (c) after FA decomposition in the fixed bed reactor together with (d-f) the corresponding histograms of the particle size distribution.

The Pd loading was measured by EDS and ICP-AES, as shown in Figure 5.6. The Pd loading of the catalyst was measured after the end of the stability test after the 6th cycle for the batch reactor and after 300 min. on the fixed bed reactor. According to the ICP-AES results, the Pd loading of the as-prepared sample was 1 wt.%, as expected from the synthesis process. However, after FA decomposition, the Pd loading decreased by 59 wt.% in the fixed bed reactor, showing severe leaching of Pd during the catalytic reaction. This fits

roughly to the observed deactivation in Figure 5.3b, suggesting a loss of active metal content as the dominant deactivation mechanism. For the catalyst used in the batch reactor during the stability test (Figure 5.4b), the activity was reduced by 50% after six cycles while only 23 wt.% of Pd was lost. This difference may be attributed to the adsorption of poisonous species such as CO on the catalyst surface, as the activity of the catalyst could be partially recovered by washing with water (Figure 5.4c). A similar recovery of the activity of Pd catalysts during FA decomposition by washing has also been seen in other works. [237], [238] A quantitative EDS analysis of around 30 randomly-selected regions of interest for each of the three catalysts deviates slightly from the ICP measurements. Considering systematic errors in EDS quantification using different transitions lines and the limited volume analyzed, the overall agreement between ICP-AES and EDS measurements is reasonable with the absolute quantification from ICP-AES being more accurate. However, the EDS measurements provide statistical information on the homogeneity of the three samples. A few measured areas exhibit significantly higher Pd loading in each of the samples indicating some inhomogeneity of the catalyst with 5-10% of the particles exhibiting significant loading differences. Nevertheless, the overall trend of decreasing Pd content is observed by EDS for the batch and the fixed bed reactor. However, for the fixed bed reactor care has to be taken with the interpretation, as a loading gradient from the inlet to the outlet is expected, which would affect the local EDS analysis.
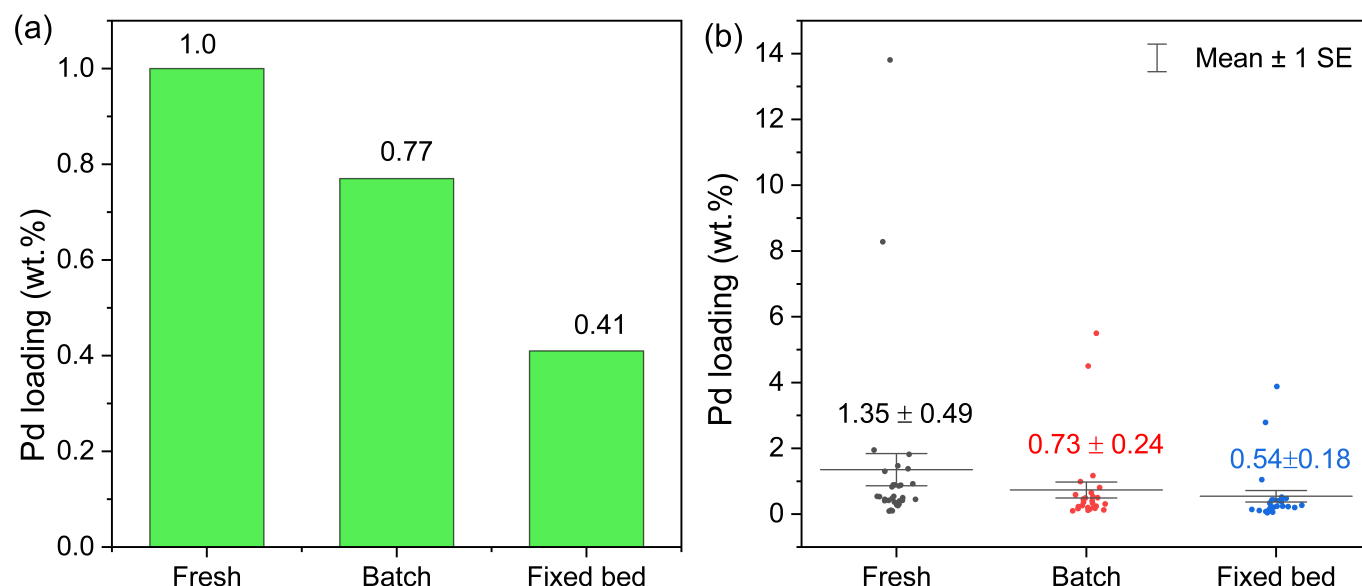
Figure 5.6: Pd loading of Pd@CMK3 catalysts measured by (a) ICP-AES and (b) EDS based on 30 regions of interest for each catalyst. SE in the EDS data represents the standard error with Std. the standard deviation and n the number of observations: $SE=Std./\sqrt{n}$.

5.6. 3D characterization by electron tomography

Electron tomography was used to further analyze the leaching behavior of Pd NPs of the Pd@CMK3 catalyst in both reactors based on three-dimensional nanoscale reconstructions. For each sample, three tilt series were acquired from different CMK3 pieces as shown in Figure 5.7 and the corresponding 3D volume rendering from the initial SIRT reconstructions can be seen in Figure 5.8.
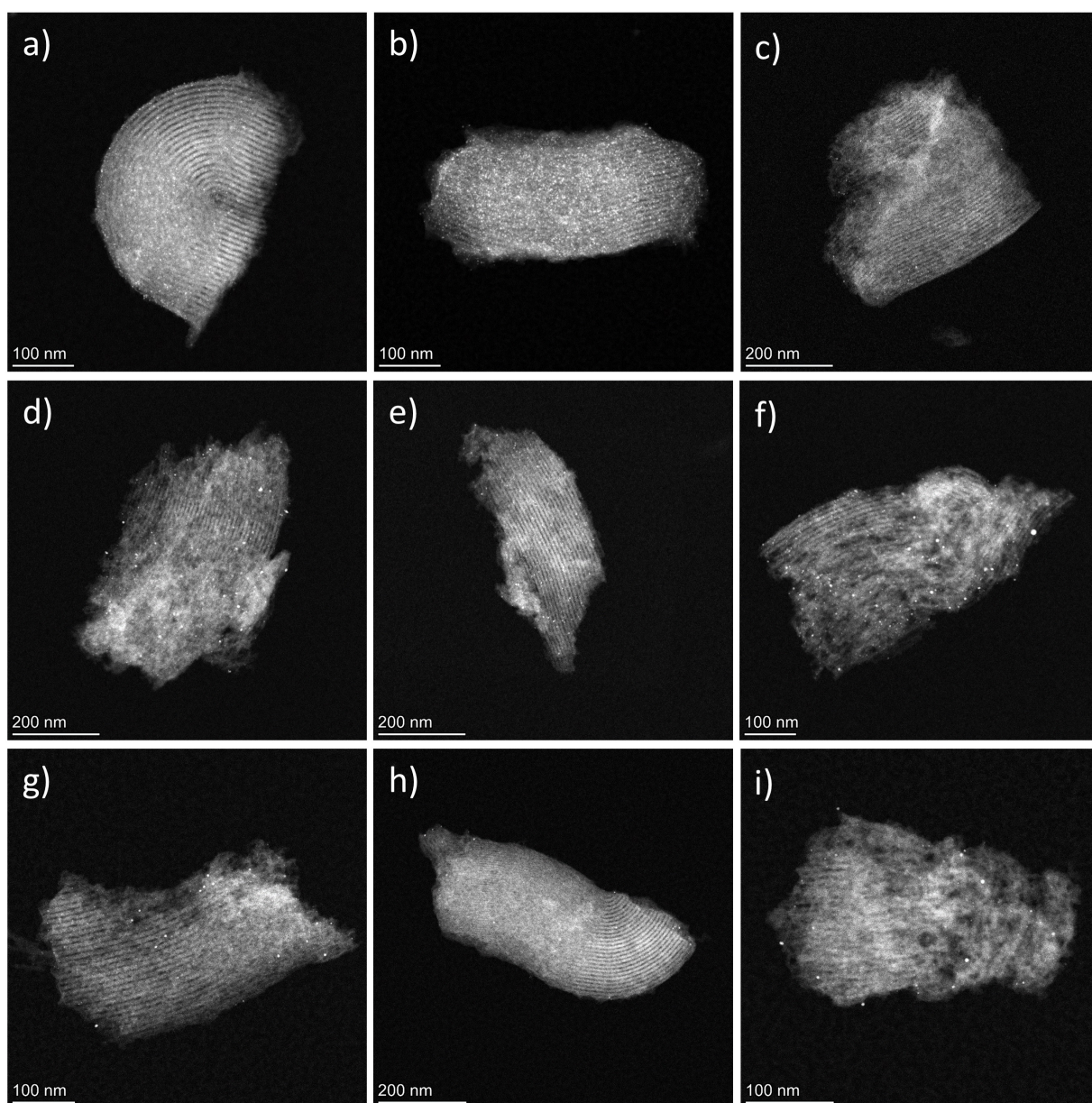
Figure 5.7: HAADF-STEM images of Pd@CMK3 catalysts for (a-c) fresh sample and after FA decomposition in (d-f) batch reactor and (g-i) fixed bed reactor.
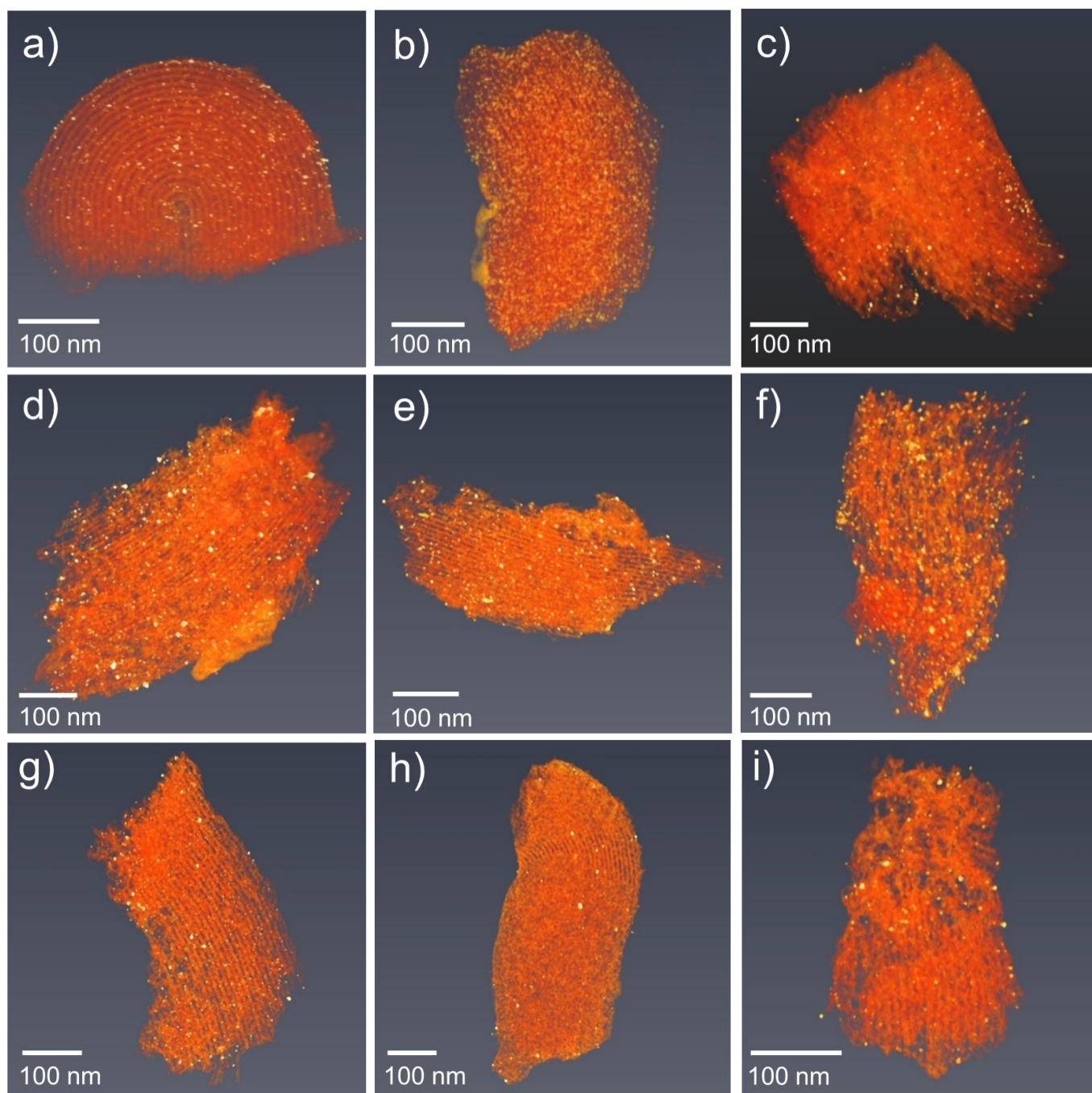
Figure 5.8: Volume rendering from initial SIRT reconstructions of Pd@CMK3 catalysts for (a-c) a fresh sample and after FA decomposition in (d-f) batch reactor and (g-i) fixed bed reactor.

After the DART reconstruction, the 3D location of all Pd NPs on the external/internal surface of CMK3 were extracted from the segmented volume. The detailed procedure for the extraction has been shown in section 5.3. Figure 5.9 shows representative 2D slices from the reconstructed volume of the three Pd@CMK3 catalysts and the corresponding rendered volumes, where Pd NPs located on the external surface are marked by red and those on the internal surface are marked by yellow circles (due to the large number of Pd NPs inside the pores, only part of them are marked in Figure 5.9a). From the reconstructed slices, it is clear that

the number of Pd particles is reduced after reaction in the batch reactor (Figure 5.9d-f) compared to the as-prepared sample (Figure 5.9a-c), while a more severe loss of Pd NPs is observed after reaction in the fixed bed reactor (Figure 5.9g-i), in agreement with the EDS and ICP results in section 5.5. At a first glance, the
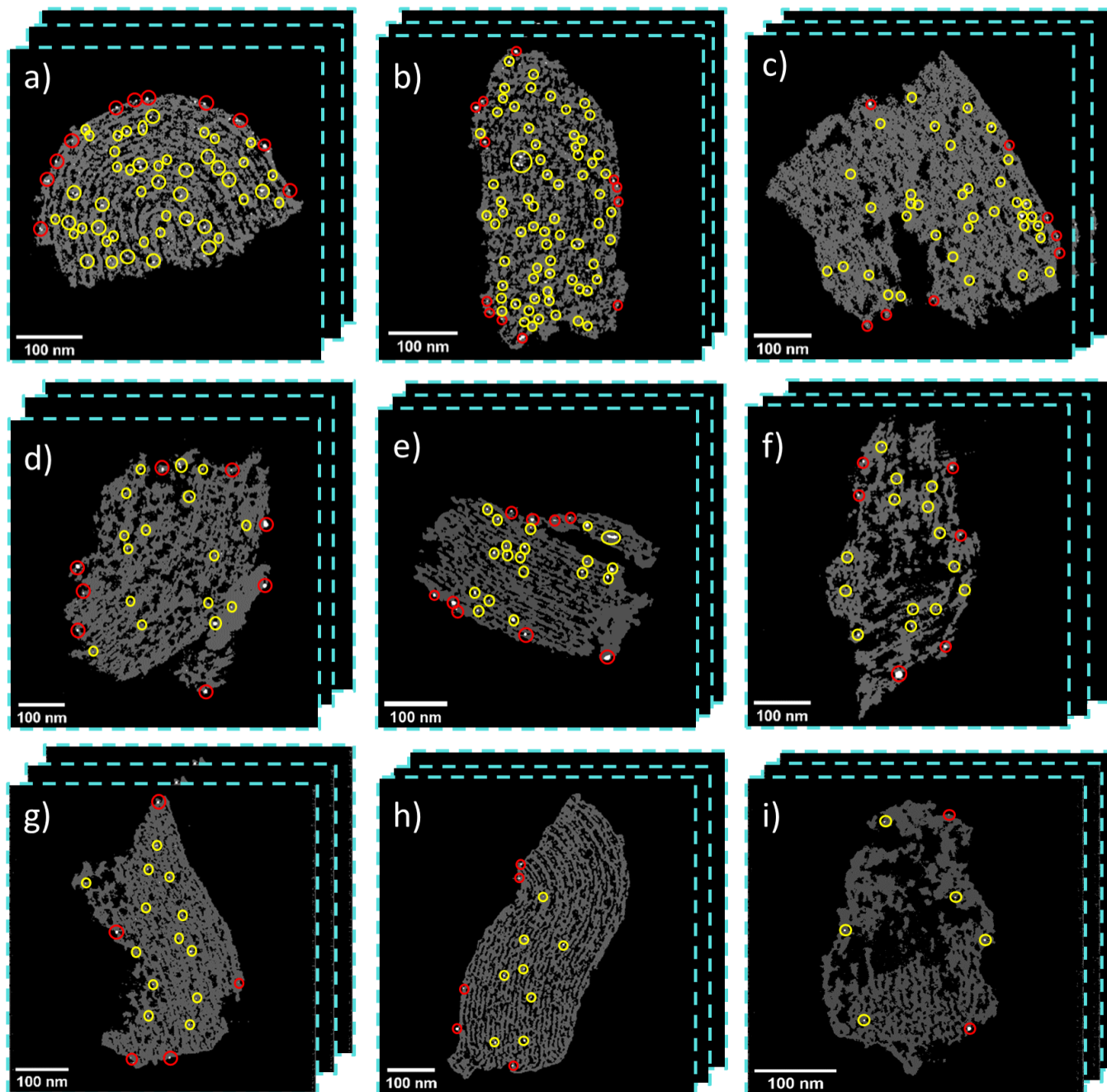
Figure 5.9: Typical 2D slices from reconstructed volumes of Pd@CMK3 catalysts for (a-c) a fresh sample and after FA decomposition in (b-f) batch reactor and (g-i) fixed bed reactor. The red and yellow circles highlight Pd nanoparticles on the external surface and internal of the porous support.

results seem to indicate that Pd NPs inside the pores seems to be easier leached than those on the external surface, which is most obvious in the case of the fixed bed reactor where most NPs inside the pores disappeared

after the reaction. This is against the expectation considering confinement effects in heterogenous catalysis where metal particles immobilized inside the porous channels often show a higher stability than those on external surfaces. [101] A possible reason might be that leached Pd NPs are redeposited on the support during the reaction as evident in Figure 5.8(d-i), where larger particles are observed on the external surface after the reactions in both reactor modes compared to the fresh sample. To get a deeper understanding of the leaching and redeposition, a quantitative analysis of the Pd NPs on the internal/external surface of the support has been performed based on the 3D reconstructions.

The Pd loading calculated from the segmented volume is shown in Figure 5.10a, which shows a same decreasing trend. These results show again a more significant leaching of Pd NPs in the fixed bed reactor compared to the batch reactor during FA decomposition. The particle diameters were also calculated from the segmented tomographic volumes using the equivalent diameter of spherical Pd particles with the same volume (Figure 5.10b). The resulting average sizes match well with those measured from the 2D STEM images in Figure 5.5d-f.
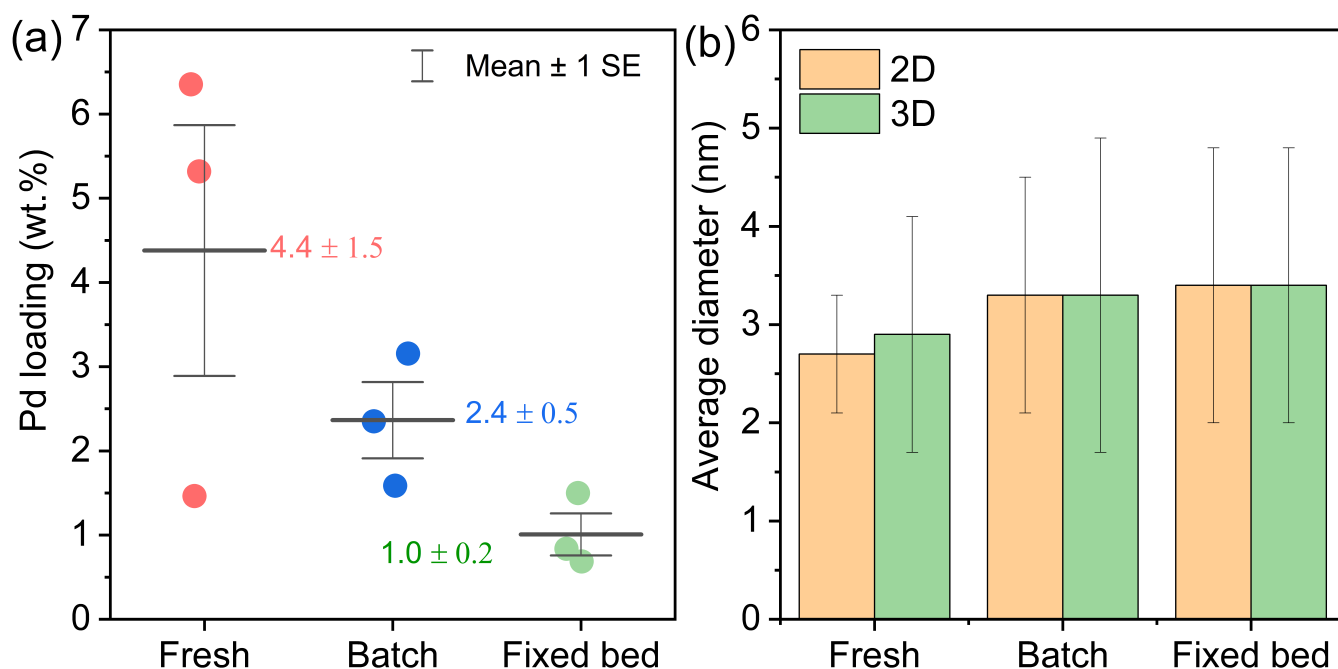
Figure 5.10: Pd loading calculated from the tomographic reconstructions.

Figure 5.11a shows the volume fraction of Pd NPs on the external surface in the fresh and used Pd@CMK3 catalysts. The volume of Pd NPs was measured by calculating the number of voxels contained in each particle after segmentation and determination of the particle location. To provide some statistical sampling, the Pd NPs from three tomograms were analyzed for each catalyst. It is obvious that the volume of Pd particles on the external surface of the support increased in both used catalysts compared to the fresh one. For the fresh sample, only 33% of Pd NPs were detected on the external surface of the CMK3 support, while most of the particles are located inside the pores due to the higher inner surface area. However, after FA decomposition in the batch reactor, the fraction of Pd NPs on the external surface increased to 45%, around 1.4 times as much as in the fresh sample, indicating that leached Pd species are preferably redeposited on the external surface, probably due to the slower diffusion rate inside the pores. After FA decomposition in the fixed bed reactor, the fraction of Pd NPs on the external surface increased to 58%. Considering the overall severe Pd loss for

this catalyst due to the constant flow of reactants and solvent through the porous support, the enrichment at the surface is surprising. A possible explanation for the high fraction of Pd on the external surface is notable redeposition taking place on the external surfaces even in the flow reactor, presumably due to a gradient of Pd species over the catalyst column. Pd NPs leach fast at the top of the column, while leached Pd species redeposit on the support surface of the catalyst located on the bottom of the column.
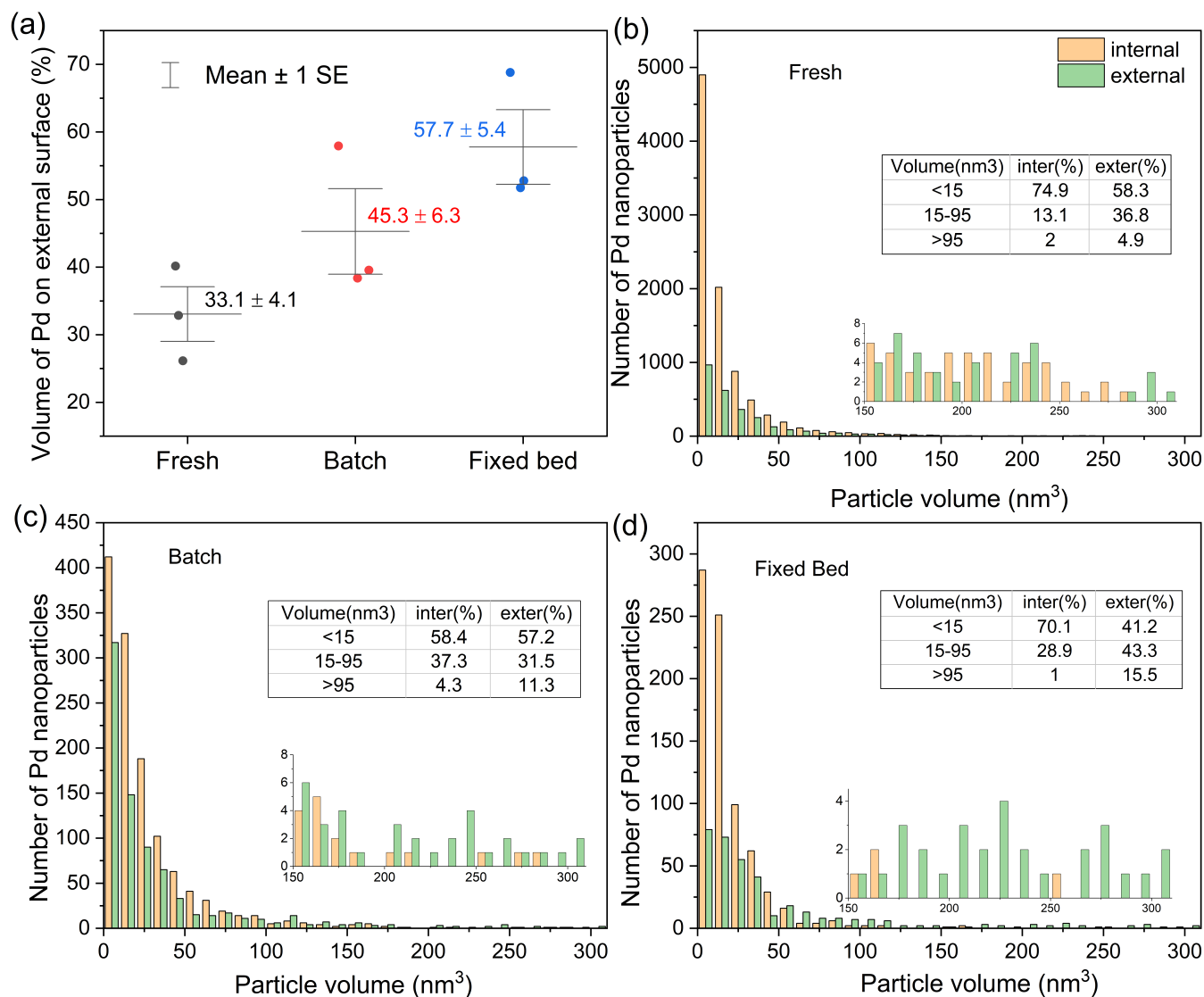
Figure 5.11: (a) The fraction of Pd NPs on the external surface for the fresh and used catalysts; number of particles distributed on the internal and external support surface of Pd@CMK3 in the (b) fresh state, (c) after reaction in the batch reactor and (d) after reaction in the fixed bed reactor. The inserted tables in b-d show the relative volume of Pd NPs within a certain volume range on the internal and external surface. The inserted histograms are closeup views of the limited data of particles with volume larger than 150 nm^3.

Further comparison of the Pd NPs located on the internal and external support surface can be found in Figure 5.11b-d, which shows the histograms of Pd NPs for various ranges of the particle volume. It is clear that all catalysts show quite homogeneous particle sizes with a high fraction of very small (<15 nm^3, corresponding to a diameter smaller than 3 nm) Pd NPs and a small fraction of large particles bigger than

95 nm^3 (corresponding to a diameter around 5.5 nm). While the size distribution of particles located on the internal and external support surface is not too different, the table in Figure 5.11b shows that the particles located on the internal surface exhibit a higher fraction of small particles compared to the particles located on the external surface, whereas larger particles are preferentially observed on the external surface. This confirms that pores can reduce the formation of big particles by ripening or agglomeration.

Looking in more detail at the catalyst used in the batch reactor, the amount of small Pd NPs on the internal and external support surface both decreased severely. The fraction of small Pd NPs ($<$15 nm^3) on the internal and external support surface are comparable, while an increased fraction of large particles ($>$95 nm^3) can be found on the external surface. Considering the strong reduction of the number of particles and only slight reduction of Pd loading ($\sim$23%) according to the ICP-AES and EDS results (Figure 5.6), the redeposition and aggregation of Pd particles plays an important role for the change of the particle size evolution. According to the diffusion simulation results from Tallarek et al., where the effective diffusion coefficient decreased rapidly with increasing particles size [11], [203], the detachment of whole Pd particles from the CMK3 support is unlikely. Therefore, the evolution of the particle size can be attributed to the dissolution of Pd particles, leading to a high Pd concentration in solution and then redeposition/ripening leads to growth of the particles. As the diffusion rate of dissolved Pd species on the external surface is faster than on the internal surface, Pd species are preferentially redeposit on the external surface. In addition, the increase of Pd NPs on the external surface provides more nuclear sites for the growth/ripening of the particles, resulting in a higher fraction of the Pd volume (Figure 5.11a) and larger particle sizes (inserted table in Figure 5.11c) on the external surface. However, the competition of dissolution and redeposition of Pd species leads to similar PSD for particles on both external and internal surface compared to the fresh sample. This is probably attributed to the reaction mixtures being constrained in the batch reactor with enough time for Pd dissolution and reposition during the reaction. Overall, these observations suggest a highly dynamic equilibrium in the batch reactor with a lot of local leaching and redeposition taking place both for particles on the internal and external support surface. Here, the limited size of the pores limits the internal particles from growing extremely big. These observations help to explain the stability of the catalyst in the batch reactor.

In case of the fixed bed reactor, even though a significant amount of Pd was lost from the catalyst, the overall particle size distribution is more or less similar to the fresh sample for particles on the internal surface of the support, where the small Pd NPs ($<$15 nm^3) comprise the highest fraction and a decreasing fraction belongs to particles with increasing size. The higher fraction of small particles compared to the batch reactor might be due to the fact that the particles were eroded continuously by the flow without much redeposition on the internal surfaces. This is not surprising as leached Pd species are easily removed from the solid support by the continuous flows and do not have enough time for redeposition due to the short diffusion path in the packed columns. A decreasing fraction of Pd NPs with a size smaller than 15 nm^3 and an increasing fraction of Pd NPs with a size larger than 15 nm^3 was observed on the external surface. This increasing fraction of larger particles on the external surface contributed to the increased average particle diameter observed in Figure 5.5f. One possible explanation for the redeposition of Pd on the external surface in the fixed bed reactor might be the existence of a gradient of Pd species in the catalyst column as discussed above for the increased fraction of particles one the external surface. The overall leaching and reposition behavior in both batch and fixed bed reactors is summarized schematically in Figure 5.12.
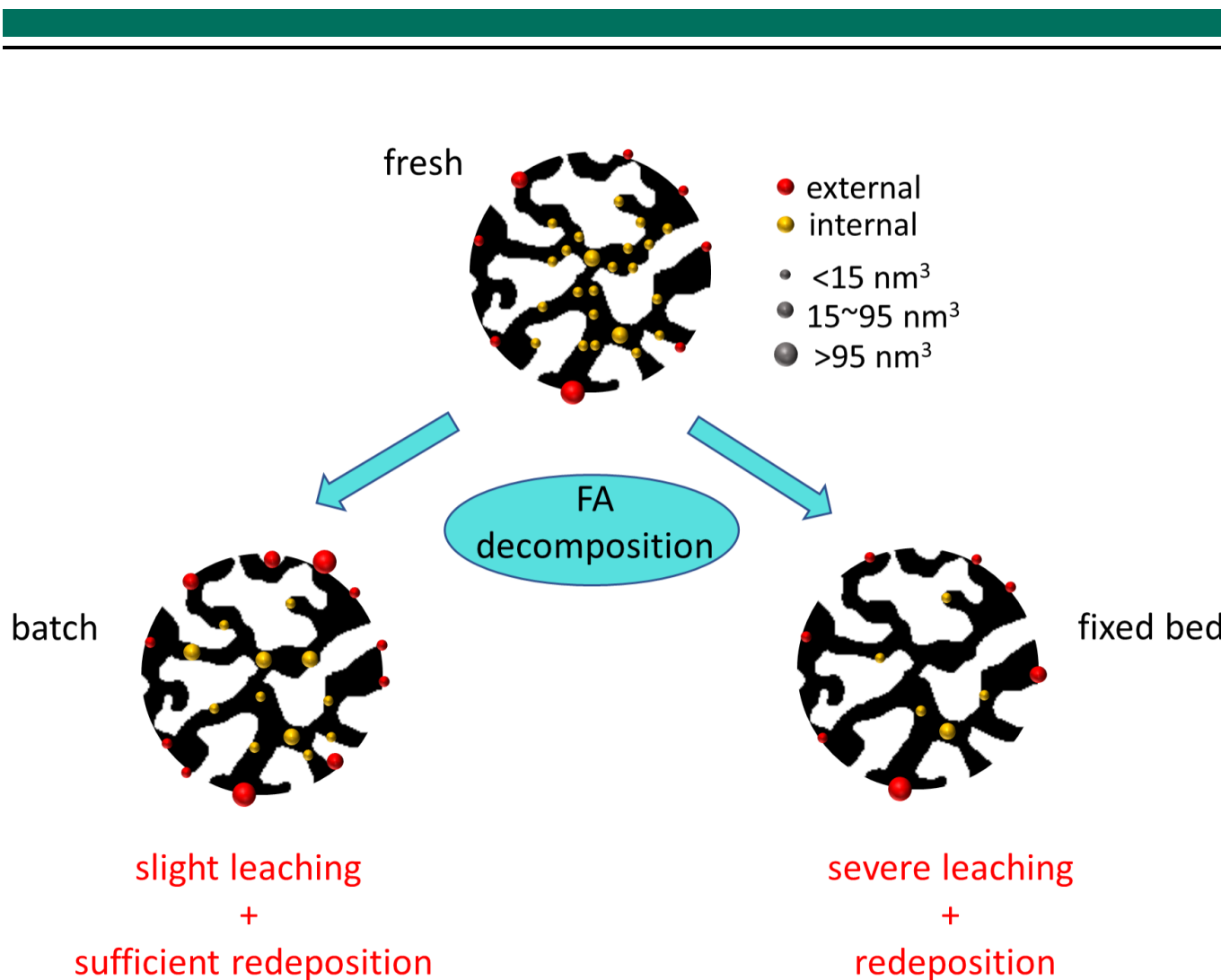
Figure 5.12: Schematic leaching and redeposition behavior of a Pd@CMK3 catalyst during formic acid decomposition in a batch and a fixed bed reactor.

The detailed structural analysis of Pd@CMK3 before and after FA decomposition provides a good understanding for the structure-performance relationship in batch and fixed bed reactors. In the fixed bed reactor, the catalyst reaches a high initial conversion during the first half hour due to the fast diffusion rate of the reactant and products by the flow of the reactants. However, as the reaction progresses, Pd nanoparticles are rapidly lost and only partially redeposited on the support surface, resulting in rapid deactivation of the catalyst. In contrast, leaching of Pd NPs in the batch reactor is much slower and the leached particles are able to redeposit both on the internal and external surfaces of the CMK3 support, thus allowing for a higher activity and better stability.

5.7. Conclusion

This work helps to unraveled the leaching and redeposition behavior of Pd@CMK3 during FA decomposition in batch and fixed bed reactors using a quantitative electron tomography analysis. The Pd NPs immobilized in mesoporous CMK3 show a higher FA conversion rate and stability in batch reactors compared to other catalysts discussed in literature such as Pd@HHT, probably due to the confinement effects of the mesopores

of CMK3. The amount of Pd leaching was measured by ICP-AES and EDS, both showing that Pd leaching from Pd@CMK3 is much more severe in the fixed bed than in the batch reactor. Quantitative analysis of the tomographic data enabled precise tracking of the evolution of the number and size distribution of the particles on the internal and external support surface. Based on the quantitative tomographic analysis, the 3D distribution of Pd NPs in the fresh and used catalysts was systematically investigated. For fresh Pd@CMK3, the particle size is quite homogenous everywhere in the support, on the internal and external support surface. After the reaction in the batch reactor, leaching decreased the fraction of small Pd particles (<15 nm^3) on the internal surface. Redeposition and ripening result in the formation of particles with intermediate size due to confinement effects inside the mesoporous space. A notable increase of the fraction of large particles (>95 nm^3) on the external surface was observed after the reaction, suggesting redeposition on the external surface. Sufficient redeposition of leached Pd NPs apparently helps to maintain a good catalytic performance during recycling tests. In contrast, more than half of the Pd was lost after the reaction in the fixed bed reactor, especially particles inside the porous support. This causes a fast deactivation during FA decomposition. However, redeposition was also observed in this case based on the increased fraction of Pd NPs on the external surface. These results demonstrate that quantitative tomography is essential for an in-depth understanding of the structural differences and how they affect the catalytic properties of a catalyst in different reactors. In turn, this information can be used to precisely design catalysts with desired properties to optimize the reaction conditions.

6. Summary and outlook

6.1. Summary

Electron tomography has become a powerful technique for imaging the 3D structure of mesoporous materials, while a quantitative and accurate interpretation of the solid/void network by ET is still a challenge due to constraints during tilt-series acquisition and reconstruction artifacts introduced by alignment errors and reconstruction algorithms. In this thesis, efforts to assess advanced reconstruction algorithms based on phantom simulations and to improve experimental data sampling by 360° ET have been performed to improve the reconstruction fidelity for mesopore structures.

In chapter 3, the tomographic reconstruction accuracy achievable by three main-stream algorithms (SIRT, TVM, DART) for mesoporous materials was evaluated based on a series of phantom simulations considering the most critical parameters for tilt series acquisition such as noise, missing wedge, number of projections and realistic misaligned effects. It was found that all three reconstruction algorithms provide a reasonable accuracy for the basic morphological description and the determination of diffusion properties of porous materials. However, DART turned out to provide the most accurate reconstruction, especially for small isolated pores and narrow channels with mainly slight randomly distributed errors in the reconstruction even in the presence of a typical missing wedge and realistic noise settings. TVM and SIRT based reconstructions result in segmented volumes with a noticeably higher relative number of misclassified pixels, which are not randomly distributed but tend to cluster leading to a breakup of structural features and a loss of small pores/necks. Therefore, they have a stronger effect on the morphological and diffusion properties. In terms to the reconstruction of experimental data, a systematic reconstruction parameter analysis for DART, indicates that noise level and a rough estimate of the structural sizes are the most important aspects to define the best reconstruction parameters.

In Chapter 4, a new sample preparation method that enables the transfer of selected individual nanoparticle or a few separated nanoparticles to a full range electron tomography holder tip has been proposed. This was achieved inside a standard FIB by employing an easily prepared tungsten tip and no other additional nano-manipulation setup was needed. The tungsten tip attaches a piece of carbon film supporting the specimen on it and is used to transfer them to the tomography holder tip. The carbon film remains stable during the acquisition of tilting series according to the well-aligned sinogram. As a proof of concept, the reconstruction results of Pt@hollow TiO_2 nanoparticles from a full range of projections showed no missing wedge artifacts compared to that from limited projections.

In Chapter 5, electron tomography was used to quantify the 3D distribution of Pd NPs supported on a mesoporous carbon (CMK3). The quantitative analysis clearly revealed the structural differences of Pd@CMK3 catalysts before and after formic acid decomposition in a batch and a fixed bed reactor. Pd particles are leached from the internal pores are turned to aggregate and redeposited on the external surface during the reaction in batch reactor, while more than half of the Pd species leached with only slight redeposition after

the reaction in fixed bed reactor. This structural difference could be correlated to their different deactivation velocity in formic acid dehydrogenation.

6.2. Outlook

Based on the fundamental study in Chapter 3, the proposed reconstruction parameter selection for the DART algorithm can be performed for real experimental data with a limited tilt range to investigate complex mesoporous materials, either with ordered or disordered pore structures. The resulting segmented reconstruction can be further used to analyze the transport properties inside the pore space. Considering the potential applications of ET for beam-sensitive materials and in situ studies, one concern could be beam damage of the specimen due to the long acquisition time of a tilt series. Although beam damage can be reduced by using larger tilt increments to reduce the electron dose during data acquisition, the reduction of the number of projections might also decrease the quality of final reconstruction. This problem might be solved by using the DART algorithm due to its promising ability in recovering small pores under large tilt increments. Similarity, this advantage of DART could be extended to the application of in situ studies, which enables the 3D observation of the structural evolution during heating or chemical reactions (such as oxidation and reduction).

Apart from the application for 3D morphological characterization by ET without missing wedge for catalyst nanoparticles as demonstrated in Chapter 4, the proposed new sample preparation method can also be extended to atomic electron tomography (AET) for precisely determining the 3D atomic positions for nanoparticles of interest. So far, few works have shown the possibility for the atomic resolution reconstruction using quantitative image processing and advance algorithms based on limited tilt series. [167], [169], [239] 360° ET would enable accessing more orientations and would thereby improve the reliability of atomically precise reconstruction, especially in the direction parallel to the electron beam. Another application that could benefit from this method is the quantitative analysis of mesoporous materials. In our previous work, it has been demonstrated that the missing wedge problem significantly limits the fidelity for 3D segmentation from a reconstruction. For example, diffusion property evaluation based on the structure model derived from DART reconstruction but with limited tilting angle range, still showed noticeable anisotropic errors, which could be attributed to the missing wedge artifacts. [12] This can be largely overcome by full-range ET so that reliable reconstructions can be achieved routinely by most of the mainstream reconstruction algorithms such as SIRT once the tilt series is well aligned and appropriate iteration numbers are performed.

With the fundamental study of the main-stream reconstruction algorithms and the experimental improvement of the data acquisition regarding the critical missing wedge problem, the methodology is now well developed for a quantitative 3D analysis of the mesoporous support. This can be used for a large number of applications with improved accuracy of reconstruction by combining a full tilt series with optimized parameters in DART. In addition to the application of a two-component system in chapter 3 and a three-component system in chapter 4 & 5, the promising ability of such 360° ET - DART technique can be extended to more complex materials with more (e.g. 4-5) components.

Reference

[1] R. L. Hay and R. A. Sheppard, "Occurrence of zeolites in sedimentary rocks: An overview", *Reviews in mineralogy and geochemistry*, vol. 45, no. 1, pp. 217–234, 2001.

[2] B. M. Al-Shehri, A. E. R. S. Khder, S. S. Ashour, and M. S. Hamdy, "A review: The utilization of mesoporous materials in wastewater treatment", *Materials Research Express*, vol. 6, 2019.

[3] M. Vallet-Regi, F. Balas, and D. Arcos, "Mesoporous materials for drug delivery", *Angew Chem Int Ed Engl*, vol. 46, no. 40, pp. 7548–58, 2007.

[4] M. Bouchoucha, M.-F. Côté, R. C.-Gaudreault, M.-A. Fortin, and F. Kleitz, "Size-controlled functionalized mesoporous silica nanoparticles for tunable drug release and enhanced anti-tumoral activity", *Chemistry of Materials*, vol. 28, no. 12, pp. 4243–4258, 2016.

[5] L. Zu, W. Zhang, L. Qu, L. Liu, W. Li, A. Yu, and D. Zhao, "Mesoporous materials for electrochemical energy storage and conversion", *Advanced Energy Materials*, vol. 10, no. 38, 2020.

[6] A. Eftekhari, "Ordered mesoporous materials for lithium-ion batteries", *Microporous and Mesoporous Materials*, vol. 243, pp. 355–369, 2017.

[7] A. Taguchi and F. Schüth, "Ordered mesoporous materials in catalysis", *Microporous and Mesoporous Materials*, vol. 77, no. 1, pp. 1–45, 2005.

[8] C. Perego and R. Millini, "Porous materials in catalysis: Challenges for mesoporous materials", *Chem Soc Rev*, vol. 42, no. 9, pp. 3956–76, 2013.

[9] F. Goettmann and C. Sanchez, "How does confinement affect the catalytic activity of mesoporous materials?", *J. Mater. Chem.*, vol. 17, no. 1, pp. 24–30, 2007.

[10] S. Wang, Q. Zhao, H. Wei, J.-Q. Wang, M. Cho, H. S. Cho, O. Terasaki, and Y. Wan, "Aggregation-free gold nanoparticles in ordered mesoporous carbons: Toward highly active and stable heterogeneous catalysts", *Journal of the American Chemical Society*, vol. 135, no. 32, pp. 11 849–11 860, 2013.

[11] D. Hlushkou, A. Svidrytski, and U. Tallarek, "Tracer-size-dependent pore space accessibility and long-time diffusion coefficient in amorphous, mesoporous silica", *The Journal of Physical Chemistry C*, vol. 121, no. 15, pp. 8416–8426, 2017.

[12] W. Wang, A. Svidrytski, D. Wang, A. Villa, H. Hahn, U. Tallarek, and C. Kubel, "Quantifying morphology and diffusion properties of mesoporous carbon from high-fidelity 3d reconstructions", *Microsc Microanal*, vol. 25, no. 4, pp. 891–902, 2019.

[13] U. Tallarek, J. Hochstrasser, F. Ziegler, X. Huang, C. Kübel, and M. R. Buchmeiser, "Olefin ring-closing metathesis under spatial confinement: Morphology–transport relationships", *ChemCatChem*, vol. 13, no. 1, pp. 281–292, 2020.

[14] J. Hochstrasser, E. Juere, F. Kleitz, W. Wang, C. Kubel, and U. Tallarek, "Insights into the intraparticle morphology of dendritic mesoporous silica nanoparticles from electron tomographic reconstructions", *J Colloid Interface Sci*, vol. 592, pp. 296–309, 2021.

[15] K. S. Sing, "Reporting physisorption data for gas/solid systems with special reference to the determination of surface area and porosity (recommendations 1984)", *Pure and applied chemistry*, vol. 57, no. 4, pp. 603–619, 1985.

[16] T. Yanagisawa, T. Shimizu, and C. Kuroda K.and Kato, "The preparation of alkyltrimethylammonium-kanemite complexes and their conversion to microporous materials", *Bulletin of the Chemical Society of Japan*, vol. 63, no. 4, pp. 988–992, 1990.

[17] A. Kresge, M. Leonowicz, R. W.J., J. Vartuli, and J. Beck, "Ordered mesoporous molecular sieves synthesized by a liquid-crystal template mechanism", *Nature*, vol. 359, no. 6397, pp. 710–712, 1992.

[18] M. Dubois, T. Gulik-Krzywicki, and B. Cabane., "Growth of silica polymers in a lamellar mesophase", *Langmuir*, vol. 9, no. 3, pp. 673–680, 1993.

[19] R. Mokaya, W. Zhou, and W. Jones, "A method for the synthesis of high quality large crystal mcm-41", *Chemical Communications*, vol. 1, pp. 51–52, 1999.

[20] J. Vartuli, K. Schmitt, C. Kresge, W. Roth, M. Leonowicz, S. McCullen, S. Hellring, J. Beck, J. Schlenker, and D. Olson, "Development of a formation mechanism for m41s materials", in *Studies in Surface Science and Catalysis*. Elsevier, 1994, vol. 84, pp. 53–60.

[21] D. Zhao, J. Feng, Q. Huo, N. Melosh, G. Fredrickson, B. Chmelka, and G. Stucky, "Triblock copolymer syntheses of mesoporous silica with periodic 50 to 300 angstrom pores", *Science*, vol. 279, no. 5350, pp. 548–552, 1998.

[22] P. Verma, Y. Kuwahara, K. Mori, R. Raja, and H. Yamashita, "Functionalized mesoporous sba-15 silica: Recent trends and catalytic applications", *Nanoscale*, vol. 12, no. 21, pp. 11 333–11 363, 2020.

[23] N. Hiyoshi, K. Yogo, and T. Yashima, "Adsorption characteristics of carbon dioxide on organically functionalized sba-15", *Microporous and Mesoporous Materials*, vol. 84, no. 1-3, pp. 357–365, 2005.

[24] X. Liu, L. Zhou, X. Fu, Y. Sun, W. Su, and Y. Zhou, "Adsorption and regeneration study of the mesoporous adsorbent sba-15 adapted to the capture/separation of co2 and ch4", *Chemical Engineering Science*, vol. 62, no. 4, pp. 1101–1110, 2007.

[25] C. Yu, Y. Yu, and D. Zhao, "Highly ordered large caged cubic mesoporous silica structures templated by triblock peo–pbo–peo copolymer", *Chemical Communications*, no. 7, pp. 575–576, 2000.

[26] J. Fan, C. Yu, F. Gao, J. Lei, B. Tian, L. Wang, Q. Luo, B. Tu, W. Zhou, and D. Zhao, "Cubic mesoporous silica with large controllable entrance sizes and advanced adsorption properties", *Angew Chem Int Ed Engl*, vol. 42, no. 27, pp. 3146–50, 2003.

[27] S. Bagshaw, E. Prouzet, and T. Pinnavaia, "Templating of mesoporous molecular sieves by nonionic polyethylene oxide surfactants", *Science*, vol. 269, no. 5228, pp. 1242–1244, 1995.

[28] F. Kleitz, S. H. Choi, and R. Ryoo, "Cubic ia3d large mesoporous silica: Synthesis and replication to platinum nanowires, carbon nanorods and carbon nanotubes", *Chem Commun (Camb)*, no. 17, pp. 2136–7, 2003.

[29] S. Che, A. E. Garcia-Bennett, T. Yokoi, K. Sakamoto, H. Kunieda, O. Terasaki, and T. Tatsumi, "A novel anionic surfactant templating route for synthesizing mesoporous silica with unique structure", *Nat Mater*, vol. 2, no. 12, pp. 801–5, 2003.

[30] R. Ryoo, S. Joo, and S. Jun, "Synthesis of highly ordered carbon molecular sieves via template-mediated structural transformation", *The Journal of Physical Chemistry B*, vol. 103, no. 37, pp. 7743–7746, 1999.

[31] S. Jun, S. Joo, R. Ryoo, M. Kruk, M. Jaroniec, Z. Liu, T. Ohsuna, and O. Terasaki, "Synthesis of new, nanoporous carbon with hexagonally ordered mesostructure", *J. Am. Chem. Soc.*, vol. 122, no. 43, pp. 10 712–10 713, 2000.

[32] R. Ryoo, S. Joo, S. Jun, T. Tsubakiyama, and O. Terasaki, "Ordered mesoporous carbon molecular sieves by templated synthesis: The structural varieties", *Stud Surf Sci Catal*, vol. 135, no. 1, pp. 150–158, 2001.

[33] K. S. Lakhi, D. H. Park, K. Al-Bahily, W. Cha, B. Viswanathan, J. H. Choy, and A. Vinu, "Mesoporous carbon nitrides: Synthesis, functionalization, and applications", *Chem Soc Rev*, vol. 46, no. 1, pp. 72–101, 2017.

[34] M. Colilla and M. Vallet-Regí, "Ordered mesoporous silica materials", in *Comprehensive Biomaterials*. 2011, pp. 497–514.

[35] Y. Ren, Z. Ma, and P. G. Bruce, "Ordered mesoporous metal oxides: Synthesis and applications", *Chem Soc Rev*, vol. 41, no. 14, pp. 4909–27, 2012.

[36] Y. Yue, Y. Li, C. A. Bridges, G. Rother, J. Zhang, J. Chen, D. K. Hensley, M. K. Kidder, B. C. Richardson, M. Parans Paranthaman, and S. Dai, "Hierarchically superstructured metal sulfides: Facile perturbation-assisted nanofusion synthesis and visible light photocatalytic characterizations", *ChemNanoMat*, vol. 2, no. 12, pp. 1104–1110, 2016.

[37] Y. Shi, Y. Wan, R. Zhang, and D. Zhao, "Synthesis of self-supported ordered mesoporous cobalt and chromium nitrides", *Advanced Functional Materials*, vol. 18, no. 16, pp. 2436–2443, 2008.

[38] W. Xuan, C. Zhu, Y. Liu, and Y. Cui, "Mesoporous metal-organic framework materials", *Chem Soc Rev*, vol. 41, no. 5, pp. 1677–95, 2012.

[39] C. Yang, B. Zibrowius, W. Schmidt, and F. Schüth, "Consecutive generation of mesopores and micropores in sba-15", *Chemistry of materials*, vol. 15, no. 20, pp. 3739–3741, 2003.

[40] M. Imperor-Clerc, P. Davidson, and A. Davidson, "Existence of a microporous corona around the mesopores of silica-based sba-15 materials templated by triblock copolymers", *Journal of the American Chemical Society,*, vol. 122, no. 48, pp. 11 925–11 933, 2000.

[41] A. Galarneau, H. Cambon, F. Di Renzo, and F. Fajula, "True microporosity and surface area of mesoporous sba-15 silicas as a function of synthesis temperature", *Langmuir*, vol. 17, no. 26, pp. 8328–8335, 2001.

[42] F. Kleitz, D. Liu, G. M. Anilkumar, I.-S. Park, L. A. Solovyov, A. N. Shmakov, and R. Ryoo, "Large cage face-centered-cubic fm3m mesoporous silica: Synthesis and structure", *The Journal of Physical Chemistry B*, vol. 107, no. 51, pp. 14 296–14 300, 2003.

[43] Y. Sakamoto, M. Kaneda, O. Terasaki, D. Zhao, J. Kim, G. Stucky, H. Shin, and R. Ryoo, "Direct imaging of the pores and cages of three-dimensional mesoporous materials", *Nature*, vol. 408, no. 6811, pp. 449–453, 2000.

[44] J. C. Vartuli, K. D. Schmitt, C. T. Kresge, W. J. Roth, M. E. Leonowicz, S. B. McCullen, S. D. Hellring, J. S. Beck, J. L. Schlenker, D. H. Olson, and E. W. Sheppard, "Development of a formation mechanism for m41s materials", in *Zeolites and Related Microporous Materials: State of the Art 1994 - Proceedings of the 10th International Zeolite Conference, Garmisch-Partenkirchen, Germany, 17-22 July 1994* (Studies in Surface Science and Catalysis), Studies in Surface Science and Catalysis. 1994, pp. 53–60.

[45] J. Rouquerol, D. Avnir, C. Fairbridge, D. Everett, J. Haynes, N. Pernicone, J. Ramsay, K. Sing, and K. Unger, "Recommendations for the characterization of porous solids (technical report)", *Pure and applied chemistry*, vol. 66, no. 8, pp. 1739–1758, 1994.

[46] F. Wang, Y. Cheng, S. Lu, K. Jin, and W. Zhao, "Influence of coalification on the pore characteristics of middle–high rank coal", *Energy & Fuels*, vol. 28, no. 9, pp. 5729–5736, 2014.

[47] F. Chang, J. Zhou, P. Chen, Y. Chen, H. Jia, S. M. Saad, Y. Gao, X. Cao, and T. Zheng, "Microporous and mesoporous materials for gas storage and separation: A review", *Asia-Pacific Journal of Chemical Engineering*, vol. 8, no. 4, pp. 618–626, 2013.

[48] Z. Wu and D. Zhao, "Ordered mesoporous materials as adsorbents", *Chem Commun (Camb)*, vol. 47, no. 12, pp. 3332–8, 2011.

[49] T. Wagner, S. Haffer, C. Weinberger, D. Klaus, and M. Tiemann, "Mesoporous materials as gas sensors", *Chem Soc Rev*, vol. 42, no. 9, pp. 4036–53, 2013.

[50] C. Perego and A. Bosetti, "Biomass to fuels: The role of zeolite and mesoporous materials", *Microporous and Mesoporous Materials*, vol. 144, no. 1-3, pp. 28–39, 2011.

[51] L. Yu, Y. Chen, M. Wu, X. Cai, H. Yao, L. Zhang, H. Chen, and J. Shi, ""manganese extraction" strategy enables tumor-sensitive biodegradability and theranostics of nanoparticles", *J Am Chem Soc*, vol. 138, no. 31, pp. 9881–94, 2016.

[52] F. Gritti, J. Hochstrasser, A. Svidrytski, D. Hlushkou, and U. Tallarek, "Morphology-transport relationships in liquid chromatography: Application to method development in size exclusion chromatography", *Journal of Chromatography A*, vol. 1620, p. 460 991, 2020.

[53] K. Taylor, J. Kim, W. Rieter, H. An, W. Lin, and W. Lin, "Mesoporous silica nanospheres as highly efficient mri contrast agents", *Journal of the American Chemical Society*, vol. 130, no. 7, pp. 2154–2155. 2008.

[54] M. Manzano and M. Vallet-Regi, "Ultrasound responsive mesoporous silica nanoparticles for biomedical applications", *Chem Commun (Camb)*, vol. 55, no. 19, pp. 2731–2740, 2019.

[55] H. Gustafsson, A. Kuchler, K. Holmberg, and P. Walde, "Co-immobilization of enzymes with the help of a dendronized polymer and mesoporous silica nanoparticles", *J Mater Chem B*, vol. 3, no. 30, pp. 6174–6184, 2015.

[56] H. Y. Chiu, W. Deng, H. Engelke, J. Helma, H. Leonhardt, and T. Bein, "Intracellular chromobody delivery by mesoporous silica nanoparticles for antigen targeting and visualization in real time", *Sci Rep*, vol. 6, p. 25 019, 2016.

[57] X. K. Wan, H. B. Wu, B. Y. Guan, D. Luan, and X. W. D. Lou, "Confining sub-nanometer pt clusters in hollow mesoporous carbon spheres for boosting hydrogen evolution activity", *Adv Mater*, vol. 32, no. 7, e1901349, 2020.

[58] I. M., T. Y., S. N., and N. S., "Remarkable effect of pore size on the catalytic activity of mesoporous silica for the acetalization of cyclohexanone with methanol", *JACS*, vol. 125, pp. 13 032–13 033, 2003.

[59] F. Ziegler, J. Teske, I. Elser, M. Dyballa, W. Frey, H. Kraus, N. Hansen, J. Rybka, U. Tallarek, and M. R. Buchmeiser, "Olefin metathesis in confined geometries: A biomimetic approach toward selective macrocyclization", *J Am Chem Soc*, vol. 141, no. 48, pp. 19 014–19 022, 2019.

[60] L. Peng, C. T. Hung, S. Wang, X. Zhang, X. Zhu, Z. Zhao, C. Wang, Y. Tang, W. Li, and D. Zhao, "Versatile nanoemulsion assembly approach to synthesize functional mesoporous carbon nanospheres with tunable pore sizes and architectures", *J Am Chem Soc*, vol. 141, no. 17, pp. 7073–7080, 2019.

[61] Y. Liu, K. Lan, S. Li, Y. Liu, B. Kong, G. Wang, P. Zhang, R. Wang, H. He, Y. Ling, A. M. Al-Enizi, A. A. Elzatahry, Y. Cao, G. Chen, and D. Zhao, "Constructing three-dimensional mesoporous bouquet-posy-like tio2 superstructures with radially oriented mesochannels and single-crystal walls", *J Am Chem Soc*, vol. 139, no. 1, pp. 517–526, 2017.

[62]   P. Horcajada, A. Rámila, J. Pérez-Pariente, and M. Vallet-Regıé, "Influence of pore size of mcm-41 matrices on drug delivery rate", *Microporous and Mesoporous Materials*, vol. 68, no. 1-3, pp. 105–109, 2004.

[63]   W. Wang, P. Wang, X. Tang, A. A. Elzatahry, S. Wang, D. Al-Dahyan, M. Zhao, C. Yao, C. T. Hung, X. Zhu, T. Zhao, X. Li, F. Zhang, and D. Zhao, "Facile synthesis of uniform virus-like mesoporous silica nanoparticles for enhanced cellular internalization", *ACS Cent Sci*, vol. 3, no. 8, pp. 839–846, 2017.

[64]   S. Brunauer, P. Emmett, and E. Teller, "Adsorption of gases in multimolecular layers", *Journal of the American chemical society*, vol. 60, no. 2, pp. 309–319, 1938.

[65]   M. Thommes and K. A. Cychosz, "Physical adsorption characterization of nanoporous materials: Progress and challenges", *Adsorption*, vol. 20, no. 2-3, pp. 233–250, 2014.

[66]   S. Lowell, J. E. Shields, M. A. Thomas, and M. Thommes, *Characterization of porous solids and powders: surface area, pore size and density*. Springer Science & Business Media, 2006, vol. 16, ISBN: 1402023022.

[67]   E. Barrett, L. Joyner, and P. Halenda, "The determination of pore volume and area distributions in porous substances. i. computations from nitrogen isotherms", *Journal of the American Chemical society*, vol. 73, no. 1, pp. 373–380, 1951.

[68]   M. Thommes, K. Kaneko, A. V. Neimark, J. P. Olivier, F. Rodriguez-Reinoso, J. Rouquerol, and K. S. W. Sing, "Physisorption of gases, with special reference to the evaluation of surface area and pore size distribution (iupac technical report)", *Pure and Applied Chemistry*, vol. 87, no. 9-10, pp. 1051–1069, 2015.

[69]   T. Young, "Iii. an essay on the cohesion of fluids", *Philosophical transactions of the royal society of London*, no. 95, pp. 65–87, 1805, ISSN: 0261-0523.

[70]   P. S. Laplace, *Traité de mécanique céleste*. de l Imprimerie de Crapelet, 1799, vol. 1.

[71]   E. W. Washburn, "The dynamics of capillary flow", *Physical review*, vol. 17, no. 3, p. 273, 1921.

[72]   H. Giesche, "Mercury porosimetry: A general (practical) overview", *Particle & Particle Systems Characterization*, vol. 23, no. 1, pp. 9–19, 2006.

[73]   S. Diamond, "Mercury porosimetry: An inappropriate method for the measurement of pore size distributions in cement-based materials", *Cement and concrete research*, vol. 30, no. 10, pp. 1517–1525, 2000.

[74]   A. Guinier, G. Fournet, and K. L. Yudowitch, "Small-angle scattering of x-rays", 1955.

[75]   T. Li, A. J. Senesi, and B. Lee, "Small angle x-ray scattering for nanoparticle research", *Chem Rev*, vol. 116, no. 18, pp. 11 128–80, 2016.

[76]   K. Kaneko, "Determination of pore size and pore size distribution: 1. adsorbents and catalysts.", *Journal of membrane science*, vol. 96, no. 1-2, pp. 59–89, 1994.

[77]   G. Porod, "Die röntgenkleinwinkelstreuung von dichtgepackten kolloiden systemen", *Kolloid-Zeitschrift*, vol. 124, no. 2, pp. 83–114, 1951.

[78]   H. Schnablegger and Y. Singh, "The saxs guide. getting acquainted with the principles", *Austria: Anton Paar GmbH*, pp. 1–124, 2013.

[79]   P. A. Midgley and R. E. Dunin-Borkowski, "Electron tomography and holography in materials science", *Nat Mater*, vol. 8, no. 4, pp. 271–80, 2009.

[80] S. Weber, K. L. Abel, R. T. Zimmermann, X. Huang, J. Bremer, L. K. Rihko-Struckmann, D. Batey, S. Cipiccia, J. Titus, D. Poppitz, C. Kübel, K. Sundmacher, R. Gläser, and T. L. Sheppard, "Porosity and structure of hierarchically porous ni/al2o3 catalysts for co2 methanation", *Catalysts*, vol. 10, no. 12, 2020.

[81] E. Ozkan, A. Hofmann, M. Votsmeier, W. Wang, X. Huang, C. Kubel, F. Badaczewski, K. Turke, S. Werner, and B. M. Smarsly, "Comprehensive characterization of a mesoporous cerium oxide nanomaterial with high surface area and high thermal stability", *Langmuir*, vol. 37, no. 8, pp. 2563–2574, 2021.

[82] A. Janssen, A. Koster, and K. de Jong, "Three-dimensional transmission electron microscopic observations of mesopores in dealuminated zeolite y", *Angewandte Chemie International Edition*, vol. 40, no. 6, pp. 1102–1104, 2001.

[83] K. P. de Jong, J. Zecevic, H. Friedrich, P. E. de Jongh, M. Bulut, S. van Donk, R. Kenmogne, A. Finiels, V. Hulea, and F. Fajula, "Zeolite y crystals with trimodal porosity as ideal hydrocracking catalysts", *Angew Chem Int Ed Engl*, vol. 49, no. 52, pp. 10 074–8, 2010.

[84] A. Koster, U. Ziese, A. Verkleij, A. Janssen, and K. De Jong, "Three-dimensional transmission electron microscopy: A novel imaging and characterization technique with nanometer scale resolution for materials science", *The Journal of Physical Chemistry B*, vol. 104, no. 40, pp. 9368–9370, 2000.

[85] A. Janssen, A. Koster, and K. de Jong, "On the shape of the mesopores in zeolite y: A three-dimensional transmission electron microscopy study combined with texture analysis", *The Journal of Physical Chemistry B*, vol. 106, no. 46, pp. 11 905–11 909, 2002.

[86] J. Zecevic, C. J. Gommes, H. Friedrich, P. E. de Jongh, and K. P. de Jong, "Mesoporosity of zeolite y: Quantitative three-dimensional study by image analysis of electron tomograms", *Angew Chem Int Ed Engl*, vol. 51, no. 17, pp. 4213–7, 2012.

[87] A. H. Janssen, I. Schmidt, C. J. H. Jacobsen, A. J. Koster, and K. P. de Jong, "Exploratory study of mesopore templating with carbon during zeolite synthesis", *Microporous and Mesoporous Materials*, vol. 65, no. 1, pp. 59–75, 2003.

[88] S. van Donk, A. H. Janssen, J. H. Bitter, and K. P. de Jong, "Generation, characterization, and impact of mesopores in zeolite catalysts", *Catalysis Reviews*, vol. 45, no. 2, pp. 297–319, 2003.

[89] J. Hochstrasser, A. Svidrytski, A. Holtzel, T. Priamushko, F. Kleitz, W. Wang, C. Kubel, and U. Tallarek, "Morphology-transport relationships for sba-15 and kit-6 ordered mesoporous silicas", *Phys Chem Chem Phys*, vol. 22, no. 20, pp. 11 314–11 326, 2020.

[90] S.-J. Reich, A. Svidrytski, A. Höltzel, J. Florek, F. Kleitz, W. Wang, C. Kübel, D. Hlushkou, and U. Tallarek, "Hindered diffusion in ordered mesoporous silicas: Insights from pore-scale simulations in physical reconstructions of sba-15 and kit-6 silica", *The Journal of Physical Chemistry C*, vol. 122, no. 23, pp. 12 350–12 361, 2018.

[91] T. J. V. Yates, J. M. Thomas, J.-J. Fernandez, O. Terasaki, R. Ryoo, and P. A. Midgley, "Three-dimensional real-space crystallography of mcm-48 mesoporous silica revealed by scanning transmission electron tomography", *Chemical Physics Letters*, vol. 418, no. 4-6, pp. 540–543, 2006.

[92] O. Ersen, J. Parmentier, L. Solovyov, M. Drillon, C. Pham-Huu, J. Werckmann, and P. Schultz, "Direct observation of stacking faults and pore connections in ordered cage-type mesoporous silica fdu-12 by electron tomography", *Journal of the American Chemical Society*, vol. 130, no. 49, pp. 16 800–16 806, 2008.

[93] E. Castillejos, P. J. Debouttiere, L. Roiban, A. Solhy, V. Martinez, Y. Kihn, O. Ersen, K. Philippot, B. Chaudret, and P. Serp, "An efficient strategy to drive nanoparticles into carbon nanotubes and the remarkable effect of confinement on their catalytic performance", *Angew Chem Int Ed Engl*, vol. 48, no. 14, pp. 2529–33, 2009.

[94] A. Villa, D. Wang, C. E. Chan-Thaw, S. Campisi, G. M. Veith, and L. Prati, "The confinement effect on the activity of au nps in polyol oxidation", *Catalysis Science & Technology*, vol. 6, no. 3, pp. 598–601, 2016.

[95] X. Pan and X. Bao, "The effects of confinement inside carbon nanotubes on catalysis", *Accounts of chemical research*, vol. 44, no. 8, pp. 553–562, 2011.

[96] A. Janssen, C. Yang, Y. Wang, F. Schüth, A. Koster, and K. De Jong, "Localization of small metal (oxide) particles in sba-15 using bright-field electron tomography", *The Journal of Physical Chemistry B*, vol. 107, no. 38, pp. 10 552–10 556, 2003.

[97] H. Friedrich, J. Sietsma, P. De Jongh, A. Verkleij, and K. De Jong, "Measuring location, size, distribution, and loading of nio crystallites in individual sba-15 pores by electron tomography", *Journal of the American Chemical Society*, vol. 129, no. 33, pp. 10 249–10 254, 2007.

[98] G. Prieto, J. Zecevic, H. Friedrich, K. P. de Jong, and P. E. de Jongh, "Towards stable catalysts by controlling collective properties of supported metal nanoparticles", *Nat Mater*, vol. 12, no. 1, pp. 34–9, 2013.

[99] E. Ward, T. Yates, J. Fernandez, D. Vaughan, and P. Midgley, "Three-dimensional nanoparticle distribution and local curvature of heterogeneous catalysts revealed by electron tomography", *The Journal of Physical Chemistry C*, vol. 111, no. 31, pp. 11 501–11 505, 2007.

[100] P. Midgley, J. Thomas, L. Laffont, M. Weyland, R. Raja, B. Johnson, and T. Khimyak, "High-resolution scanning transmission electron tomography and elemental analysis of zeptogram quantities of heterogeneous catalyst", *The Journal of Physical Chemistry B*, vol. 108, no. 15, pp. 4590–4592, 2004.

[101] W. Wang, A. Villa, C. Kübel, H. Hahn, and D. Wang, "Tailoring the 3d structure of pd nanocatalysts supported on mesoporous carbon for furfural hydrogenation", *ChemNanoMat*, vol. 4, no. 11, pp. 1125–1132, 2018.

[102] Y. Liu, Y. Zhai, Y. Xia, W. Li, and D. Zhao, "Recent progress of porous materials in lithium-metal batteries", *Small Structures*, vol. 2, no. 5, 2021.

[103] F. Lin, D. Nordlund, T. C. Weng, Y. Zhu, C. Ban, R. M. Richards, and H. L. Xin, "Phase evolution for conversion reaction electrodes in lithium-ion batteries", *Nat Commun*, vol. 5, p. 3358, 2014.

[104] X. Jin, Y. Han, Z. Zhang, Y. Chen, J. Li, T. Yang, X. Wang, W. Li, X. Han, Z. Wang, X. Liu, H. Jiao, X. Ke, M. Sui, R. Cao, G. Zhang, Y. Tang, P. Yan, and S. Jiao, "Mesoporous single-crystal lithium titanate enabling fast-charging li-ion batteries", *Adv Mater*, e2109356, 2022.

[105] Y. Yao, K. J. Czymmek, R. Pazhianur, and A. M. Lenhoff, "Three-dimensional pore structure of chromatographic adsorbents from electron tomography", *Langmuir*, vol. 22, no. 26, pp. 11 148–11 157, 2006.

[106] T. J. Slater, A. Macedo, S. L. Schroeder, M. G. Burke, P. O Brien, P. H. Camargo, and S. J. Haigh, "Correlating catalytic activity of ag-au nanoparticles with 3d compositional variations", *Nano Lett*, vol. 14, no. 4, pp. 1921–6, 2014.

[107] K. Jarausch, P. Thomas, D. N. Leonard, R. Twesten, and C. R. Booth, "Four-dimensional stem-eels: Enabling nano-scale chemical tomography", *Ultramicroscopy*, vol. 109, no. 4, pp. 326–37, 2009.

[108]   B. Goris, S. Turner, S. Bals, and G. Van Tendeloo, "Three-dimensional valency mapping in ceria nanocrystals", *ACS nano*, vol. 8, no. 10, pp. 10 878–10 884, 2014.

[109]   O. Nicoletti, F. de la Pena, R. K. Leary, D. J. Holland, C. Ducati, and P. A. Midgley, "Three-dimensional imaging of localized surface plasmon resonances of metal nanoparticles", *Nature*, vol. 502, no. 7469, pp. 80–4, 2013.

[110]   S. Bals, B. Goris, L. M. Liz-Marzan, and G. Van Tendeloo, "Three-dimensional characterization of noble-metal nanoparticles and their assemblies by electron tomography", *Angew Chem Int Ed Engl*, vol. 53, no. 40, pp. 10 600–10, 2014.

[111]   P. Torruella, R. Arenal, F. de la Pena, Z. Saghi, L. Yedra, A. Eljarrat, L. Lopez-Conesa, M. Estrader, A. Lopez-Ortega, G. Salazar-Alvarez, J. Nogues, C. Ducati, P. A. Midgley, F. Peiro, and S. Estrade, "3d visualization of the iron oxidation state in feo/fe3o4 core-shell nanocubes from electron energy loss tomography", *Nano Lett*, vol. 16, no. 8, pp. 5068–73, 2016.

[112]   N. Y. Jin-Phillipp, C. T. Koch, and P. A. van Aken, "Toward quantitative core-loss eftem tomography", *Ultramicroscopy*, vol. 111, no. 8, pp. 1255–61, 2011.

[113]   G. Möbus, R. C. Doole, and B. J. Inkson, "Spectroscopic electron tomography", *Ultramicroscopy*, vol. 96, no. 3-4, pp. 433–451, 2003.

[114]   G. Cliff and G. Lorimer, "The quantitative analysis of thin specimens", *Journal of Microscopy*, vol. 103, no. 2, pp. 203–207, 1975.

[115]   D. Zanaga, T. Altantzis, J. Sanctorum, B. Freitag, and S. Bals, "An alternative approach for zeta-factor measurement using pure element nanoparticles", *Ultramicroscopy*, vol. 164, pp. 11–6, 2016.

[116]   P. Burdet, Z. Saghi, A. N. Filippin, A. Borras, and P. A. Midgley, "A novel 3d absorption correction method for quantitative edx-stem tomography", *Ultramicroscopy*, vol. 160, pp. 118–129, 2016.

[117]   T. J. A. Slater, A. Janssen, P. H. C. Camargo, M. G. Burke, N. J. Zaluzec, and S. J. Haigh, "Stem-edx tomography of bimetallic nanoparticles: A methodological investigation", *Ultramicroscopy*, vol. 162, pp. 61–73, 2016.

[118]   W. Albrecht and S. Bals, "Fast electron tomography for nanomaterials", *The Journal of Physical Chemistry C*, vol. 124, no. 50, pp. 27 276–27 286, 2020.

[119]   S. Koneti, L. Roiban, F. Dalmas, C. Langlois, A.-S. Gay, A. Cabiac, T. Grenier, H. Banjak, V. Maxim, and T. Epicier, "Fast electron tomography: Applications to beam sensitive samples and in situ tem or operando environmental tem studies", *Materials Characterization*, vol. 151, pp. 480–495, 2019.

[120]   L. Roiban, S. Li, M. Aouine, A. Tuel, D. Farrusseng, and T. Epicier, "Fast operando electron nanotomography", *J Microsc*, vol. 269, no. 2, pp. 117–126, 2018.

[121]   H. Vanrompay, E. Bladt, W. Albrecht, A. Beche, M. Zakhozheva, A. Sanchez-Iglesias, L. M. Liz-Marzan, and S. Bals, "3d characterization of heat-induced morphological changes of au nanostars by fast in situ electron tomography", *Nanoscale*, vol. 10, no. 48, pp. 22 792–22 801, 2018.

[122]   W. Albrecht, E. Bladt, H. Vanrompay, J. D. Smith, S. E. Skrabalak, and S. Bals, "Thermal stability of gold/palladium octopods studied in situ in 3d: Understanding design rules for thermally stable metal nanoparticles", *ACS Nano*, vol. 13, no. 6, pp. 6522–6530, 2019.

[123]   A. Skorikov, W. Albrecht, E. Bladt, X. Xie, J. E. S. van der Hoeven, A. van Blaaderen, S. Van Aert, and S. Bals, "Quantitative 3d characterization of elemental diffusion dynamics in individual ag@au nanoparticles with different shapes", *ACS Nano*, vol. 13, no. 11, pp. 13 421–13 429, 2019.

[124] T. Printemps, G. Mula, D. Sette, P. Bleuet, V. Delaye, N. Bernier, A. Grenier, G. Audoit, N. Gambacorti, and L. Herve, "Self-adapting denoising, alignment and reconstruction in electron tomography in materials science", *Ultramicroscopy*, vol. 160, pp. 23–34, 2016.

[125] A. Zurner, M. Doblinger, V. Cauda, R. Wei, and T. Bein, "Discrete tomography of demanding samples based on a modified sirt algorithm", *Ultramicroscopy*, vol. 115, pp. 41–9, 2012.

[126] J. M. Muñoz-Ocaña, A. Bouziane, F. Sakina, R. T. Baker, A. B. Hungría, J. J. Calvino, A. M. Rodríguez-Chía, and M. López-Haro, "Optimization of stem-haadf electron tomography reconstructions by parameter selection in compressed sensing total variation minimization-based algorithms", *Particle & Particle Systems Characterization*, vol. 37, no. 6, 2020.

[127] B. Goris, W. Van den Broek, K. J. Batenburg, H. Heidari Mezerji, and S. Bals, "Electron tomography based on a total variation minimization reconstruction technique", *Ultramicroscopy*, vol. 113, pp. 120–130, 2012.

[128] G. Van Eyndhoven, M. Kurttepeli, C. J. Van Oers, P. Cool, S. Bals, K. J. Batenburg, and J. Sijbers, "Pore reconstruction and segmentation (pores) method for improved porosity quantification of nanoporous materials", *Ultramicroscopy*, vol. 148, pp. 10–19, 2015.

[129] K. J. Batenburg and J. Sijbers, "Dart: A practical reconstruction algorithm for discrete tomography", *IEEE Trans Image Process*, vol. 20, no. 9, pp. 2542–53, 2011.

[130] D. N. Mastronarde, "Dual-axis tomography: An approach with alignment methods that preserve resolution", *Journal of structural biology*, vol. 120, no. 3, pp. 343–352, 1997.

[131] I. Arslan, J. R. Tong, and P. A. Midgley, "Reducing the missing wedge: High-resolution dual axis tomography of inorganic materials", *Ultramicroscopy*, vol. 106, no. 11-12, pp. 994–1000, 2006.

[132] S. Lanzavecchia, F. Cantele, P. L. Bellon, L. Zampighi, M. Kreman, E. Wright, and G. A. Zampighi, "Conical tomography of freeze-fracture replicas: A method for the study of integral membrane proteins inserted in phospholipid bilayers", *J Struct Biol*, vol. 149, no. 1, pp. 87–98, 2005.

[133] D. J. Larson, T. Prosa, R. M. Ulfig, B. P. Geiser, and T. F. Kelly, "Local electrode atom probe tomography", *New York, US: Springer Science*, vol. 2, 2013.

[134] K. Jarausch and D. N. Leonard, "Three-dimensional electron microscopy of individual nanoparticles", *J Electron Microsc (Tokyo)*, vol. 58, no. 3, pp. 175–83, 2009.

[135] M. Distaso, B. Apeleo Zubiri, A. Mohtasebi, A. Inayat, M. Dudák, P. Kočí, B. Butz, R. Klupp Taylor, W. Schwieger, E. Spiecker, and W. Peukert, "Three-dimensional and quantitative reconstruction of non-accessible internal porosity in hematite nanoreactors using 360° electron tomography", *Microporous and Mesoporous Materials*, vol. 246, pp. 207–214, 2017.

[136] E. Padgett, R. Hovden, J. C. DaSilva, B. D. A. Levin, J. L. Grazul, T. Hanrath, and D. A. Muller, "A simple preparation method for full-range electron tomography of nanoparticles and fine powders", *Microsc Microanal*, vol. 23, no. 6, pp. 1150–1158, 2017.

[137] T. Przybilla, B. A. Zubiri, A. M. Beltrán, B. Butz, A. G. F. Machoke, A. Inayat, M. Distaso, W. Peukert, W. Schwieger, and E. Spiecker, "Transfer of individual micro- and nanoparticles for high-precision 3d analysis using 360° electron tomography", *Small Methods*, vol. 2, no. 1, 2018.

[138] B. Apeleo Zubiri, J. Wirth, D. Drobek, S. Englisch, T. Przybilla, T. Weissenberger, W. Schwieger, and E. Spiecker, "Correlative laboratory nano-ct and 360° electron tomography of macropore structures in hierarchical zeolites", *Advanced Materials Interfaces*, vol. 8, no. 4, 2020.

[139] B. Goris, T. Roelandts, K. J. Batenburg, H. Heidari Mezerji, and S. Bals, "Advanced reconstruction algorithms for electron tomography: From comparison to combination", *Ultramicroscopy*, vol. 127, pp. 40–7, 2013.

[140] D. Chen, B. Goris, F. Bleichrodt, H. H. Mezerji, S. Bals, K. J. Batenburg, G. de With, and H. Friedrich, "The properties of sirt, tvm, and dart for 3d imaging of tubular domains in nanocomposite thin-films and sections", *Ultramicroscopy*, vol. 147, pp. 137–48, 2014.

[141] J. Radon, "Über die bestimmung von funktionen durch ihre integralwerte längs gewisser mannig-faltigkeiten", *Ber. Verh. Sächs Akad. Wiss.*, vol. 69, pp. 262–277, 1917.

[142] J. Radon and P. translator: Parks, "On the determination of functions from their integral values along certain manifolds", *IEEE transactions on medical imaging*, vol. 5, no. 4, pp. 170–176, 1986.

[143] A. Cormack, "Representation of a function by its line integrals, with some radiological applications", *Journal of applied physics*, vol. 34, no. 9, pp. 2722–2727, 1963.

[144] G. N. Hounsfield, "A method of and apparatus for examination of a body by radiation such as x-ray or gamma radiation", *Patent Specification 1283915*, 1972.

[145] A. De Rosier D.J.and Klug, "Reconstruction of three dimensional structures from electron micrographs", *Nature*, vol. 271, no. 5124, pp. 130–134, 1968.

[146] W. Hoppe, R. Langer, G. Knesch, and C. Poppe, "Protein-kristallstrukturanalyse mit elektronenstrahlen", *Naturwissenschaften*, vol. 55, no. 7, pp. 333–336, 1968.

[147] R. Hart, "Electron microscopy of unstained biological material: The polytropic montage", *Science*, vol. 159, no. 3822, pp. 1464–1467, 1968.

[148] M. Spontak R.J.and Williams and D. Agard, "Three-dimensional study of cylindrical morphology in a styrene-butadiene-styrene block copolymer", *Polymer*, vol. 29, no. 3, pp. 387–395, 1988.

[149] P. A. Midgley and M. Weyland, "3d electron microscopy in the physical sciences: The development of z-contrast and eftem tomography", *Ultramicroscopy*, vol. 96, no. 3-4, pp. 413–431, 2003.

[150] M. Weyland, P. Midgley, and J. Thomas, "Electron tomography of nanoparticle catalysts on porous supports: A new technique based on rutherford scattering", *The Journal of Physical Chemistry B*, vol. 105, no. 33, pp. 7882–7886, 2001.

[151] D. B. Williams and C. B. Carter, "Transmission electron microscopy", *Systematic Materials Analysis*, vol. 4, pp. 407–432, 1978.

[152] B. J. Inkson, "Scanning electron microscopy (sem) and transmission electron microscopy (tem) for materials characterization", in *Materials characterization using nondestructive evaluation (NDE) methods*. Elsevier, 2016, pp. 17–43.

[153] Web Page. [Online]. Available: `https://en.wikipedia.org/wiki/Transmission_electron_microscopy;%20https://en.wikipedia.org/wiki/Scanning_transmission_electron_microscopy`.

[154] Y. Ma, R. Zhang, Y. Tang, Y. Ma, J. H. Teo, T. Diemant, D. Goonetilleke, J. Janek, M. Bianchini, A. Kondrakov, *et al.*, "Single-to few-layer nanoparticle cathode coating for thiophosphate-based all-solid-state batteries", *ACS Nano*, 2022.

[155] D. Kitsche, F. Strauss, Y. Tang, N. Bartnick, A.-Y. Kim, Y. Ma, C. Kübel, J. Janek, and T. Brezesinski, "A quasi-multinary composite coating on a nickel-rich ncm cathode material for all-solid-state batteries", *Batteries & Supercaps*, e202100397, 2022.

[156] Y. Ma, J. H. Teo, F. Walther, Y. Ma, R. Zhang, A. Mazilkin, Y. Tang, D. Goonetilleke, J. Janek, M. Bianchini, *et al.*, "Advanced nanoparticle coatings for stabilizing layered ni-rich oxide cathodes in solid-state batteries", *Advanced Functional Materials*, p. 2 111 829, 2022.

[157] P. W. Hawkes, "The electron microscope as a structure projector", in *Electron Tomography: Three-Dimensional Imaging with the Transmission Electron Microscope*, J. Frank, Ed. Boston, MA: Springer US, 1992, pp. 17–38.

[158] J. Banhart, *Advanced tomographic methods in materials research and engineering*. OUP Oxford, 2008, vol. 66.

[159] R. K. Leary and P. A. Midgley, "Electron tomography in materials science", in *Springer Handbook of Microscopy*, P. W. Hawkes and J. C. H. Spence, Eds. Cham: Springer International Publishing, 2019, pp. 1279–1329.

[160] J. Frank, "Electron tomography: Methods for three-dimensional visualization of structures in the cell", *Springer*, 2006.

[161] I. Arslan, T. Yates, N. Browning, and P. Midgley, "Embedded nanostructures revealed in three dimensions", *Science*, vol. 309, no. 5744, pp. 2195–2198, 2005.

[162] A. B. Hungría, J. J. Calvino, and J. C. Hernández-Garrido, "Haadf-stem electron tomography in catalysis research", *Topics in Catalysis*, vol. 62, no. 12-16, pp. 808–821, 2019.

[163] X. Ke, S. Bals, D. Cott, T. Hantschel, H. Bender, and G. Van Tendeloo, "Three-dimensional analysis of carbon nanotube networks in interconnects by electron tomography without missing wedge artifacts", *Microsc Microanal*, vol. 16, no. 2, pp. 210–7, 2010.

[164] E. Biermans, L. Molina, K. J. Batenburg, S. Bals, and G. Van Tendeloo, "Measuring porosity at the nanoscale by quantitative electron tomography", *Nano Lett*, vol. 10, no. 12, pp. 5014–9, 2010.

[165] R. Crowther, D. DeRosier, and A. Klug, "The reconstruction of a three-dimensional structure from projections and its application to electron microscopy", *Proceedings of the Royal Society of London. A. Mathematical and Physical Sciences*, vol. 317, no. 1530, pp. 319–340, 1997.

[166] G. R., "Determination of a common origin in the micrographs of tilt series in three-dimensional electron microscopy", *Ultramicroscopy*, vol. 9, no. 1-2, pp. 167–173, 1982.

[167] M. C. Scott, C. C. Chen, M. Mecklenburg, C. Zhu, R. Xu, P. Ercius, U. Dahmen, B. C. Regan, and J. Miao, "Electron tomography at 2.4-angstrom resolution", *Nature*, vol. 483, no. 7390, pp. 444–7, 2012.

[168] Y. Yang, J. Zhou, F. Zhu, Y. Yuan, D. J. Chang, D. S. Kim, M. Pham, A. Rana, X. Tian, Y. Yao, S. J. Osher, A. K. Schmid, L. Hu, P. Ercius, and J. Miao, "Determining the three-dimensional atomic structure of an amorphous solid", *Nature*, vol. 592, no. 7852, pp. 60–64, 2021.

[169] J. Miao, P. Ercius, and S. J. Billinge, "Atomic electron tomography: 3d structures without crystals", *Science*, vol. 353, no. 6306, 2016.

[170] R. Bracewell, "Strip integration in radio astronomy", *Australian Journal of Physics*, vol. 9, no. 2, pp. 198–217, 1956.

[171] H. Friedrich, P. De Jongh, A. Verkleij, and K. De Jong, "Electron tomography for heterogeneous catalysts and related nanostructured materials", *Chemical reviews*, vol. 109, no. 5, pp. 1613–1629, 2009.

[172] S. Karczmarz, "Angenaherte auflosung von systemen linearer glei-chungen", *Bull. Int. Acad. Pol. Sic. Let., Cl. Sci. Math. Nat.*, pp. 355–357, 1937.

[173] R. Gordon, R. Bender, and G. T. Herman, "Algebraic reconstruction techniques (art) for three-dimensional electron microscopy and x-ray photography", *J. theor. Biol.*, 1970.

[174] P. Gilbert, "Iterative methods for the three-dimensional reconstruction of an object from projections", *J. theor. Biol.*, vol. 36, no. 1, pp. 105–117, 1972.

[175] J. Park, H. Elmlund, P. Ercius, J. Yuk, D. Limmer, Q. Chen, K. Kim, S. Han, D. Weitz, A. Zettl, and A. Alivisatos, "3d structure of individual nanocrystals in solution by electron microscopy", *Science*, vol. 349, no. 6245, pp. 290–295, 2015.

[176] J. Pryor A., Y. Yang, A. Rana, M. Gallagher-Jones, J. Zhou, Y. H. Lo, G. Melinte, W. Chiu, J. A. Rodriguez, and J. Miao, "Genfire: A generalized fourier iterative reconstruction algorithm for high-resolution 3d imaging", *Sci Rep*, vol. 7, no. 1, p. 10 409, 2017.

[177] S. Venkatakrishnan, L. Drummy, M. Jackson, M. De Graef, J. Simmons, and C. Bouman, "Bayesian tomographic reconstruction for high angle annular dark field (haadf) scanning transmission electron microscopy (stem)", in *2012 IEEE Statistical Signal Processing Workshop (SSP)*, IEEE, pp. 680–683.

[178] M. Azubel, J. Koivisto, S. Malola, D. Bushnell, G. Hura, A. Koh, H. Tsunoyama, T. Tsukuda, M. Pettersson, H. Häkkinen, and R. Kornberg, "Electron microscopy of gold nanoparticles at atomic resolution", *Science*, vol. 345, no. 6199, pp. 909–912, 2014.

[179] Y. Yang, C. C. Chen, M. C. Scott, C. Ophus, R. Xu, A. Pryor, L. Wu, F. Sun, W. Theis, J. Zhou, M. Eisenbach, P. R. Kent, R. F. Sabirianov, H. Zeng, P. Ercius, and J. Miao, "Deciphering chemical order/disorder and material properties at the single-atom level", *Nature*, vol. 542, no. 7639, pp. 75–79, 2017.

[180] J. Zhou, Y. Yang, Y. Yang, D. S. Kim, A. Yuan, X. Tian, C. Ophus, F. Sun, A. K. Schmid, M. Nathanson, H. Heinz, Q. An, H. Zeng, P. Ercius, and J. Miao, "Observing crystal nucleation in four dimensions using atomic electron tomography", *Nature*, vol. 570, no. 7762, pp. 500–503, 2019.

[181] Y. Chen, J. Ma, Q. Feng, L. Luo, P. Shi, and W. Chen, "Nonlocal prior bayesian tomographic reconstruction", *Journal of Mathematical Imaging and Vision*, vol. 30, no. 2, pp. 133–146, 2007.

[182] D. Pelt, K. Batenburg, and J. Sethian, "Improving tomographic reconstruction from limited data using mixed-scale dense convolutional neural networks", *Journal of Imaging*, vol. 4, no. 11, 2018.

[183] E. Bladt, D. M. Pelt, S. Bals, and K. J. Batenburg, "Electron tomography based on highly limited data using a neural network reconstruction technique", *Ultramicroscopy*, vol. 158, pp. 81–8, 2015.

[184] W. van Aarle, K. J. Batenburg, and J. Sijbers, "Optimal threshold selection for segmentation of dense homogeneous objects in tomographic reconstructions", *IEEE Trans Med Imaging*, vol. 30, no. 4, pp. 980–9, 2011.

[185] N. Volkmann, "Methods for segmentation and interpretation of electron tomographic reconstructions", in *Cryo-EM, Part C: Analyses, Interpretation, and Case studies* (Methods in Enzymology), Methods in Enzymology. 2010, pp. 31–46.

[186] J. Zečević, K. P. de Jong, and P. E. de Jongh, "Progress in electron tomography to assess the 3d nanostructure of catalysts", *Current Opinion in Solid State and Materials Science*, vol. 17, no. 3, pp. 115–125, 2013.

[187] N. otsu, "A tlreshold selection method from gray-level histograms", *IEEE Trans Image Process*, 1979.

[188] T. Kanungo, D. M. Mount, N. S. Netanyahu, C. D. Piatko, R. Silverman, and A. Y. Wu, "An efficient k-means clustering algorithm: Analysis and implementation", *IEEE transactions on pattern analysis and machine intelligence*, vol. 24, no. 7, pp. 881–892, 2002.

[189] C. Kübel, D. Niemeyer, R. Cieslinski, and S. Rozeveld, "Electron tomography of nanostructured materials – towards a quantitative 3d analysis with nanometer resolution", *Materials Science Forum*, vol. 638-642, pp. 2517–2522, 2010.

[190] K. J. Batenburg and J. Sijbers, "Optimal threshold selection for tomogram segmentation by projection distance minimization", *IEEE Trans Med Imaging*, vol. 28, no. 5, pp. 676–86, 2009.

[191] K. J. Batenburg and J. Sijbers, "Adaptive thresholding of tomograms by projection distance minimization", *Pattern Recognition*, vol. 42, no. 10, pp. 2297–2305, 2009.

[192] T. Aste and T. Di Matteo, "Emergence of gamma distributions in granular materials and packing models", *Phys Rev E Stat Nonlin Soft Matter Phys*, vol. 77, no. 2 Pt 1, p. 021 309, 2008.

[193] H. S. Carslaw and J. C. Jaeger, "Conduction of heat in solids", Clarendon Press, Report, 1959.

[194] W. van Aarle, W. J. Palenstijn, J. De Beenhouwer, T. Altantzis, S. Bals, K. J. Batenburg, and J. Sijbers, "The astra toolbox: A platform for advanced algorithm development in electron tomography", *Ultramicroscopy*, vol. 157, pp. 35–47, 2015.

[195] L. C, Y. W, and Z. Y, "User's guide for tval3: Tv minimization by augmented lagrangian and alternating direction algorithms", *CAAM report*, vol. 20, no. 46-47, p. 4, 2009.

[196] C. Li, "An efficient algorithm for total variation regularization with applications to the single pixel camera and compressive sensing", *Master's Thesis, Rice University*, 2010.

[197] T. Furnival, R. K. Leary, and P. A. Midgley, "Denoising time-resolved microscopy image sequences with singular value thresholding", *Ultramicroscopy*, vol. 178, pp. 112–124, 2017.

[198] N. Mevenkamp, P. Binev, W. Dahmen, P. M. Voyles, A. B. Yankovich, and B. Berkels, "Poisson noise removal from high-resolution stem images based on periodic block matching", *Advanced Structural and Chemical Imaging*, vol. 1, no. 1, 2015.

[199] J. Boulanger, C. Kervrann, P. Bouthemy, P. Elbau, J. B. Sibarita, and J. Salamero, "Patch-based nonlocal functional for denoising fluorescence microscopy image sequences", *IEEE Trans Med Imaging*, vol. 29, no. 2, pp. 442–54, 2010.

[200] A. Jezierska, C. Chaux, J.-C. Pesquet, H. Talbot, and G. Engler, "An em approach for time-variant poisson-gaussian model parameter estimation", *IEEE Transactions on Signal Processing*, vol. 62, no. 1, pp. 17–30, 2014.

[201] M. Makitalo and A. Foi, "Noise parameter mismatch in variance stabilization, with an application to poisson-gaussian noise estimation", *IEEE Trans Image Process*, vol. 23, no. 12, pp. 5348–59, 2014.

[202] C. R. A., D. D. J., and K. A., "The reconstruction of a three-dimensional structure from projections and its application to electron microscopy", *Proc. Roy. Soc. Lond. A*, vol. 317, no. 1530, pp. 319–340, 1970.

[203] S.-J. Reich, A. Svidrytski, D. Hlushkou, D. Stoeckel, C. Kübel, A. Höltzel, and U. Tallarek, "Hindrance factor expression for diffusion in random mesoporous adsorbents obtained from pore-scale simulations in physical reconstructions", *Industrial & Engineering Chemistry Research*, vol. 57, no. 8, pp. 3031–3042, 2018.

[204] M. Liebertseder, D. Wang, G. Cavusoglu, M. Casapu, S. Wang, S. Behrens, C. Kubel, J. D. Grunwaldt, and C. Feldmann, "Nacl-template-based synthesis of tio2-pd/pt hollow nanospheres for h2o2 direct synthesis and co oxidation", *Nanoscale*, vol. 13, no. 3, pp. 2005–2011, 2021.

[205] P. J. Bryant, H. S. Kim, Y. C. Zheng, Yang, and R., "Technique for shaping scanning tunneling microscope tips", *Review of Scientific Instruments*, vol. 58, no. 6, pp. 1115–1115, 1987.

[206] S. Patane, E. Cefali, A. Arena, P. G. Gucciardi, and M. Allegrini, "Wide angle near-field optical probes by reverse tube etching", *Ultramicroscopy*, vol. 106, no. 6, pp. 475–9, 2006.

[207] Y. Khan, H. Al-Falih, Y. Zhang, T. K. Ng, and B. S. Ooi, "Two-step controllable electrochemical etching of tungsten scanning probe microscopy tips", *Rev Sci Instrum*, vol. 83, no. 6, p. 063 708, 2012.

[208] J. Ibe, P. Bey Jr, S. Brandow, R. Brizzolara, N. Burnham, D. Dilella, K. Lee, C. Marrian, and R. Colton, "On the electrochemical etching of tips for scanning tunneling microscopy", *Journal of Vacuum Science & Technology A: Vacuum, Surfaces, and Films*, vol. 8, no. 4, pp. 3570–3575, 1990.

[209] J. Perezjuste, I. Pastorizasantos, L. Lizmarzan, and P. Mulvaney, "Gold nanorods: Synthesis, characterization and applications", *Coordination Chemistry Reviews*, vol. 249, no. 17-18, pp. 1870–1901, 2005.

[210] A. R. Tao, S. Habas, and P. Yang, "Shape control of colloidal metal nanocrystals", *Small*, vol. 4, no. 3, pp. 310–325, 2008.

[211] H. Wang, K. Kurata, T. Fukunaga, H. Takamatsu, X. Zhang, T. Ikuta, K. Takahashi, T. Nishiyama, H. Ago, and Y. Takata, "In-situ measurement of the heat transport in defect- engineered free-standing single-layer graphene", *Sci Rep*, vol. 6, p. 21 823, 2016.

[212] J. Kremer, D. Mastronarde, and J. McIntosh, "Computer visualization of three-dimensional image data using imod", *Journal of structural biology*, vol. 116, pp. 71–76, 1996.

[213] C. Wang, L. Han, R. Zhang, H. Cheng, L. Mu, K. Kisslinger, P. Zou, Y. Ren, P. Cao, F. Lin, and H. L. Xin, "Resolving atomic-scale phase transformation and oxygen loss mechanism in ultrahigh-nickel layered cathodes for cobalt-free lithium-ion batteries", *Matter*, vol. 4, no. 6, pp. 2013–2026, 2021.

[214] M. Yue, H. Lambert, E. Pahon, R. Roche, S. Jemei, and D. Hissel, "Hydrogen energy systems: A critical review of technologies, applications, trends and challenges", *Renewable and Sustainable Energy Reviews*, vol. 146, 2021.

[215] A. Yamashita, M. Kondo, S. Goto, and N. Ogami, "Development of high-pressure hydrogen storage system for the toyota "mirai"", SAE Technical Paper, Report 0148-7191, 2015.

[216] W. Xu, Q. Li, and M. Huang, "Design and analysis of liquid hydrogen storage tank for high-altitude long-endurance remotely-operated aircraft", *International Journal of Hydrogen Energy*, vol. 40, no. 46, pp. 16 578–16 586, 2015.

[217] J. Weitkamp, M. Fritz, and S. Ernst, "Zeolites as media for hydrogen storage", in *Proceedings from the ninth international zeolite conference*, Elsevier, pp. 11–19.

[218] R. Ströbel, J. Garche, P. Moseley, L. Jörissen, and G. Wolf, "Hydrogen storage by carbon materials", *Journal of power sources*, vol. 159, no. 2, pp. 781–801, 2006.

[219] Y. H. Hu and L. Zhang, "Hydrogen storage in metal–organic frameworks", *Advanced Materials*, vol. 22, no. 20, E117–E130, 2010.

[220] M. Rashid, M. K. Al Mesfer, H. Naseem, and M. Danish, "Hydrogen production by water electrolysis: A review of alkaline water electrolysis, pem water electrolysis and high temperature water electrolysis", *International Journal of Engineering and Advanced Technology*, 2015.

[221] A. Karkamkar, C. Aardahl, and T. Autrey, "Recent developments on hydrogen release from ammonia borane", *Mater Matters*, vol. 2, pp. 6–9, 2007.

[222] M. Grasemann and G. Laurenczy, "Formic acid as a hydrogen source–recent developments and future trends", *Energy & Environmental Science*, vol. 5, no. 8, pp. 8171–8181, 2012.

[223] D. Wang, H. He, L. Han, R. Lin, J. Wang, Z. Wu, H. Liu, and H. L. Xin, "Three-dimensional hollow-structured binary oxide particles as an advanced anode material for high-rate and long cycle life lithium-ion batteries", *Nano Energy*, vol. 20, pp. 212–220, 2016.

[224] K. Tedsree, T. Li, S. Jones, C. W. Chan, K. M. Yu, P. A. Bagot, E. A. Marquis, G. D. Smith, and S. C. Tsang, "Hydrogen production from formic acid decomposition at room temperature using a ag-pd core-shell nanocatalyst", *Nat Nanotechnol*, vol. 6, no. 5, pp. 302–7, 2011.

[225] A. Kosider, D. Blaumeiser, S. Schoetz, P. Preuster, A. Bösmann, P. Wasserscheid, J. Libuda, and T. Bauer, "Enhancing the feasibility of pd/c-catalyzed formic acid decomposition for hydrogen generation–catalyst pretreatment, deactivation, and regeneration", *Catalysis Science & Technology*, vol. 11, no. 12, pp. 4259–4271, 2021.

[226] D. Zhang, F. Ye, T. Xue, Y. Guan, and Y. M. Wang, "Transfer hydrogenation of phenol on supported pd catalysts using formic acid as an alternative hydrogen source", *Catalysis Today*, vol. 234, pp. 133–138, 2014.

[227] N. S. Biradar, A. A. Hengne, S. N. Birajdar, R. Swami, and C. V. Rode, "Tailoring the product distribution with batch and continuous process options in catalytic hydrogenation of furfural", *Organic Process Research & Development*, vol. 18, no. 11, pp. 1434–1442, 2014.

[228] Y. Wang, P. Prinsen, K. S. Triantafyllidis, S. A. Karakoulia, P. N. Trikalitis, A. Yepez, C. Len, and R. Luque, "Comparative study of supported monometallic catalysts in the liquid-phase hydrogenation of furfural: Batch versus continuous flow", *ACS Sustainable Chemistry & Engineering*, vol. 6, no. 8, pp. 9831–9844, 2018.

[229] D. Cantillo and C. O. Kappe, "Immobilized transition metals as catalysts for cross-couplings in continuous flow—a critical assessment of the reaction mechanism and metal leaching", *ChemCatChem*, vol. 6, no. 12, pp. 3286–3305, 2014.

[230] S. MacQuarrie, J. H. Horton, J. Barnes, K. McEleney, H. P. Loock, and C. M. Crudden, "Visual observation of redistribution and dissolution of palladium during the suzuki-miyaura reaction", *Angew Chem Int Ed Engl*, vol. 47, no. 17, pp. 3279–82, 2008.

[231] C. G. Frost and L. Mutton, "Heterogeneous catalytic synthesis using microreactor technology", *Green Chemistry*, vol. 12, no. 10, 2010.

[232] Y. Yang, S. Ogasawara, G. Li, and S. Kato, "Dendrimer-stabilized pd polymer composites: Drastic suppression of pd leaching and fine catalysis sustainability", *Polymer Journal*, vol. 47, no. 4, pp. 340–347, 2015.

[233] K. Köhler, R. Heidenreich, J. Krauter, and J. Pietsch, "Highly active palladium/activated carbon catalysts for heck reactions: Correlation of activity, catalyst properties, and pd leaching", *Chemistry–A European Journal*, vol. 8, no. 3, pp. 622–631, 2002.

[234] D. Motta, F. J. S. Trujillo, N. Dimitratos, A. Villa, and L. Prati, "An investigation on aupt and aupt-bi on granular carbon as catalysts for the oxidation of glycerol under continuous flow conditions", *Catalysis Today*, vol. 308, pp. 50–57, 2018.

[235] M. A. Newton, D. Ferri, C. J. Mulligan, I. Alxneit, H. Emerich, P. B. J. Thompson, and K. K. Hii, "In situ study of metal leaching from pd/al2o3 induced by k2co3", *Catalysis Science & Technology*, vol. 10, no. 2, pp. 466–474, 2020.

[236] F. Sanchez, M. H. Alotaibi, D. Motta, C. E. Chan-Thaw, A. Rakotomahevitra, T. Tabanelli, A. Roldan, C. Hammond, Q. He, T. Davies, A. Villa, and N. Dimitratos, "Hydrogen production from formic acid decomposition in the liquid phase using pd nanoparticles supported on cnfs with different surface properties", *Sustainable Energy & Fuels*, vol. 2, no. 12, pp. 2705–2716, 2018.

[237] X. Wang, G.-W. Qi, C.-H. Tan, Y.-P. Li, J. Guo, X.-J. Pang, and S.-Y. Zhang, "Pd/c nanocatalyst with high turnover frequency for hydrogen generation from the formic acid–formate mixtures", *International Journal of Hydrogen Energy*, vol. 39, no. 2, pp. 837–843, 2014.

[238] J.-P. Zhou, J. Zhang, X.-H. Dai, X. Wang, and S.-Y. Zhang, "Formic acid–ammonium formate mixture: A new system with extremely high dehydrogenation activity and capacity", *International Journal of Hydrogen Energy*, vol. 41, no. 47, pp. 22 059–22 066, 2016.

[239] R. Xu, C. C. Chen, L. Wu, M. C. Scott, W. Theis, C. Ophus, M. Bartels, Y. Yang, H. Ramezani-Dakhel, M. R. Sawaya, H. Heinz, L. D. Marks, P. Ercius, and J. Miao, "Three-dimensional coordinates of individual atoms in materials revealed by electron tomography", *Nat Mater,* vol. 14, no. 11, pp. 1099–103, 2015.

List of Publications (during PhD)

[1] X. Huang, Y. Tang, C. Kübel, and D. Wang, "Precisely picking nanoparticles by a "nano-scalpel" for 360° electron tomography", *Microscopy and Microanalysis*, pp. 1–8, 2022.

[2] X. Huang, D. Hlushkou, D. Wang, U. Tallarek, and C. Kübel, "Quantitative analysis of mesoporous structures by electron tomography: A phantom study", *Ultramicroscopy, accepted*, p. 113 639, 2022.

[3] X. Huang, I. Barlocco, A. Villa, C. Kübel, and D. Wang, "Disclosing the leaching behavior of pd@cmk3 catalysts in formic acid decomposition by electron tomography", *Nanocale Advances, submitted*, 2022.

[4] O. Schade, P. Dolcet, A. Nefedov, X. Huang, E. Saraçi, C. Wöll, and J.-D. Grunwaldt, "The influence of the gold particle size on the catalytic oxidation of 5-(hydroxymethyl)furfural", *Catalysts*, vol. 10, no. 3, 2020.

[5] F. Tajoli, N. Dengo, M. Mognato, P. Dolcet, G. Lucchini, A. Faresin, J. D. Grunwaldt, X. Huang, D. Badocco, M. Maggini, C. Kübel, A. Speghini, T. Carofiglio, and S. Gross, "Microfluidic crystallization of surfactant-free doped zinc sulfide nanoparticles for optical bioimaging applications", *ACS Appl Mater Interfaces*, vol. 12, no. 39, pp. 44 074–44 087, 2020.

[6] U. Tallarek, J. Hochstrasser, F. Ziegler, X. Huang, C. Kübel, and M. R. Buchmeiser, "Olefin ring-closing metathesis under spatial confinement: Morphology–transport relationships", *ChemCatChem*, vol. 13, no. 1, pp. 281–292, 2020.

[7] J. Wang, Y. Cui, Q. Wang, K. Wang, X. Huang, D. Stenzel, A. Sarkar, R. Azmi, T. Bergfeldt, S. S. Bhattacharya, R. Kruk, H. Hahn, S. Schweidler, T. Brezesinski, and B. Breitung, "Lithium containing layered high entropy oxide structures", *Sci Rep*, vol. 10, no. 1, p. 18 430, 2020.

[8] S. Wang, D. E. Doronkin, M. Hahsler, X. Huang, D. Wang, J. D. Grunwaldt, and S. Behrens, "Palladium-based bimetallic nanocrystal catalysts for the direct synthesis of hydrogen peroxide", *ChemSusChem*, vol. 13, no. 12, pp. 3243–3251, 2020.

[9] S. Weber, K. L. Abel, R. T. Zimmermann, X. Huang, J. Bremer, L. K. Rihko-Struckmann, D. Batey, S. Cipiccia, J. Titus, D. Poppitz, C. Kübel, K. Sundmacher, R. Gläser, and T. L. Sheppard, "Porosity and structure of hierarchically porous Ni/Al_2O_3 catalysts for CO_2 methanation", *Catalysts*, vol. 10, no. 12, 2020.

[10] E. Özkan, A. Hofmann, M. Votsmeier, W. Wang, X. Huang, C. Kübel, F. Badaczewski, K. Turke, S. Werner, and B. M. Smarsly, "Comprehensive characterization of a mesoporous cerium oxide nanomaterial with high surface area and high thermal stability", *Langmuir*, vol. 37, no. 8, pp. 2563–2574, 2021.

[11] S. Capelli, I. Barlocco, F. M. Scesa, X. Huang, D. Wang, F. Tessore, A. Villa, A. Di Michele, and C. Pirola, "Pd–au bimetallic catalysts for the hydrogenation of muconic acid to bio-adipic acid", *Catalysts*, vol. 11, no. 11, 2021.

[12] I. Barlocco, S. Capelli, X. Lu, S. Bellomi, X. Huang, D. Wang, L. Prati, N. Dimitratos, A. Roldan, and A. Villa, "Disclosing the role of gold on palladium – gold alloyed supported catalysts in formic acid decomposition", *ChemCatChem*, vol. 13, no. 19, pp. 4210–4222, 2021.

[13] O. Jin, Y. Shang, X. Huang, X. Mu, D. V. Szabó, T. T. Le, S. Wagner, C. Kübel, C. Pistidda, and A. Pundt, "Microstructural study of MgB_2 in the $LiBH_4 - MgH_2$ composite by using tem", *Nanomaterials*, vol. 12, no. 11, 2022.

[14] O. Jin, Y. Shang, X. Huang, D. V. Szabó, T. T. Le, S. Wagner, T. Klassen, C. Kübel, C. Pistidda, and A. Pundt, "Transformation kinetics of $LiBH_4 - MgH_2$ for hydrogen storage", *Molecules*, vol. 27, no. 20, 2022.

[15] S. Weber, R. T. Zimmermann, J. Bremer, K. L. Abel, D. Poppitz, N. Prinz, J. Ilsemann, S. Wendholt, Q. Yang, R. Pashminehazar, F. Monaco, P. Cloetens, X. Huang, C. Kübel, E. Kondratenko, M. Bauer, M. Bäumer, M. Zobel, R. Gläser, K. Sundmacher, and T. L. Sheppard, "Digitization in catalysis research: Towards a holistic description of a Ni/Al_2O_3 reference catalyst for CO_2 methanation", *ChemCatChem*, 2022.

[16] S. Chen, X. Huang, D. Schild, D. Wang, K. C, and S. Behrens, "Pd-in intermetallic nanoparticles with high catalytic selectivity for liquid-phase semihydrogenation of diphenylacetylene", *Nanoscale, accepted*, 2022.

[17] E. Costa, X. Huang, C. Kübel, X. Cheng, K. Schladitz, A. Hofmann, U. Göbel, and S. B., "Effects of hydrothermal treatment on mesopore structure and connectivity in complex $Ce_xZr_{1-x-y}Y_yLa_zO_{2-\sigma}$ mixed oxides", *Langmuir, under review*, 2022.

[18] K. Wang, X. Mu, W. Hua, X. Huang, D. Stenzel, J. Wang, Z. Ding, Y. Cui, Q. Wang, H. Ehrenberg, B. Breitung, and K. C., "Synergy between cations resulting in a stable conductive nanoscale network in a high-entropy metal oxide lithium ion battery anode", *Nature Communication, under review*, 2022.

[19] B. Sarma, J. Jelic, D. Neukum, D. Doronkin, X. Huang, F. Studt, and G. J., "Tracking and understanding dynamics of atoms and clusters of late transition metals with in-situ drift and xas spectroscopy assisted by dft", *The Journal of Physical Chemistry, Submitted*, 2022.

A. Curriculum Vitae

Personal Information：

   Name: Xiaohui Huang

   Nationality： Chinese

   Date of birth： 13-12-1993

   Place of birth： Guangxi, China

Education：

PhD in Material Science	2019 - 2022
Technical University of Darmstadt, Darmstadt, Germany.	
Master of Science in Physical Chemistry	2015 - 2018
University of Science and Technology of China, Hefei, China.	
Bachelor of Engineering in Chemical Engineering & Technology	2011 - 2015
Harbin Institute of Technology, Harbin, China.	

B. Acknowledgements

Time flies by, and the completion of this thesis marks the end of my more than 20 years of systematic studies. I would first like to thank myself for my efforts and insistence over the years. Also, thanks to the help of many other people, I have become the better version of myself I am today.

I would like to thank my supervisor Prof. Christian Kübel for giving me the opportunity to study for a doctorate in Germany. During the regular academic discussions I have with him about my research topic, I have a clearer and deeper understanding of electron tomography. His rigorous attitude towards scientific research and the hard-working spirit have also benefited me a lot. These invaluable experiences have taught me that scientific research needs to really figure out the reasons behind it, rather than just get pretty data out of a black box to publish good papers. Thanks to my daily supervisor Dr. Di Wang for the training in TEM and the patient guidance in my daily research work, and especially for his full support when I encountered difficulties. For me, he is more like a kind elder and also a strong backer during my studies as a Ph.D student.

I would like to thank Prof. Ulrich Tallarek and Dr. Dzmitry Hlushkou for their contributions to diffusion simulation in my research work and for the valuable discussions. Also, I would like to thank Prof. Alberto Villa and Dr. Illaria Barlocco for their enormous contributions in catalyst synthesis, catalytic testing and scientific discussions.

I would also like to thank Dr. Xiaoke Mu, Dr. Yushu Tang, Charlotte Neidiger and Ou Jin for their valuable suggestions and advice for my research work. My thanks also extend to Dr. Dorothee-Vinga Szabo, Dr. Sabine Schlabach, Dr. Torsten Scherer, Dr. Georgian Melinte, Dr. Wu Wang, Dr. Alexey Boubnov, Dr. Svetlana Korneychuk, Dr. Carina Maliakkal, Dr. Andrey Mazikin, Dr. Mehrdad Jalali, Vanessa Wollersen, Sangjun Kang, Ziming Ding, Yuting Dai, Vahid Tavakkoli, Yi Wu, Maximilian Töllner, Lucas Brauch, Ajai Rai Lakshmi Nilayam and all other members of the electron microscopy & spectroscopy group (EMSG) for their friendly support in my research. I would also like to thank Dr. Kai Wang and his wife Can Su for our precious friendship these past few years.

Additionally, I would like to thank the China Scholarship Council (CSC) for the financial support during my PhD research in Germany. I would also like to thank Karlsruhe Nano Micro Facility (KNMFi) for the usability support of the microscope.

Last but not least, I am deeply grateful to my parents and my sisters for their constant support throughout my life. And I particularly thank my grandmother, who gave me the deepest love and the best times of my childhood. This happy time has given me the courage to face whatever difficulties and frustrations I encounter. Although you have left me for many years, you will always live in my heart and I really miss you. Special thanks to my boyfriend (I should use ex- now) for his unconditional support, understanding and encouragement over the past seven years. I hope we will one day meet again.